ATOM ABSTRACTION IN THE INTERACTION OF F_2 AND XeF_2 WITH Si(100)

by

DAVID GOSALVEZ-BLANCO

B.S. THE UNIVERSITY OF CALIFORNIA AT BERKELEY
(1992)

SUBMITTED TO THE DEPARTMENT OF CHEMISTRY
IN PARTIAL FULFILLMENT OF THE REQUIREMENTS
FOR THE DEGREE OF
DOCTOR OF PHILOSOPHY

AT THE

MASSACHUSSETTS INSTITUTE OF TECHNOLOGY

SEPTEMBER 1997

© Massachusetts Institute of Technology 1997
All rights reserved

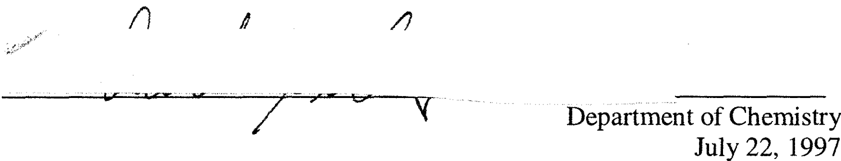

Signature of Author
Department of Chemistry
July 22, 1997

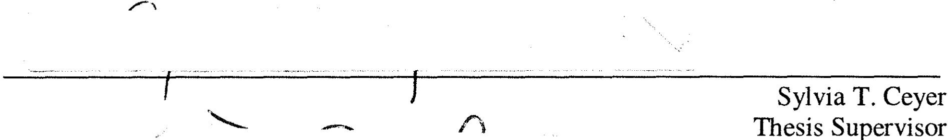

Certified by
Sylvia T. Ceyer
Thesis Supervisor

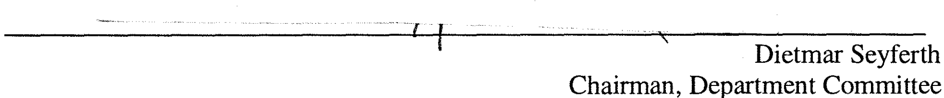

Accepted by
Dietmar Seyferth
Chairman, Department Committee

SEP 17 1997

This doctoral thesis has been examined by a Committee of the Department of Chemistry as follows:

Professor Robert J. Silbey ____
Chairman

Professor Sylvia T. Ceyer ____
Thesis Supervisor

Professor Keith A. Nelson ____

ATOM ABSTRACTION IN THE INTERACTION
OF F_2 AND XeF_2 WITH Si(100)

by

DAVID GOSALVEZ-BLANCO

Submitted to Department of Chemistry on
July 22, 1997 in partial fulfillment of the
requirements for the Degree of Doctor of Philosophy
in Chemistry

ABSTRACT

The chemisorption dynamics of thermal energy F_2 and XeF_2 interacting with Si(100) are investigated in an ultra-high vacuum molecular beam scattering chamber. The apparatus is equipped with a differentially pumped line-of-sight quadrupole mass spectrometer which enables the detection of highly reactive radical species produced during the gas-surface interaction. The interaction of thermal energy F_2 with Si(100) 2x1 can lead to three different outcomes: unreactive scattering, two-atom adsorption, and single-atom abstraction. The absolute probabilities of each of these reaction channels are determined. Since both the scattered F and F_2 ionize to produce F^+, the F product is primarily distinguished on the basis of its different velocity and dependence on exposure. A detailed mass balance of the incident and scattered fluorine allows for the determination of the absolute reaction probabilities and the fluorine coverage on the Si surface as a function of F_2 exposure. The unreactive scattering probability, P_0, is 0.05±0.01 on the clean surface but rapidly increases with surface coverage, reaching unit probability at saturation coverage. The two-atom adsorption probability, P_2, exhibits an initial value of 0.85±0.03 on the clean surface and drops linearly with coverage, vanishing at saturation coverage. The single-atom abstraction probability starts at a value of 0.10±0.03 for the clean surface, then goes through a maximum value of 0.3±0.85 at a coverage of approximately 0.5 ML, and finally drops to zero on the fluorine saturated surface. The total reaction probability is 0.95±0.04. The fluorine coverage obtained by integrating the exposure dependent reaction probabilities saturates at a value of 1.06±0.05 ML. The value of the saturation coverage coupled with helium diffraction measurements on the clean and fluorinated Si(100) 2x1 surface confirm that the Si dangling bonds are both the abstraction and adsorption sites, and that no Si—Si dimer or bulk bonds are cleaved during the chemisorption of F_2. Within the detection sensitivity of the apparatus, no silicon containing etch products are observed with thermal F_2 incident on a 250 K Si surface.

Three phenomenological models based on the lattice-gas formalism are shown to reproduce the major features of the data and provide some insight into the adsorption and abstraction mechanisms. Atom abstraction occurs when an incident F_2 molecule finds an empty site onto which to adsorb, but its complementary F atom does not. The orientation of the bond axis of the incident F_2 with respect to the surface is one factor that affects the ability of the second F atom to find a reactive site onto which to bind. The occupation of the Si atoms surrounding the initial abstraction site, is a second factor which determines the likelihood that the complementary F atom is ejected to the gas phase. Following an abstraction event, the ejected F atom may find a reactive site and also adsorb on the surface. The linear dependence of the two-atom adsorption probability with fluorine coverage suggests that a single Si dimer pair is most likely responsible for the adsorption of two fluorine atoms from a single incident F_2 molecule.

Single-atom abstraction is also demonstrated in the interaction of XeF_2 with Si(100) by the mass spectrometric identification of XeF ejected to the gas phase. The identification of XeF is complicated by the dissociative ionization of unreactively scattered XeF_2 and by the ionization of Xe arising from the two-atom adsorption process. The exposure dependence as well as the velocity and angular distributions of XeF_2^+, XeF^+, Xe^+ and F^+ are used to confirm the abstraction a single F atom from an incident XeF_2 molecule. The exposure dependence of the XeF^+ signal is reminiscent of that observed for the F atoms ejected in the interaction of F_2 with Si(100). The XeF product is primarily observed at scattering angles near the surface normal, with its intensity rapidly decreasing with increasing scattering angle. The unusual angular and exposure dependence of the ejected XeF product are exploited to deconvolute the mass spectrometer signals into the neutral products giving rise to them. The XeF fragment ejected from the surface gains some of the reaction's exothermicity as evidenced by its translational excitation, which is confirmed by time-of-flight measurements. The exothermicity of the reaction is also observed to induce the gas phase dissociation of the ejected XeF fragment. The chemically induced dissociation of XeF is inferred from the observation of very fast F^* atoms thought to arise from the gas phase decomposition of vibrationally or electronically excited XeF^*.

Thesis Supervisor: Sylvia T. Ceyer

Title: Professor of Chemistry

ACKNOWLEDGEMENTS

The work presented in this thesis is the product of the combined efforts of over a dozen people for the last ten years. I would like to thank the first generation of "BiMPs" because their careful design and construction of the apparatus afforded me the chance to work with one of the best instruments in the business. In addition, many of the key ideas and experiments that laid down the foundation of the F_2 work must be credited to them. From my early years in the project I would like to thank Dr. Julius Yang, Dr. Yulin Li and Dr. David Pullman for teaching me the intricacies of the apparatus. Dave was responsible for innumerable improvements to the apparatus as well as for the design of many of the experiments aimed at calibrating the flux of the incident beam and scattered products. I benefited greatly from Dave's extensive experience with molecular beams and vacuum technology as well as from his programming ability. Most of the computer code utilized for the data acquisition and analysis, which greatly simplified my work, must be credited to him. His dedication to the project, his unlimited patience and endless good humor made him an ideal coworker during many late night runs.

My contributions to the project are shared with Dr. Thanos Tsekouras and Matthew Tate. Thanos relentlessly challenged all my bad ideas and helped turn them into reasonable ones. I could always count on him to catch and correct my many careless mistakes both in dealing with the apparatus and analyzing the experimental results. His uncanny ability to fix and improve the apparatus kept us up and running through many vacuum mishaps. I have certainly missed Thanos' oversight during the preparation of my thesis. I can assure the reader that the many inaccuracies and typographical errors found in this work would have certainly been eradicated by Thanos. Matthew Tate joined the project and rapidly took the helm. It is customary for the senior students to teach the new members of the team, but in the Matthew's case, he quickly learned the few things that I could teach him and then proceeded to teach me the many things I did not know. His addition to the project catalyzed the completion of the F_2 experiments and has added new dimensions to the XeF_2 work of which he has now taken charge. It has been a pleasure working with Matthew over the past three years, and wish him the best of luck in his future scientific endeavors.

The latest additions to the project include Stacey Eckman and Dr. Massimo Bertino. Stacey brings and endless supply of friendly smiles and a positive attitude to the group. Her constant words of encouragement and occasional candy bar kept me going through the long writing sessions. Massimo has quickly become a close friend, and I regret not being able to spend more time with him before my departure. I wish him luck in his scientific career and hope that we will cross paths again in the future.

I have also enjoyed keeping up a friendly rivalry with the "LiMP" team. Kerstin Haug and Thomas Bürgi deserve credit for putting up with my constant teasing while they tried to tune their EELS spectrometer. I am grateful to Judson Holt for the use of his personal computer during a fatal hard drive crash in the last stages of the writing of this thesis, and for putting up with all my bad jokes about Rice University.

In a more personal note, I would like to thank my close friends and family. My first years at MIT were marked by close friendships with Chris Murray, Ted Trautman, Marc Wefers and Sean Daley. We had some great times together and I hope that we keep in

touch in the years to come. Fernando Bergasa has also been a close friend over the past six years, and I have enjoyed our many conversations about subjects ranging from the paradoxes of quantum mechanics or the intricacies of protein folding, to the right amount of vodka to add to a sangria.

Cathy and Victoria have given me the motivation to keep working through the hard times. I love you both more than life itself, and would like to thank Cathy for all her love, support and encouragement over the past five years. My parents deserve my most heartfelt gratitude for their generosity and unwavering support in all my endeavors. After a long 10 year absence from their side I look forward to spending some quality time with them. I thank Sherilyn, Jim and Jaime Harrison for their boundless generosity and support of Cathy, Victoria and me. Charles Edgar and Carolyn McCarthy have been a constant source of support and have provided some very welcomed hospitality during our Cape Cod escapades. I am greatly indebted to the Fordyce family for adopting me during my college years and continued support after I left California. I hope we can keep up our wonderful friendship in spite of the long distance between us.

Finally, I would like to thank my advisor Sylvia Ceyer. Her uncompromising commitment to involve herself in only the highest quality scientific research is solely responsible for her international prestige. She has pushed me for the last six years to strive for the best possible work and patiently waited for the results that she knew could be achieved. Without her determination, the quality of the work here presented would have greatly suffered from my haste. I am also very grateful to Sylvia for her extensive help in editing and proofreading the many revisions of this manuscript. This work is as much hers as it is mine.

TABLE OF CONTENTS

ABSTRACT 3

ACKNOWLEDGEMENTS 5

LIST OF FIGURES 9

LIST OF TABLES 11

PREFACE 12

1 CHAPTER I: THE INTERACTION OF F_2 WITH Si (100) 16

1.1 INTRODUCTION 17

1.2 EXPERIMENTAL APPARATUS 21
1.2.1 Description 21
1.2.2 Modifications to the Apparatus 27
1.2.2.1 Attachment of Crystal Temperature Thermocouple 27
1.2.2.2 Changes to Detector Box Turbo Molecular Pumps 29
1.2.2.3 Detector Box Pin-hole 30

1.3 SUMMARY OF EXPERIMENTAL RESULTS 33
1.3.1 Time-of-flight Measurements of the Scattered F and F_2 33
1.3.2 Exposure Dependence of the Scattered F and F_2 42
1.3.3 Thermal Desorption Measurements 47
1.3.4 Helium Atom Diffraction Measurements 53

1.4 EXPOSURE DEPENDENCE OF THE FLUORINE COVERAGE 60
1.4.1 The Probabilities of the Reaction Channels 60
1.4.1.1 Measurement of the Electron Impact Ionization Cross-sections 68
1.4.1.2 Determination of the Quadrupole Transmission Function 72
1.4.2 Scattering Angle Dependence of the Reaction Probabilities 74
1.4.3 Calculation of the Exposure Dependent Surface Coverage 79
1.4.4 Determination of Molecular Beam Fluxes 82
1.4.4.1 Determination of the Flux of Single Component Molecular Beams 82
1.4.4.2 Determination of the Flux of Seeded Molecular Beams 86
1.4.4.3 Pumping Speed Measurements 89
1.4.4.4 Measurement of the Reaction Chamber Volume 92
1.4.4.5 Ion Gauge Sensitivity Correction Factor 93

1.5 DISCUSSION 97
1.5.1 Physical Picture Resulting from the Experimental Results 97
1.5.2 Qualitative Features of the F_2 + Si (100) Potential Energy Surface 99
1.5.3 The Dependence of the Reaction Probabilities on Fluorine Coverage 104
1.5.3.1 Lattice-gas Model for the Dissociative Chemisorption of F_2 on Si(100) 107
1.5.3.2 Three-state Lattice-gas Model 121
1.5.3.3 Extended Three-state Lattice-gas Model 135

1.6 CONCLUSIONS 140

2 CHAPTER II. THE INTERACTION OF Si(100) WITH XeF_2 141

2.1 INTRODUCTION 142
2.1.1 An Overview of Previous Experimental Work 142
2.1.1.1 Measurements of the Si Etch Rates 143
2.1.1.2 Identification of the Gas-phase Etch Products 144
2.1.1.3 Composition and Growth of the Fluorinated Surface Layer 145
2.1.2 Atom Abstraction in the Interaction of XeF_2 with Si(100) 148
2.1.3 Background on XeF_2 150
2.1.3.1 The Discovery of XeF_2 and Noble Gas Compounds 150

2.1.3.2 Physical Properties of XeF_2 ... 152
2.1.3.3 Thermodynamic Properties of XeF_2 ... 152
2.1.3.4 Mass Spectrometry of XeF_2 ... 154
2.1.3.5 XeF_2 Effusive Beams ... 155

2.2 EXPERIMENTAL ... 157
2.2.1 Production of Seeded Supersonic XeF_2 Beams ... *157*
2.2.1.1 XeF_2 Mixing Cylinders ... 157
2.2.1.2 Passivation Issues ... 159
2.2.2 Characterization of Seeded Supersonic XeF_2 Beams ... *163*
2.2.2.1 Mass Spectra of XeF_2 Beams ... 163
2.2.2.2 Van der Waals Clustering in the Beam ... 166
2.2.2.3 Velocity Distribution of Seeded XeF_2 Beams ... 175
2.2.3 Fragmentation of XeF_2 by Electron Impact Ionization ... *178*
2.2.3.1 Scattering from an Inert SiO Surface ... 179

2.3 RESULTS ... 188
2.3.1 Observation of Unreactively Scattered XeF_2 ... *192*
2.3.2 Identification of Atom Abstraction by Observation of XeF ... *197*
2.3.3 Observation of Scattered Xe Product ... *205*
2.3.4 Other Evidence for the Reaction of XeF_2 with Si(100) ... *223*
2.3.4.1 Thermal Desorption Products and Surface Fluorine Coverage ... 223
2.3.4.2 Identification of the Order of the Adsorbed Products by Helium Diffraction ... 230
2.3.5 Preliminary Results at Higher XeF_2 Incident Energy ... *235*
2.3.5.1 XeF_2/He Scattered from Si(100) ... 235

2.4 DISCUSSION ... 241

2.5 CONCLUSIONS ... 257

3 APPENDICES ... 258

APPENDIX A: ERROR ANALYSIS ... 259

APPENDIX B: UNCERTAINTY IN CROSS-CORRELATION TOF ... 276

APPENDIX C: ATTENUATION OF THE MOLECULAR BEAM ... 280

APPENDIX D: RELATIVE TDS PRODUCT YIELD ... 285

APPENDIX E: MINIMUM SQUARE SCALING ALGORITHMS ... 290

LIST OF FIGURES

Figure 1.1 Schematic Diagram of the UHV Beam-surface Scattering Apparatus 26
Figure 1.2 Straight-Through Signal as a Function of Pin-hole Position 32
Figure 1.3 Time-of-Flight Spectra of Scattered 1%F_2/Kr 38
Figure 1.4 F_2 and SiF_2 Time-of-flight Spectra from a 1000 K Si(100) Surface 39
Figure 1.5 Time-of-flight Spectra of F Atoms Ejected from a 1000K Si(100) 40
Figure 1.6 Energy Distributions of F-atoms from 250K and 1000 K Surfaces 41
Figure 1.7 Exposure Dependence of Scattered F^+ and F_2^+ Signal 46
Figure 1.8 Thermal Desorption Spectra of Si(100) Exposed to 1%F_2/Ar 51
Figure 1.9 Total Fluorine Thermal Desorption Yield as a Function of F_2 Exposure 52
Figure 1.10 Structure of Unreconstructed and Reconstructed Si(100) 58
Figure 1.11 He Diffraction Spectra of a Clean and Fluorinated Si(100) 59
Figure 1.12 Exposure Dependence of F_2 Reaction Probabilities 67
Figure 1.13 Angular Distribution of Scattered F and F_2 77
Figure 1.14 Reaction Probabilities Measured at Various Scattering Angles 78
Figure 1.15 Fluorine Coverage as a Function of F_2 Exposure 80
Figure 1.16 Coverage Dependence of F_2 Reaction Probabilities 81
Figure 1.17 Pumping Speed Curves for Ar and Ne 91
Figure 1.18 Ar Expansion Measurement for Ion Gauge Calibration 96
Figure 1.19 Reaction Probabilities Predicted by the Lattice-gas Model 119
Figure 1.20 Lattice-gas Model Probabilities as a Function of Coverage 120
Figure 1.21 Reaction Probabilities Predicted by Three-state Model 133
Figure 1.22 Three-state Model Probabilities as a Function of Coverage 134
Figure 1.23 Extended Three-state Model Probabilities as a Function of Coverage 139
Figure 2.1 Initial Time Evolution of the XeF_2 Fragments from the Clean Nozzle 162
Figure 2.2 Mass Spectrum of Xe Isotopes from a Xe/Ar Molecular Beam 164
Figure 2.3 Mass Spectrum of XeF_2/He Molecular Beam 165
Figure 2.4 Mass Spectrum of XeF_2/Kr Molecular Beam 170
Figure 2.5 High and Low Resolution Mass Spectra of XeF_2/Ar Molecular Beam 171
Figure 2.6 Fit of XeF_2/Ar Signal to a $\mathbf{XeF_2^+}$ and $[Xe\text{--}Ar]^+$ Superposition 172
Figure 2.7 Mass Spectra of Xe/Ar and XeF_2/Ar Molecular Beams 173
Figure 2.8 Mass Spectra Demonstrating the Existence of XeF_2--Ar in the Beam 174
Figure 2.9 Time-of-flight Spectra of XeF_2/Kr and XeF_2/Ar Beams 176
Figure 2.10 Time-of-flight Spectra of XeF_2/He/Ar Beams 177
Figure 2.11 XeF_2 Scattered from Inert Silicon Oxide Surfaces 184

Figure 2.12 Thermal Desorption Products from Inert Surface 185
Figure 2.13 Thermal Desorption Products from Inert Surface 186
Figure 2.14 Angular Distribution of Scattered XeF_2 from a Silicon Oxide Surface 187
Figure 2.15 Scattered Products as a Function of Exposure to a XeF_2/Ar Beam 190
Figure 2.16 Scattering Angle Dependence of the XeF_2/Si Reaction Products 191
Figure 2.17 Angular Distribution of Scattered XeF_2 195
Figure 2.18 Time-of-flight Spectra of XeF_2 Unreactively Scattered from Si(100) 196
Figure 2.19 XeF from Atom Abstraction Detected as XeF^+ 201
Figure 2.20 Exposure Dependence XeF Product at Eight Scattering Angles 202
Figure 2.21 Angular Distribution of XeF Product 203
Figure 2.22 Time-of-flight Spectra of Scattered XeF^+ Signal 204
Figure 2.23 Partial Deconvolution of Xe^+ Signal detected at 0° 213
Figure 2.24 Partially Deconvoluted Xe^+ as a Function of Scattering Angle 214
Figure 2.25 Deconvolution of Xe and XeF Contributions to the Xe^+ Signal 215
Figure 2.26 Comparison of XeF Product Detected as XeF^+ and Xe^+ 216
Figure 2.27 Time-of-flight Spectra of Scattered Xe^+ Signal 217
Figure 2.28 Time-of-flight Spectra of Scattered F^+ Signal 218
Figure 2.29 Angular Distribution of SiF_3^+ 221
Figure 2.30 Time-of-flight Spectra of Scattered SiF_3^+ Signal 222
Figure 2.31 Thermal Desorption Products from Si(100) Exposed to XeF_2 227
Figure 2.32 Comparison of TD Products from F_2 and XeF_2 Fluorination 228
Figure 2.33 TD Product Yield as a Function of Exposure to XeF_2/Ar 229
Figure 2.34 He Diffraction Spectra of Clean and XeF_2 Exposed Si(100) 232
Figure 2.35 He Diffraction Spectra as a Function of XeF_2/Ar Exposure 233
Figure 2.36 Peak He-diffraction Intensity as a Function of XeF_2/Ar Exposure 234
Figure 2.37 Scattered Products as a Function of Exposure to 0.2% XeF_2/He 238
Figure 2.38 Scattered Products as a Function of Exposure to 0.05% XeF_2/He 239
Figure 2.39 TD Product Yield as a Function of Exposure to XeF_2/He 240
Figure 2.40 Exposure Dependence of the XeF_2 and Etch Products 253
Figure 2.40 Exposure Dependence of Xe and XeF Products 254
Figure 2.41 Total Reaction Probability of a XeF_2/Ar Beam Exposed to Si(100) 255
Figure 2.42 Comparison of Angular Distribution of XeF^+ and Xe^+ Signals 256
Figure 3.1 Main Chamber Pressure as a Function of Beam Stagnation Pressure 284
Figure 3.2 Angular Distributions of Thermal Desorption Products 289

LIST OF TABLES

Table 1-1 Parameters Describing Velocity Distribution of F_2 in Seeded Beams............25
Table 1-2 Absolute Values Required for Calculation of Reaction Probabilities 66
Table 1-3 Values Required for Calculation of F_2 Ionization Cross-sections...................71
Table 1-4 Values Required for Calculation of Relative Transmissivity..........................74
Table 1-5 Values Required for Determination of Fluxes by Steady-state Method..........84
Table 1-6 Values Required for Determination of Fluxes by the Stagnant Method..........85
Table 1-7 Flux of Pure Ar and Ne Molecular Beams 86
Table 1-8 Values Required for Determination of Seeded Beam Fluxes..........................88
Table 1-9 Flux of Seeded Molecular Beams...89
Table 1-10 Pumping Speeds..90
Table 1-11 Values Required for the Determination of Ion Gauge Correction Factors 95
Table 2-1 Some Physical Properties of XeF_2..154
Table 2-2 Parameters Describing Velocity Distribution of XeF_2 in Seeded Beams 175
Table 2-3 Cracking Ratios for XeF_2..183
Table 3-1 Estimated Uncertainties in the Determination of the Pure Beam Flux.........265
Table 3-2 Estimated Uncertainties in the Seeded Beam Flux Determination................268
Table 3-3 Estimated Uncertainty in the Determination of F_2 and F Velocity Ratio 269
Table 3-4 Estimated Uncertainties for the Determination of Transmission Ratio 272
Table 3-5 Estimated Uncertainties for the Determination of Cross-section Ratio.........273
Table 3-6 Values Required for Determination of Expected Pressure Ratio 283
Table 3-7 Values Required for the Calculation of Relative TDS Yield........................288

PREFACE

The dry etching of silicon is an essential reaction in the manufacturing of semiconductor based electronic devices in very large scale integrated circuits (VLSI). Dry etching involves the reaction of silicon with an ignited plasma typically containing CF_4 as well as inert buffer gases. The thermodynamic driving force behind the etching reaction is the large Si-F bond energy (~140 kcal/mol) and the ultimate formation of stable but volatile SiF_X products (i.e. SiF_4, Si_2F_6 , Si_3F_8...). The most active chemical species in the plasma is believed to be the F atoms which, due to their open shell electronic structure readily attack the silicon surface. Emphasis has also been placed on the importance of "chemical sputtering", an ill-defined superposition of physical sputtering and chemical reactions, in which the combination of chemically reactive neutrals and ionic species present in the plasma are believed to enhance cooperatively the etch rate of the Si surface. Many mechanisms have been proposed for this reaction, but no definitive experimental confirmation has yet been obtained.

Extensive work has been performed over the last twenty years on simplified model systems. These studies include numerous measurements of the etch rates and reaction kinetics as well as molecular beam studies aimed at clarifying the dynamics of the interaction. A number of experiments designed to investigate this reaction have used F_2 and XeF_2 as convenient sources of fluorine atoms for the reaction. An interesting, yet puzzling result is that, at room temperature, XeF_2 etches silicon at a rate approximately 10,000 times faster than F_2. In addition, it is found that the etch rate of Si with XeF_2 is at least one order of magnitude faster than that of F atoms. This observation casts some doubt on the importance of the open shell nature of the F atom, and calls for an explanation of the unusually large etch rates obtained with the less thermodynamically favorable reactant, XeF_2

Previous work in the Ceyer group has established some important facts about the reactivity of F_2 molecules with the Si(100) surface which may help to understand the underlying reasons for the unusually high XeF_2 reactivity, and may also shed new light on the mechanism for the plasma reaction. Low energy, molecular F_2 is found to dissociatively chemisorb onto a clean Si(100) 2x1 reconstructed surface. Helium diffraction results show that the incoming F_2 exclusively fluorinates the Si dangling bonds (1 dangling bond/Si atom) producing a monolayer structure which retains the clean surface (2x1) periodicity. This observation implies that low energy fluorine can break neither the Si surface dimer bonds nor the bonds between the top and second layer of Si atoms. This monolayer saturation coverage is consistent with the low etching rate measured for F_2, since etching requires cleavage of the dimer and second layer Si bonds. In addition, the existence of a novel mechanism by which the F_2 molecule adsorbs on the dangling bonds has been demonstrated. Briefly, this new mechanism, denoted "F atom abstraction", consists of the abstraction of a single fluorine atom by a Si dangling bond from a fluorine molecule impinging on the surface, with the subsequent ejection of the complementary F atom. Depending on the orientation of the F_2 molecule as it approaches the surface, the complementary atom may be ejected either away from or towards the surface. In the latter case, if the ejected atom encounters an empty dangling bond site, it may also adsorb on the surface. Although the ejected atom gains a significant amount of translational energy from the exothermicity of the bond breaking step, and may be propelled into the Si with higher than thermal velocities, it is found not to break dimer or second layer Si bonds, as verified by helium diffraction.

The first half of the present investigation extends the study of the interaction of F_2 with Si(100), corroborating the inability of F_2 to fluorinate the Si surface beyond a saturation coverage of 1 ML. A careful quantitative analysis of F_2 scattering data allows for the determination of the F_2 reaction probability, from which the surface fluorine

coverage is calculated as a function of F_2 exposure. The measurement of the reaction probability from mass spectrometric data requires the determination of various electron ionization cross-sections as well as the careful calibration of reactant flux and mass spectrometer sensitivity. The experimental details of the absolute F_2 reaction probability measurement, and its subsequent use to measure the surface coverage are the primary subjects of Chapter I. Determination of the saturation coverage as 1 ML is consistent with the helium diffraction results, and confirms the inability of F_2 to cleave Si—Si dimer bonds and thus to etch Si.

In contrast, studies have shown that XeF_2 can fluorinate the Si surface well beyond the monolayer limit encountered in the F_2 reaction. This result is consistent with the high etch rates, since it is believed that the etching proceeds via a thick (~7 ML) SiF_x reaction overlayer. The main difference between F_2 and XeF_2 must lie in the ability of the latter to break surface and lattice bonds and thus fluorinate the silicon surface beyond the single-monolayer limit. A hypothesis is proposed that XeF_2 is able to fluorinate the surface to higher coverages than F_2 because the XeF molecule is able to transfer, due to its large mass, a large fraction of its incident kinetic energy to the silicon lattice, thus creating local excitations or distortions of the lattice which activate the reaction of F with the lattice. In the case of F_2, the hypothesis notes that F_2 is too light to transfer a large enough fraction of its energy to the surface to induce the lattice distortions which activate the reaction. The importance of kinetic energy transfer is also supported by the observation that XeF_2 has a faster etching rate than the much more reactive, but lighter, fluorine atom, which cannot vibrationally excite the surface. The role of energy transfer may be additionally important because it could account for the enhanced reactivity observed under plasma conditions, since many of the very energetic ionic species present in the plasma do transfer a substantial amount of momentum to the lattice and thus maintain a supply of vibrationally excited reactive sites on the silicon surface.

Although the experimental confirmation of the energy transfer hypothesis is beyond the scope of the current investigation, an important step towards demonstrating its validity is currently undertaken. The first step in assessing the validity of the proposed hypothesis is the corroboration of the existence of the F atom abstraction mechanism in the interaction of XeF_2 with a Si(100). The work presented in Chapter II establishes the operability of the F atom abstraction mechanism in the XeF_2/Si system by the mass spectrometric identification of the ejected XeF fragment. Furthermore, the velocity distribution of the XeF product is measured and found to be consistent with a large degree of translational excitation of the ejected fragment, likely arising from the exothermicity of the abstraction reaction. A XeF fragment propelled towards the fluorinated Si surface has both the large of momentum required to induce local vibrational excitation of the lattice, and the thermodynamic instability of the weakly bound F atom. The challenge of assessing the relative importance of momentum transfer and reactant stability in the unusually high reactivity of XeF_2 towards Si remains ahead[1,2].

[1] M. R. Tate, Massachusetts Institute of Technology, in preparation.

[2] S. C. Eckman, Massachusetts Institute of Technology, in preparation.

1 CHAPTER I: THE INTERACTION OF F_2 WITH Si (100)

1.1 INTRODUCTION

An important function of a surface in heterogeneous catalysis or chemical vapor deposition is to cleave a bond of an incident gas phase molecule. This cleavage process is commonly referred to as dissociative chemisorption, and results in the chemical binding of the incident molecule to the surface as two separate adsorbates. Because the surface-to-adsorbate bonds in the majority of gas-surface interactions are weaker than the internal bond of the impinging molecule, the energetic cost required to break the internal bond in the impinging molecule necessitates the formation of two adsorbate-surface bonds in order to render the overall process exothermic.

Based on the investigation of the reactivity of gas phase F_2 incident on a Si(100) 2x1 surface, Ceyer et al.[3] have demonstrated a new mechanism for dissociative chemisorption termed atom abstraction. Atom abstraction differs from the classic dissociative chemisorption process in that only one of the two molecular fragments of the incoming species binds to the surface. In the specific case of the interaction of F_2 with a Si, a single Si-F bond is formed at the surface with the subsequent release of the complementary F atom into the gas phase. Since the abstraction mechanism is thermodynamically allowed only if enough energy is released upon formation of a single gas-surface bond to offset the energetic cost incurred to break the original bond, it is only expected to occur in systems in which a very strong bond can form between the surface and a gas phase molecular fragment. The interaction of F_2 with the Si(100) surface is such a system.

Ab initio calculations[4] of the binding of a gas phase F atom and a Si surface dangling bond estimate the Si-F bond energy to be 6.4 eV. This bond strength is very large

---

[3] Y. L. Li, D. P. Pullman, J. J. Yang, A. A. Tsekouras, D. B. Gosalvez, K. B. Laughlin, Z. Zhang, M. T. Schulberg, D. J. Gladstone, M. McGonigal and S. T. Ceyer, *Phys. Rev. Lett.* **74**, 2603 (1995)

[4] C. J. Wu and E. A. Carter, Phys. Rev. B **45**, 9065 (1992)

compared to the 1.4 eV binding energy of the gas phase F_2 molecule. The energy released upon formation of a single Si-F bond would then greatly exceed the energy needed to break the F-F bond giving a net 4.8 eV exothermicity for the abstraction process. Simultaneous formation of two Si-F bonds is clearly not thermodynamically necessary for the dissociation of F_2, and thus a single F atom can be abstracted by the surface with the concomitant release of the complementary F atom into the gas phase. Similar abstraction mechanisms have been well documented in gas phase reactions, but they have never been experimentally corroborated in gas-surface interactions prior to the work of Ceyer et al[3]. Simultaneously with the first experimental observation, abstraction was observed for the F_2/Si reaction by molecular dynamics trajectory calculations performed by Stillinger and Weber[5]. The occurrence of F atom abstraction by the Si dangling bonds means that in the plasma environment used in commercial Si etching applications, the surface reaction is contributing to the production of reactive F atoms which are believed to be the most reactive species. Kinetic models of the plasma etching environment should therefore take into account the rate of production of F atoms by the abstraction mechanism.

Experimental confirmation of the proposed F-atom abstraction mechanism involves the detection of the scattered F atom after it fails to form a bond to the silicon surface. The reactive nature of the ejected F atoms is likely responsible for the failure of numerous published studies of the interaction of fluorine and fluorinated hydrocarbons with silicon to detect the atom abstraction mechanism. Undoubtedly, if a scattered F atom is allowed to collide with the reaction chamber walls before detection, it will adsorb and hence not be observed. In addition, although this new mechanism for dissociative chemisorption is a general one and must be occurring in other exothermic molecule-surface systems, it has also gone undetected in all other systems. The successful

[5] T. A. Weber and F. H. Stillinger, J. Chem. Phys., **92**, 6239 (1990)

identification of the atom abstraction mechanism in the case of the interaction of F_2 with Si is directly attributable to the unique features of the molecular beam-surface scattering apparatus which is briefly described in Section 1.2.1. In particular, the use of a beam coupled with a line-of-sight, triply-differentially-pumped mass spectrometer allows the detection of the highly reactive F radicals produced by the abstraction reaction.

Direct observation of scattered F atoms was first achieved by time-of-flight velocity measurements of a low energy F_2 molecular beam scattered from a Si(100) surface. Helium atom diffraction studies of the structure of the fluorinated surface coupled with the determination that the abstraction mechanism ceases at 1 ML fluorine coverage strongly suggest that not only are the dangling bonds on each Si atom the adsorption sites, but that they are also the abstraction sites. However, the complementary F atom does not necessarily scatter into the gas phase. It may be trapped by a second reactive site encountered during its outgoing trajectory and bind. Whether the scattered F atom is propelled away from the surface or towards a reactive site depends on the orientation of the incident F_2 molecule. Measurement of the evolution of the reaction products as a function of exposure to the F_2 molecular beam yields information about the coverage dependence of the abstraction mechanism. For example, an elaborate analysis of these measurements as a function of exposure yields a quantitative determination of the absolute reaction probability for each channel as a function of coverage. Armed with the knowledge of the absolute reaction probabilities, the evolution of the fluorine coverage with F_2 exposure and a saturation coverage of 1 ML are determined. The unusual dependencies of the reaction probabilities on coverage suggest a strong dependence of the F_2 reaction probability on both the orientation of the incident F_2 molecule and on the dimer structure of the Si(100) 2x1 surface.

Section 1.2 gives a brief description of the experimental apparatus used for this investigation as well as of some minor modifications implemented since the apparatus

was last described[6]. Section 1.3 presents a summary of the results of time-of-flight measurements, exposure dependence of scattering products, thermal desorption spectroscopy, and helium diffraction measurements needed to establish the existence of the atom abstraction mechanism. A more detailed discussion of these experiments has been given by Yang[6]. Section 1.4 concentrates on the additional measurements, such as the incident beam flux and the F_2 ionization cross-sections necessary to obtain quantitative information about the coverage dependence of the abstraction mechanism. Section 1.5 presents a discussion of the qualitative aspects of the potential energy surface derived from the experimental results, as well as three empirical models aimed at understanding the dynamical and chemical interactions that dictate the coverage dependence of the reaction probabilities.

[6] J. J. Yang, Ph.D. Thesis, Massachusetts Institute of Technology, (1993)

1.2 EXPERIMENTAL APPARATUS

1.2.1 Description

All experiments presented in this work were conducted in an ultra-high vacuum (UHV) molecular beam surface scattering apparatus. A detailed description of this apparatus as well as its design criteria have been given elsewhere[7,8,9,10]. Only a brief description of its essential components is presented here.

The single crystal Si(100) sample is positioned inside an UHV main chamber with a base pressure of approximately $6x10^{-11}$ Torr. This low pressure is essential to ensure that the silicon surface remains free of adsorbed contaminants during the duration of the experiments. Reactants (i.e. F_2) are introduced via a differentially pumped, supersonic molecular beam precisely coupled to the UHV main chamber. The molecular beam impinges on the Si surface where the etching reaction takes place. The scattered molecules are then detected by a line-of-sight, triply differentially pumped, electron impact ionization, quadrupole mass spectrometer. The mass spectrometer is rotatable about the center of the crystal, thereby allowing the angular distribution of molecules scattered from the surface to be measured. A pseudo-random slotted chopper wheel mounted at the entrance to the first differential pumping stage of the mass spectrometer modulates the scattered molecules for the purpose of velocity analysis using a time-of-flight technique. A schematic representation of the apparatus is given in Figure 1.1.

The supersonic molecular beam is produced by expanding a dilute mixture of either F_2 or XeF_2 seeded in a noble gas carrier through a 100 μm diameter orifice. The center of

---

[7] S. T Ceyer, D. J. Gladstone, M. McGonigal, and M. T. Schulberg, Physical Methods of Chemistry, edited by B. W. Rossitier and R. C. Baetzold (Wiley, New York, 1933), 2nd ed., Vol. IXA, p. 383

[8] M. McGonigal, Ph.D. Thesis, Massachusetts Institute of Technology, (1989)

[9] D. J. Gladstone, Ph.D. Thesis, Massachusetts Institute of Technology, (1989)

[10] M. T. Schulberg, Ph.D. Thesis, Massachusetts Institute of Technology, (1990)

the expanded beam passes through a skimmer placed 5.6 mm from the nozzle. Two differential pumping chambers, separated by collimating apertures, ensure a collisionless expansion environment and minimize the effusive gas contribution into the main chamber. The collimating apertures define a rectangular beam cross-section of 6.4 mm by 4.5 mm at the center of the silicon crystal. The nozzle to sample distance is 13.6 cm. Typical stagnation pressures behind the nozzle range from 100 to 600 Torr leading to beam fluxes in the range of 10^{16} to 10^{18} cm^{-2} sec^{-1} (10-1000 ML sec^{-1}). These seeded supersonic beams allow the reactants to reach the surface with a well defined angle of incidence and translational energy. The angle of incidence can be varied from 0° to 90° with respect to the surface normal. The range of translational energies attainable by seeding depends on the kind and relative amounts of seed and carrier gas. For the case of F_2, translational energies can be varied between 0.1 and 14 kcal $mole^{-1}$. Table 1-1 gives a summary of the velocity and translational energy of the F_2 beams used in this investigation.

The Si(100) samples used are approximately 2.5 cm in diameter and 525 μ thick. They are cut out of 10 cm diameter wafers supplied by either Monsanto or Sematech. The samples provided by Monsanto are lightly n-doped with a resistivity of 8-12 Ω-cm, while the Sematech ones are p-type with similar resistivity. No dependence on Si doping is observed in any of the experiments conducted during this investigation. The machining and mounting procedure has been described by Yang[11]. In order to obtain a good surface quality, the machined samples are wet etched in dilute HF following the procedure described by Shiraki et al.[12] before insertion into the vacuum chamber.

Neutral products scattering or desorbing from the surface must be ionized before they can be detected. Non-selective, but efficient ionization of the reaction products is

---

[11] J. J. Yang, Ph.D. Thesis, Massachusetts Institute of Technology, p. 37, (1993)

[12] A. Ishizaka and Y. Shiraki, J. Electrochem. Soc. **133**, 666 (1986)

performed by use of a Brink's[13,14] type electron bombardment ionizer. The neutral product beam is ionized by crossing a shower of 70 eV electrons produced by heating a tungsten filament. The ions are born inside a cylindrical grid at a potential of 45 eV above the filament bias voltage and are then extracted out of the ionization region and focused by an Einzel lens onto the entrance of the quadrupole mass filter[15]. Only ions of a pre-selected mass-to-charge ratio emerge at the exit of the quadrupole field were they are counted by a channel electron multiplier. The overall efficiency of this ionization and detection scheme is estimated to be approximately one in 10^6 particles entering the ionization region.

In order to limit detection to products arising exclusively from the reaction at the silicon surface, the entire detector is placed inside a housing containing three differentially pumped chambers separated by small rectangular collimating apertures. The detector housing collimating slits are designed so that only a portion of the Si surface exposed to the incoming molecular beam is imaged onto the ionization region, ensuring that the detector's line-of-sight is limited to products traveling in a straight line from the surface. Any products having undergone further reaction by collisions with the chamber walls are not likely to be detected. The differential pumping scheme maintains a collisionless gas phase environment and minimizes the effusive gas load onto the ionization region by pumping away particles not directly in the line-of-sight of the detector. In order to further reduce the background gas load in the ionization region, and to prevent excessive outgassing from hot metal surfaces near the filament, the walls of the ionization chamber are cooled to liquid nitrogen temperatures. Line-of-sight detection coupled with the maintenance of low background pressures in both the reaction chamber

---

[13] Y. T. Lee, J. D. MacDonald, P. R. Le Breton, and D. R. Herschbach, Rev. of Sci. Instr. **40**, 1402 (1969)

[14] Gilbert O. Brink, Rev. of Sci. Instr. **37**, 857 (1966)

[15] P. E. Miller, M. B. Denton, J. of Chem. Ed. **63**, 617 (1986)

and inside the detector housing enables the detection of unstable or reactive products. For example, detection of the highly reactive F radicals expected to arise from an abstraction event is made possible by the line-of-sight alignment of the triply-differentially pumped spectrometer housing. This arrangement prevents the F radicals from being depleted through collisions with the chamber walls or background gas before they can be detected.

Detection of molecules desorbed or scattered from the surface is not limited to the narrow acceptance angle defined by the collimating slits on the detector housing. The entire distribution of molecules scattered from the surface is measurable by rotation of the detector and its housing around the center of the crystal, allowing the angular distribution of the molecules scattered in the plane defined by the molecular beam and the line-of-sight of the detector to be collected. Symmetry considerations and reasonable assumptions about the out-of-plane scattering must be used to account for the complete product distribution about a hemispherical shell centered on the sample surface.

The entrance to the detector chamber is fitted with a cross-correlation chopper wheel for measurement of the velocity distribution of the scattered molecules by a time-of-flight technique. The wheel modulates the scattered beam into short pulses of gas with a well defined starting position and time. The time necessary for the molecules in each pulse to travel the known distance between the chopper and the ionizer is measured, thus yielding the velocity of the scattered molecules. To maximize the signal, a pseudo-random modulation sequence of slits is carved on the chopper wheel, which has a 50% duty cycle. The high duty cycle of the modulation sequence causes some overlap of the scattered gas pulses as they travel towards the detection region. The measured spectrum must then be deconvoluted using the known modulation pattern to yield the time-of-flight distribution. A good description of the cross-correlation technique as applied to time-of-

flight measurements has been given by Comsa et al[16].

The most important capabilities of the molecular beam-surface scattering apparatus used in this investigation are summarized as follows: 1) allows control of the energy and angle of incidence of the reactants impinging on the surface. 2) maintains a low base pressure in the reaction chamber to ensure surface cleanliness and a collisionless gas phase environment. 3) provides line-of-sight detection capable of collecting even the most reactive radicals scattered from the surface. 4) renders the complete angular distribution of reaction products. 5) gives the translational energy distribution of those products.

Table 1-1 Parameters Describing Velocity Distribution of F_2 in Seeded Beams

600 Torr Beam	Average Velocity	Beam Temp.	Average F_2 Energy
1% F_2/Kr	384±0.1m sec^{-1}	1.59±0.02 K	0.67±0.005 kcal mol^{-1}
1% F_2/Ar	547±0.1 m sec^{-1}	2.13±0.02 K	1.36±0.005 kcal mol^{-1}
0.25% F_2/He	1684±0.3 m sec^{-1}	28.4±0.18 K	12.9±0.004 kcal mol^{-1}
Pure Ne	812±5 m sec^{-1}	13.1±0.71 K	1.59±0.01 kcal mol^{-1}

For explanation of the uncertainties see the section on error analysis of seeded beam fluxes presented in Appendix A.

[16] R. David, K. Kern, P. Zeppenfeld and G. Comsa, Rev. Sci. Instrum. **57**, 2771 (1986)

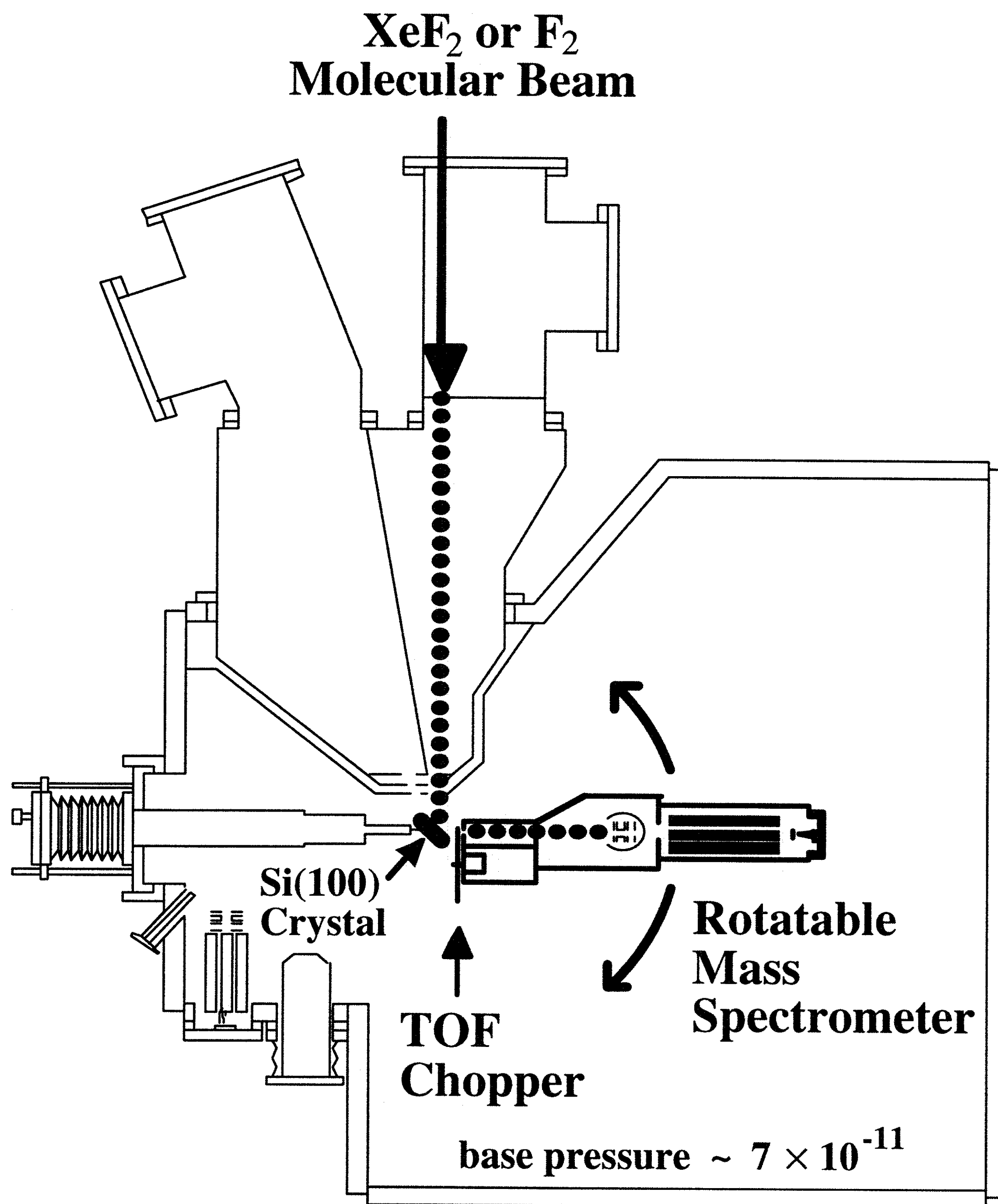

Figure 1.1 Schematic Diagram of the UHV Beam-surface Scattering Apparatus

1.2.2 Modifications to the Apparatus

1.2.2.1 Attachment of Crystal Temperature Thermocouple

The temperature of the silicon crystal mounted inside the UHV chamber can be varied from 120 K up to its melting point by a combination of heating and cooling. The lowest temperatures are achieved by connecting the sample support to a liquid nitrogen filled reservoir via a thick copper braid. The sample is resistively heated by applying a voltage difference across the support clamps and hence running a current across the silicon wafer. The desired temperature is obtained by an optimal control feedback circuit described elsewhere[17]. The feedback circuit requires accurate real-time measurements of the crystal temperature, which is measured by an Omega Instruments type-C (W-5%Re/W-26%Re) thermocouple attached to back of the silicon wafer. Good thermal contact between the thermocouple and the silicon substrate is essential for accurate and reproducible temperature measurements. Two different approaches have been used in these investigation to ensure proper attachment of the thermocouple to the crystal.

As a first approach, the thermocouple junction produced by spot welding the 0.005" thick Re-W wire leads was glued to the back of the crystal. Since the sample is routinely heated to temperatures above 1000 K and rapidly cooled to 250 K in a UHV environment, the glue must have some very special properties. Aside from the obvious UHV compatibility issues, the glue must possess the following properties: 1) good adherence to the silicon substrate, 2) its coefficient of thermal expansion must be similar to that of silicon so as not to fracture under the stress of thermal cycling, 3) it must withstand temperatures in excess of 1300 K, 4) it must efficiently conduct heat from the silicon substrate to the thermocouple junction.

The glue of choice was Aremco Ceramabond Ultratemp 516, a zirconium silicate

[17] D. J. Gladstone, Ph.D. Thesis, Massachusetts Institute of Technology, p.123, (1989)

base cement which satisfies all the above listed properties. A small dab of glue was placed on the back of the silicon wafer and the thermocouple junction was pressed against it until the glue hardened. The glue was then cured in accordance to the manufacturer's specifications. The curing schedule required introducing the end of the manipulator and the sample holder into a small oven for several hours. Proper curing of the glue led to well-attached thermocouples that gave accurate and reproducible surface temperature measurements. The gluing and curing procedure, however, proved to be hard to reproduce. The success rate of this attachment method was approximately 30 to 50 %. Unsuccessful gluing attempts, in which the thermocouple separated from the crystal, would become apparent only after investing several days to bake the chamber and clean the silicon crystal. An alternate, more reliable method of attaching the thermocouple to the sample was then devised.

The alternate attachment method does not involve the use of glue. Instead, a pair of screws is used to securely pin two thermocouples to the back of the silicon sample. First, each thermocouple junction is spot welded to a small square tantalum tab of approximately 2.5 mm on each side and 75 μm thick. A bracket spot-welded across the back of the sample holder provides two threaded holes for the attachment screws. A piece of insulating ceramic material (silica) is placed between the screw tip and the tantalum tab which is then sandwiched against the back of the silicon sample. The ceramic piece electrically insulates the thermocouple junction from the grounded bracket and screw. The screw must provide a secure hold to insure good thermal contact between the thermocouple and the silicon, but care must be taken not to over tighten it since excess force may cause the silicon wafer to bulge and crack upon heating.

The mechanical attachment of a thermocouple with a screw gives adequate temperature readings for the feedback of the temperature control circuit, and has proven to be more durable than gluing. The peak desorption temperatures obtained during

thermal desorption experiments performed with mechanically attached thermocouples are however, typically lower than the peak temperatures obtained by gluing. In addition, the reproducibility of thermal desorption temperatures was significantly better for glued than for screwed thermocouples. These observations suggest that the thermal contact between the silicon and the screwed thermocouple is not as good as that obtained by using the zirconium glue. Although screwing the thermocouple to the back of the crystal allows for an easy and durable way to control the crystal temperature, it is not ideal for measurements that require an accurate and reproducible measurement of the absolute surface temperature.

1.2.2.2 Changes to Detector Box Turbo Molecular Pumps

The differential pumping scheme used for the rotatable mass spectrometer has been previously described in detail[7,8,10]. Some changes have been made to the pumps during the course of this investigation and are briefly described here. In order to increase the pumping speed of the first differential pumping region of the mass spectrometer housing, the existing ion pump was replaced with a Balzers TPU 330 turbomolecular pump identical to those used in the second and third pumping stages. A Balzers TPC 121 controller is used to drive the new pump. The foreline of this new pump was connected to the common foreline of the two existing turbo pumps. The Balzers TPU 110 turbomolecular pump used to provide backing pressure for the large turbo pumps was replaced by a Balzers TMH 065 turbomolecular drag pump. Pneumatically actuated butterfly valves (Key High Vacuum Products models QBV-75-P-SS16 and QBV-150-P-SS40) were placed at both ends of the drag pump. All forelines between the turbo pumps and the backing turbo pump were shortened to approximately one foot and widened to a diameter of one inch so as to maximize the pumping speed. A thermocouple vacuum gauge tube was added at the inlet of the mechanical pump that backs the turbomolecular drag pump. A new interlock and control system has been built

to monitor and protect all four turbomolecular pumps. Details of this interlock circuit are presented elsewhere[18].

1.2.2.3 Detector Box Pin-hole

The line-of-sight of the mass spectrometer can be rotated to coincide with the molecular beam axis. This configuration is denoted as a "straight-through" position, and is necessary for measuring the velocity distribution and intensity of the incident molecular beams. However, the apertures in the detector chamber are designed to maximize the signal from the scattered molecules. So, when the detector is aligned in the straight-through configuration the gas load becomes too large, causing excessive ion densities in the ionization region. While the ion densities can be easily reduced by lowering the ionization current, the quantitative measurements described in Section 1.4 require the incident beam intensity to be measured under the exact ionization conditions used in the scattering experiments. A way is then needed to reduce the gas load admitted into the detector chamber so that the spectrometer can be operated at higher ionization currents without the detrimental effects of excessive ion density.

In order to reduce the gas load, an additional limiting aperture was placed in front of the detector housing entrance. The new aperture was fabricated from a commercially available 12.5 μ pin-hole at the center of a 3.3 mm disk which was spot welded around a larger hole in a piece of tantalum foil. The tantalum foil is attached to a 1 mm thick rectangular tantalum plate measuring 3x1 cm, which is in turn bolted to the detector-box beam valve support rod. The use of this limiting aperture ensures that the gas load in the straight-through configuration is approximately equal to the gas load arising from a beam scattered off the surface.

The position of the pin-hole aperture with respect to the detector entrance can be

[18] Matthew R. Tate, thesis in preparation.

controlled by rotating the detector valve feedthrough. A profile of the mass spectrometer signal as a function of the beam valve feedthrough position is shown in Figure 1.2. The signal intensity is determined by recording and integrating a time-of-flight spectrum at each pinhole position. The maximum of the intensity profile corresponds to the position at which the pin-hole is aligned with the centerline of the ionization region, which is obtained by turning the detector valve 12 turns from its fully open position. Note that the detection sensitivity rapidly decreases as the pin-hole moves away from the ionizer's centerline. It is therefore very important to ensure the pin-hole position is accurately reproduced when comparing straight-through measurements.

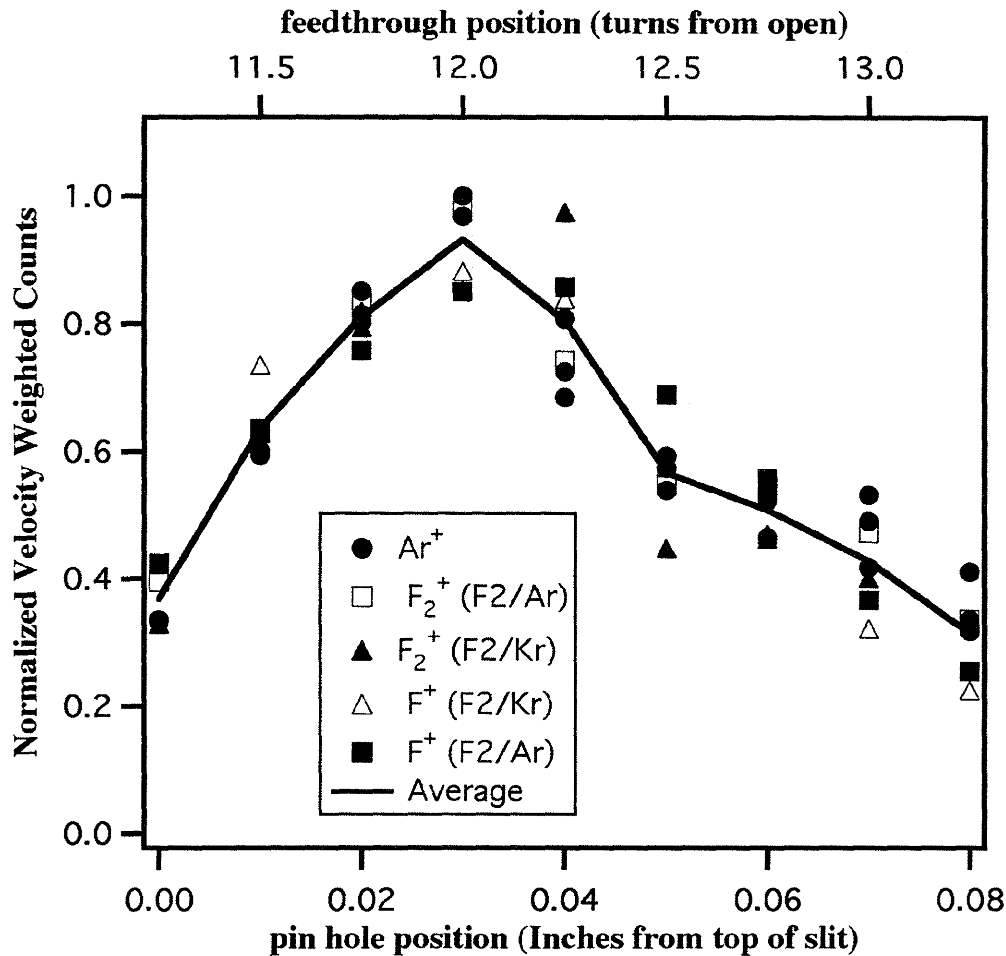

Figure 1.2 Straight-Through Signal as a Function of Pin-hole Position

Optimal pin-hole alignment is obtained by turning the detector valve feedthrough 12 turns from its fully open position. The onset of the signal seen at approximately 11 turns corresponds to the top edge of the rectangular limiting aperture at the entrance to the detector chamber. The 12 turn position corresponds to having the pin-hole centered, 0.03" from the top edge of the 0.078" high aperture.

1.3 SUMMARY OF EXPERIMENTAL RESULTS

1.3.1 Time-of-flight Measurements of the Scattered F and F_2

When a F_2 molecule impinges upon an adsorbate-free Si surface three pathways are possible: 1) The molecule may unreactively scatter back to the gas phase without any chemical change taking place. 2) The F_2 molecule could undergo an abstraction reaction in which one F atom remains bound to the surface while its partner scatters back to the gas phase. 3) The incident F_2 can dissociatively chemisorb by leaving both fluorine atoms bound to the surface. The first pathway is readily identifiable by detection of either the parent ion F_2^+ with a mass-to-charge ratio of 38, or the fragment ion F^+ with m/e =19 of unreactively scattered F_2 molecules with the electron impact ionization mass spectrometer. The second pathway, involving atom abstraction is in principle identifiable by mass spectrometric detection of F atoms as the parent F^+ ion at m/e=19. However, their signal would be superimposed on the m/e=19 signal produced from the cracking of F_2 in the electron bombardment ionizer.

A challenge then arises in distinguishing the ejected fluorine atoms from the fraction of the unreactively scattered F_2 that gets fragmented to F^+ during ionization. Fortunately, the two neutrals giving rise to the superimposed signals can be differentiated on the basis of their different velocities. The unreactively scattered F_2 is expected to inelastically scatter or even partially accommodate on the surface upon collision. It would then scatter back to the gas phase with a broad velocity distribution. On the other hand, an F atom ejected during the abstraction event may be translationally excited from the large amount of energy released by the exothermicity of the reaction. The ejected fluorine atoms would then leave the surface with a faster and narrower velocity distribution than the thermalized, unreactively scattered F_2.

These expectations are borne out in the time-of-flight velocity measurements of the

scattered reaction products. Figure 1.3 (a) shows time-of-flight spectra of products scattered from a 250 K Si(100) surface exposed to a 600 Torr, 1% F_2/Kr beam (E_i=0.66 kcal mol^{-1}), incident at 0° for a total exposure to 0.2 ML of fluorine atoms. The scattered products are collected as m/e=38 and 19 at a detection angle of 35° with respect to the surface normal. The chopper is spun at 280 Hz and the data are collected into 255 channels each with a width of 14 μsec.

The filled circles correspond to signal detected at m/e=38, and therefore can be attributed to the parent ion of the unreactively scattered F_2. The solid line represents a fit to a Maxwell-Boltzmann distribution with a characteristic temperature of 240 K, which is approximately equal to the temperature of the surface, indicating an almost complete accommodation of the incident F_2 translational energy. The hollow circles in Figure 1.3 (a) correspond to signal detected at m/e=19, which arises from the superposition of directly ionized ejected F atoms and unreactively scattered F_2 molecules that fragment to F^+ upon ionization. The spectrum displays a bimodal distribution consisting of a fast, narrow peak at early arrival times followed by a broader, slow component at later arrival times. The broad, slow peak is attributed to unreactively scattered F_2 while the sharper, fast feature is identified as F atoms ejected in the abstraction process. There is good agreement between the velocity distribution of the F_2^+ signal and the slow contribution to the F^+ signal as should be expected since they both arise from the same neutral molecule, namely unreactively scattered F_2. Figure 1.3 (b) shows the time-of-flight distribution obtained by point-by-point subtraction of the two distributions presented in panel (a). The net distribution is attributed to ejected F atoms. This observation constitutes the first direct confirmation of the fluorine atom abstraction mechanism.

The ejected F atom signal is fitted to a supersonic velocity distribution[19] with

[19] See Appendix B for a description of the supersonic functional form and fitting procedure.

average velocity of 1100 m sec^{-1} corresponding to an average translational energy, $\frac{1}{2}m\overline{v^2}$, of 3.2 kcal mol^{-1}. Given that the average translational energy of the impinging F_2 beam is known to be 0.66 kcal mol^{-1}, it is clear that the scattered F atoms possess a greater translational energy than available in the incident beam. The high translational energy of the ejected F suggests that part of the exothermicity of the abstraction reaction is channeled into translational energy of F. However, the exothermicity released upon formation of a single Si-F bond is calculated to be 110 kcal mol^{-1}, implying that only about 3% of the available energy released in the reaction is channeled into translational excitation of the ejected F fragment.

To confirm the origin of the translational excitation of the scattered F atoms, the time-of-flight measurements are repeated while holding the crystal temperature at 1000 K. A 3.8% F_2/Kr beam (0.67 kcal mole^{-1}) is incident on the hot surface at 0°, while the scattered signals are detected at 35°. The total fluorine exposure is estimated to be about 240 ML of F atoms per Si on the surface. Figure 1.4 (a) shows the unreactively scattered F_2 signal (m/e=38) fitted to a Maxwell-Boltzmann distribution with a characteristic temperature of 495 K, which corresponds to an average velocity of 619 m sec^{-1} ($\frac{1}{2}m\overline{v^2}$ = 1.97 kcal mol^{-1}) for the scattered F_2. Comparison of the energy of the unreactively scattered F_2 to the average energy expected for F_2 desorbing from a 1000 K surface ($2kT$=3.98 kcal mol^{-1}) reveals that F_2 gains some translational energy upon collision with the hot surface, but it does not fully accommodate with the crystal surface. Figure 1.4 (b) shows the time-of-flight distribution of the SiF_2 etch product detected as SiF^+ at m/e=47. As expected, the SiF^+ etch product desorbs with a thermal velocity distribution at 1004 K, reflecting the temperature of the crystal, and with a corresponding average velocity of 669 m sec^{-1}.

The F^+ signal (m/e=19), demonstrating the existence of F atoms ejected from the hot surface, is presented in Figure 1.5 (a). Before the velocity distribution of the ejected F

atoms can be determined, the contributions from F_2 and SiF_2 cracking must be subtracted from the m/e=19 signal. The F_2 and SiF_2 contributions to the F^+ signal, as estimated from their respective fragmentation patterns, are also shown in Figure 1.4 (a). The net F-atom signal, presented in Figure 1.5 (b), is obtained by subtracting the F_2 and SiF_2 contributions from the raw m/e=19 signal. The fit of the net F-atom arrival time distribution yields a translational temperature of 961 K, corresponding to an average velocity of 1219 m sec^{-1} ($\frac{1}{2}m\overline{v^2}$=3.8 kcal mol^{-1}).

The velocity distribution of the F atoms ejected during the abstraction reaction with the hot (1000 K) Si surface is very similar to that obtained from the surface at 250 K. This point is further illustrated in Figure 1.6, where both velocity distributions have been converted into translational energy distributions and are plotted together. The similarity of the two energy distributions demonstrates that the translational activation of the ejected F atoms is independent of the surface temperature. This observation strongly suggests that the source of the translational excitation of the ejected F atom should be ascribed to the exothermicity released during formation of the complementary surface bond.

Time-of-flight results presented so far are limited to a single angle of incidence (θ_i= 0°), and a single angle of detection (θ_{scat}=35°). A complete study of the scattered velocities of F_2 and F from a 250 K crystal, as a function of incident angle, scattering angle, and F_2 exposure has been presented by Yang[20]. The velocities of both F and F_2 are found to remain constant at all angles and exposures. The invariance with respect to angle and exposure of the unreactively scattered F_2 velocity is consistent with full surface accommodation. Surface accommodation is not surprising, since the incident energy of the F_2 is comparable to the thermal energy of the 250 K crystal.

[20] J. J. Yang, Ph.D. Thesis, Massachusetts Institute of Technology, p. 120, (1993)

1.3 Summary of Experimental Results

The picture that emerges from the analysis of the time-of-flight velocity measurements of the scattered reaction products can be summarized as follows. During the early stages of fluorination of a 250 K Si(100) surface, a substantial fraction of the incoming F_2 molecules undergo an abstraction reaction in which a fluorine atom scatters into the gas phase carrying away about 3% of the reaction exothermicity. Even at low fluorine coverages, unreactively scattered F_2 is present. This F_2 appears to fully accommodate with the crystal surface as suggested by a thermal velocity distribution characterized by the temperature of the surface.

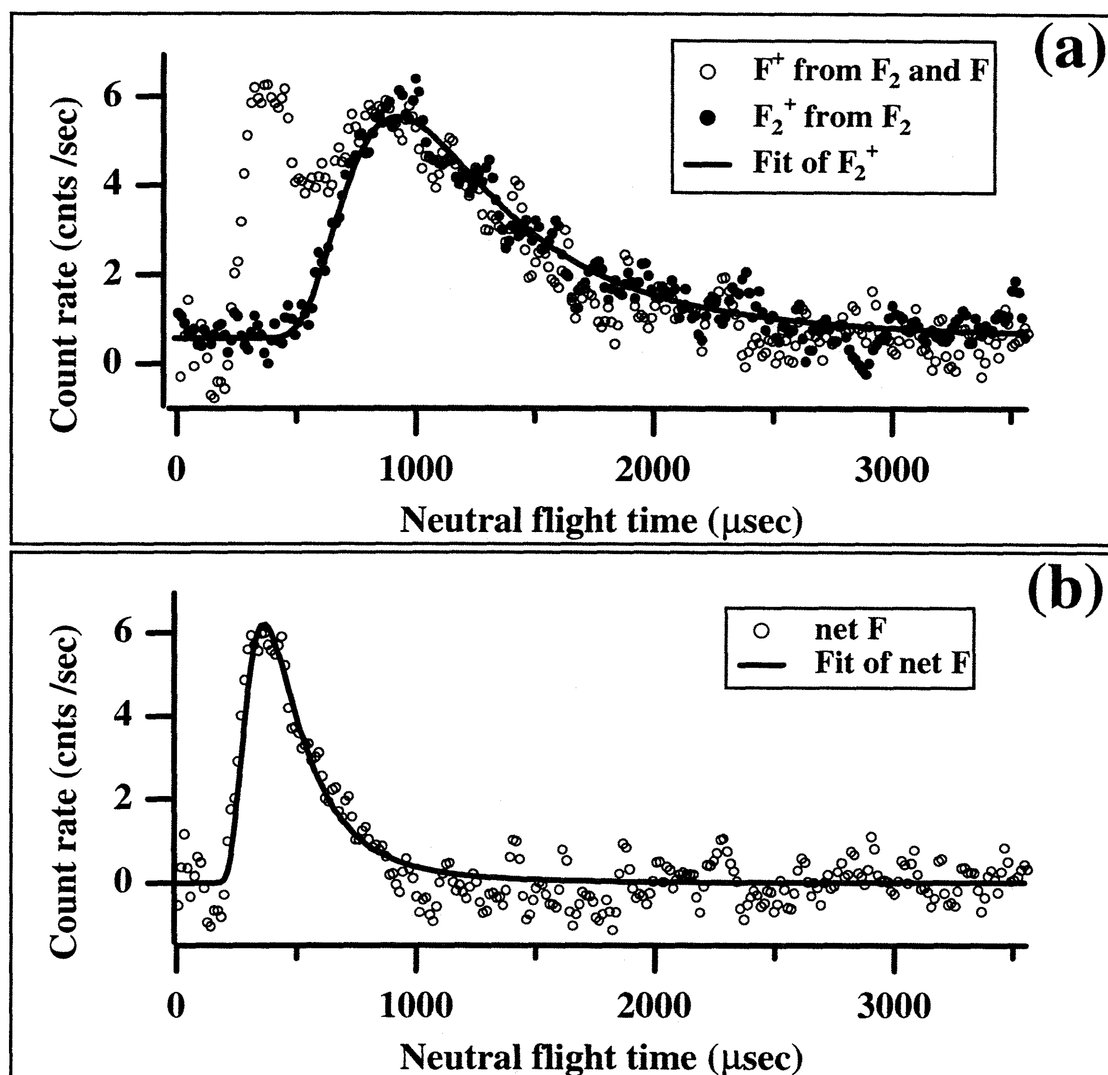

Figure 1.3 Time-of-Flight Spectra of Scattered 1% F_2/Kr

Time-of-flight spectra of species scattered at 35° from a 250 K Si(100) surface during exposure to ~ 0.2 ML of F from a 1% F_2/Kr (E_i= 0.66 kcal mol^{-1}) beam incident at 0°. (a) Filled circles correspond to m/e= 38 signal (F_2^+ from unreactively scattered F_2). Solid line is a fit of a Maxwell-Boltzmann distribution at 240 K to the data. The average velocity is 436 m sec^{-1}($\frac{1}{2}m\overline{v^2}$ =0.95 kcal mol^{-1}). Hollow circles are m/e=19 signal arising from the superposition of F-atoms from abstraction and unreactively scattered F_2 fragmented upon ionization. (b) Time-of-flight distribution of the net F atom signal obtained from point-by-point subtraction of the data in (a). The solid line is a fit to a Maxwell-Boltzmann distribution at 781 K corresponding to an average velocity of 1100 m sec^{-1} ($\frac{1}{2}m\overline{v^2}$ = 3.2 kcal mol^{-1}).

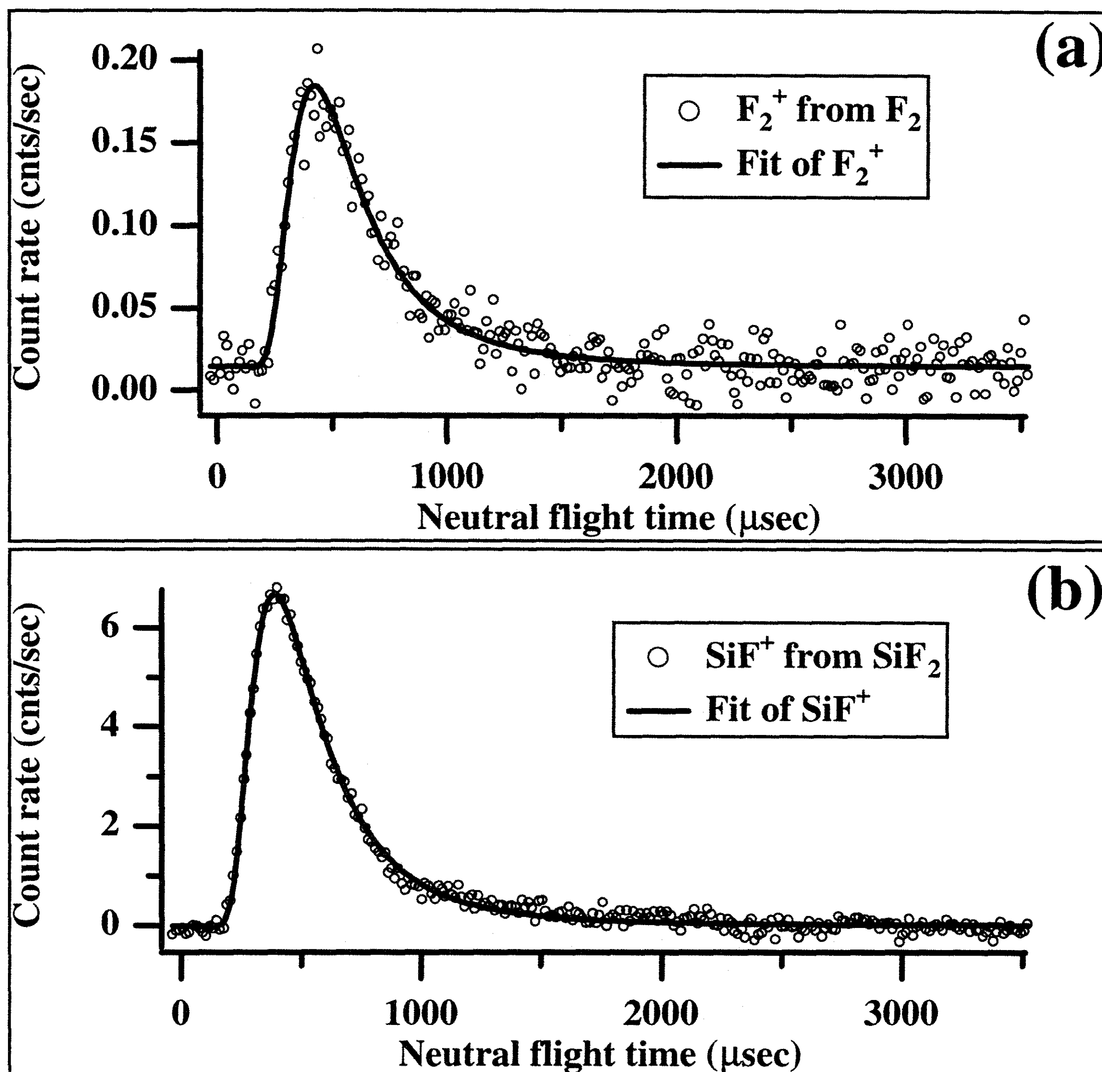

Figure 1.4 F_2 and SiF_2 Time-of-flight Spectra from a 1000 K Si(100) Surface

Time-of-flight spectra of species scattered at 35° from a 1000 K Si(100) surface during exposure to ~ 46 ML of F from a 3.8% F_2/Kr (E_i= 0.67 kcal mol^{-1}) beam incident at 0°. (a) Circles correspond to m/e=38 signal (F_2^+ from unreactively scattered F_2). Solid line is a fit of a Maxwell-Boltzmann distribution at 495 K to the data. The average velocity is 619 m sec^{-1} ($\frac{1}{2}m\overline{v^2}$ =1.97 kcal mol^{-1}). (b) Circles correspond to m/e=47 signal (SiF^+ from desorbing SiF_2). Solid line is a fit of a Maxwell-Boltzmann distribution at 1004 K with a corresponding velocity of 669 m sec^{-1} ($\frac{1}{2}m\overline{v^2}$ =3.98 kcal mol^{-1}).

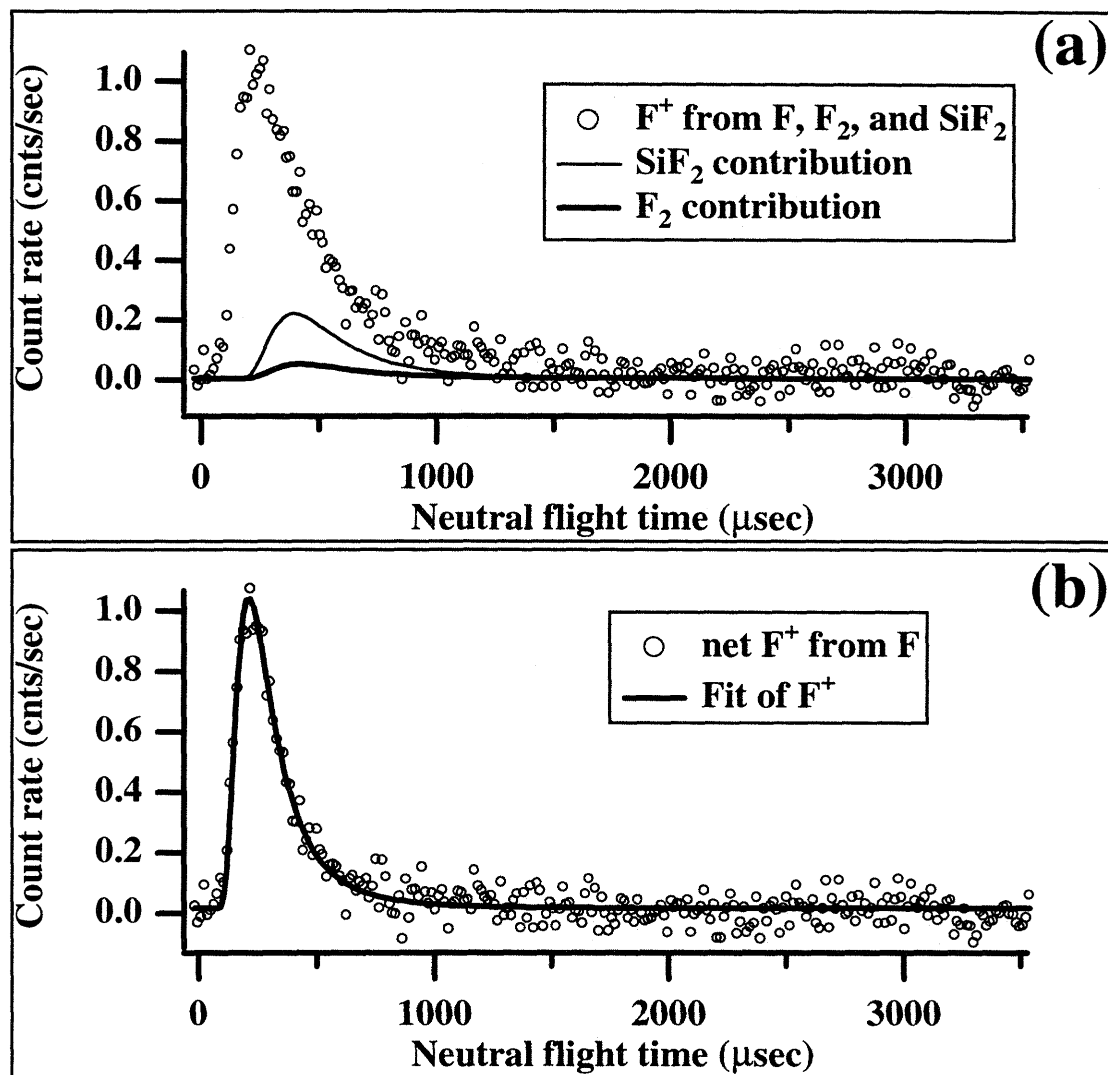

Figure 1.5 Time-of-flight Spectra of F Atoms Ejected from a 1000K Si(100)

Time-of-flight spectra of F^+ at m/e=19 scattered at 35° from a 1000 K Si(100) surface during exposure to ~ 46 ML of F from a 3.8% F_2/Kr (E_i=0.67 kcal mol^{-1}) beam incident at 0°. (a) Raw m/e=19 signal (circles). SiF_2 etch product estimated from its fragmentation pattern (thin solid line). Unreactively scattered F_2 estimated from its fragmentation pattern (thick solid line). (b) Net F signal obtained by subtraction SiF_2 and F_2 contributions from raw F^+ (circles). Fit of a Maxwell-Boltzmann distribution at 961 K (solid line), with a corresponding average velocity of 1219 m sec^{-1} ($\frac{1}{2}m\overline{v^2}$=3.8 kcal mol^{-1}).

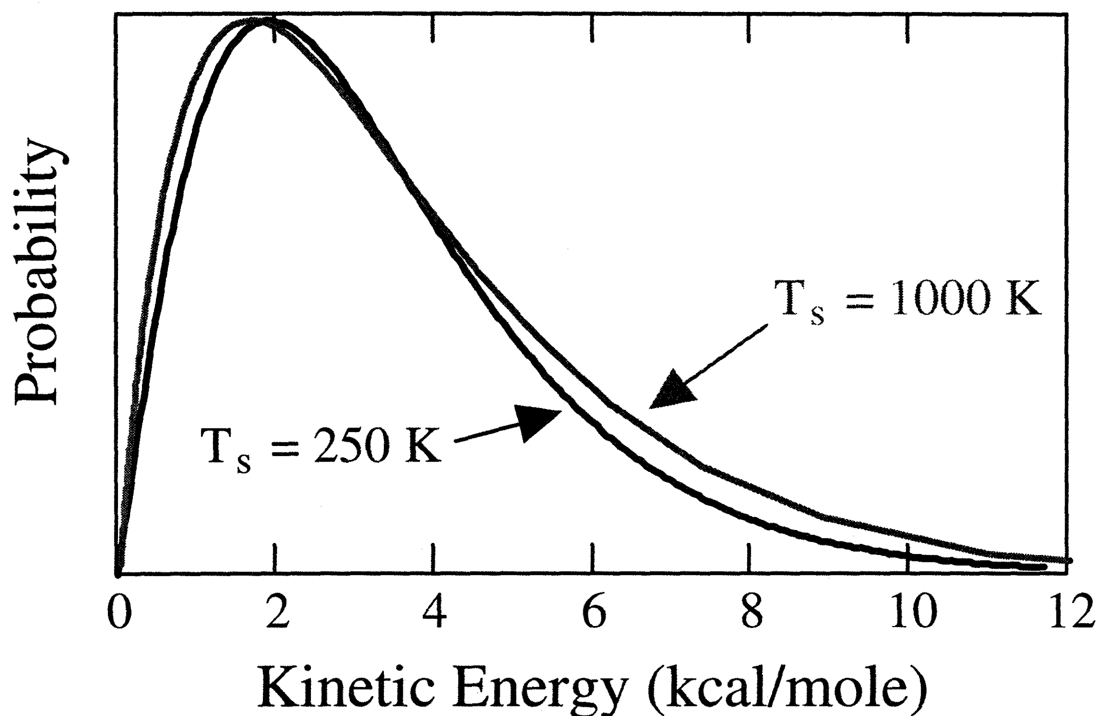

Figure 1.6 Energy Distributions of F-atoms from 250K and 1000 K Surfaces

Translational energy distributions determined from the time-of-flight distributions of F atoms ejected from a 250 K and 1000 K Si(100) surface. The two energy distributions are nearly identical suggesting that surface temperature does not play a role in the translational activation of the F atoms released during the abstraction event.

1.3.2 Exposure Dependence of the Scattered F and F_2

The experimental verification of the atom abstraction mechanism was made possible by deconvoluting the two contributions to the m/e=19 signal based on the different translational energies with which a F atom and F_2 molecule scatter from the surface. This section describes the abstraction mechanism as a function of fluorine coverage, where the separation of the two contributions at m/e=19 is achieved on the basis of the different coverage dependencies of the scattered F and F_2 molecules. A different coverage dependence is expected because the abstraction process requires unoccupied Si surface sites while unreactive scattering is most likely to occur from occupied or fluorinated sites.

The exposure dependence measurements consist of simultaneously monitoring the total flux of scattered products at m/e=38 and 19 while the Si surface is exposed to a molecular beam with a well defined flux of F_2 molecules. The total scattered flux represents the fraction of the incident flux that has not adsorbed onto the Si surface. A careful mass-balance analysis of these data, which requires the precise knowledge of the absolute incident and scattered fluxes, yields the probability of each of the reaction channels which in turn provides a way to calculate the fluorine coverage as a function of exposure.

In a typical scattering experiment, the Si(100) surface is held at 250 K and exposed to a fluorine containing beam with a well defined incident angle and translational energy. The species that scatter from the surface are collected by multiplexing the mass spectrometer to alternate between m/e=38 and 19 with a dwell time of 0.1 seconds per measurement and a dead time between measurements of 0.005 seconds. The exact time of exposure is determined by opening and closing a computer controlled beam flag located in the beam path in the second stage. For the purpose of baseline subtraction data are also collected for 20 seconds before and after the beam is allowed to enter the main chamber.

Figure 1.7 displays the scattered signals as a 1%F_2/Kr (E_i= 0.66 kcal mol^{-1}) beam incident at 0° impinges on a 250 K Si(100) surface. Since accurate knowledge of the F_2 flux in the beam is required for the quantitative analysis of these data, the stagnation pressure of the beam is lowered to 200 Torr in order to avoid the complications that arise from limited differential pumping in the beam-line (see Appendix C). The filled circles in Figure 1.7 (a) correspond to the mass spectrometer signal at m/e=38 collected at a scattering angle of 35°. Aside from the lower stagnation pressure, these are the same scattering conditions that are used for the time-of-flight data presented in Figure 1.3. The counter dwell time is 0.095 seconds, but the ordinate of the plot has been scaled to counts per second. The abscissa of this plot has been converted to represent the F_2 exposure in ML of F atoms per Si surface site.

At first glance, the data are consistent with a Langmuir adsorption process. At low exposures there are many available empty sites on the surface, so very little fluorine is observed to scatter unreactively, because the incoming fluorine has many sites on which to adsorb. As the exposure increases and more surface sites become passivated by the adsorption of fluorine, the likelihood of an unreactive scattering event increases, as can be seen from the increase in F_2^+ signal. Eventually, the unreactively scattered flux levels off to a constant value indicating either a passivation of all available surface sites or the onset of a steady-state equilibrium.

A steady-state process would require the desorption of either F atoms or fluorinated silicon products in order to constantly regenerate reactive surface sites. However, no SiF_x products are observed to evolve from the surface under these scattering conditions. Additionally, given the strength of the Si-F bond, no fluorine atoms will desorb from the 250 K surface once they are bound. Therefore, the conclusion is reached that a saturation coverage is reached, at which point every incident F_2 unreactively scatters from the passivated surface.

The first clue of complexity beyond the simple Langmuirian adsorption comes from a detailed scrutiny of the m/e=19 signal represented by the hollow circles on Figure 1.7 (a). As discussed earlier, two neutrals contribute to the m/e=19 signal. However, under the assumption that the surface coverage saturates, only unreactively scattered F_2 contributes to the m/e=19 signal at high exposures, thus providing a convenient way to deconvolute the two superimposed signals. The intensity of the F_2^+ signal is scaled to match that of the F^+ signal at long exposures (saturation coverage). The scaled m/e=38 signal corresponds to the amount of F_2 that fragments to F^+ upon electron impact ionization. The fact that the scaled F^+ and F_2^+ traces do not overlap at low exposures indicates that there is an additional source of F^+. The difference between the signal intensity at these two masses is ascribed to the presence of F-atom abstraction. Figure 1.7 (b) is obtained by a point-by-point subtraction of the two signals in (a). It corresponds to the dependence of the net scattered F atom signal on exposure, and corroborates the existence of the abstraction event.

The exposure dependence of the net F atom signal appears to be quite unusual. In the limit of zero coverage, the ejected F atom signal is clearly non-zero. This non-zero value implies that even when there are many unoccupied reactive sites available for the more energetically favorable process leading to adsorption of both F atoms, a non-negligible fraction of the incoming F_2 molecules undergo the less energetically favorable abstraction process. As fluorine exposure is increased and the number of available reactive sites is reduced, a maximum is observed in the net F-atom signal. This maximum implies that there is some intermediate coverage regime for which the process of depositing a single atom onto the surface without the concomitant adsorption of its partner is more probable than at higher or lower coverages. Ultimately, as more and more surface sites become fluorinated, the availability of reaction sites decreases, drastically reducing the probability of F atom adsorption and/or ejection.

1.3 Summary of Experimental Results

The picture that emerges from this set of molecular beam reflectivity measurements is the following. The first F_2 molecules to impinge on the pristine Si(100) surface have many available adsorption sites and most likely dissociate by the addition of both F atoms to the surface. A few of the incoming F_2 molecules may, however, approach the clean surface with an unfavorable orientation allowing only one of the F atoms to bind to the surface with the other one scattering to the gas phase. As the coverage increases, the adsorption of both F atoms becomes a less likely process, while atom abstraction, which only requires a single isolated empty site, becomes more viable. Atom abstraction then becomes an important channel until all isolated single empty sites are occupied. Once all sites are filled, the fluorination reaction ceases, and all incident F_2 molecules are unreactively scattered and detected in the gas phase.

Although the data as presented in Figure 1.7 clearly confirm the existence of the abstraction mechanism and yields some qualitative information about the relative importance of the atom abstraction and unreactive scattering channels, it begs for a more quantitative interpretation. Towards this end, an accurate value for the absolute flux of both the incident beam and the scattered products is sought, so that a mass balance calculation can be performed to yield the absolute reaction probabilities for the three available reaction channels: two-atom adsorption, atom abstraction, and unreactive scattering. Armed with the knowledge of the reaction probabilities, a direct correlation between F_2 exposure and fluorine coverage can then be made. The details of this quantitative analysis of the scattering measurements is presented in Section 1.4. The most significant result obtained from this quantitative analysis is the determination that surface saturation is reached at a coverage of 1 ML.

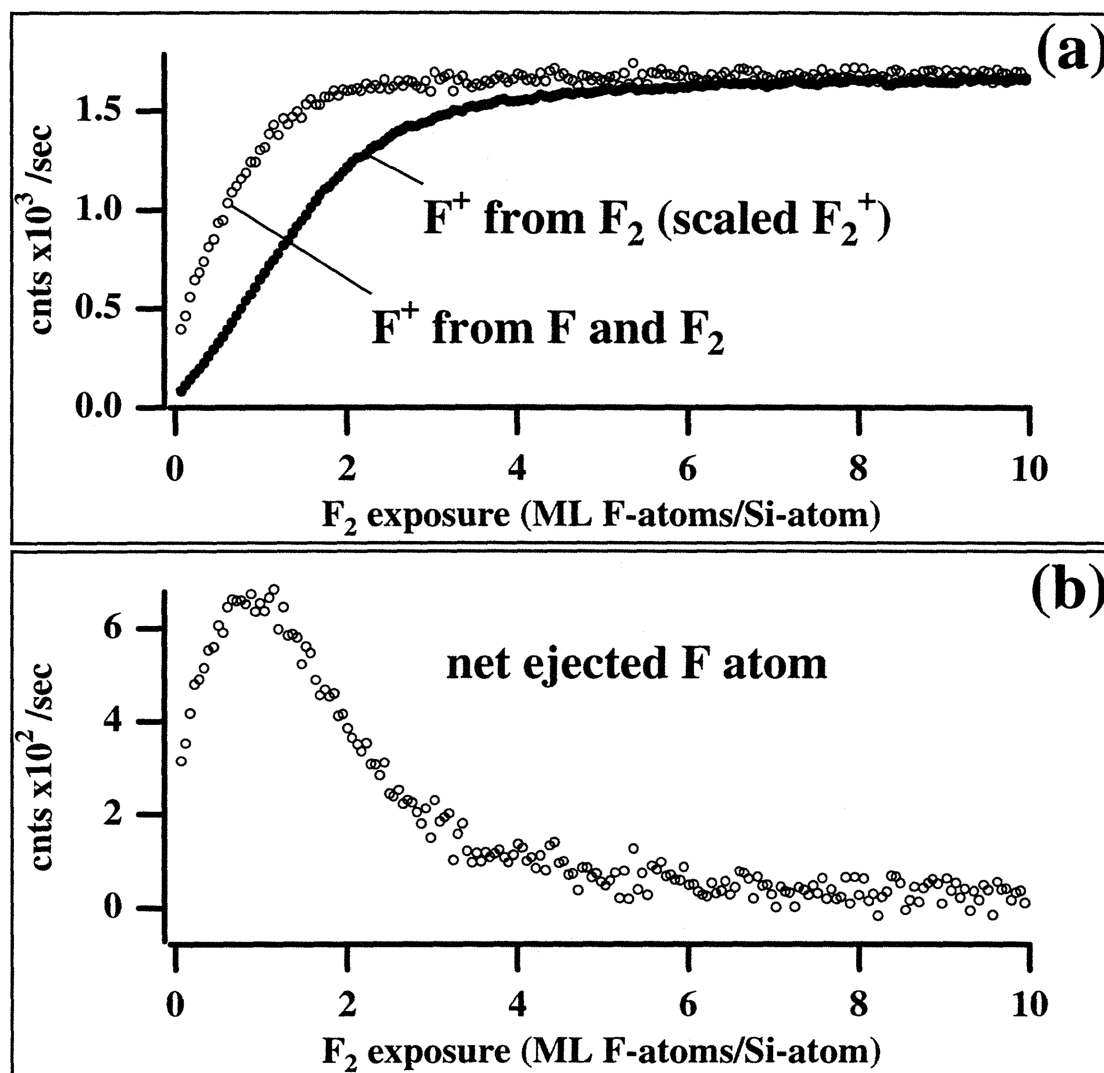

Figure 1.7 Exposure Dependence of Scattered F^+ and F_2^+ Signal

Species scattered at 35° from a 250 K Si(100) surface during exposure to ~ 0.1 ML sec^{-1} of F_2 from a 1% F_2/Kr beam (E_i=0.66 kcal mol^{-1}) incident at 0°. (a) Filled circles correspond to m/e= 38 signal scaled to represent the F^+ contribution from scattered F_2. Hollow circles correspond to m/e =19 signal arising from the superposition of F atoms from abstraction and unreactively scattered F_2 which fragments to F^+ upon ionization. (b) Signal obtained by point-by-point subtraction of the two traces in (a), represents the exposure dependence of the net F atoms arising from the abstraction mechanism.

1.3.3 Thermal Desorption Measurements

The scattered F and F_2 signals presented in the above section suggest that a saturation coverage is reached after exposure to approximately 3 ML of a 0.66 kcal mol^{-1} F_2/Kr molecular beam. In the interpretation of the scattering results, saturation of the surface coverage was inferred from the observation that the unreactively scattered signal reaches a constant level (see Figure 1.7 (a)). As previously discussed, a constant level only implies that a constant reaction probability has been reached, and does not necessarily demonstrate that the reaction has completely stopped. An alternate measurement is desired that might confirm the assumption that a saturation coverage is reached.

Thermal desorption measurements offer a complementary probe of the adsorption process. The amount of fluorine uptake during exposure to F_2 can be determined by monitoring the amount of silicon fluoride products desorbed during a temperature ramp of the Si surface. Assuming that all fluorine is removed from the surface during the temperature ramp, the integrated area of the desorption product signals should be proportional to the amount of fluorine that was originally adsorbed on the surface. Thermal desorption studies provide a more direct measure of the amount of fluorine adsorbed on the surface, and can be used to confirm whether the Si(100) truly saturates upon exposure to the low energy F_2 beam. A thermal desorption study and a thorough discussion of the confirmation of complete saturation has been presented by Yang[21]. Only the main results of this study are presented in this section.

In a thermal desorption measurement, the surface is first exposed to a F_2 molecular beam which causes a fluorine adlayer to form. The amount of fluorine on the surface depends on the extent and conditions of the exposure. After a given amount of fluorine

[21] J. J. Yang, Ph.D. Thesis, Massachusetts Institute of Technology, p. 144, (1993)

adsorbs, the crystal is gradually heated from the temperature at which the exposure took place to approximately 1100 K with a rate of 5 K sec^{-1} while the desorbing products are monitored with the mass spectrometer positioned along the surface normal. The triply differentially pumped line-of-sight mass spectrometer is used so that only reaction products coming directly from the surface are detected. The mass spectrometer is multiplexed to count alternately at two different m/e settings with a dwell time of 0.1 seconds. Signals are observed at m/e=66 (SiF_2^+) and m/e=85 (SiF_3^+), and are assigned to SiF_2 and SiF_4 respectively. The SiF_4 product is detected as SiF_3^+ rather than as the parent SiF_4^+ because it is known to readily fragment upon electron ionization. SiF_2 and SiF_4 are the only products observed to desorb as the result of the thermal decomposition of the fluorine adlayer, in agreement with the results of Schulberg[22] and Engstrom et al.[23]

Figure 1.8 shows the thermal desorption spectra from a 250 K Si(100) exposed to approximately 11 ML of F_2 from a 1.4 kcal mol^{-1} 1%F_2/Ar beam incident at 59° with respect to the surface normal. From the scattering results presented in the previous section, these exposure conditions are thought to produce a saturated fluorine overlayer. The SiF_2 product presented in Figure 1.8 (a) desorbs at a rapid rate centered at a surface temperature of ~800 K. The desorption is asymmetric with a small shoulder on the rising edge. The SiF_4 product in Figure 1.8 (b) is seen to desorb over a wide temperature range centered around 690 K with a smaller amount of desorption at approximately 500 K.

The question of whether the coverage saturates can be addressed by a study of the total SiF_2 and SiF_4 thermal desorption yield as a function of F_2 exposure. A properly weighted sum of the integrated SiF_2 and SiF_4 desorption products is proportional to the fluorine coverage originally present on the surface. An absolute measurement of the amount of fluorine present on the surface is not possible since it would require a

[22] M. T. Schulberg, Ph.D. Thesis, Massachusetts Institute of Technology, p.146, (1990)
[23] J. R. Engstrom, M. M. Nelson, and T. Engel, Surf. Sci. **215**, 437 (1989)

knowledge of the absolute electron impact ionization cross-section for both detected products, the relative transmission efficiency of each mass through the quadrupoles and the absolute geometric factors governing the collection efficiency of the detector. It is, however, necessary to at least account for the relative difference in the detection sensitivity of the two desorption products in order to properly weigh their respective contribution to the total desorption yield.

An estimate of the ratio of SiF_2 and SiF_4 detection sensitivities, based on gas-phase ionization cross-sections, and crudely estimated transmission efficiencies has been made by Schulberg[22] and later modified by Yang[24] to also take into account the markedly different angular distributions of the SiF_2 and SiF_4 products. An error, however, exists in the computation of the integrated area under the product angular distribution curves, which causes Yang's value of the ratio of SiF_4 to SiF_2 product yield to be slightly overestimated. In order to correct this error without diverging from the main focus of this section, the details of the amended derivation of the ratio of SiF_4 to SiF_2 thermal desorption product yield are deferred to the discussion in Appendix D.

For the current purpose, it suffices to say that SiF_4 is determined to be the minor thermal desorption product with a yield of approximately 0.063 times that of SiF_2. Since each SiF_4 caries twice as much fluorine than SiF_2, then about 12% of the fluorine present on the saturated surface is detected as SiF_4. With this relative yield in mind, the total fluorine yield as a function of F_2 exposure is obtained by adding the total SiF_2 detected to 12% of the total SiF_4 product.

Figure 1.9 shows the sum of the integrated SiF_2 signal plus 12% of the SiF_4 desorption signal versus F_2 exposure. The quantity given by the plot's ordinate does not account for the absolute mass-spectrometer detector efficiency, and therefore has no

[24] J. J. Yang, Ph.D. Thesis, Massachusetts Institute of Technology, p. 152, (1993)

significance in terms of the absolute surface coverage. The shape of the curve does, however, provide a direct correlation between surface exposure and coverage. The fluorine surface coverage is seen to rapidly increase over the low exposure regime, but gradually grows to a nearly constant value for higher exposures. The saturation of the thermal desorption product represents direct evidence that surface fluorination has nearly ceased at the higher exposures. A more detailed analysis of the desorption yield data estimates[25] the adsorption probability at high exposures to be bound by an upper limit of less than 10^{-3}. This result thus confirms the almost complete saturation of the coverage after long exposure to F_2 incident at low energy.

The picture that emerges from these thermal desorption studies can be summarized as follows. The initial fluorination of the silicon surface occurs very rapidly and efficiently, reflecting the high sticking probability of F_2 on the clean surface. This rapid fluorination is evidenced by the rapid increase of the total thermal desorption product yield at low exposures. A saturation coverage is eventually reached at which time the desorption yield settles to a near constant value. A sticking probability lower than 1.8% is estimated for the fully fluorinated surface. The surface does continue to uptake fluorine, but at a negligibly slow rate. No confirmation is available of the surface sites responsible for this slow fluorine uptake seen at large exposures.

---

[25] D. P. Pullman, private communication

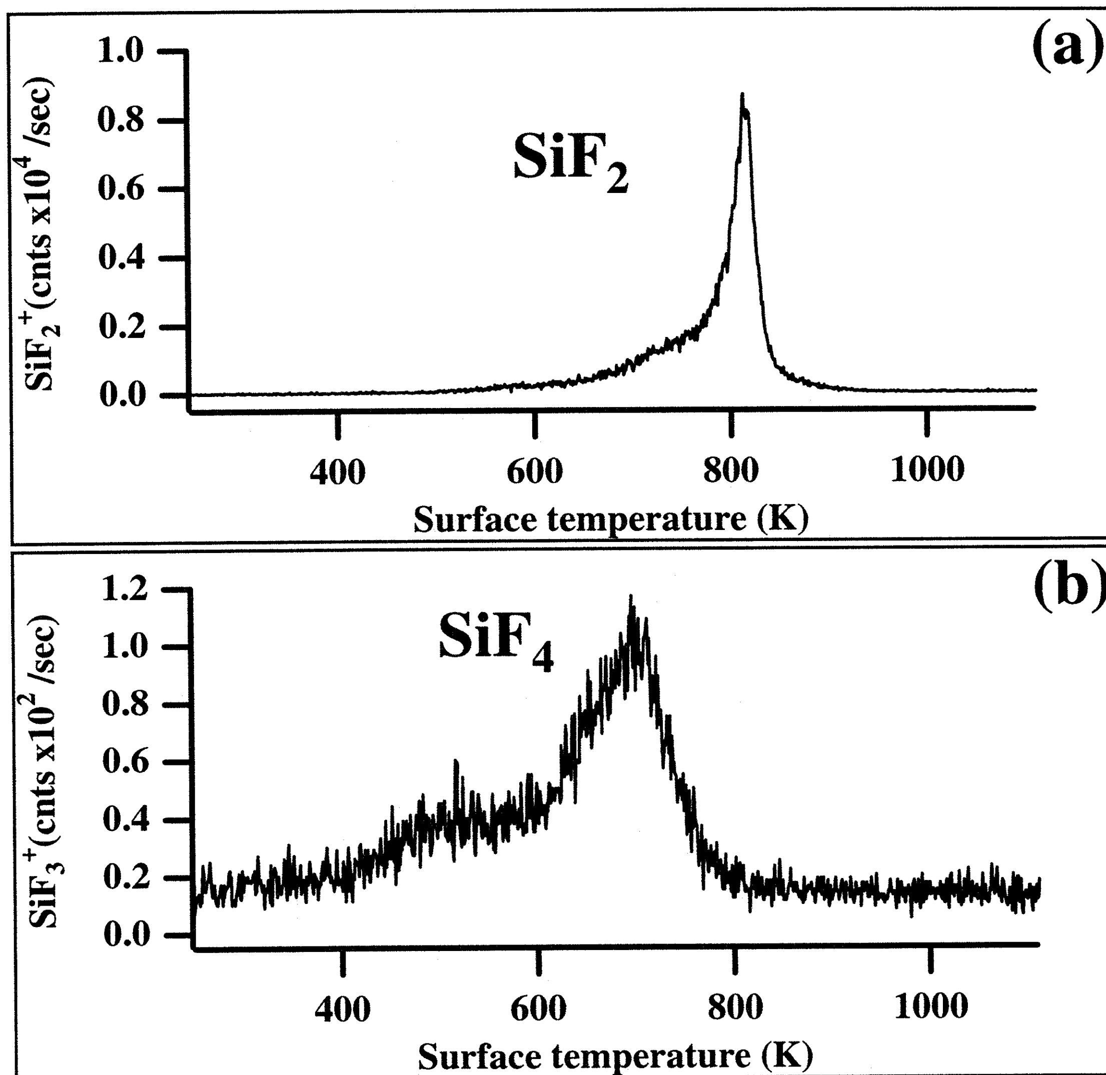

Figure 1.8 Thermal Desorption Spectra of Si(100) Exposed to 1%F_2/Ar

250 K Si(100) exposed to 10.7 ML of F_2 from a 1%F_2/Ar beam (E_i=1.4 kcal mol^{-1}) incident at 59°. Thermal desorption products collected with line-of-sight spectrometer positioned normal to the surface. Ramp rate 5 K sec^{-1}. (a) SiF_2 desorption product detected at m/e = 66 (SiF_2^+) (b) SiF_4 detected at m/e= 85 (SiF_3^+).

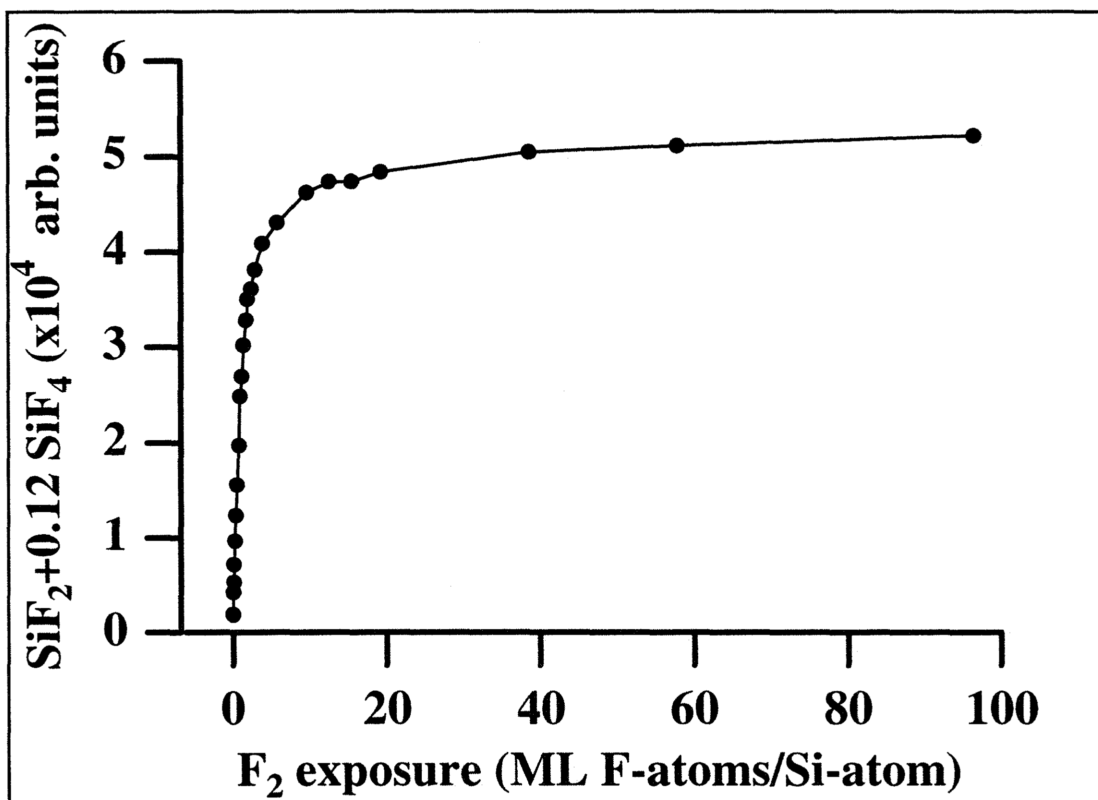

Figure 1.9 Total Fluorine Thermal Desorption Yield as a Function of F_2 Exposure

Total fluorine yield obtained from the weighted sum of the integrated thermal desorption signals of SiF_2 and SiF_4 after a 250 K Si(100) surface was exposed to a 1%F_2/Ar (E_i=1.4 kcal mol^{-1}) beam for the exposures plotted on the horizontal axis. Integrated signals are weighted to account for differences in velocities, ionization cross-sections, and angular distributions of the two desorbing products.

1.3.4 Helium Atom Diffraction Measurements

The results of both the exposure dependence of the scattered F and F_2 and the thermal desorption product yield are consistent with saturation of the surface coverage. Furthermore, the results of the quantitative analysis of the exposure dependence of the scattered signals to be presented in Section 1.4 indicates that saturation is reached with 1ML of fluorine coverage. Comparison of helium diffraction measurements from the clean and fluorinated Si(100) surface presented in this section are also consistent with 1 ML saturation coverage.

Low-energy electron diffraction (LEED) is the most commonly used technique to obtain structural information about surfaces and their adlayers. There are however, two inherent disadvantages of LEED that complicate its use in the study of the fluorine-silicon system. First, the large penetration depth of the incident electrons results in multilayer scattering which makes the interpretation of the LEED patterns difficult. Second, the large cross-section for electron-stimulated-desorption of F results in the depletion of the fluorine adlayer when exposed to the low energy electron beam, and hence precludes the use of LEED for studies of fluorine adsorption. Helium diffraction offers an alternate, less invasive method for obtaining information about the long range periodic structure of both the clean and fluorine covered Si surface. He atoms do not penetrate the top layer and thus eliminate the complications of multilayer scattering. In addition, He atoms incident with 0.27 kcal mole^{-1} do not disrupt the fluorine adlayer.

Helium diffraction is the ideal tool for determining the long range periodicity of both clean and fluorinated Si surfaces. It is based on the wave nature of the light He atoms. A He atom of the appropriate de Broglie wavelength can coherently scatter from the repulsive periodic potential presented by the surface. The constructive and destructive interference of the scattered He waves gives rise to a modulation of the intensity profile of the scattered-He angular distribution. The pattern of this intensity modulation contains

valuable information about the periodicity of the scattering potential and hence of the underlying structure of the surface. The condition for constructive interference of atoms elastically scattered from a periodic surface potential is given by the Bragg equation:

$$n\lambda_{He} = d(\sin\theta_{scat} - \sin\theta_i) \tag{1.1}$$

where n is the diffraction order, d is the bulk lattice parameter, λ_{He} is the wavelength of the He atoms, and θ_i and θ_{scat} are the incident and scattering angles respectively. This mathematical expression states that, for a given angle of incidence, constructive interference is obtained at a scattering angle for which the path difference traveled by the interfering waves equals an integer number (n) of wavelengths (λ_{He}). In a simple interpretation, the diffraction order is then the number of wavelengths corresponding to the path difference between two constructively interfering waves. The angular separation between peaks in the diffraction spectrum is inversely proportional to the separation (d) between the periodic features in the potential causing the diffraction.

The present He diffraction studies of the clean Si(100) surface corroborate the well-documented (2x1) periodicity of the reconstructed Si surface previously demonstrated by LEED studies[26] and calculations[27] subsequently confirmed by scanning tunneling microscopy[28]. Bulk silicon crystallizes in the tetrahedral diamond structure characterized by the formation of a cubic lattice in which each Si atom is covalently bonded to three other Si atoms. If an ideal Si crystal is cleaved along the (100) direction, the exposed surface atoms would appear equally spaced on a square lattice, each forming two bonds to the atoms in the second layer, and exposing two dangling bonds at the gas-surface interface. However, when a real Si crystal is cleaved, it minimizes its surface free energy by reducing the number of highly reactive dangling bonds. Neighboring surface Si atoms

---

[26] R. E. Schlier and H. E. Farnsworth, J. Chem. Phys. **30**, 4 (1959)
[27] D. J. Chadi, Phys Rev. Lett. **43**, 43 (1979)
[28] R. J. Hammers, R. M. Tromp, and J. E. Demuth, Phys. Rev. B **34**, 5343 (1986)

are paired, forming surface Si—Si bonds which slightly distort the tetrahedral structure of the outermost 4-5 bulk layers, but which overall lowers the lattice energy. The reconstruction of the surface to form "silicon dimers" changes the periodicity of the top silicon layer. The reconstructed surface is made up of rows of silicon dimers separated by a distance equal to two times the bulk lattice parameter in one direction, while maintaining the original unit cell separation in the perpendicular direction. The resulting surface periodicity is referred to as a 2x1 reconstruction indicating the new rectangular dimensions of the surface unit cell. The structure of both the reconstructed and unreconstructed Si (100) surface are shown in Figure 1.10 (a) and (b).

Chemically, the main effect of the surface reconstruction is the elimination of one dangling bond at each Si atom, leaving a single dangling bond per Si atom available for fluorination. The reactivity of these remaining surface dangling bonds has been predicted[4] to resemble that of a free-radical electron. It is then expected that the silicon dangling bonds should be the preferred adsorption sites for the fluorine adlayer. Since there is exactly one dangling bond per surface silicon atom, a fluorine coverage of 1 ML can be obtained by filling all available dangling bond sites. The question then arises of whether the fluorination process stops with the filling of all dangling bonds, or whether it continues by reacting with the Si—Si dimer bonds or Si—Si bonds between the first and second layer. The answer to this question can be obtained by comparing the surface structure of the fully fluorinated silicon adlayer to that of the clean Si (100) 2x1 surface.

The scattering apparatus previously described allows He diffraction measurements to be made by scattering a beam of 50% He/Ar from the Si surface and detecting the elastically scattered He signal with the line-of-sight mass spectrometer. A seeded beam is used to slow the He such that its wavelength matches the size of the surface periodicity. The angular dependence of the diffracted He can be obtained by manually rotating the detector a fraction of a degree every 2 or 3 seconds. Further experimental

details about the He diffraction measurements can be found in Yang's thesis[29]. Figure 1.11 (a) shows the helium diffraction spectrum of a clean Si(100) 2x1 reconstructed surface. Experimental details are given in the figure caption. The zero order feature corresponds to specular ($\theta_i = \theta_{scat}$) scattering, the trivial solution of the Bragg equation. The second feature, labeled half order, arises from interfering waves from sites separated by a distance equal to twice the bulk lattice parameter. The half order feature is a clear signature for the 2x1 lattice reconstruction for which the distance between silicon dimer rows is double the Si bulk lattice parameter. The presence of this feature directly correlates with the presence of Si—Si dimer bonds on the surface. The first order feature is associated with one full lattice parameter separation of the surface sites, and arises from the periodic repetition of dimers within a given row which are separated by a distance equal to the bulk lattice parameter even after reconstruction. The peak positions of the diffraction features in the spectrum yield a lattice spacing of 3.73 Å, within 3% of the accepted value.

Figure 1.11 (b) shows a similar He diffraction spectrum for Si(100) that has been fluorinated by extensive exposure to a 1%F_2/Kr beam (see figure caption for experimental details). The exposure is such that saturation coverage has been reached. The marked similarities between the fluorinated and clean-surface He diffraction spectra strongly suggests the 2x1 unit cell of the two surfaces is equivalent. The differences in the intensities between the clean and fluorinated surface spectra result from the different corrugation depths of the scattering potential of the clean and fluorine covered surfaces. The presence of an intense half order peak in Figure 1.11 (b) is consistent with the Si—Si dimer bond remaining intact during fluorination by exposure to the 0.66 kcal mol^{-1} F_2 beam. If the dimer bonds are not broken, then the only available sites for fluorination are the dangling bonds, which would limit the maximum possible surface coverage to 1 ML.

---

[29] J. J. Yang, Ph.D. Thesis, Massachusetts Institute of Technology, p. 100, (1993)

Although the presence of the half order peak in the fluorinated surface suggests compellingly that the dimer bonds remain intact and that the fluorine coverage saturates at 1 ML, it does not provide definite proof. For example, consider a situation in which the dimer bonds are cleaved giving rise to a fluorinated silicon surface in which rows of Si atoms alternate between being monofluorinated and difluorinated. This configuration would maintain a 2x1 periodicity but the coverage would be 1.5 ML. However, the quantitative analysis based on the mass balance of the scattered molecules presented in Section 1.4 yields a saturation coverage of 1 ML which rules out this alternative surface structure.

The picture that emerges from this He diffraction study is as follows. The clean surface clearly displays the periodicity characteristic of a 2x1 reconstructed Si(100) surface. The surface is described as alternating rows of Si—Si dimers separated by a lattice parameter d within a given row and a distance 2d between dimer rows. Each Si on the surface has a single dangling bond available for fluorination. Each dangling bond can act to abstract a F atom from an incoming F_2 molecule. Given the appropriate orientation of the incoming F_2, the second F atom may be ejected into the gas phase. The complementary F atom will otherwise be propelled towards the surface where it will bind if it finds an available dangling bond site. If no dangling bonds are available the ejected atom will scatter from an occupied site and return to the gas phase. No other surface sites are accessible to the incoming low energy (0.66 kcal mol^{-1}) fluorine. The He diffraction data strongly suggest that no Si—Si dimer bonds are broken, and no significant amount of silicon is etched from the surface. The surface eventually gets saturated with 1 ML of fluorine as confirmed by the quantitative analysis of the scattered F and F_2 presented in the next section.

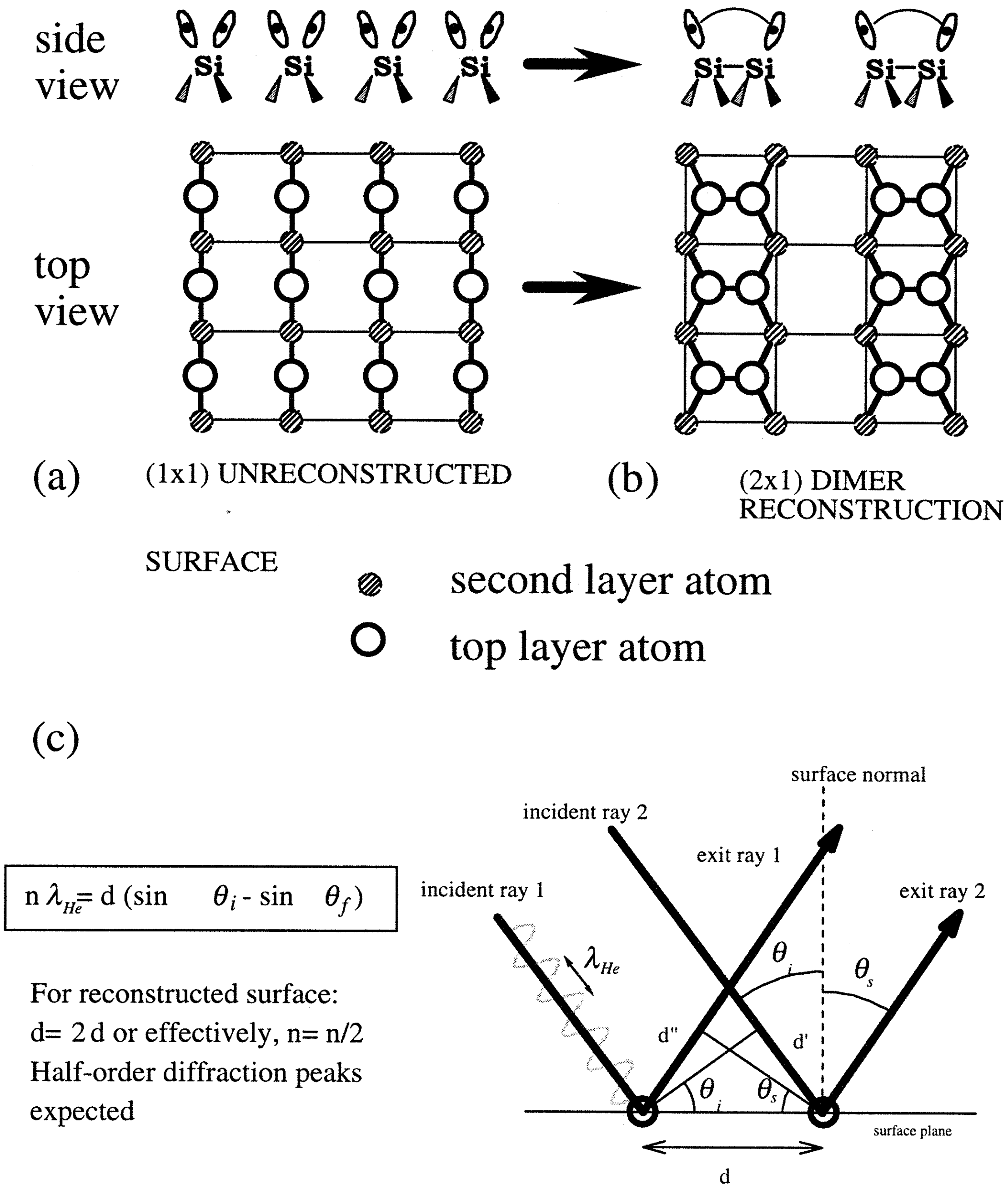

Figure 1.10 Structure of Unreconstructed and Reconstructed Si(100)

(a) Unreconstructed surface shows equally spaced Si surface atoms on a square dxd unit cell. Each surface Si has two dangling bonds. (b) Reconstructed surface shows rows of Si-Si dimers with a 2dxd unit cell, and a single dangling bond per surface Si atom. (c) Pictorial representation of the path difference of two scattering He atom waves leading to coherent interference.

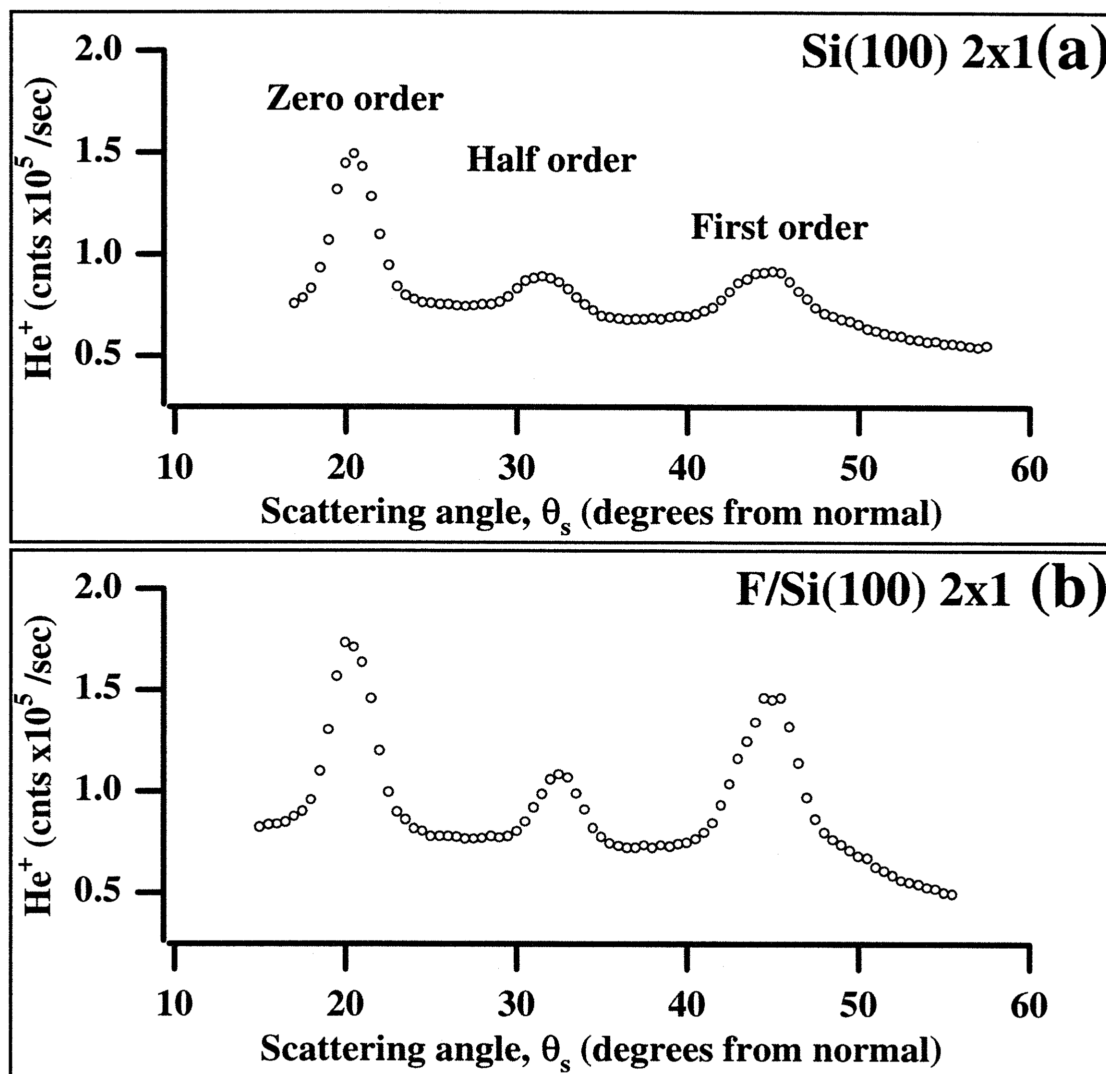

Figure 1.11 He Diffraction Spectra of a Clean and Fluorinated Si(100)

(a) He diffraction scan along the [10] direction of a clean 250 K Si(100) 2x1 surface. 50%He/Ar beam (E_i=0.27 kcal mol^{-1} He atoms, λ_{He}=1.33 Å) incident at 20° and detected at 0.5° degree increments. The half order peak is a signature for the Si-Si surface dimer bond. (b) Same surface saturated with fluorine by exposure to ~6 ML of 1%F_2/Kr, θ_i= 20° prior to a similar diffraction scan. The persistence of the half order peak demonstrates that the Si-Si dimer bonds remain intact upon fluorination.

1.4 Exposure Dependence of the Fluorine Coverage

This section presents a quantitative analysis of the scattered F and F_2 signals as a function of F_2 exposure. A mass balance comparing the incident and scattered fluorine fluxes yields the absolute reaction probabilities as well as the amount of fluorine adsorbed on the surface as a function of fluorine exposure. The saturation coverage is established to be 1 ML, confirming that fluorine simply decorates the highly reactive Si dangling bonds but is not able to break the Si—Si dimer bonds, so it remains inert to further fluorination.

Sections 1.4.1 and 1.4.3 present the mathematical formalism required to calculate the exposure dependence of the reaction probabilities and fluorine coverage from the F and F_2 scattering data. Additional measurements required for the calculation of the reaction probabilities, including the electron ionization cross-sections and quadrupole transmissivities of F and F_2 are discussed in Sections 1.4.1.1 and 1.4.1.2, respectively. Section 1.4.2 addresses the scattering angle dependence of the reaction probabilities and finally, Section 1.4.4 presents the details of the beam flux calibrations required for the determination of the surface coverage.

1.4.1 The Probabilities of the Reaction Channels

A fluorine molecule scattering from the silicon surface is assumed to follow one of three possible reaction channels:

1.) **Unreactive scattering** is the channel in which the F_2 molecule, after interacting with the surface, scatters back to the gas phase where it is detected after electron bombardment ionization as either F_2^+ or F^+.

2.) **Fluorine atom abstraction** is the channel in which one of the fluorine atoms is captured by the surface while its partner scatters back to the gas phase where it can be ionized and detected as F^+.

3.) **Two-atom abstraction** is the channel in which both fluorine atoms are captured by the silicon surface and thus no scattered products are detected in the gas phase.

The probabilities of these three channels are given by:

$$P_0(\varepsilon) = \frac{\text{scattered } F_2 \text{ flux}}{\text{incident } F_2 \text{ flux}} = \frac{I_{F_2}^{scat}(\varepsilon)}{I_{F_2}^{scat}(\infty)} \quad (1.2)$$

$$P_1(\varepsilon) = \frac{\text{scattered F flux}}{\text{incident } F_2 \text{ flux}} = \frac{I_{F}^{scat}(\varepsilon)}{I_{F_2}^{scat}(\infty)} \quad (1.3)$$

$$P_2(\varepsilon) = (1 - P_0(\varepsilon) - P_1(\varepsilon)) \quad (1.4)$$

where the numerical subscripts on the probabilities, P, correspond to the number of fluorine atoms that remain on the surface after each scattering event and ε is the F_2 exposure. The incident F_2 flux, $I_{F_2}^{inc}$, is set equal to the scattered F_2 flux in the limit of infinite exposure, $I_{F_2}^{scat}(\infty)$, because once the surface is fully fluorinated, all incoming fluorine molecules are assumed to scatter unreactively with unit probability. In order to calculate these probabilities, expressions for the scattered fluxes, $I_{F}^{scat}(\varepsilon)$ and $I_{F_2}^{scat}(\varepsilon)$, in terms of measurable quantities must be obtained.

The signal collected by the mass spectrometer is proportional to the number density of ions produced at m/e=38 and m/e=19 upon ionization or dissociative ionization of the neutral products (F_2 and F). The mass spectrometer signals detected at a scattering angle, θ_s, are related to the scattered fluxes by

$$S_{38}(\varepsilon,\theta_s) = \frac{I_{F_2}^{scat}(\varepsilon,\theta_s) \times \sigma_{F_2 \to F_2^+} \times T_{38}}{v_{F_2}} \quad (1.5)$$

and

$$S_{19}(\varepsilon,\theta_s) = \frac{I_{F_2}^{scat}(\varepsilon,\theta_s) \times \sigma_{F_2 \to F^+} \times T_{19}}{v_{F_2}} + \frac{I_{F}^{scat}(\varepsilon,\theta_s) \times \sigma_{F \to F^+} \times T_{19}}{v_F} \quad (1.6)$$

where $S(\varepsilon, \theta_s)$ is the exposure and scattering angle dependent signal at the mass-to-charge ratio denoted by the subscript, σ is the appropriate electron-impact ionization cross-section at the electron energy used for the measurement, v is the flux-weighted average velocity of the scattered neutral indicated, and T is the transmissivity of the given ion through the quadrupole mass-filter. A proportionality factor, composed of the product of the current density of bombarding electrons in the ionizer and the length of the ionization region is not included. However, since both quantities comprising the neglected factor are independent of the mass-to-charge of the detected signal, they cancel in the ratios used to define the probabilities in Eqnts. (1.2)-(1.4).

Equation (1.6) shows that there are two contributions to the signal at m/e=19. The first contribution comes from the fragmentation of F_2 in the ionizer while the second arises from the ionization of scattered F atoms. This signal can thus be written as

$$S_{19}(\varepsilon,\theta_s) = S_{19}^{F_2}(\varepsilon,\theta_s) + S_{19}^{F}(\varepsilon,\theta_s) \tag{1.7}$$

where the superscripts indicate the neutral species giving rise to the signal at the m/e indicated by the subscripts.

Solving for $I_{F_2}^{scat}$ from Eq. (1.5) yields

$$I_{F_2}^{scat}(\varepsilon,\theta_s) = \frac{S_{38}(\varepsilon,\theta_s)\times v_{F_2}}{\sigma_{F_2\to F_2^+}\times T_{38}} \tag{1.8}$$

And substituting Eq. (1.8) into Eq. (1.6) and solving for I_F^{scat} yields

$$I_F^{scat}(\varepsilon,\theta_s) = \left(S_{19}(\varepsilon,\theta_s) - \frac{S_{38}(\varepsilon,\theta_s)\times\sigma_{F_2\to F^+}\times T_{19}}{\sigma_{F_2\to F_2^+}\times T_{38}} \right) \times \left(\frac{v_F}{\sigma_{F\to F^+}\times T_{19}} \right) \tag{1.9}$$

Next an expression for $P_1(\varepsilon,\theta_s)$ is given by taking the ratio of Eq. (1.9) to Eq. (1.8), which is evaluated in the infinite exposure limit.

$$P_1(\varepsilon,\theta_s) = \left(\frac{v_F}{v_{F_2}}\right)\left(\frac{\sigma_{F_2\to F_2^+}}{\sigma_{F\to F^+}}\right)\left(\frac{T_{38}}{T_{19}}\right)\left(\frac{1}{S_{38}(\infty,\theta_s)}\right)\left(S_{19}(\varepsilon,\theta_s) - \frac{S_{38}(\varepsilon,\theta_s)\times\sigma_{F_2\to F^+}\times T_{19}}{\sigma_{F_2\to F_2^+}\times T_{38}} \right) \tag{1.10}$$

All quantities to the right of the equal sign in Eq. (1.10), except for $\sigma_{F \to F^+}$, can be measured. The fluorine atom ionization cross-section is taken from a measurement by Freund et al.[30] The expression contained in the last bracket is now simplified by defining the F_2 cracking fraction. The cracking fraction gives the relative amounts of F_2^+ and F^+ obtained upon electron impact ionization of F_2. Since the surface is believed to be passivated at high coverages, the scattered signal at long exposures arises only from unreactively scattered F_2, and hence the cracking fraction, α, is given as the ratio of the scattered signals at m/e=19 and 38 (ratio of Eq.(1.6) to Eq.(1.5)) at long exposures

$$\alpha = \text{Cracking fraction} = \frac{S_{19}(\infty)}{S_{38}(\infty)} \tag{1.11}$$

or equivalently,

$$\alpha = \frac{\sigma_{F_2 \to F^+} \times T_{19}}{\sigma_{F_2 \to F_2^+} \times T_{38}} \tag{1.12}$$

with $I_F^{scat}(\infty)$ set equal to zero. Now, the last bracket in the expression for P_1 in Eq. (1.10) reduces to

$$\left(S_{19}(\varepsilon,\theta_s) - S_{38}(\varepsilon,\theta_s) \times \alpha\right) = S_{19}^F(\varepsilon,\theta_s) \tag{1.13}$$

where S_{19}^F is the net signal at m/e=19 due to F atoms that scatter from the surface and is obtained by subtracting the contribution of dissociatively ionized F_2 from the total signal detected at m/e=19. The three reaction probabilities can then be written in terms of experimentally measurable quantities

$$P_0(\varepsilon,\theta_s) = \frac{S_{38}(\varepsilon,\theta_s)}{S_{38}(\infty,\theta_s)} \tag{1.14}$$

$$P_1(\varepsilon,\theta_s) = \left(\frac{v_F}{v_{F_2}}\right)\left(\frac{\sigma_{F_2 \to F_2^+}}{\sigma_{F \to F^+}}\right)\left(\frac{T_{38}}{T_{19}}\right)\left(\frac{S_{19}^F(\varepsilon,\theta_s)}{S_{38}(\infty,\theta_s)}\right) \tag{1.15}$$

[30] Todd R. Hayes, Robert C. Wetzel, and Robert Freund, Phys. Rev. A **35**, 578, (1987)

$$P_2(\varepsilon,\theta_s) = (1 - P_0(\varepsilon,\theta_s) - P_1(\varepsilon,\theta_s)) \tag{1.16}$$

The probability for unreactive scattering, $P_0(\varepsilon,\theta_s)$, given in Eq. (1.14), requires the measurement of the mass spectrometer signal at m/e=38 and detection angle θ, as a function of F_2 exposure. The F_2 velocity has been shown to be independent of exposure (see Section 1.3.1), so it cancels from the P_0 expression. The fluorine exposure is determined from the flux of the incident beam, the absolute value of which has been given in Section 1.4.4.

Equation (1.15) gives the probability that one fluorine atom is captured by the surface while its partner scatters back to the gas phase at an angle θ_s with respect to the surface normal. The interpretation of this expression is quite intuitive. The abstraction probability is the ratio of the net F atom signal to the long time signal at m/e=38 multiplied by the scaling factors that take into account the detection sensitivity, such as ionization cross-sections, neutral velocities, and quadrupole transmissivities. The expression for P_1 can however be rewritten in a more compact form which eliminates the transmissivity ratio. Solving for $\sigma_{F_2 \to F^+}$ in Eq. (1.12) and substituting into Eq. (1.10) yields

$$P_1(\varepsilon,\theta_s) = \left(\frac{v_F}{v_{F_2}}\right)\left(\frac{\sigma_{F_2 \to F^+}}{\sigma_{F \to F^+}}\right)\left(\frac{S_{19}(\varepsilon,\theta_s)}{S_{19}(\infty,\theta_s)} - \frac{S_{38}(\varepsilon,\theta_s)}{S_{38}(\infty,\theta_s)}\right) \tag{1.17}$$

The value of $\sigma_{F_2 \to F^+}$ is experimentally determined as described in the Section 1.4.1.1, while the value of $\sigma_{F \to F^+}$ is obtained from the literature[30]. Although Eq. (1.17) is less intuitive than Eq. (1.15), it eliminates the transmission function ratio and minimizes the propagated error.

Procedurally, since data from multiple measurements are averaged in order to improve the quality of the signal, the last bracket of Eq. (1.17) is rewritten to give,

$$P_1(\varepsilon,\theta_s)=\left(\frac{v_F}{v_{F_2}}\right)\left(\frac{\sigma_{F_2\rightarrow F^+}}{\sigma_{F\rightarrow F^+}}\right)\left(\frac{1}{N}\sum_N\frac{S_{19}(\varepsilon,\theta_s)}{S_{19}(\infty,\theta_s)}-\frac{1}{N}\sum_N\frac{S_{38}(\varepsilon,\theta_s)}{S_{38}(\infty,\theta_s)}\right) \qquad (1.18)$$

where N is the number of scattering measurements averaged. As seen in Eq. (1.18), each measurement of the signals at m/e =19 and 38 is normalized to its value at long exposure. The normalized signals are then subtracted to obtain a quantity proportional to the net F atoms scattered into the gas phase. The velocities of the scattered F and F_2 have been measured, and their results are presented in Section 1.3.1. The determination of the F_2 electron impact ionization cross-sections is presented in Section 1.4.1.1. Once P_0 and P_1 have been obtained, P_2 follows by the mass-balance condition expressed in Eq. (1.16).

Table 1-2 summarizes the values of all quantities required for the determination of the three reaction probabilities. The dependence of these probabilities on exposure, as obtained from these values, is presented in Figure 1.12. Figure 1.12 (a) shows $P_0(\varepsilon,\theta_s{=}35°)$, the unreactive scattering probability, as determined from Eq. (1.14). Its near zero value in the zero coverage limit means that the adsorption probability is near unity. P_0 rapidly increases as surface sites become occupied and eventually reaches unit probability, implying that the surface has become fully passivated by the presence of the fluorine adlayer. The abstraction probability, $P_1(\varepsilon,\theta_s{=}35°)$, shown in Figure 1.12 (b) is approximately 0.1 in the limit of zero F_2 exposure. The probability of an abstraction event gradually increases to a maximum value of 0.3, after which P_1 gradually decreases to zero as the surface coverage approaches saturation. Figure 1.12 (c) gives the two-atom absorption probability, $P_2(\varepsilon,\theta_s{=}35°)$, as determined by the mass balance condition in Eq. (1.16). The two-atom adsorption channel dominates at low coverages with a probability of 0.85. As surface sites begin to fill, this channel gives way to the more favorable abstraction process and ultimately vanishes as unreactive scattering completely dominates the long exposure regime.

Table 1-2 Absolute Values Required for Calculation of Reaction Probabilities

Quantity	Symbol	Measured value	Source
Average velocity of scattered F_2	v_{F_2}	436 ± 14 m sec^{-1}	Section (1.3.1)
Average velocity of scattered F	v_F	1100 ± 60 m sec^{-1}	Section (1.3.1)
F_2 partial cross-section (70 eV)	$\sigma_{F_2 \rightarrow F^+}$	$0.26 \pm 0.05 x 10^{-16}$ cm^2	Section (1.4.1.1)
F-atom cross-section (70 eV)	$\sigma_{F \rightarrow F^+}$	$0.87 \pm 0.17 x 10^{-16}$ cm^2	Freund et al.[30]
Transmission ratio	T_{38}/T_{19}	0.89 ± 0.15	Section (1.4.1.2)
Incident flux from 1%F_2/Kr beam	I_F^{inc}	0.18 ± 0.01 ML F sec^{-1}	Section (1.4.4.2)

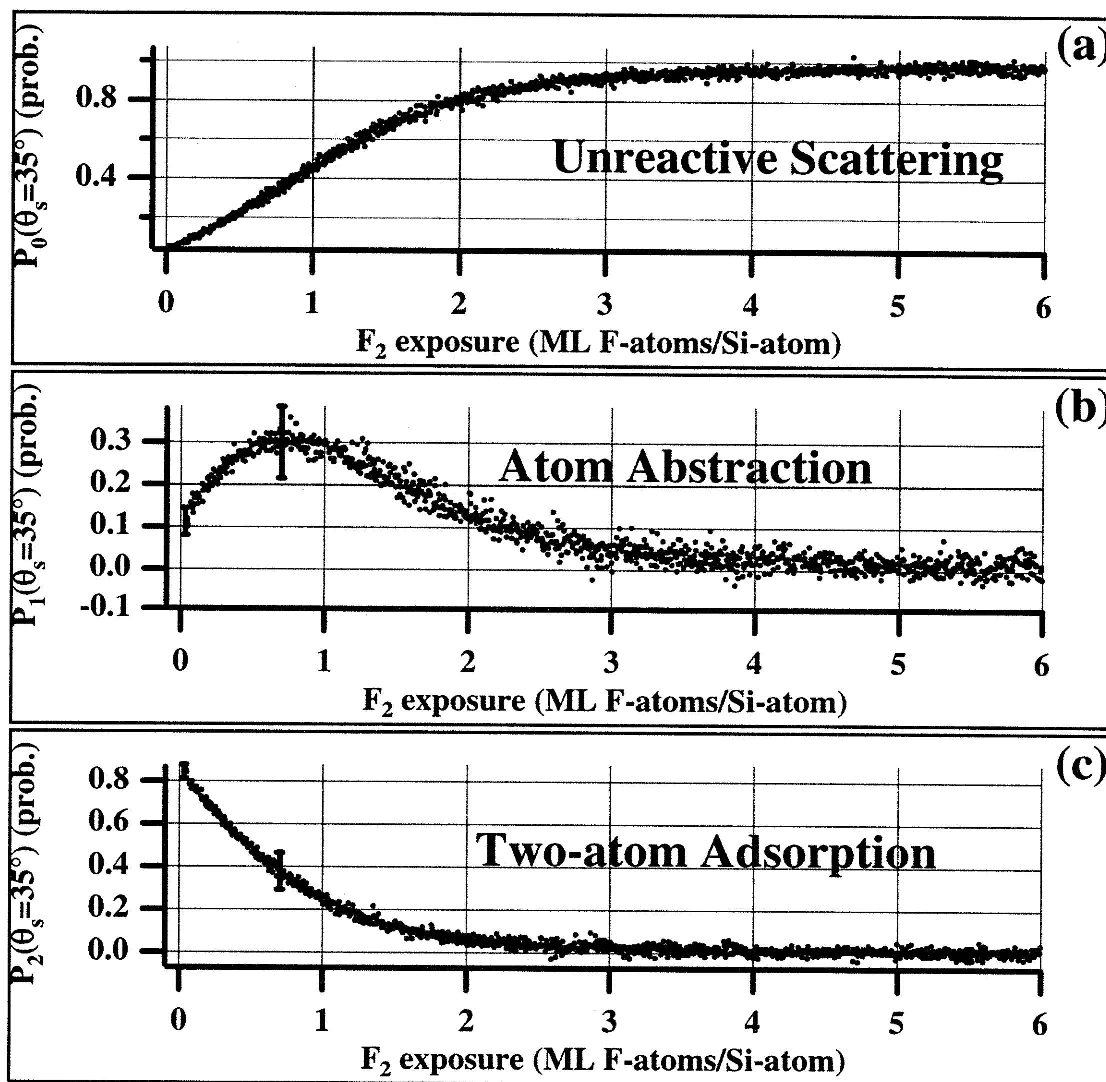

Figure 1.12 Exposure Dependence of F_2 Reaction Probabilities

Reaction probabilities measured at θ_s=35° derived from the scattering data of Figure 1.7. (a) Unreactive scattering probability, P_0. (b) F-atom abstraction probability, P_1. (c) Two-atom adsorption probability, P_2.

1.4.1.1 Measurement of the Electron Impact Ionization Cross-sections

The ion signal expected at a given m/e= M from a known particle flux I_M entering the mass spectrometer with velocity V_M is given by

$$S_M = \frac{\sigma_{M \to M^+} I_{e^-} d_{e^-} T_M I_M}{v_M} \tag{1.19}$$

where $\sigma_{M \to M^+}$ is the ionization cross-section, T_M is the transmissivity of ions M^+ through the quadrupole, I_{e^-} is the current density of bombarding electrons, and d_{e^-} is the length of the ionization region. Aside from the flux and velocity of the particles, there are four other factors that determine the absolute number of particles detected. The flux of electrons in the ionizer, expressed as the product of I_{e^-} and d_{e^-}, is an instrument dependent quantity and since it does not depend on the m/e being detected, it cancels in the ratio of two signals. The transmissivity of ions through the quadrupole filter, T_M, depends on the m/e as well as the resolution setting of the spectrometer. The relative transmissivity of two masses must be known for an accurate ratio of mass spectrometer signals to be obtained. The procedure for determining relative transmission ratios is discussed in Section (1.4.1.2). The ionization cross-section, $\sigma_{M \to M^+}$, of a molecule subjected to electron bombardment is an intrinsic property that determines the efficiency with which species M is ionized by electrons of a given energy. Any attempt at extracting quantitative information from mass spectrometer measurements requires an accurate knowledge of the absolute ionization cross-sections of all species ionized.

The absolute measurement of an ionization cross-section requires either the knowledge of all quantities in Eq. (1.19), or the knowledge of another cross-section from which to reference the new measurement. Since no absolute values for I_{e^-} , d_{e^-} or T_M are available for the present apparatus, previously known cross-sections are used as reference for these measurements. The determination of the electron impact ionization cross-sections of F_2 is accomplished by referencing to the ionization cross-section of Ar. A

reliable value for the Ar ionization cross-section has been given by Freund et al.[31] and recently improved by Smith et al.[32]

The most direct measurement of the $\sigma_{F_2 \to F^+}$ cross-section required for the calculation of P_1 is obtained from time-of-flight distributions of a 1%F_2/Ar beam. A 1%F_2/Ar beam is chosen for the following reasons. First, this beam contains both the molecule for which the cross-section needs to be determined (F_2) and the reference species (Ar) for which the cross-section is already well-established. Additionally, since the two components in the mixture have nearly the same mass, the detrimental effects of Mach number focusing (Section 1.4.4.2) and quadrupole transmissivity (Section 1.4.1.2) are eliminated.

Straight-through signals measured at m/e=36 ($^{36}Ar^+$) and m/e=38 (F_2^+) are related to the ionization cross-sections as

$$S_{36} = \frac{\sigma_{Ar \to Ar^+} T_{36} I_{^{36}Ar} I_{e^-} d_{e^-}}{v_{Ar}} \tag{1.20}$$

$$S_{38} = \frac{\sigma_{F_2 \to F_2^+} T_{38} I_{F_2} I_{e^-} d_{e^-}}{v_{F_2}} \tag{1.21}$$

The less abundant isotope ^{36}Ar is chosen so as to avoid the excess signal obtained from the straight-through measurement of the most abundant isotope, ^{40}Ar. In the ratio of these two signals, the product of I_{e^-} and d_{e^-} cancels, and the resulting equation can be rearranged to give the desired cross-section in terms of known quantities

$$\sigma_{F_2 \to F_2^+} = \left(\frac{S_{F_2}^{F_2/Ar}}{S_{36}^{F_2/Ar}} \right) \left(\frac{v_{F_2}}{v_{Ar}} \right) \left(\frac{T_{36}}{T_{38}} \right) \left(\frac{[^{36}Ar]}{[F_2]} \right) \sigma_{Ar \to Ar^+} \tag{1.22}$$

where the fluxes of fluorine, I_{F_2}, and argon, $I_{^{36}Ar}$, simplify to their nominal

[31] R. C. Wetzel, F. A. Baiocchi, T. R. Hayes, and R. S. Freund, Phys. Rev. A **35**, 559 (1987)

[32] H. C. Straub, P. Renault, B. G. Lindsay, K. A. Smith, and R. F. Stebbings, Phys. Rev. A **52**, 1115 (1995)

concentrations in the seeded mixture, $[F_2]$ and $[^{36}Ar]$, since the 1%F_2/Ar beam exhibits no Mach number focusing (see Section 1.4.4.2). The mass spectrometer signal of the 1%F_2/Ar mixture at m/e=38 arises from both the F_2^+ ions and the ^{38}Ar isotope. The contribution of the ^{38}Ar isotope, as measured from a pure Ar beam, S_{38}^{Ar}, must be subtracted from the m/e=38 signal, $S_{38}^{F_2/Ar}$, to yield the F_2 contribution, $S_{F_2}^{F_2/Ar}$. The literature value[33] for the relative abundance of the ^{36}Ar isotope is used in determining $[^{36}Ar]$ in Eq. 1.22.

The signals at m/e=38 and 36 are collected as time-of-flight distributions which are weighted by their measured velocity and integrated to obtain velocity-weighted total counts, $VWC\,S_{F_2}^{F_2/Ar}$ and $VWC\,S_{36}^{F_2/Ar}$. The above expression thus simplifies to

$$\sigma_{F_2\to F_2^+} = \left(\frac{VWC\,S_{F_2}^{F_2/Ar}}{VWC\,S_{36}^{F_2/Ar}}\right)\left(\frac{T_{36}}{T_{38}}\right)\left(\frac{[^{36}Ar]}{[F_2]}\right)\sigma_{Ar\to Ar^+} \tag{1.23}$$

where the average velocities have been incorporated into the velocity-weighted counts. The ratio of transmissions is assumed to be near unity, given the small mass difference between ^{36}Ar and $^{38}F_2$.

Following similar arguments, the value of the flux weighted counts at m/e=19 from a 1%F_2/Kr beam is used to determine the cross-section that is actually needed in the calculation of P_1 shown in Eq. (1.18)

$$\sigma_{F_2\to F^+} = \left(\frac{VWC\,S_{19}^{F_2/Kr}}{VWC\,S_{38}^{F_2/Kr}}\right)\left(\frac{T_{38}}{T_{19}}\right)\sigma_{F_2\to F_2^+} \tag{1.24}$$

where the concentrations in the seeded mixture cancel because the signals at m/e=19 and 38 come from the same neutral species. A krypton seeded beam is used to avoid the overlap of the F^+ signal (m/e=19) with the Ar^{2+} signal (m/e=20) present in the 1%F_2/Ar beam. The transmission ratio T_{19}/T_{38} is determined as discussed in Section (1.4.1.2).

[33] The commission on Atomic Weights and Isotopic Abundances "Table of Isotopic Compositions of the Elements as Determined by Mass Spectrometry," (1989)

Finally, the total cross-section for ionization and dissociative ionization of F_2 is obtained from the sum of the partial ionization cross-sections

$$\sigma_{F_2 \to F_2^+ + F^+} = \sigma_{F_2 \to F_2^+} + \sigma_{F_2 \to F^+} \tag{1.25}$$

Table 1-3 gives a summary of the values of all quantities required to determine the F_2 electron impact ionization cross-sections. The values of the cross-sections obtained at 70 eV in this investigation are

$$\sigma_{F_2 \to F_2^+} = 0.74 \pm 0.03 \text{ x } 10^{-16} cm^2 \tag{1.26}$$

$$\sigma_{F_2 \to F^+} = 0.26 \pm 0.05 \text{ x } 10^{-16} cm^2 \tag{1.27}$$

$$\sigma_{F_2 \to F_2^+ + F^+} = 1.00 \pm 0.06 \text{ x } 10^{-16} cm^2 \tag{1.28}$$

No partial ionization cross-sections of F_2 are available in the literature for comparison. The value obtained for the total ionization cross-section is, however, in excellent agreement with the value measured by Stevie and Vasile[34].

Table 1-3 Values Required for Calculation of F_2 Ionization Cross-sections

Quantity	Symbol	Measured value	Source
m/e=38 signal from 1%F_2/Ar	$VWC\,S_{38}^{F_2/Ar}$	1.87±0.03 x10^7 cnts sec^{-1}	
^{36}Ar signal from 1%F_2/Ar	$VWC\,S_{36}^{Ar}$	1.83±0.04 x10^7 cnts sec^{-1}	
^{38}Ar signal from pure Ar	$VWC\,S_{38}^{Ar}$	3.48±0.1 x10^6 cnts sec^{-1}	
F_2 signal from 1%F_2/Kr	$VWC\,S_{38}^{F_2/Kr}$	7.54±0.09 x10^6 cnts sec^{-1}	
F signal from 1%F_2/Kr	$VWC\,S_{19}^{F_2/Kr}$	2.95±0.06 x10^6 cnts sec^{-1}	
Ar cross-section (70 eV)	$\sigma_{Ar \to Ar^+}$	2.67 ± 0.09 x10^{-16} cm^2	Smith et al.[32]
^{36}Ar isotope abundance	[^{36}Ar]	0.337 %	Ref[33]
F_2 concentration in 1%F_2/Ar	[F_2]	1.0% nominal	from mixture
Transmission ratio	T_{36}/T_{38}	~ 1	

[34] F. A. Stevie and M. J. Vasile, J. Chem. Phys. **74**, 5106 (1981)

1.4.1.2 Determination of the Quadrupole Transmission Function

A critical value in the measurement of the ionization cross-sections is the relative ion collection efficiency, or relative transmissivity, of the m/e=38 and m/e=19 ions in the mass spectrometer. Once a neutral is ionized, it traverses the quadrupoles and is detected by the channel electron multiplier. The efficiency of this process depends on the mass-to-charge ratio of the ionized fragment. In addition, any change in the ionization environment and/or the quadrupole's resolution setting may affect the relative transmission efficiency. It is therefore necessary to determine experimentally the ratio of transmissivities under the identical conditions to those with which the scattering data are collected.

The mass spectrometer signal, S_M, at a mass-to-charge ratio M is given by

$$S_M = \frac{I_M \sigma_{M \to M^+} T_M I_{e^-} d_{e^-}}{v_M} \qquad (1.29)$$

where the symbols are defined as in Eq. (1.18). Without knowledge of the absolute values of the ionization length, d_{e^-}, and electron current, I_{e^-}, only the relative transmission ratio between pairs of species detected at different mass-to-charge ratios is obtainable.

The method to determine the transmissivity ratio is based on comparing the signal of two beams of known flux, which contain species that fragment to ions at the desired mass-to-charge ratio. Since the ratio of the fluxes of the two beams is proportional to the ratio of the signals detected in the mass spectrometer, and given the known values for the electron impact ionization cross-sections and the average velocities of the two beams, the transmission ratio can be determined. The availability of accurate values for the partial ionization cross-sections of Ar and Ne is used to obtain the transmissivity of Ne^+ and Ar^+.

The ratio of Eq. (1.29) for Ar and Ne is rearranged to yield

$$\frac{T_{Ar}}{T_{Ne}} = \left(\frac{S^{Ar}}{S^{Ne}}\right)\left(\frac{\sigma_{Ne\to Ne^+}}{\sigma_{Ar\to Ar^+}}\right)\left(\frac{v_{Ar}}{v_{Ne}}\right)\left(\frac{I_{Ne}}{I_{Ar}}\right) \tag{1.30}$$

where S is the mass spectrometer signal for the neutral indicated by the superscript, $\sigma_{Ar\to Ar^+}$ and $\sigma_{Ne\to Ne^+}$ are the partial electron impact ionization cross-sections at 70 eV, and v and I are the average velocity and incident flux of the beams, respectively. Argon and Ne are chosen because of their closeness in mass to F_2 and F which are the products whose reaction probabilities are measured.

Since a F_2 seeded Kr beam is used for the reaction probability measurements, it would be best to measure the Ar and Ne signals needed to calculate the transmission ratio using Kr as a carrier gas. Use of 1%Ar/Kr and 1%Ne/Kr would ensure that the environment of the ionizer closely resembles that present during the scattering measurements. A complication, however, arises in the determination of the Ar and Ne flux in the seeded molecular beams because the large mass difference between carrier Kr gas and the seed gases produces substantial Mach number focusing during the expansion. See Section (1.4.4.2) for a discussion of seeded beam flux measurements, and the effect of Mach number focusing.

To avoid the complications of Mach number focusing, the most reliable way to obtain the transmission ratio is to collect and fit time-of-flight spectra while pure, rather than seeded, Ar and Ne beams are allowed to enter into the mass-spectrometer housing. In measurements of straight-through time-of-flight of pure Ar and Ne beams, the most abundant isotopes cannot be used due to the high signal levels they produce. Therefore, less abundant species such as ^{36}Ar and ^{22}Ne are used. The velocities obtained from the fit of the time-of-flight distributions are used to calculate velocity-weighted counts (VWC) which yield an expression for the transmissivity ratio

$$\frac{T_{36}}{T_{22}} = \left(\frac{VWC\,S_{36}^{Ar}}{VWC\,S_{22}^{Ne}}\right)\left(\frac{\sigma_{Ne\rightarrow Ne^+}}{\sigma_{Ar\rightarrow Ar^+}}\right)\left(\frac{I_{^{22}Ne}}{I_{^{36}Ar}}\right) \quad (1.31)$$

where the average velocities are incorporated into the transform of the time-of-flight distribution, and the fluxes appearing in the last factor are determined from the known flux of the pure Ar and Ne beams combined with the known natural isotope abundances. Table 1-4 summarizes the values of all quantities required to determine the transmission ratio. The value obtained can be used to approximate the transmission ratio needed to determine the F_2 ionization cross-section in Eq. (1.24).

$$\frac{T_{36}}{T_{22}} \approx \frac{T_{38}}{T_{19}} = 0.89 \pm 0.15. \quad (1.32)$$

Table 1-4 Values Required for Calculation of Relative Transmissivity

Quantity	Symbol	Measured value	Source
^{36}Ar velocity weighted counts	$VWC\,S_{36}^{Ar}$	$2.02\pm0.04\ \text{x}10^{7}$ cnts sec^{-1}	
^{22}Ne velocity weighted counts	$VWC\,S_{22}^{Ne}$	$1.42\pm0.02\ \text{x}10^{8}$ cnts sec^{-1}	
Ar ionization cross-section	$\sigma_{Ar\rightarrow Ar^+}$ (70 eV)	$2.67 \pm 0.09\ \text{x}10^{-16}$ cm^2	Smith et al.[32]
Ne ionization cross-section	$\sigma_{Ne\rightarrow Ne^+}$ (70 eV)	$0.488\pm0.07\ \text{x}10^{-16}$ cm^2	Freund et al.[31]
^{36}Ar isotope abundance	[^{36}Ar]	0.33656±0.000001%	Ref.[33]
^{22}Ne isotope abundance	[^{22}Ne]	9.2469±0.00001%	Ref.[33]
^{36}Ar Flux	$I_{^{36}Ar}$	0.062±0.001 ML sec^{-1}	Sec. 1.4.4
^{22}Ne Flux	$I_{^{22}Ne}$	2.19±0.1 ML sec^{-1}	Sec. 1.4.4

1.4.2 Scattering Angle Dependence of the Reaction Probabilities

The scattered F and F_2 signals as a function of exposure presented in Section 1.3.2 are limited to a single detection angle, θ_s=35°. Similarly, the reaction probabilities, $P_0(\varepsilon,\theta_s=35°)$, $P_1(\varepsilon,\theta_s=35°)$ and $P_2(\varepsilon,\theta_s=35°)$ discussed in Section 1.4.1 and displayed in Figure 1.12 only take into account the F and F_2 collected at 35° with respect to the

surface normal. One of the main goals of this investigation is to determine the absolute fluorine coverage on the surface as a function of F_2 exposure. Calculation of the coverage requires the knowledge of the <u>total</u> reaction probabilities, that is, the probabilities integrated over all scattering angles. The total reaction probabilities are given by the following expressions, derived by integrating Eqs. (1.14), (1.15) and (1.16) over all scattering angles

$$\mathrm{P}_0(\varepsilon) = \iint \frac{S_{38}(\varepsilon,\theta_s,\phi)}{S_{38}(\infty,\theta_s,\phi)} \sin\theta_s d\theta_s d\phi \qquad (1.33)$$

$$\mathrm{P}_1(\varepsilon) = \left(\frac{v_F}{v_{F_2}}\right)\left(\frac{\sigma_{F_2\to F_2^+}}{\sigma_{F\to F^+}}\right)\left(\frac{T_{38}}{T_{19}}\right)\iint\left(\frac{S_{19}^F(\varepsilon,\theta_s,\phi)}{S_{38}(\infty,\theta_s,\phi)}\right)\sin\theta_s d\theta_s d\phi \qquad (1.34)$$

$$P_2(\varepsilon) = \iint (1 - P_0(\varepsilon,\theta_s,\phi) - P_1(\varepsilon,\theta_s,\phi))\sin\theta_s d\theta d\phi \qquad (1.35)$$

where ϕ is the azimuthal scattering angle.

Scattered F and F_2 signals must then be collected at all scattering angles. Figure 1.13 summarizes the results of scattering a 1%F_2/Kr beam incident at 0° onto a Si(100), and detecting the F and F_2 scattered signals at the range of detection angles accessible to the rotatable mass spectrometer (θ_s=35-85°). The unreactively scattered F_2 signal (m/e=38) is presented at two different surface coverages. The square markers correspond to F_2 scattered from the surface at the exposure at which the abstraction probability reaches its maximum. The circles represent the F_2 at long exposures for which the surface coverage has been saturated. The net F-atom signal (m/e=19) is also shown, as triangles, at the exposure at which the maximum of P_1 is reached. Finally, the unreactively scattered F_2 signal from a SiO surface known to be inert to fluorine attack is also included in the figure, as diamonds. These data clearly show that the angular distribution of the scattered products is the same for both F and F_2 regardless of the fluorine coverage present on the surface. In fact, the scattered F_2 angular distribution is even the same as that obtained from an oxygen covered surface. This result indicates that the reaction probabilities are

independent of detection angle, and that therefore the θ_s dependence can be eliminated from the integrals in Eqs. (1.33), (1.34) and (1.35).

The out-of-plane scattering region described by the angle ϕ cannot be accessed since the mass spectrometer is designed to rotate around the center of the crystal, but always in the plane defined by the surface and the incident molecular beam. The assumption is made that the out-of-plane scattering is either isotropic, or at least equal for both F and F_2 scattered species, so that the ϕ dependence is also eliminated from the integrals. This assumption is supported by the observation that the F and F_2 angular distributions are identical when the crystal azimuth is rotated by 45°.

Given the common angular distribution of F and F_2, the total reaction probabilities are the same as those determined at any given detection angle. In particular, the θ_s=35° data presented in Figure 1.12 can be taken to represent the total reaction probabilities $P_0(\varepsilon)$, $P_1(\varepsilon)$ and $P_2(\varepsilon)$ required to calculate the fluorine coverage. To illustrate the invariance of the reaction probabilities with detection angle, Figure 1.14 shows the calculated probabilities as measured at four different detection angles. The F and F_2 scattering data were collected at 35° (circles), 45° (squares), 55° (triangles) and 65° (diamonds) with respect to the surface normal while a 200 Torr 1%F_2/Kr beam was incident at 0° on the Si(100) surface. Within the experimental error, the four sets of data give indistinguishable reaction probabilities and are therefore set equal to $P_0(\varepsilon)$, $P_1(\varepsilon)$ and $P_2(\varepsilon)$.

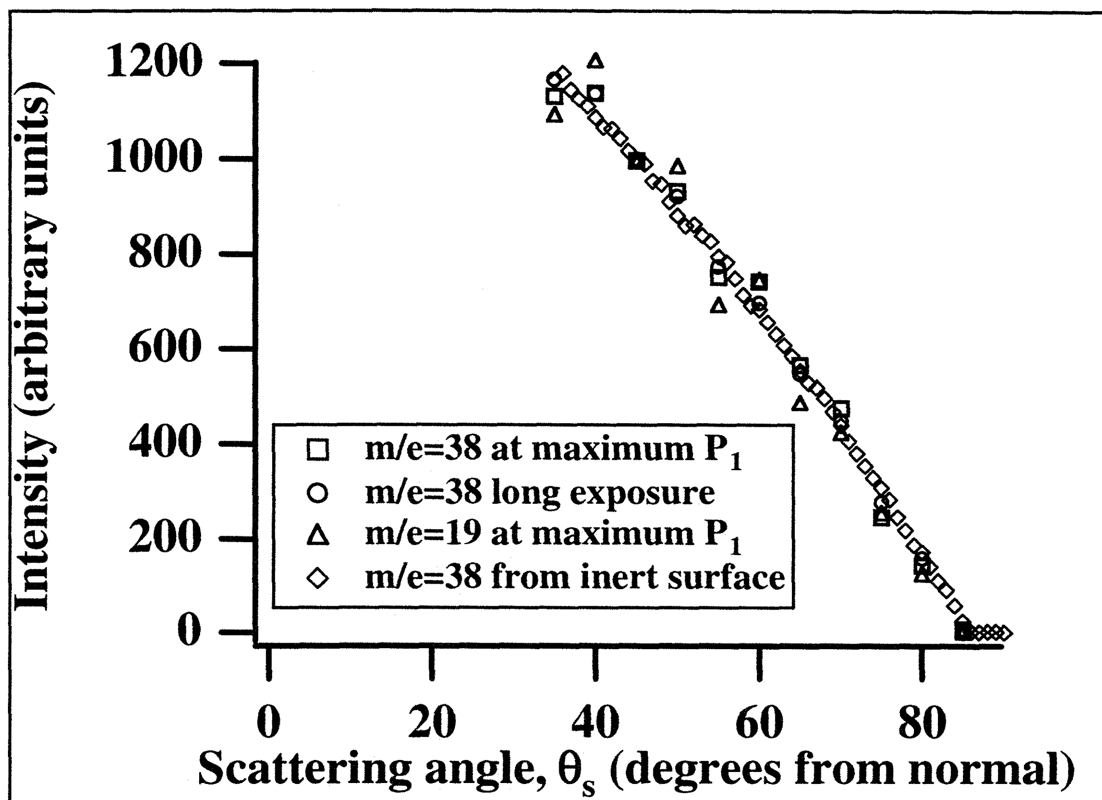

Figure 1.13 Angular Distribution of Scattered F and F_2

Scattering angle dependence of F and F_2 signals from 1%F_2/Kr (E_i=0.66 kcal mol^{-1}) beam impinging on a Si(100) surface at 0° incidence. Products are detected in the angular range accessible to the rotatable mass spectrometer (35°-85°). F_2 signals (m/e=38) are shown for the intermediate coverage corresponding to the maximum in P_1 (squares), and for saturation coverage obtained after long exposures (circles). The net F-atom signal (triangles) is shown at the exposure corresponding to the maximum of P_1. The scattered F_2 signal from a SiO surface which is known to be inert to attack by fluorine is also shown (diamonds). All signals have been scaled to illustrate that they follow the same broad, near cosine, angular distribution.

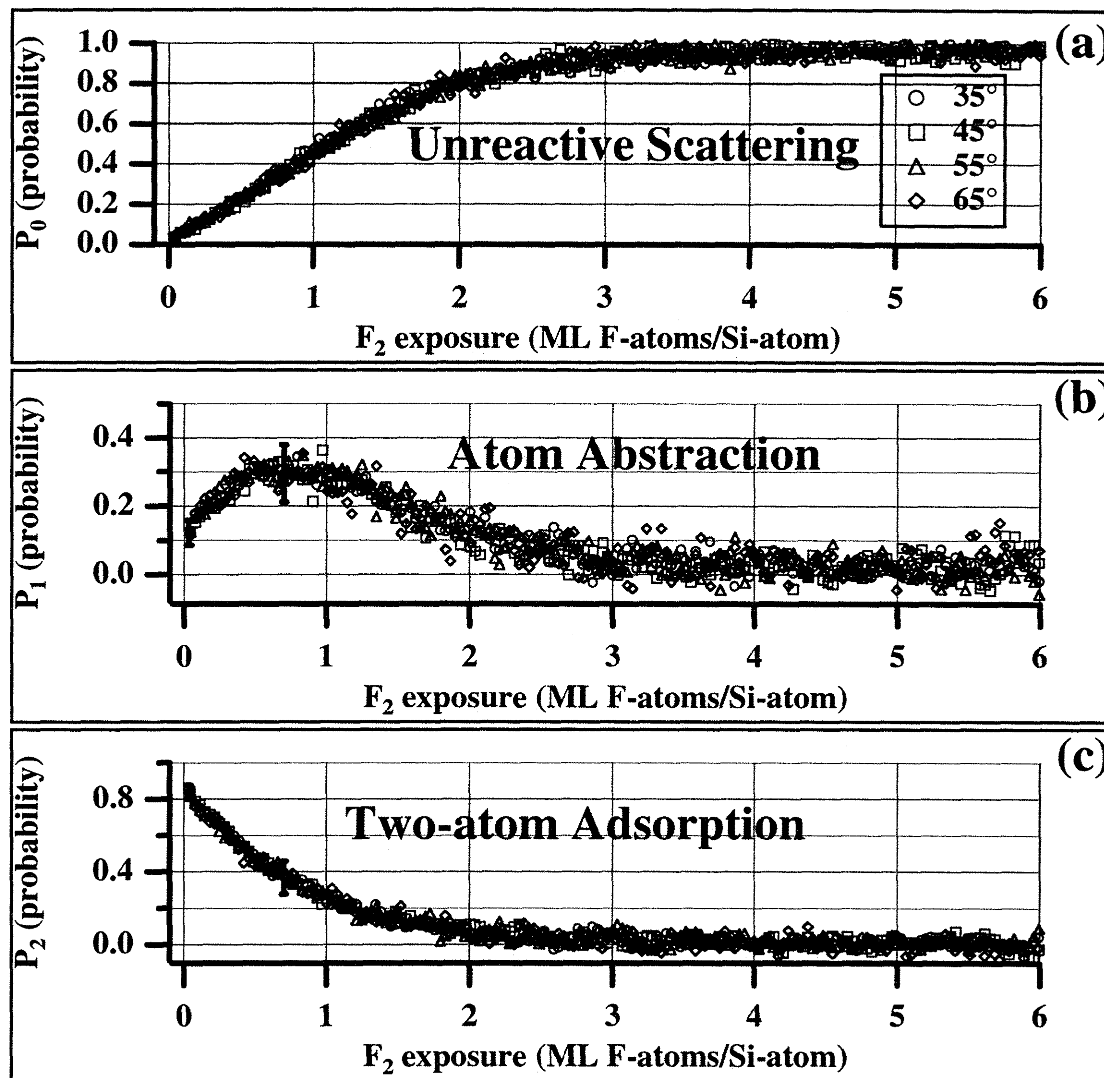

Figure 1.14 Reaction Probabilities Measured at Various Scattering Angles

Reaction probabilities determined from F and F_2 scattering data collected at four different detection angles. The 250 K Si(100) surface was exposed to a 1%F_2/Kr (E_i=0.66 kcal mol^{-1}) beam incident at 0°. Probabilities resulting from data collected at 35° (circles), 45° (squares), 55° (triangles), 65° (diamonds) are completely indistinguishable, verifying the angular independence of the F and F_2 scattering on exposure.

1.4.3 Calculation of the Exposure Dependent Surface Coverage

Having obtained $P_1(\varepsilon)$ and $P_2(\varepsilon)$, the probabilities for adsorption of fluorine atoms onto the Si surface as a function of exposure, the fluorine coverage can be now calculated. By definition of the probabilities, there will be P_1 fluorine atoms plus $2P_2$ fluorine atoms adsorbed on the surface for each incoming fluorine molecule. Summing over all incoming F_2 molecules, the coverage, $\theta(\varepsilon)$, can be written as

$$\theta(\varepsilon) = \int_0^{\varepsilon} (P_1(\varepsilon) + 2P_2(\varepsilon)) I_{F_2/Kr} d\varepsilon \tag{1.36}$$

where $I_{F_2/Kr}$ is the incident fluorine molecule flux per monolayer of surface Si atoms. Using the definition of P_2 in Eq. (1.16)

$$P_1 + 2P_2 = P_1 + 2(1 - P_0 - P_1), \tag{1.37}$$

Eq. (1.36) is rewritten as

$$\theta(\varepsilon) = \int_0^{\varepsilon} (2 - 2P_0(\varepsilon) - P_1(\varepsilon)) I_{F_2/Kr} d\varepsilon\,. \tag{1.38}$$

Equation (1.38) is an expression for the coverage as a function of exposure written in terms of the two measured probabilities.

Figure 1.15 shows the coverage as a function of exposure determined from the incident F_2 flux given in Section (1.4.4.2) and the probabilities shown in Figure 1.12. As expected, the coverage rapidly increases from a low value at initial exposures to a saturation level of approximately 1.0 ML at exposures above 25 ML of 1%F_2/Kr. This plot of the fluorine coverage as a function of exposure is then used to recast the probabilities given in Figure 1.12 in terms of coverage, rather than exposure. The reaction probabilities expressed as a function of coverage are presented in Figure 1.16. It is worth noting that the maximum in the abstraction probability is observed at approximately 0.5 ML coverage.

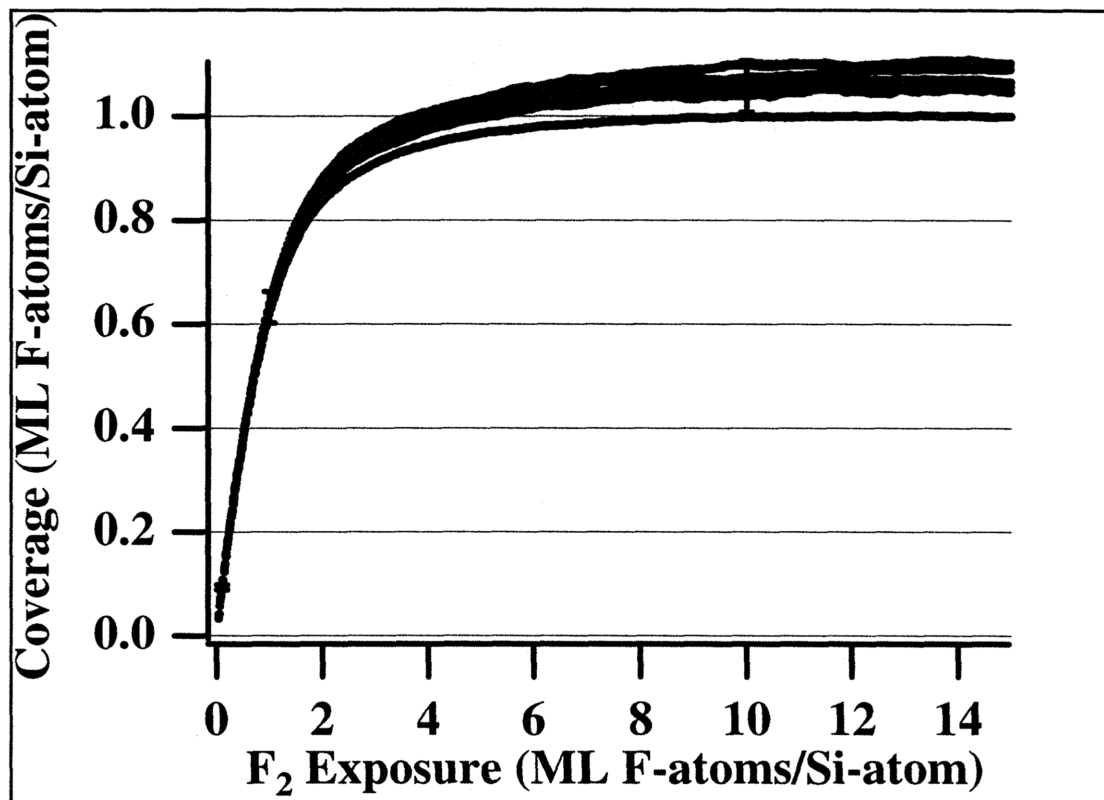

Figure 1.15 Fluorine Coverage as a Function of F_2 Exposure

Fluorine coverage as a function of F_2 exposure determined from the incident F_2 flux given in Section (1.4.4.2) and the probabilities shown in Figure 1.12

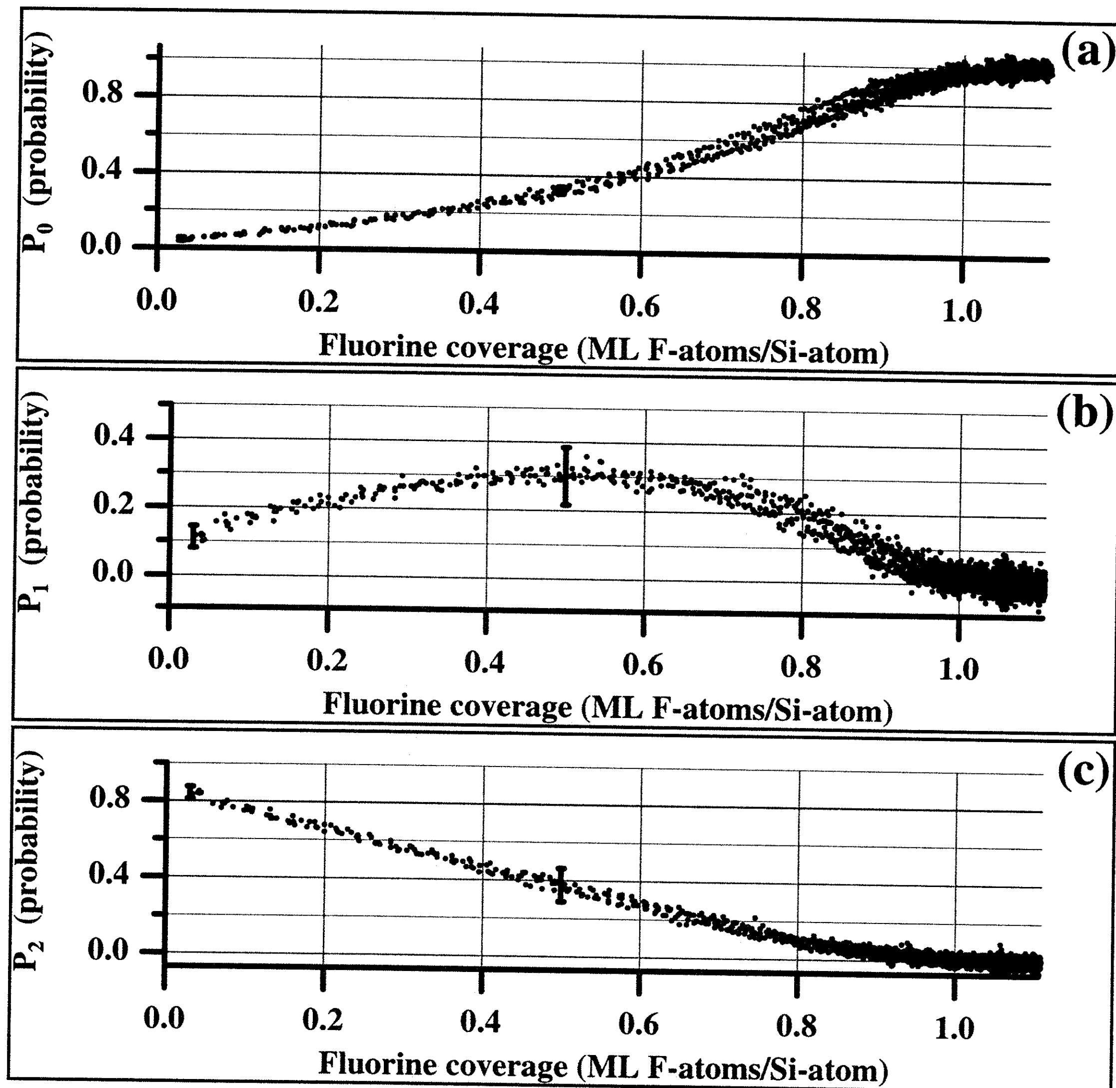

Figure 1.16 Coverage Dependence of F_2 Reaction Probabilities

The three reaction probabilities are shown as a function of fluorine coverage. The exposure axis from Figure 1.12 has been converted to coverage by using the plot shown in Figure 1.15.

1.4.4 Determination of Molecular Beam Fluxes

1.4.4.1 Determination of the Flux of Single Component Molecular Beams

Quantitative interpretation of the molecular beam scattering data presented in this investigation mandates the accurate knowledge of the flux of F_2 impinging on the Si surface. The molecular beam enters the main chamber through a collimating slit and impinges upon a spot of area A_{spot} on the surface. Its flux, I_{in}, is determined by measuring the change in the number density, N, of particles inside the main chamber. The number density is given by the pressure, P, temperature, T, and volume, V, of the gas in the main chamber. Mathematically, the change in N is expressed as,

$$I_{in}A_{spot} = \frac{dN}{dt} = \frac{d}{dt}\left(\frac{PV}{kT}\right) \tag{1.39}$$

where the term on the right is the time derivative of the ideal gas law. Carrying out the derivative and solving for the flux impinging on the surface yields,

$$I_{in} = \left(\frac{V}{kTA_{spot}}\right)\left(\frac{dP}{dt}\right) + \left(\frac{P}{kTA_{spot}}\right)\left(\frac{dV}{dt}\right) \tag{1.40}$$

Equation (1.40) shows that the beam flux impinging on the crystal can be determined by monitoring the changes in pressure and volume inside the reaction chamber upon introduction of the molecular beam into or its withdrawal from the main chamber.

A word of caution is required with respect to the correlation between the beam flux impinging on the crystal and the main chamber pressure rise caused by the molecular beam. Care must be taken to ensure that there is no significant effusive gas load entering the main chamber from the differential pumping stages of the beam. An effusive gas load caused by inadequate pumping would result in the introduction of an additional gas load into the main chamber, which would contribute to the measured pressure rise, but which would not directly impinge on the crystal. Such an effusive load would cause an overestimate of the molecular beam flux as determined from the main chamber pressure

rise. A more detailed discussion of the effusive load and beam attenuation problems caused by insufficient pumping in the differential stages of the beam-line is presented in Appendix C.

There are two approaches to measuring the molecular beam flux. In the first one, the beam is allowed to enter the main chamber until a steady-state pressure is achieved. At steady state, the time derivative of the pressure is equal to zero, so the first term in Eq. (1.40) vanishes. The volume derivative in the second term corresponds to the pumping speed of the system, S_p. The flux at the surface is then given by,

$$I_{in} = \left(\frac{PS_P}{kTA_{spot}} \right) \tag{1.41}$$

This experiment requires the measurement of the steady-state absolute pressure, P, in the main chamber and the absolute pumping speed, S_p, of the gas making up the molecular beam. The determination of the pumping speed for various gases is presented in Section 1.4.4.3. The pressure is measured by a nude Bayard-Alpert ionization gauge, which determines pressure based on the ion current collected by a thin wire as the ambient gas is ionized by electron bombardment from a heated filament. The ion current collected is proportional to the density and hence the pressure of the ambient gas. The proportionality constant, however, depends on the identity of the gas being ionized. Ionization gauges are typically calibrated for N_2. A correction factor accounting for the different ionization efficiency of the gas being measured must be used to correct the gauge reading.

Taking this correction factor into consideration, Eq. (1.41) can then be rewritten as,

$$I_{in} = \left(\frac{P_{obs} C_F S_P}{kTA_{spot}} \right) \tag{1.42}$$

where P_{obs} is the pressure reading obtained from the ionization gauge, and C_F is the

carrier-gas dependent correction factor. A detailed discussion of how the correction factor is determined is given in Section (1.4.4.5). A summary of the values of all quantities required for the determination of the beam fluxes of both pure Ar and pure Ne molecular beams are given in Table 1-5.

Table 1-5 Values Required for Determination of Fluxes by Steady-state Method

Quantity	Symbol	Measured value	Source
Observed pressure with Ar beam	P_{obs}^{Ar}	7.5-7.9±0.05 x 10^{-8} Torr	
Observed pressure with Ne beam	P_{obs}^{Ne}	1.8±0.05 x 10^{-8} Torr	
Ar ion gauge correction factor	C_F^{Ar}	1.31±0.01	Section (1.4.4.5)
Ne ion gauge correction factor	C_F^{Ne}	5.29±0.15	Section (1.4.4.5)
Pumping speed of Ar	S_p^{Ar}	1070±11 liter sec^{-1}	Section (1.4.4.3)
Pumping speed of Ne	S_p^{Ne}	1480±15 liter sec^{-1}	Section (1.4.4.3)
Area of beam spot on crystal	A_{spot}	2.86±0.04 x 10^{-5} m^2	Section (1.2.1)

The alternate method for determining beam fluxes is based on introducing the beam into the evacuated main chamber in the absence of pumping. The main chamber is isolated from the pumps by closing diffusion pump gate valve, detector-box beam valve, and chopper box gate valve. The beam is then introduced into the main chamber while the pressure rise due to incoming flux is measured with the ionization gauge. In the absence of pumping, the time derivative of the volume (the pumping speed) in the second term of Eq. (1.40) is equal to zero. The flux is then given by,

$$I_{in} = \left(\frac{V_{chamber}}{kTA_{spot}}\right)\left(\frac{dP}{dt}\right) = \left(\frac{V_{chamber}}{kTA_{spot}}\right)\left(\frac{\Delta P}{\Delta t}\right) \qquad (1.43)$$

This method for the determination of the incident flux, I_{in}, requires the volume of the isolated chamber, $V_{chamber}^{stagnant}$, and the rate of pressure rise, $(\Delta P/\Delta t)$, to be known. A discussion of the determination of the chamber volume is given in Section (1.4.1). Its value as well as values typical for the pressure rises for Ar and Ne molecular beams are

summarized in Table 1-6. The fluxes obtained from using Eq. (1.43) with the values given in Table 1-6 are shown in Table 1-7.

Table 1-6 Values Required for Determination of Fluxes by the Stagnant Method

Quantity	Symbol	Measured value	Source
Pressure rise with Ar beam	$\left(\frac{\Delta P}{\Delta t}\right)_{Ar}$	9.7±0.1 x10^{-8} Torr sec^{-1}	
Pressure rise with Ne beam	$\left(\frac{\Delta P}{\Delta t}\right)_{Ne}$	3.0±0.1 x10^{-8} Torr sec^{-1}	
Volume of stagnant chamber	$V_{chamber}^{stagnant}$	870±10 liters	Section (1.4.4.4)
Area of beam spot on crystal	A_{spot}	2.86±0.04 x 10^{-5} m^2	Section (1.2.1)

Table 1-7 presents the measured fluxes for the pure Ar and Ne beams using both the steady-state pressure and stagnant-volume methods described above. The results from both methods are in excellent agreement, confirming the validity of both procedures for determining the flux of molecular beams containing a single component.

Beam fluxes are expressed in units of particles per unit time per unit area (typically atoms sec^{-1} cm^{-2}). A particularly well-suited unit for flux impinging onto a single crystal surface is ML sec^{-1}, where a monolayer (ML) is defined as one particle per surface site. In this case, a monolayer is an Ar or Ne atom per Si atom on the surface. There are 6.84x10^{14} Si atoms cm^{-2} on the Si(100) surface. Table 1-7 gives the flux for the Ar and Ne molecular beams expressed in both sets of units.

The molecular beams used in the investigation of the interaction of F_2 and Si typically contain a small amount of F_2 seeded in a carrier gas such as Ar or Kr. The question then arises of how to measure the flux of F_2 in seeded, two component molecular beams. A discussion of this topic is presented in the next section.

Table 1-7 Flux of Pure Ar and Ne Molecular Beams

Quantity	Symbol	Measurement Method			
		Steady-state		Stagnant volume	
		$cm^{-2}\ sec^{-1}$	$ML\ sec^{-1}$	$cm^{-2}\ sec^{-1}$	$ML\ sec^{-1}$
Flux of Pure Ar Beam	I_{in}^{Ar}	1.22×10^{16}	17.8±0.3	1.28×10^{16}	18.7
Flux of Pure Ne Beam	I_{in}^{Ne}	1.64×10^{16}	24±1	1.59×10^{16}	23.3

1.4.4.2 Determination of the Flux of Seeded Molecular Beams

In principle, the F_2 flux onto the Si surface from a seeded F_2 beam can be estimated from the knowledge of the flux of a pure beam of the carrier gas plus that of the nominal composition of the gas mixture used in the expansion. In practice, however, a complication arises. In a seeded molecular beam in which the mass of the carrier gas is substantially different from that of the seeded gas, the relative concentration of the two components after expansion is different from the stagnation composition and is not uniform across the beam. This concentration change upon expansion is known as Mach number focusing[35,36,37].

Although the main effect of an isentropic expansion through a small orifice is the quenching of all degrees of freedom into a single direction of translation parallel to the beam axis, some residual translation is always present along the axis perpendicular to the beam. The difference in transverse velocity of species with a different mass causes a change in concentration along the cross-section of the beam. Lighter particles tend to retain a larger transverse velocity, and hence get preferentially depleted from the center of the beam. Since the beam is collimated immediately upon expansion and prior to entering the main chamber, the downstream concentration of seeded beams favors the

[35] D. R. Miller, Atomic and Molecular Beam Sources, G. Scoles, ed. New York: Oxford University Press, (1988)

[36] P. K. Sharma, E. L. Knuth, and W. S. Young, J. Chem. Phys. **64**, 4345 (1976)

[37] V. H. Reis and J. B. Fenn, J. Chem. Phys. **39**, 3240 (1963)

heavier component in the mixture. This phenomenon precludes the use of the nominal F_2 concentration in the mixing cylinder to determine the incident fluorine flux of a seeded beam. An indirect method has therefore been devised to obtain the flux of seeded beams.

Advantage can be taken of the similarity between the masses of F_2 and Ar to prepare a reference $1\%F_2/Ar$ mixture which has negligible Mach number focusing. The F_2 flux of this beam can thus be determined from the nominal composition of the mixture. The F_2 flux of a $1\%F_2/Ar$ beam will thus be 0.01 times the flux of a pure Ar beam, whose flux is in turn determined from the pressure rise it causes in the chamber. The F_2 mass spectrometer signal from a $1\%F_2/Ar$ beam can then be used as a reference to compare against other F_2 seeded beams.

A time-of-flight spectrum of the F_2 signal in the reference $1\%F_2/Ar$ beam is measured and fitted to a functional form for a supersonic velocity distribution given by Yang[38]. From the fit, the velocity and the integrated counts are combined to give velocity-weighted counts (VWC). The F_2 flux of another seeded beam can be obtained by comparing the VWC obtained from its time-of-flight spectrum to those of the reference mixture. For example, the flux, $I_{F_2/Kr}$, of the $1\%F_2/Kr$ beam used in the scattering measurements is given by,

$$I_{F_2/Kr} = \left(\frac{VWC\, S_{F_2}^{F_2/Kr}}{VWC\, S_{F_2}^{F_2/Ar}} \right) I_{Ar} \tag{1.44}$$

where $VWC\, S_{F_2}^{F_2/Kr}$ is the F_2 time-of-flight signal detected at m/e=38 from a $1\%F_2/Kr$ beam, I_{Ar} is the flux of a pure Ar beam, and $VWC\, S_{F_2}^{F_2/Ar}$ is the F_2 signal from the $1\%F_2/Ar$ reference beam which is measured at m/e=38 after subtraction of the ^{38}Ar isotope contribution from a pure Ar beam, $VWC\, S_{38}^{Ar}$. That is,

---

[38] J. J. Yang, Ph.D. Thesis, Massachusetts Institute of Technology, p. 43, (1993)

$$VWC\,S_{F_2}^{F_2/Ar} = VWC\,S_{38}^{F_2/Ar} - VWC\,S_{38}^{Ar} \qquad (1.45)$$

A similar procedure is used to determine the flux of 1%Ne/Kr and 1%Ar/Kr beams which are used for the determination of the relative transmission ratio presented in Section (1.4.1.2). Table 1-8 summarizes the values of all quantities required for the determination of the fluxes of the three seeded beams used in this study. The fluxes obtained from these values substituted into Eq. (1.44) are given in Table 1-8. The effect of Mach number focusing is clearly seen in that the measured centerline concentrations of the lighter seed species are significantly lower than the nominal concentrations in the mixtures.

Table 1-8 Values Required for Determination of Seeded Beam Fluxes

Quantity	Symbol	Measured value	Source
F_2 signal from 1%F_2/Kr	$VWC\,S_{F_2}^{F_2/Kr}$	6.88±0.09 cnts sec^{-1}	
m/e=38 signal from 1%F_2/Ar	$VWC\,S_{38}^{F_2/Ar}$	1.83±0.03 x10^7 cnts sec^{-1}	
^{38}Ar signal from pure Ar	$VWC\,S_{38}^{Ar}$	3.54±0.1 x10^6 cnts sec^{-1}	
^{40}Ar signal from 1%Ar/Kr	$VWC\,S_{40}^{Ar/Kr}$	5.38±0.2 x10^7 cnts sec^{-1}	
^{20}Ne signal from 1%Ne/Kr	$VWC\,S_{20}^{Ne/Kr}$	5.22±0.3 x10^6 cnts sec^{-1}	
^{22}Ne signal from pure Ne	$VWC\,S_{22}^{Ne}$	2.11±0.1 x10^8 cnts sec^{-1}	
Flux of pure Ar beam	I_{Ar}	18.3±0.3 ML sec^{-1}	Table 1-7
Flux of pure Ne beam	I_{Ne}	23.7±1.1 ML sec^{-1}	Table 1-7

Table 1-9 Flux of Seeded Molecular Beams

Quantity	Symbol	Measured value	% flux[a]
Flux of F_2 in 1%F_2/Ar beam	$I_{F_2/Ar}$	0.183±0.03 ML sec^{-1}	1.0 %
Flux of F_2 in 1%F_2/Kr beam	$I_{F_2/Kr}$	0.085±0.003 ML sec^{-1}	N/A
Flux of Ar in 1%Ar/Kr beam	$I_{Ar/Kr}$	0.11±0.002 ML sec^{-1}	0.58 %
Flux of Ne in 1%Ne/Kr beam	$I_{Ne/Kr}$	0.062±0.003 ML sec^{-1}	0.26 %

flux relative to neat beam

1.4.4.3 Pumping Speed Measurements

The pumping speed needed for the determination of the beam fluxes by the steady-state pressure method can be determined from the decay constant of the pressure drop upon initiation of pumping. The time, *t*, required to pump gas out of a chamber of volume, $V_{chamber,}$ from a starting pressure, P_{start}, to a pressure, P, can be expressed as

$$t = \left(\frac{V_{chamber}}{S_p} \right) \times ln\left(\frac{P_{start}}{P} \right) \qquad (1.46)$$

where S_p is the pumping speed. This expression can be rearranged to yield

$$P(t) = P_{start} e^{\frac{-S_p t}{V_{chamber}}} \qquad (1.47)$$

A pressure record as a function of time is obtained by monitoring the mass-spectrometer signal in the main chamber after the load from a molecular beam is blocked, and the chamber allowed to pump. Sample pressure records for Ar and Ne obtained by monitoring mass spectrometer signal with the main chamber mass spectrometer are presented in Figure 1.17. The data are fit to an exponential decay, and the pumping speed, S_p, is obtained by multiplying the time needed for the pressure to drop to 1/e of its initial value times the chamber volume, $V_{chamber}$. The fitting is most easily accomplished by a linear regression of a ln(P_{start}/P) vs. time plot. It is however important to make sure that the recorded pressure decay is truly exponential. In some instances, the initial mass-spectrometer signal (obtained immediately after blocking the molecular beam) was so high that the counting electronics were saturated. The value of the first few points on the

pump-down curve were then artificially low, and thus should not be used in the fitting process. To determine which points in the pressure record are valid, the slope (S_p/ $V_{chamber}$) of points number 1 to 15 after blocking the beam was determined. Next, the slope using points 2 to 16, 3 to 17 , 4 to 18 and so on were determined. The 15 point slopes (i.e. slopes based on moving a window of 15 points) were plotted vs. the number of orders of magnitude in decline of the measured pressure signal. For cases in which the initial saturation of the counters occurred, the slopes over the first order of magnitude decline were small compared to the slopes at lower pressures (later times), and thus the initial points had to be neglected in fitting the slope to be used for the determination of the pumping speed. The solid lines in Figure 1.17 show the exponential fit over the range where the pump-down curves appear to be well behaved.

The results obtained for the pumping speed of different rare gases are presented in Table 1-10.

Table 1-10 Pumping Speeds

Rare Gas	Pumping Speed
He	2550 ± 30 l sec^{-1}
Ne	1480 ± 15 l sec^{-1}
Ar	1070 ± 10 l sec^{-1}

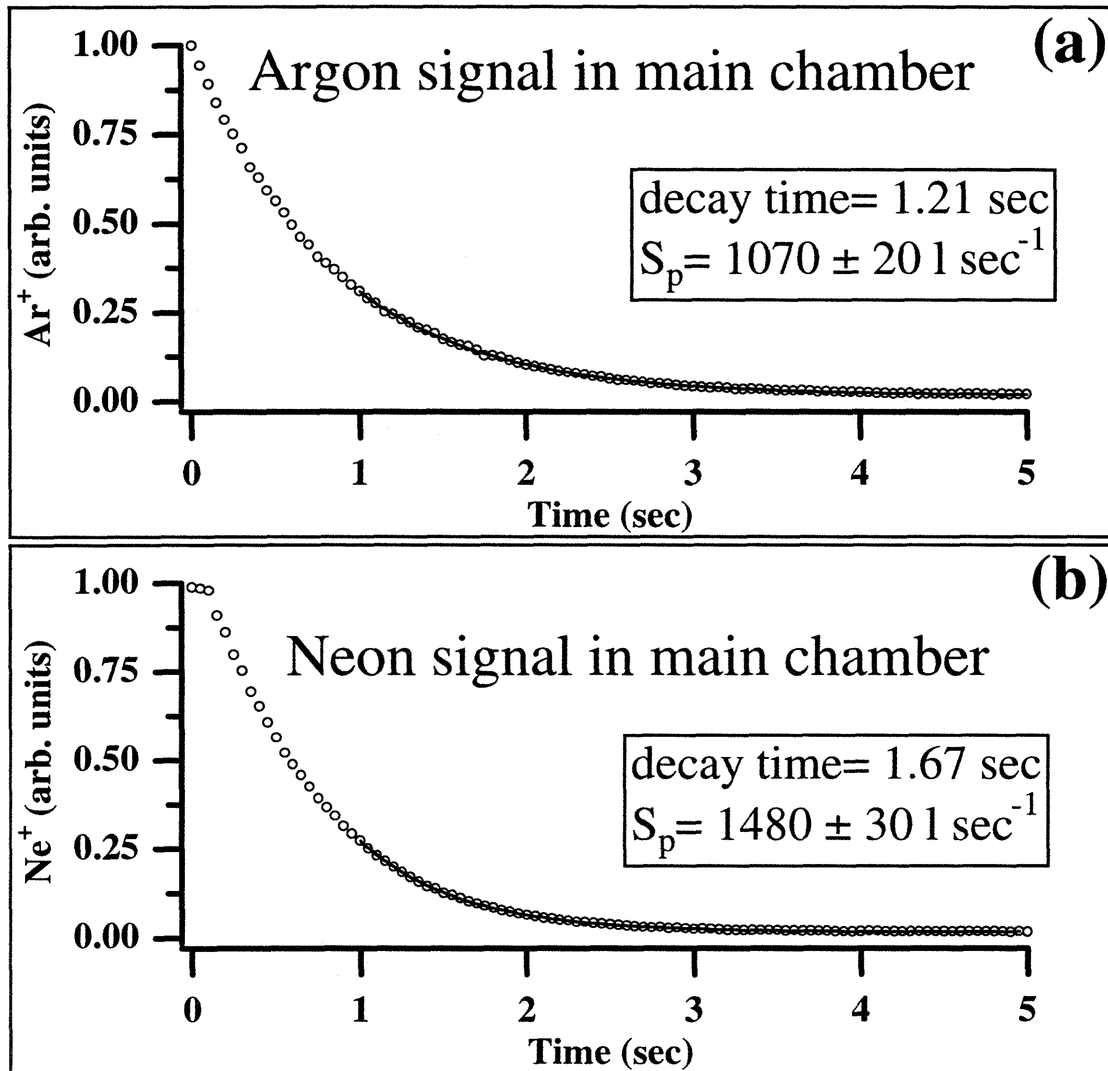

Figure 1.17 Pumping Speed Curves for Ar and Ne

Ar and Ne mass spectrometer signal measured at m/e of 40 and 20, respectively. The fit to the exponential portion of the curve serves to determine the pumping speed of the chamber.

1.4.4.4 Measurement of the Reaction Chamber Volume

In order to determine the ionization-gauge correction factor and the single component beam flux, an accurate measurement of the volume of the reaction chamber is necessary. This volume was both calculated from the chamber drawings and experimentally measured.

The volume of the chamber is experimentally determined by expanding a known quantity of gas into the reaction chamber and using a Baratron® absolute pressure gauge, directly attached to the main chamber, to measure the pressure rise after the expansion. All valves leading to pumps were closed in order to isolate the chamber from all sources of pumping, including the differential pumping of the Teflon seals on the chamber doors. The stagnant chamber volume is obtained from

$$V_{chamber}^{stagnant} = \left(\frac{P_{cal}}{P_{final}}\right) V_{cal} \qquad (1.48)$$

where P_{cal} is the pressure inside the calibrated volume, P_{final} is the final chamber pressure after expansion, and V_{cal} is the calibrated volume used in the expansion. The '*stagnant*' superscript, indicates that the measured volume is that of the chamber with the gate valve closed. This value is the one to be used for calculating the ion gauge correction factor as described in Section 1.4.4.5.

A small volume is accurately measured by differential weighing before and after filling it with distilled water. This volume, generally referred to as the "small calibrated volume" is determined to be 1.745 ml. The pressure of gas that can be introduced into the calibrated volume is limited by the maximum pressure tolerable by the Baratron's diaphragm (5000 Torr). Since this amount of gas is too small to yield a measurable pressure upon its expansion into the main chamber, a larger calibrated volume, an entire section of the gas manifold, was used. It is calibrated by expanding 5000 Torr of gas from the small calibrated volume into it. The larger calibrated volume is found to be 871

times larger than the small calibrated volume, that is 1520 ml. When 5000 Torr of gas are expanded from this volume into the main chamber, the resulting pressure in the main chamber is on the order of 8 Torr, which is measurable by the Baratron gauge. The same expansion is repeated successively for averaging purposes. The averaged result of several such expansions gives a value of

$$V_{chamber}^{stagnant} = 870 \pm 10 \text{ liters} \tag{1.49}$$

where the uncertainty represents one standard deviation from the mean of the repeated measurements.

The volume calculated from the drawings is 886 liters. This number is, however, expected to be larger than the measured volume, since it includes the volume between the main chamber gate valve and the liquid nitrogen cooled baffle. This value then corresponds to the volume of the chamber with the gate valve in the open position, and it is the value to be used for calculating pumping speeds as described in Section 1.4.4.3.

$$V_{chamber} = 886 \pm 10 \text{ liters} \tag{1.50}$$

1.4.4.5 Ion Gauge Sensitivity Correction Factor

The procedure for calibrating the ionization gauge is very similar to that used for measuring the volume of the chamber. A known pressure of gas, measured with the Baratron gauge, is expanded from the small calibrated volume (1.745 ml) into the main chamber. All sources of pumping are again isolated from the chamber. The pressure resulting after expansion is measured with the ionization gauge and compared to the expected pressure rise as calculated from the amount of gas expanded and the known volume of the chamber.

The lowest pressure of gas that can be accurately measured with the Baratron gauge is approximately 0.5 Torr. Even this relatively small amount of gas when expanded from

the small calibrated volume into the main chamber raises the main chamber pressure to about the 10^{-6} Torr range. This value is approximately one order of magnitude higher than the typical pressure rise due to the molecular beams used in the scattering experiments. In order to lower the pressure in the small calibrated volume, an intermediate expansion had to be performed. A few Torr of gas trapped in the small calibrated volume were expanded into the larger calibrated volume of 1520 ml. The pressure after expansion, although no longer measurable by the Baratron gauge, was calculated from the volume ratio between the small and large calibrated volumes. In all cases, the expansion of this small amount of gas in the small calibrated volume produced a pressure increase of about 10^{-7} Torr, comparable to the pressure rise in the chamber upon the introduction of the molecular beams.

Use of the main chamber diffusion pump is necessary to evacuate thoroughly the manifold before the final expansion. This step insures the removal of any residual amount of gas present in the manifold which would, added to the expanded gas, contribute to an artificially high pressure rise. Failure to do this repeatedly manifested itself in the irreproducibility of the ultimate main chamber pressure.

The main chamber pressure is monitored before and during the expansion. The pressure slowly increases linearly with time after the chamber is isolated from all sources of pumping because of leaks and outgassing of the chamber walls. This linear portion of the trace is fitted and extrapolated in time to the point where the pressure stabilizes following the expansion of the gas. The section of the pressure record after the expansion is also fitted to a line. The pressure rise, ΔP_{expan}, due to the gas expanded into the chamber is determined by subtracting the two fitted lines. An example of pressure rise data from a gas expansion as well as the fits are presented in Figure 1.18. The results from four such runs, using Ar as the gas, are averaged to determine the ion gauge correction factor according to

$$C_F^{Ar} = \left(\frac{P_{cal} V_{cal}}{\Delta P_{\exp an} V_{chamber}^{stagnant}} \right) \qquad (1.51)$$

where as before, P_{cal} is the pressure inside the calibrated volume, V_{cal}, before the expansion, and $V_{chamber}^{stagnant}$ is the volume of the stagnant (gate valve closed) chamber. Table 1-11 summarizes the values required to obtain the correction factor for the sensitivity of the ion gauge to Ar and Ne. The resulting value for Ar is

$$C_F^{Ar} = 1.31 \pm 0.01 \qquad (1.52)$$

and following a similar procedure, the correction factor for Ne is found to be

$$C_F^{Ne} = 5.29 \pm 0.15. \qquad (1.53)$$

Table 1-11 Values Required for the Determination of Ion Gauge Correction Factors

Quantity	Symbol	Measured Value	Source
Ar pressure in calibrated volume	P_{cal}^{Ar}	1.5-10.2±01.4 Torr	
Ne pressure in calibrated volume	P_{cal}^{Ne}	5.1-13.4±0.14 Torr	
Pressure rise due to Ar expansion	$\Delta P_{\exp an}^{Ar}$	2.3-7.6±0.01-0.05 x10^{-6} Torr	
Pressure rise due to Ne expansion	$\Delta P_{\exp an}^{Ne}$	1.9-4.9±0.03-0.04 x10^{-6} Torr	
Calibrated Volume	V_{cal}	1.745±0.01 x10^{-3} l	Sec. (1.4.4.4)
Stagnant chamber volume	$V_{chamber}^{stagnant}$	870±10 l	Sec. (1.4.4.4)

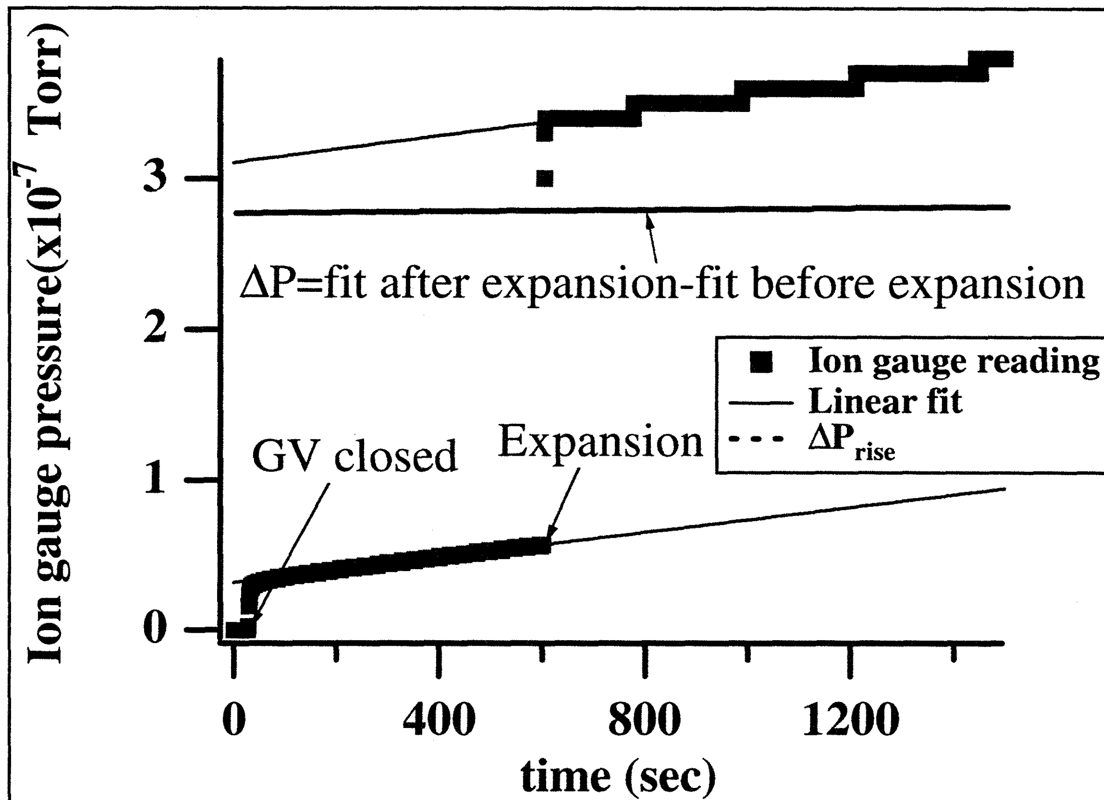

Figure 1.18 Ar Expansion Measurement for Ion Gauge Calibration

Example of a pressure rise measurement during Ar expansion into main chamber. These data are used to determine correction factor for the ionization gauge sensitivity to Ar.

1.5 DISCUSSION

1.5.1 Physical Picture Resulting from the Experimental Results

The scattering data presented in Section 1.3 confirm the existence of three reaction channels in the interaction of F_2 with a Si(100) 2x1 surface. First, the incident F_2 can scatter from the surface without undergoing any chemical change (unreactive scattering). Second, one of the F atoms from the incident molecule can be abstracted by a Si dangling with the complementary atom being ejected to the gas phase (atom abstraction). Third, adsorption of both F atoms from an incident molecule can take place if the ejected atom encounters a reactive dangling bond during its outgoing trajectory (two-atom adsorption).

The unreactive channel is evidenced by the detection of F_2 molecules scattering from the surface over a broad range of angles and with a velocity distribution characteristic of the surface temperature. In spite of the high reactivity expected for F_2 on a clean Si surface, a small probability of unreactive scattering is observed even in the limit of zero coverage. An initial unreactive scattering probability of 0.05 is estimated by extrapolation of the unreactively scattered signal to zero exposure. The few unreactive scattering events on the clean surface may arise from an unfavorable orientation of the molecular axis of the incident F_2, an unfavorable impact parameter within the Si(100) 2x1 unit cell, or by the presence of non-reactive defect sites on the surface. In contrast to its low probability at low coverage, unreactive scattering is observed to be the dominant channel for the interaction of F_2 with a highly fluorinated Si surface, indicating the inertness of the F_2 with it.

Atom abstraction is confirmed by the mass spectrometric detection of the ejected F atoms. The F^+ signal from the ejected F atoms is distinguished from the F^+ arising from the dissociative ionization of the unreactively scattered F_2 on the basis of its different velocity and exposure dependence. The velocity distribution of the ejected F atoms

reflects a large translational energy compared to that of the incident F_2 beam. The translational excitation arises from the exothermicity of the reaction. The translational energy of the ejected F atom, however, only accounts for approximately 3% of the available exothermicity. The abstraction channel is operable in the limit of zero coverage, with a probability of approximately 0.1 determined by extrapolating the measured probability to zero exposure. The unusual exposure dependence of the abstraction probability is discussed in detail in this section

While the F atom that is not abstracted can scatter back into the gas phase, it does not necessarily do so. The ejected F atom may be caught on its outgoing trajectory by an adjacent Si dangling bond and adsorb. It is also possible for both atoms to be simultaneously abstracted by two nearest neighbor dangling bonds if the F_2 molecular axis is favorably aligned upon its initial collision. Confirmation of the two-atom adsorption process is obtained by comparing the total F_2 adsorption probability, P_t, to the probability for single atom abstraction, P_1. P_t is given by $1\text{-}P_0$ where P_0 is the probability for unreacted F_2 to scatter from the surface. The difference $P_t\text{-}P_1$ gives P_2, the probability for two-atom adsorption, which is found to be maximum in the limit of zero coverage. A value of 0.85 is estimated for P_2 by extrapolation of P_2 to zero exposure.

A combination of He diffraction, reactive scattering and thermal desorption measurements confirms the Si dangling bonds as the primary sites for F atom abstraction and adsorption. The He diffraction measurements show that the half-order diffraction beam, which is a signature for the presence of Si—Si dimers on the surface, persists after fluorination. Fluorine is thus observed to adsorb as an ordered overlayer with a 2x1 unit cell, consistent with only the dangling bonds being involved in the adsorption process. The reactive scattering data are used to measure the absolute fluorine coverage on the saturated surface. Integration of the two reaction probabilities that lead to fluorine adsorption yields the amount of fluorine on the surface. Since each abstraction event

contributes a single atom towards the surface coverage, while each two-atom adsorption event contributes two atoms, the total coverage is obtained by integrating the quantity $2P_2+P_1$ over the F_2 exposure. The coverage is observed to saturate at 1 ML, which is consistent with the passivation of the Si dangling bonds. The thermal desorption measurements independently confirm that saturation coverage is reached by showing that regardless of the amount of additional exposure to F_2, a constant amount of fluorinated products desorb from the surface. These observations confirm that the reaction of F_2 with Si(100) occurs at the dangling bond sites of the surface dimers, leaving the Si—Si dimer bonds intact. The low etch rates observed for molecular F_2 are a direct consequence of its inability to cleave the dimer bonds and thus to fluorinate the surface beyond a coverage of 1 ML.

1.5.2 Qualitative Features of the F_2 + Si (100) Potential Energy Surface

The experimental results discussed in the previous section can be used to determine some qualitative aspects of the interaction potential between a gas phase F_2 molecule and a Si(100) surface. In particular, the angular and translational energy distributions of the scattered F and F_2 products are a direct consequence of the shape of the interaction potential, and can thus be utilized to yield some information about it.

The major feature of the potential energy surface (PES) describing the abstraction reaction is the thermodynamics of the interaction. The driving force behind abstraction is the formation of a single Si—F surface bond, which provides enough energy (6.4 eV) to offset the energetic cost of cleaving the F_2 bond (1.4 eV). The relative stability of the Si—F and F—F bonds thus determines the energy difference between the entrance and exit channels of the PES. Further details about the shape of the interaction potential manifest themselves in the detailed dynamics of the reaction products.

The ejected F atoms are observed to have a large average velocity (1100 m sec^{-1}) compared to that of the incident F_2/Kr beam (384 m sec^{-1}). A scattered F atom acquires

its translational excitation from the exothermicity released during the formation of the Si—F surface bond as evidenced by the independence of its translational energy distribution on surface temperature (see Figure 1.6). Additionally, the F atoms are observed to scatter with a broad angular distribution nearly identical to that observed for the unreactively scattered F_2 (see Figure 1.13), and with an average velocity independent of the angle at which they are detected. It is worth noting, however, that the average translational energy of the scattered F atoms is 0.14 eV, which only accounts for a small fraction of the available 4.8 eV released by the Si—F bond formation. The large difference between the reaction exothermicity and the energy of the ejected F atoms, as well as its angular and velocity distributions, are a consequence of interaction potential.

A potential energy surface consistent with only a small fraction of the reaction exothermicity being channeled into the translation of the ejected F atom might involve a transition state in which the ejected F atom is largely decoupled from the Si—F bond being formed. The small amount of translational energy observed for the ejected F atom suggests an attractive PES with an early barrier. That is, the transition state occurs early in the entrance channel, where the Si—FF distance is large. Once passed the barrier, the attractiveness of the PES pulls the abstracted F into the Si dangling bond, thus producing a vibrationally excited Si—F on the surface. The complementary F atom is released to the gas phase with little translational energy, and no memory of its original scattering direction. The angular distribution of the ejected F atoms is expected to be broad, since it should reflect the isotropic orientation of the incident F_2 molecules. In addition, since the ejected F atoms may be directed towards the surface, their already low kinetic energy may be further dissipated through inelastic collisions with fluorinated sites on the surface. This dissipation mechanism would also contribute to the broad angular distribution of scattered F atoms, as well as to the invariance of the F-atom velocity with scattering angle. A large fraction of the 4.7 eV released during the abstraction reaction is

channeled into the vibrational excitation of the Si—F on the surface. The reaction exothermicity is then mostly dissipated via excitation of bulk and surface phonons, and/or the electronic excitations of species at the surface.

Although the angular distributions of the scattered F and F_2 have been shown to be nearly identical, the velocity distribution of the unreactively scattered F_2 reflects an entirely different scattering mechanism than that of the F atoms. The velocity distribution of F_2 unreactively scattered from a 250 K Si surface (see Figure 1.3) fits a Maxwellian functional form with a characteristic temperature near to that of the surface, 240 K, and an average velocity of 436 m sec^{-1}. For the case of F_2 elastically scattering from a Si surface at 250 K the average velocity expected for the direct scattering mechanism would be approximately equal to the average velocity of the incident F_2 (384 m sec^{-1}), whereas the average velocity expected from the trapping-desorption mechanism given by $\sqrt{9\pi k_b T/8m}$ would be approximately 440 m sec^{-1}. The observed average velocity of 436 m sec^{-1} indicates the near accommodation of F_2 with the surface. In the case of F_2 scattering from a Si surface at 1000 K, the degree of accommodation with the surface is less, since the characteristic temperature of the Maxwell-Boltzmann fit, 554 K, is substantially lower than the surface temperature, reflecting a direct inelastic scattering mechanism.

Molecular dynamics simulations to examine the reactivity of an F_2 molecule with a Si surface were initially carried out by Stillinger and Weber[39,40]. They used an empirical many-body potential energy function comprised of two- and three-atom interactions. The terms of the potential involving only either Si or fluorine interactions were taken from the known Si and F_2 potentials. The cross-terms involving Si and F interactions were empirically derived to match the bond length, bond strength and vibrational frequency of

[39] F. H. Stillinger and T. A. Weber, Phys. Rev. Lett. **62**, 2144 (1989)
[40] T. A. Weber and F. H. Stillinger, J. Chem. Phys. **92**, 6239 (1990)

Si—F. The Stillinger-Weber (SW) potential has been modified by Weakliem, Wu, and Carter[41] (WWC) who performed an *ab initio* calculation for the Si—F interactions. Classical trajectory calculations using either interaction potential theoretically predict the three observed reaction channels: unreactive scattering, F-atom abstraction, and two-atom adsorption. Furthermore, Carter et al.[42] used the WWC potential to calculate the initial adsorption probability for each of the reaction channels under conditions comparable to those used in the current experiments.

The first observation upon comparison of the experimental results presented in the current work to the above theoretical studies is that in spite of predicting the feasibility of the atom abstraction process, the scattering velocity calculated for the ejected F atom is considerably larger than that observed experimentally. Carter et al.[42] report F atoms ejected with an average velocity of approximately 2000 m sec^{-1} using an incident F_2 energy of 1.8 kcal mol^{-1} while the experimental value under similar conditions was of the order of 1000 m sec^{-1}. Since they attribute the translational excitation to the repulsive forces dictated by the Si—F—F interaction potential, the discrepancy between the calculated and observed velocity of the ejected F atoms reflect the inadequacy of the WWC potential.

Further discrepancies between theory and experiment arise in the comparison of the reaction probabilities at zero coverage. Carter reports an attempt to model the reaction under the experimental conditions used in the current investigation, namely an incident energy of 0.67 kcal mol^{-1} for F_2 and a surface temperature of 250 K. The trajectory calculations yield a value of 0.19 for the initial two-atom adsorption probability, P_2, and a value of 0.81 for the F atom abstraction probability, P_1. Carter defines the initial adsorption probability, S_0, as the ratio of the number of F atoms that bind to the surface

---

[41] P. C. Weakliem, C. J. Wu, and E. A. Carter, Phys. Rev. Lett. **69**, 200 (1992)

[42] L. E. Carter, S. Khodabandeh, P. C. Weakliem, and E. A. Carter, J. Chem. Phys. **100**, 2277 (1994)

vs the total number of F atoms impinging on the surface. In terms of the reaction probabilities, S_0 is given by $P_2+0.5P_1$, so the initial F_2 adsorption probability calculated by Carter is 0.59. In contrast, the experimentally derived value for the zero-coverage atom abstraction and two-atom adsorption probabilities are 0.10 and 0.85 respectively, and the initial adsorption probability, as defined by Carter, is 0.90. Not only is the agreement in S_0 poor, but the relative importance of the abstraction and two-atom adsorption probabilities are nearly reversed. The theoretical result obtained using the WWC interaction potential greatly overestimates the probability of single atom abstraction at the expense of underestimating the likelihood of the two-atom adsorption process. This observation, combined with the overestimate of the ejected F atom velocity suggests that the WWC interaction potential overestimates the repulsive interaction felt by the ejected F atom in the Si—F—F transition state.

Carter's calculations more closely reproduce the experimental results of Engstrom, Nelson and Engel[43], in which the 1.48 kcal mol^{-1} F_2 is directed at a Si(100) surface held in the 120-600 K temperature range. The initial adsorption probability under these conditions, as determined by x-ray photoelectron spectroscopy (XPS), is reported to be 0.46±0.02. The value calculated by Carter using similar conditions is 0.57±03, which is in agreement with the experimentally derived result, if the absolute accuracy of ±20% for the XPS measurement is taken into account. The low value for S_0 reported by Engstrom et al. is in poor agreement with the value obtained in the current investigation. In spite of the different incident angle and translational energy, it is difficult to rationalize the large discrepancy in the measured initial adsorption probability (0.46 for XPS study vs 0.90 for the current work). Furthermore, Engstrom's measurement of the amount of fluorine on the saturated surface yields a coverage of 1.5 ML, which implies that Si—Si dimer or subsurface bonds are broken, contrary to the He diffraction results presented in Section

[43] J. R. Engstrom, M. M. Nelson, and T. Engel, Surf. Sci. **215**, 437 (1989)

1.3.4. The discrepancy in both the saturation coverage and initial adsorption probability put into question the accuracy of the XPS measurement for the determination of fluorine coverage on the Si surface.

The ability of F_2 to cleave dimer and subsurface bonds has also been addressed by the molecular dynamics simulations. Weakliem and Carter[44] conclude that the exothermicity of the Si—F bond formation is enough to cause Si—Si bonds to cleave, and hence initiate the etching process by allowing for fluorination beyond the 1ML saturation limit. It is likely, however, that the limited thermal conduction of the finite size Si slab used to model the effectively infinite Si bulk causes insufficient dissipation of the exothermicity away from the surface bonds. The importance of correctly modeling the energy dissipation by the Si bulk is illustrated by Stillinger and Weber's early work[39], which demonstrated that surface melting and SiF_x ($x>1$) product formation occurs in simulations where the energy released by the reaction is allowed to remain in the Si cluster, whereas no Si—Si bond cleavage or etch product is observed if a fraction of the energy is periodically removed from the cluster in an attempt to approximate the thermal conduction into the bulk. The validity of Carter's use of a finite slab to model the Si bulk is put into question, and further casts doubts on the integrity of calculated values for P_1 and P_2.

1.5.3 The Dependence of the Reaction Probabilities on Fluorine Coverage

The results of the amounts of scattered F and F_2 as a function of incident F_2 exposure that are presented in Section 1.3.2, combined with their quantitative analysis discussed in Section 1.4, lead to the determination of the exposure dependent reaction probabilities for the F_2/Si interaction shown in Figure 1.12. These probabilities are integrated following the procedure described in Section 1.4.3 to yield the fluorine coverage, and ultimately the

[44] P. C. Weakliem and E. A. Carter, J. Chem. Phys. **98**, 737 (1993)

coverage dependence of the reaction probabilities as presented in Figure 1.16. A qualitative discussion of the coverage dependence of the reaction probabilities provides some important insight into the reaction mechanism governing the fluorine adsorption.

The first point in each of the three reaction probabilities presented in Figure 1.12 corresponds to the clean (zero fluorine coverage) Si surface. The initial values of the probabilities are P_1=0.10±0.03 and P_2=0.85±0.03 yielding a total reaction probability in the limit of zero coverage of 0.95±0.04, or an unreactive scattering probability, P_0, of 0.05±0.01. The high initial value of P_2 implies that the majority of the incident F_2 molecules undergo two-atom adsorption on the clean Si surface, because the complementary F atom has a large probability of finding an empty Si bond near the initial abstraction site. The non-zero value of the abstraction probability, P_1, in the limit of zero exposure suggests that there are some incident orientations of the incoming F_2 molecule for which one of the F atoms is not able to sample any of the reactive sites and scatters back to the gas phase. F_2 molecules which impinge on the surface with their bond axis oriented perpendicularly to the surface could allow for the F atom closest to the surface to be abstracted by a Si dangling bond, with the top fluorine atom scattering backwards without a chance to interact with other surface sites in its outgoing trajectory. The nonzero value of the unreactive scattering probability, P_0, indicates that even at near-zero coverage, there are some collision events which do not lead to fluorine adsorption. Non-reactive collisions may result from unfavorable orientations of the incident molecule and/or unfavorable impact parameters that do not promote the abstraction of the first fluorine atom.

As the surface coverage increases, the two-atom adsorption probability, P_2, decreases, while the unreactive scattering probability, P_0, increases. Helium diffraction data presented in Section 1.3.4, coupled with the value of the fluorine saturation coverage strongly suggest that the Si dangling bond sites are both the abstraction and adsorption

sites. The Si—Si dimer bonds and the subsurface bonds are known[3] to be inert to attack by F_2 molecules incident with an energy of 0.66 kcal mol^{-1}. Therefore, as the amount of fluorine adsorbed on the surface increases, the number of dangling bond sites available to abstract and adsorb F atoms from the incoming F_2 decreases. Since two sites are required for each two-atom adsorption event to occur, the gradual depletion of the dangling bond sites is responsible for the almost monotonic decrease of the two-atom adsorption probability. While the two-atom adsorption channel is observed to decrease with coverage, the single atom abstraction probability, P_1 is observed to increase. The increase of the abstraction probability in the range from zero to 0.5 ML can be understood in terms of the relative abundance of vacant and occupied dangling bond sites. Once an initial abstraction event occurs, the probability that the complementary F atom scatters to the gas phase, rather than adsorbs onto the surface, depends on the availability of reactive sites adjacent or near to the Si atom where the initial abstraction occurred and the orientation of the incident F_2 molecules. As the coverage increases, the number of Si dangling bonds available to adsorb the second F atom decreases. The filled sites serve to block the adsorption of the second fluorine atom, and hence force its ejection to the gas phase, thereby driving the increase of the abstraction probability. Beyond half-monolayer coverage, both the abstraction and two-atom adsorption probabilities are observed to decrease. This drop in reactivity can be understood in terms of the decrease in the number of reactive sites available for the initial abstraction step which is required for both reactions channels. The decrease of reactive sites is most clearly evidenced in the monotonic increase of the unreactive scattering probability, P_0. The maximum in P_1 occurs as a result of the competition between the number of unfilled sites available for abstraction of the first F atom which decreases with coverage and the number of filled sites to scatter the second F atom into the gas phase which increases with coverage. When 1 ML coverage is reached, all available surface sites are occupied by fluorine atoms, hence the reaction probabilities P_1 and P_2 reach a constant value of zero,

while the unreactive scattering probability, P_0, reaches its asymptotic value of unity. Since F_2 incident with a translational energy of 0.66 kcal mol^{-1} is not able to attack the fully fluorinated surface, the coverage saturates and no further reaction is observed.

So far, only a qualitative discussion of the coverage dependence of the three reaction pathways considered in the interaction of F_2 with Si(100) has been presented. In the next section, a quantitative analytical model is proposed which attempts to more precisely define a physical picture consistent with the observed probabilities. Section 1.5.3.1, a simple model for dissociative chemisorption previously presented by Yang[45] is summarized. Sections 1.5.3.2 and 1.5.3.3 present the modifications and extensions to the model which more closely capture the physically relevant parameters governing the fluorine chemisorption mechanism.

1.5.3.1 Lattice-gas Model for the Dissociative Chemisorption of F_2 on Si(100)

The assumptions of the simple analytical model, describing the chemisorption process of F_2 incident on a Si(100) surface, as proposed by Yang are:

1) The Si(100) is represented by a fixed number of potentially reactive sites, each of which can accommodate one adsorbed F atom.
2) The reactive sites are arranged in a two-dimensional square lattice, so that each reactive Si atom has eight equivalent nearest neighbors.
3) Once a fluorine atom is adsorbed at a particular site, it can neither desorb nor diffuse to another site.
4) Chemisorption of both F atoms from an incident F_2 requires two adjacent (or more accurately, any two) vacant sites.
5) There are two mechanisms termed "neighbor-independent" (*ni*) and "occupied neighbor" (*on*), by which single F atom abstraction occurs. In *ni*-abstraction, single atom adsorption can occur at any single vacant site, independent of nearest-neighbor occupancy status, while in *on*-abstraction, the probability for single-atom abstraction at any available site is directly proportional to the number of neighboring sites which are occupied.

[45] J. J. Yang, Ph.D. Thesis, Massachusetts Institute of Technology, p. 164, (1993)

Under these assumptions, the adsorption of both F atoms from an incident F_2 molecule requires the use of two unoccupied surface sites. The presence of adsorbates on the surface is treated via a modified lattice-gas model in which the occupancy of lattice sites is assumed to proceed in a random order and where no interactions are allowed between the adatoms. The probability of the two-atom adsorption process thus depends on the fractional coverage, Θ, of fluorine occupied surface sites. Since the coverage is known to saturate at one monolayer, the probability that a Si dangling bond site is available to abstract one of the F atoms from an incident F_2 is given by $(1-\Theta)$, the fractional coverage of unoccupied (reactive) sites. The probability that a second vacant site is simultaneously available for adsorption of the second F atom is then given by $(1-\Theta)^2$. The expression predicting the coverage dependence of the two-atom adsorption probability, P_2, is then given by

$$P_2(\Theta) = S_2\,(1-\Theta)^2 \qquad (1.54)$$

where the scaling factor S_2, which has a value between zero and one, accounts for those configurations of the incident F_2 molecule which lead to non-reactive collisions, or which do not allow the second atom to adsorb (for example, F_2 approaching with its bond axis nearly perpendicular to the surface plane).

Note that the above expression allows for the second F atom to adsorb on any vacant site anywhere on the surface. The fractional coverage, Θ, is a quantity averaged over the entire surface, and does not provide a way of distinguishing the sites adjacent to the abstraction site from all other sites on the surface. The $(1-\Theta)^2$ dependence allows for the second F atom to adsorb on any vacant surface site, regardless of whether or not it is a nearest-neighbor to the site where the initial atom abstraction occurred.

One possible mechanism by which the complementary F atom could access vacant sites far away from the initial abstraction site, is for the exothermicity of the initial Si—F

bond formation to propel the second F atom in a trajectory nearly parallel to the surface. Such "hot-atom" mechanisms, leading to the chemisorption of two fragments of the same incident molecule at distant surface sites, have been proposed[46] in the interaction of O_2 with metal surfaces such as Pt and Al. No direct evidence exists, however, to support the validity of the hot-atom mechanism in the case of F_2 interacting with Si(100). Furthermore, the applicability of the hot-atom mechanism to the F_2/Si system may be hampered by the corrugated nature of the Si(100) surface. While it may be reasonable to expect oxygen atoms to travel substantial distances across a flat metal surface, a hot F atom traversing a corrugated Si(100) surface is much more likely to suffer collisions with the buckled Si—Si dimers and thus scatter out to the gas-phase before finding an empty site on which to bind. This is in fact one of the mechanisms by which the single-atom abstraction channel, which will be discussed below, may be enhanced.

According to the last assumption in the model, the single-atom abstraction mechanism is divided into two contributions arising from distinct physical processes. The first contribution, neighbor-independent abstraction, accounts for those incident F_2 orientations in which the second F atom is ejected away from the Si surface, and thus has no chance to interact with other surface sites regardless of the state of their occupancy. The probability for this neighbor-independent abstraction process is only determined by the availability of unoccupied sites on which the initial abstraction takes place. The neighbor independent abstraction probability is then given by

$$\mathrm{P}_1^{\mathrm{ni}}(\Theta) = S_1^{ni}(1-\Theta) \tag{1.55}$$

where S_1^{ni}, a scaling factor with a value between zero and one, accounts for those incident F_2 molecules which do not have the required orientation to eject the second fluorine atom away from the surface.

---

[46] J. Wintterlin, R. Schuster, and G. Ertl, Phys. Rev. Lett. **77**, 123 (1996)

As indicated by its name, "occupied neighbor" abstraction, the second contribution to the abstraction probability is dependent on the occupancy of a second site. When an incident F_2 molecule approaches the surface with an orientation such that after the first F atom is abstracted, its partner is able to sample the adjacent surface sites, two outcomes are possible. If the sampled site is vacant, the F atom is free to adsorb, and hence the overall process is simply two-atom adsorption leading to fluorination of two sites. On the other hand, if the sampled site is occupied, the adsorption of the second F atom will be blocked leading to scattering of the complementary F atom into the gas phase. At any given fractional coverage, Θ, the probability of occupied neighbor abstraction is assumed to be proportional to the number of occupied sites surrounding the site of the initial abstraction. Yang has shown[47] that, on average, the number of occupied sites adjacent to an initial abstraction site should follow a $\Theta(1-\Theta)$ dependence. The $(1-\Theta)$ factor corresponds to the number of empty sites available for the initial abstraction event, while the Θ factor accounts for the fraction of sites which are occupied. Yang's derivation is reasonable, as long as the F-atom abstraction and the subsequent adsorption of the second F-atom occur at random sites on the surface, with no preferential role given to the eight nearest-neighbor sites. Therefore, under these assumptions, the occupied neighbor abstraction probability is given by,

$$P_1^{on}(\Theta) = S_1^{on}\,\Theta(1-\Theta) \tag{1.56}$$

where S_1^{on} has a value between zero and four, since the maximum value of the product $\Theta(1-\Theta)$ is equal to 0.25. This scaling factor accounts for the existence of F_2 orientations which are either non-reactive, or lead to chemisorption of both F atoms despite the complementary atom's encountering an occupied site.

The expression predicting the total abstraction probability, P_1, can be obtained by

[47] J. Yang, Ph.D. Thesis, Massachusetts Institute of Technology, p. 168, (1993)

combining the contributions of Eqs. (1.55) and (1.56) to yield,

$$\mathrm{P}_1(\Theta) = (S_1^{ni} + S_1^{on}\,\Theta)(1-\Theta) \tag{1.57}$$

Finally, the third reaction probability, P_0, which accounts for unreactive scattering is given by the mass balance condition,

$$\mathrm{P}_0(\Theta)=1-\mathrm{P}_1(\Theta)-\mathrm{P}_2(\Theta) \tag{1.58}$$

The above expressions for the three reaction probabilities have been derived on the basis of their expected dependence on the surface coverage. Since the experimental data leading to the determination of the reaction probabilities is recorded as a function of F_2 exposure, and only later converted to a function of coverage, it is useful for the purpose of comparing the model to the experimental data to recast Eqs. (1.54), (1.57) and (1.58) in terms of F_2 exposure rather than fluorine coverage. The relationship between the F_2 exposure, ε, determined by the incident fluorine flux, I_{F_2}, and fluorine coverage, Θ, is given by the following rate equation

$$\frac{d\Theta}{d\varepsilon} = I_{F_2}(2\mathrm{P}_2 + \mathrm{P}_1) \tag{1.59}$$

which states that each incident F_2 molecule that undergoes a two-atom abstraction event populates two sites while each molecule undergoing a single atom abstraction event populates a single site. Yang has shown that the analytical solution to this differential equation leads to the following expression relating exposure and coverage,

$$\Theta(\varepsilon) = \frac{(2S_2 + S_1^{ni})(e^{S_1\varepsilon} - 1)}{S_1 + (2S_2 + S_1^{ni})(e^{S_1\varepsilon} - 1)} \tag{1.60}$$

where S_1 is the sum of the neighbor-independent (*ni*) and occupied neighbor (*on*) scaling factors

$$S_1 = S_1^{ni} + S_1^{on} \tag{1.61}$$

Substituting Eq. (1.60) into Eqs. (1.54), (1.57) and (1.58), the three reaction probabilities can be expressed as a function of exposure

$$P_2(\varepsilon) = S_2\left(\frac{S_1}{S_1 + (2S_2 + S_1^{ni})\left(e^{S_1\varepsilon} - 1\right)}\right)^2 \tag{1.62}$$

$$P_1(\varepsilon) = \frac{S_1^{ni} + (2S_2 + S_1^{ni})\left(e^{S_1\varepsilon} - 1\right)}{\left(1 + \frac{\left(2S_2 + S_1^{ni}\right)}{S_1}\left(e^{S_1\varepsilon} - 1\right)\right)^2} \tag{1.63}$$

$$P_0(\varepsilon) = 1 - \frac{S_2 + S_1^{ni} + (2S_2 + S_1^{ni})\left(e^{S_1\varepsilon} - 1\right)}{\left(1 + \frac{\left(2S_2 + S_1^{ni}\right)}{S_1}\left(e^{S_1\varepsilon} - 1\right)\right)^2} \tag{1.64}$$

The above equations show that the exposure dependence of the reaction probabilities can be expressed solely in terms of the three scaling factors S_1^{ni}, S_1^{on} and S_2. Each of the three scaling factors can be determined directly from the data since in the limit of zero coverage or zero exposure (ε=0), P_1 and P_0 reduce to

$$P_1(\varepsilon = 0) = S_1^{ni} \tag{1.65}$$

$$P_0(\varepsilon = 0) = 1 - S_2 - S_1^{ni} \tag{1.66}$$

Therefore, two of the three scaling factors are determined from the experimental values of P_1 and P_0 extrapolated to zero exposure. Furthermore, by solving for the coverage at which the derivative of Eq. (1.63) equals zero (i.e. the maximum of the abstraction probability vs coverage curve) one obtains

$$P_1^{max} = \frac{1}{S_1^{on}}\left(S_1^{ni} + S_1^{on}\right)^2 \tag{1.67}$$

and solving for S_1^{on},

$$S_1^{on} = 2P_1^{max} - S_1^{ni} + 2\sqrt{P_1^{max}(P_1^{max} - S_1^{ni})} \tag{1.68}$$

provides a method to extract the third scaling factor from the experimentally-determined maximum in the single-atom abstraction probability.

Figure 1.19 reproduces the experimentally-determined reaction probabilities as a function of exposure previously shown in Section 1.4.1. It can be seen that the value of P_1 in the zero coverage limit is approximately 0.1, while its maximum value is approximately 0.3. Similarly, P_0 has a value of 0.05 in the limit of zero coverage. Using these values to solve for the appropriate scaling factors in Eqs. (1.65), (1.66) and (1.68) yields

$$S_1^{ni} = 0.1 \tag{1.69}$$

$$S_2 = 0.85 \tag{1.70}$$

$$S_1^{on} = 0.98 \tag{1.71}$$

The model's predictions for the three reaction probabilities as a function of exposure are overlaid on the data shown in Figure 1.19. As seen in Figure 1.19 (b), the model approximately reproduces the observed dependence of the single-atom abstraction probability, P_1, on exposure, and in particular, closely matches the data at low exposures. While the choice of scaling factors, which are directly extracted from the data, guarantees the exact agreement of the calculated and measured probabilities at zero exposure and at the exposure at which P_1 is maximum, the good agreement over the entire range of exposures suggests that the model captures the main physical features affecting the abstraction process at low F_2 exposures.

At low F_2 exposures, the fluorine coverage is low and the number of available reaction sites is large. Therefore, the abstraction probability is primarily expected to arise from the neighbor independent mechanism in which the orientation of the F_2 bond axis

precludes the second F atom from adsorbing on one of the many vacant sites. The agreement between the model and the experimental data in the low coverage regime suggests that the neighbor independent abstraction mechanism is the primary channel for abstraction, and hence that the orientation of the incident F_2 molecule plays an important role in the abstraction process. The importance of the orientation of the incident F_2 molecules in the abstraction process is observed in molecular dynamic simulations[42] previously discussed. The calculated initial abstraction probability is determined to be higher for F_2 molecules incident with roughly perpendicular orientations relative to the surface plane than for those with a near parallel approach.

At higher F_2 exposures, the values predicted by the model overestimate the abstraction probability. At higher coverages, the abstraction mechanism of the occupied neighbor type becomes increasingly important. Occupied neighbor abstraction requires an occupied site to block the adsorption of the second F atom. As explained above, sites close to the initial abstraction site are no different than any other sites on the surface. The probability of atom abstraction in the model is based on the statistical probability of the second atom encountering a blocking site anywhere on the entire surface. The fact that the model overestimates the probability of abstraction at higher exposures suggests that it fails to capture the physical parameters governing the adsorption process at higher surface coverage.

Keeping within the basic framework of the model, Yang offers two explanations that could cause the abstraction probability to decrease more rapidly than predicted at high exposures. The first explanation involves steric hindrance of the original abstraction site by the presence of occupied sites surrounding it. The premise is that at high coverage, the few sites available for the initial abstraction event are likely surrounded by a large number of occupied sites which could sterically hinder the initial abstraction of the F atom and thus increase the probability of unreactive scattering at the expense of both

single- and two- atom adsorption. Yang further argues that this blocking of potential abstraction sites may not scale linearly with the number of occupied nearest neighbors, since the steric hindrance may not be significant until a given fraction of nearest neighbor sites are occupied.

The second explanation for the relative inefficiency of the abstraction channel at higher coverages is based on the possible influence of an attractive interaction between an impinging F_2 molecule and the Si surface or a reacting F_2 molecule and a Si dangling bond neighboring the original abstraction site. The presence of an attractive interaction could either steer the impinging F_2 into an orientation favorable for two-atom adsorption, or orient the reacting F_2 molecule's bond axis such that the ejected F atom is preferentially directed towards an empty site. Such attractive interactions would clearly enhance the two-atom adsorption process at the expense of single-atom abstraction. The coverage dependence of the neighbor occupied abstraction mechanism would no longer obey a linear relationship to the number of occupied sites, but would rather have to be weighted to account for the enhanced reactivity of certain sites, which would most likely be those adjacent to the initial abstraction site.

Figure 1.19 (c) presents the comparison between the experimental and modeled two-atom adsorption probabilities. The general shape of the exposure dependence given by the model agrees well with experiment. The quantitative agreement at zero coverage or zero exposure is guaranteed by the choice of the S_2 scaling factor, which is extracted directly from the data. Closer scrutiny reveals that for the low exposure regime, the model underestimates the probability of two-atom abstraction. The higher P_2 values that are observed are consistent with the ejected F atom not sampling the sites in a random manner, but rather being preferentially attracted towards certain empty sites possessing an enhanced reactivity.

Finally, Figure 1.19 (a) presents the comparison of the measured and calculated

unreactive scattering probabilities. As required by the mass balance condition ($P_0+P_1+P_2=1$), the P_0 channel reflects the observed discrepancies between the modeled and the experimental values of P_1 and P_2. The model first overestimates the unreactive probability as a consequence of having underestimated the two-atom adsorption channel, P_2, and at higher coverage it underestimates the unreactive contribution as a consequence of having overestimated the abstraction probability, P_1. The differences between the model and the data are emphasized in Figure 1.20, where both the experimentally-derived and modeled reaction probabilities are presented as function of coverage. The fluorine coverage is calculated using Eq. (1.36) for the experimental data, and Eq. (1.60) for the model. It is apparent from this plot that the functional forms used by the model to describe the chemisorption process do not accurately reproduce the observed reaction probabilities over the entire range of fluorine coverage. The reasonably good agreement observed for the P_1 curves, particularly at lower coverages, is ascribed to the success of the model in capturing the importance of neighbor-independent abstraction.

The first explanation offered by Yang to account for the discrepancies between the modeled and observed reaction probability is based on steric hindrance of the incident F_2 molecule. The steric hindrance of initial adsorption sites would contribute to lower the predicted values of both P_1 and P_2 at higher coverage, at the expense of increasing the unreactive scattering probability, P_0. The steric hindrance mechanism would therefore only help improve the agreement of the modeled P_1 with experiment, but would fail in improving the agreement of the P_2 curves. In contrast, the second explanation, based on giving a unique (attractive) character to empty sites adjacent to the original abstraction site, would lower P_1 at higher coverages while increasing P_2, which in turn slightly decreases P_0. Distinguishing sites near and far from the initial abstraction event may then provide a way to improve the agreement between the model and the data for all three reaction channels.

The limitations of the simple model proposed by Yang arise from its inability to differentiate the nearest neighbor sites from other sites far from the initial abstraction site. The use of the fractional surface coverage, Θ, does not provide information about the location of a given site, or its relationship to the original adsorption event. Rather, the fractional Si coverage simply indicates whether a site is statistically vacant or occupied and hence available to adsorb or to block the ejected F atom, regardless of its location relative to the site of the initial F_2 impact. In addition, the assumption that all surface sites are evenly distributed in a square lattice with eight equivalent nearest neighbors is not consistent with the well documented dimer structure of the Si(100) 2x1 surface, in which each Si atom only has one nearest neighbor.

The simple model presented in this section, with all of its limitations, still captures the essential aspects of the measured reaction probabilities. The interplay between the abstraction, two-atom adsorption and unreactive scattering channels is on a first approximation governed by the competition between the availability of reactive Si dangling bonds and unreactive fluorinated sites. The model confirms that two-atom adsorption is favored by an abundance of reactive sites, fluorine abstraction is most prevalent when a comparable number of vacant and occupied (blocking) sites exist, and unreactive scattering dominates when few vacant sites remain on the surface. In addition, the model also suggests the importance of the orientation of the incident F_2 in the abstraction process, in particular at low fluorine coverages for which neighbor independent abstraction is most important. A clearer physical picture of the adsorption mechanisms at higher surface coverages is precluded by the model's inability to discriminate amongst surface sites, as well as its inaccurate representation of the surface structure. Further details regarding the binding site of the ejected F atom cannot be extracted from this model. The following section discusses modifications and extensions

proposed by Tate[48] which attempt to incorporate into the model a more realistic representation of the Si surface as well as to differentiate between the nearest-neighbor sites and those far removed from the original abstraction site.

---

[48] M. R. Tate, private communication

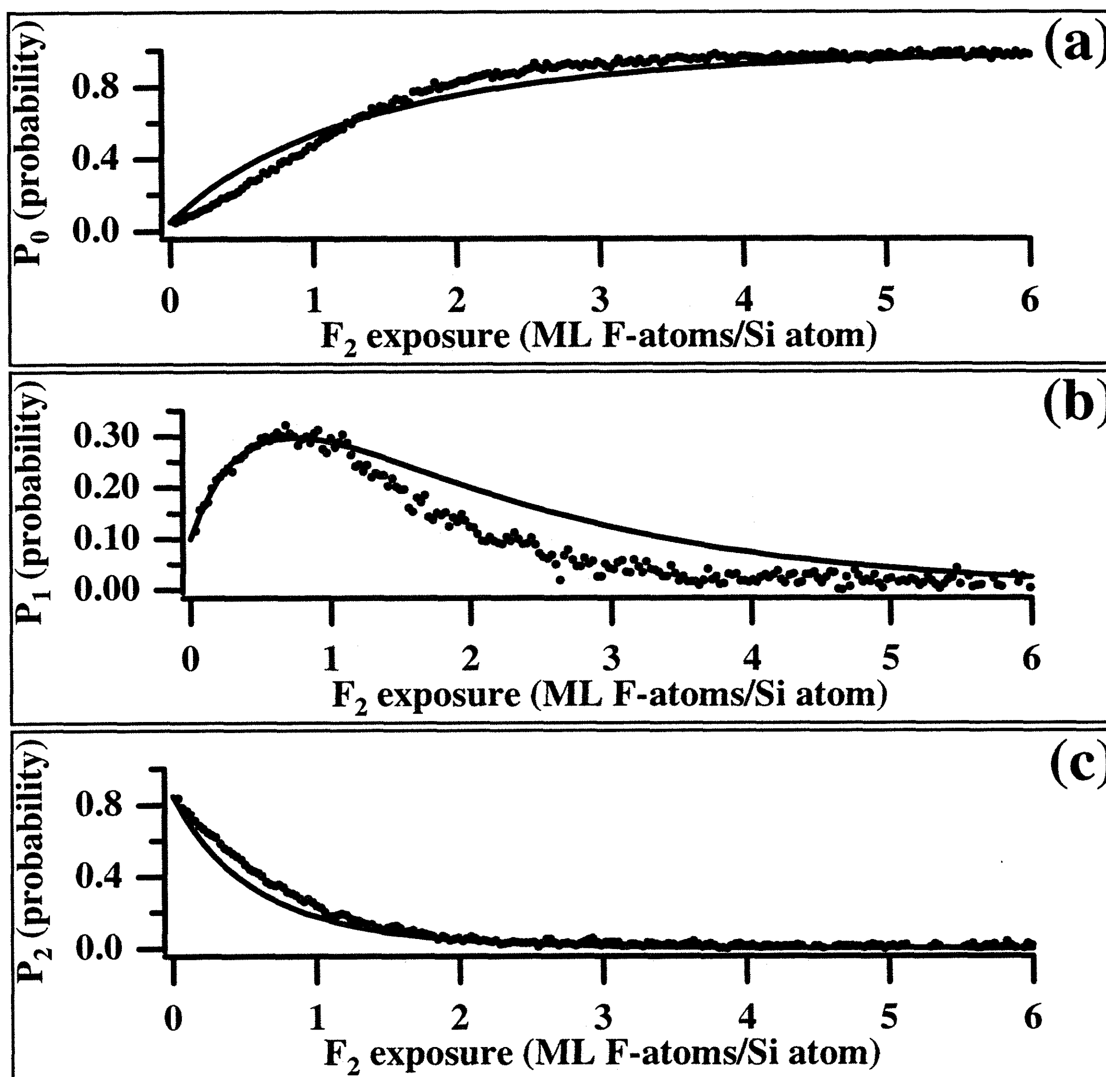

Figure 1.19 Reaction Probabilities Predicted by the Lattice-gas Model

Comparison of lattice-gas model (solid lines) and measured reaction probabilities. (a) unreactive scattering, P_0, (b) single-atom abstraction, P_1, and (c) two-atom adsorption, P_2, probabilities as a function of F_2 exposure. Experimental curves have been described in Figure 1.12.

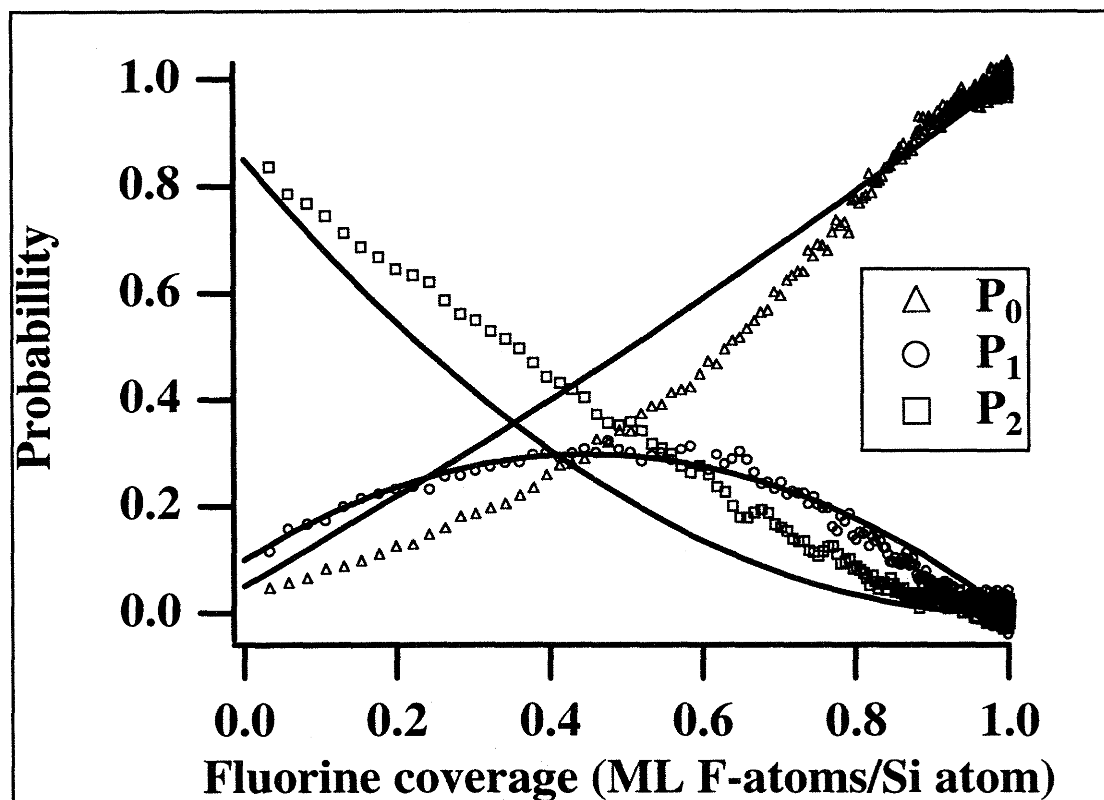

Figure 1.20 Lattice-gas Model Probabilities as a Function of Coverage

Comparison of lattice-gas model (solid lines) and measured reaction probabilities as a function of fluorine coverage. Data taken from Figure 1.12.

1.5.3.2 Three-state Lattice-gas Model

The major modification proposed by Tate consists of redefining surface sites to encompass not just a single Si atom, but a pair of Si dangling bonds. The pairing of Si atoms is justified by the well-documented existence of Si dimers on the 2x1 reconstructed Si(100) surface[26,28,27] where each atom of the Si dimer has a single dangling bond. The occupancy of each site has now three possible "states": 1) a site is *empty* when both Si dangling bonds are available for reaction, 2) a site is *half-filled* when one of the two dangling bonds is occupied by a fluorine atom while the other remains available for reaction, and 3) the site is *filled* when both dangling bonds are occupied by adsorbed F atoms rendering the site unreactive. The use of three-state sites allows the occupancy of one Si atom near the dangling bond where the initial abstraction takes place to be noted, and to be distinguished from that of all other surface Si atoms. Creating a distinction between one Si atom and the rest of the atoms on the surface allows the three state model to test the importance of attractive interactions between the incident or reacting F_2 towards that particular surface site. The rest of the assumptions introduced with the original lattice-gas model are preserved. The three-state model thus simply represents an extension of the lattice-gas model in which the occupancy of a Si atom near the initial abstraction site is monitored independently of all other surface sites.

The assumptions of the lattice-gas model can be rewritten in the language of "three-state" sites as follows:

1) The Si(100) is represented by a fixed number of reactive sites. Each site is made up of a pair of Si atoms each of which can accommodate one adsorbed F atom. Each site can therefore adsorb two F atoms.
2) The sites are arranged in a two-dimensional square lattice where each one has eight nearest-neighbor sites. Each individual Si atom within a site, however, has one nearest-neighbor atom, namely the other atom in that site.
3) Once a fluorine atom is adsorbed at a particular site it cannot desorb, nor diffuse within or between sites.

4) Chemisorption of both F atoms from an incident F_2 molecule may occur within an *empty* site with both F atoms adsorbing on it or at an *empty* or *half-filled* site with the second F atom finding a different site on which to bind. The probability of the latter process is expected to be proportional to the total fraction of Si dangling bonds present on the surface.

5) There are two mechanisms, termed "neighbor independent" (*ni*) and "occupied neighbor" (*on*) abstraction by which a single F atom can adsorb on the surface. In *ni*-independent abstraction, a single F atom can adsorb on any reactive Si dangling bond, be it in an *empty* or *half-filled* site, while the probability that the complementary F atom scatters to the gas-phase is completely independent of surface occupancy. The *on*-abstraction probability may occur on a *half-filled* site where the vacant half provides for the adsorption of the abstracted F atom while the occupied half of the site blocks the adsorption of the complementary F atom forcing it to scatter away. Abstraction may, however, also occur at either an *empty* or *half-filled* site with the adsorption of the second F atom being blocked by a F atom bound on a different site.

In the simple lattice-gas model described in the previous section, the adsorption sites, which correspond to single Si dangling bonds, could be thought of as an ensemble of "two-state" systems each of which can be either *empty* or *filled.* Mathematically, the "state" of each site is expressed in terms of the single variable, Θ, which gives the fractional coverage in monolayers of *filled* sites on the surface. In the case of F_2/Si, the value of Θ is restricted to lie between zero (clean Si surface) and one (F saturated surface) so the fractional coverage of *empty* sites is given by $1-\Theta$. The extension of the model to an ensemble of three-state systems requires the use of two variables to keep track of the "state" of each site on the surface. The first variable, Θ_1, represents the fractional fluorine coverage (in ML of F atoms) associated with *half-filled* sites. The subscript serves to denote that this coverage arises from sites that only contribute a single F atom to the surface coverage. Similarly, Θ_2, represents the fractional fluorine coverage (in ML of F atoms) associated with *filled* sites, and its subscript denotes that each site contributes two F atoms to the surface coverage. While Θ_2, the coverage from *filled* sites, can range between zero (for the clean surface) and one (for the fluorine saturated surface in which all sites are *filled*), Θ_1, the coverage from *half-filled* sites, is restricted to a maximum value of 0.5 ML obtained when every site is *half-filled.*

The probability for both atoms from an incident F_2 molecule to be adsorbed on a single site scales with the availability of Si atoms in totally *empty* sites. The fraction of Si atoms in *empty* sites is given by $1-(2\Theta_1+\Theta_2)$, where the factor of two accounts for the fact that although a *half-filled* site only contributes one fluorine atom to the fractional coverage, it eliminates both of its Si atoms as potential candidates for the F_2 to adsorb within that site. The probability for two-atom adsorption occurring at any two reactive Si dangling bonds, regardless of their relative location and neighbor occupancy is proportional to $(1-(\Theta_1+\Theta_2))^2$. The sum $(\Theta_1+\Theta_2)$ is equal to Θ as defined in the simple lattice-gas model, and gives the number of occupied Si atoms across the surface. The quantity $1-(\Theta_1+\Theta_2)$ thus represents the number of available dangling bonds on the surface, and this quantity is squared since the availability of two dangling bonds is required to accommodate the F_2 molecule. The two-atom adsorption probability predicted by the three-state lattice-gas model is then given by

$$P_2(\Theta_1,\Theta_2) = S_2(1-(\Theta_1+\Theta_2))^2 + S_2'(1-(2\Theta_1+\Theta_2)) \tag{1.72}$$

where the first term is equivalent to the P_2 expression given in the simple lattice-gas model presented above, and the second term accounts for the probability that both F atoms from the incident F_2 molecule adsorb on a single empty site. The scaling factor, S_2', accounts for orientations of the incident F_2 molecule which may lead to unreactive collisions and/or single-atom abstraction events regardless of the availability of *empty* sites on the surface. The prime on the S_2' symbol is used to differentiate it from the similar scaling factor used in the first term. The ratio of the two scaling factors provides an estimate of the likelihood that a F atom ejected after an abstraction event adsorbs on the same site as its partner. Physically, this single-site two-atom adsorption might be enhanced by a preferential alignment of the bond axis of the incident F_2 molecule with respect to the abstraction site such that the second F atom is ejected in the direction of the vacant Si within that site, or by a preferential steering of the ejected F atom towards the

empty dangling bond. The S_2' scaling factor thus provides a way to incorporate the importance of attractive interactions between the incident F_2 and one of the reactive atoms on the surface, namely the one paired to the Si atom where the abstraction takes place.

The modified model retains the idea of neighbor-independent abstraction, which provides a mechanism for a single F atom to be adsorbed on the surface even at low coverages when few occupied sites are available to block the adsorption of the complementary F atom. The neighbor-independent abstraction mechanism can take place on either an *empty* or a *half-filled* site since it only requires one Si dangling bond for the initial adsorption, and does not depend on the occupancy of any other Si dangling bond. The neighbor-independent contribution to the abstraction probability is proportional to the fraction of reactive Si atoms regardless of whether they are part of an *empty* or a *half-filled* site. The fraction of Si atoms that can lead to neighbor-independent abstraction is then given by $1-(\Theta_1+\Theta_2)$ which represents the number of available Si dangling bonds on the surface.

The three state model also retains the concept of the occupied neighbor mechanism for single-atom abstraction, but it keeps track of whether occupied neighbor abstraction preferentially occurs at a *half-filled* or at an *empty* site. The occupied neighbor mechanism can take place on a *half-filled* site, where the empty dangling bond serves to abstract the initial F atom, while the occupied Si acts to block the second F atom from adsorbing. The probability of abstraction at a *half-filled* site with the blocking occurring within that site is proportional to the number of *half-filled* sites which is given by Θ_1.

Alternatively, *on*-abstraction can occur at any reactive Si dangling bond, with the adsorption of the complementary F atom being blocked by a F atom from a neighboring site. This process requires a reactive site for the initial abstraction event and thus its probability is proportional to $1-(\Theta_1+\Theta_2)$. In addition, the probability that the second atom

is prevented from adsorbing at a neighboring site is proportional to the number of occupied sites on the surface which is given by (Θ_1+Θ_2). The expression for the single-atom abstraction probability is thus given by

$$P_1(\Theta_1,\Theta_2) = S_1^{ni}(1-(\Theta_1+\Theta_2)) + S_1^{on}(1-(\Theta_1+\Theta_2))(\Theta_1+\Theta_2) + S_1'^{on}\Theta_1 \tag{1.73}$$

where the first term is the *ni*-abstraction, the second term corresponds to *on*-abstraction involving an empty and an occupied Si atom on two distinct sites, and the third term accounts for abstraction occurring within a single *half-filled* site.

Finally, the unreactive scattering probability is obtained from P_1 and P_2 by use of the mass balance condition.

$$P_0(\Theta_1,\Theta_2) = 1 - P_1 - P_2 \tag{1.74}$$

While the fractional coverages Θ_1 and Θ_2 are useful quantities for determining the functional form of the reaction probabilities dictated by the model's assumptions, they are not quantities that are measurable in this experiment. It is therefore desirable to convert the above expressions into functions of measurable quantities such as F_2 exposure, ε, or total fractional coverage, Θ.

The fluorine coverage associated with *half-filled* sites, Θ_1, arises from either atom abstraction on an *empty* site, or two-atom adsorption involving a pair of *empty* sites. It is important, however, to note that Θ_1 is not a monotonically increasing function of exposure. For each adsorption event occurring at an *empty* site on the surface, Θ_1 increases by one fluorine atom, while for each adsorption event occurring at a *half-filled* site Θ_1 decreases by one fluorine atom, since the site is no longer *half-filled*. The dependence between Θ_1 and exposure is determined by accounting for the events which change the coverage associated with *half-filled* sites and it is given by the following rate equation

$$\frac{d\Theta_1}{d\varepsilon} = I_{F_2}\begin{bmatrix}(S_1^{ni} + S_1^{on}(\Theta_1 + \Theta_2))(1-(2\Theta_1 + \Theta_2)) + 2S_2(1-(2\Theta_1 + \Theta_2))^2 \\ -(S_1^{ni} + S_1^{on}(\Theta_1 + \Theta_2))\Theta_1 - 2S_2\Theta_1^2 - S_1'^{on}\Theta_1\end{bmatrix} \tag{1.75}$$

The first two terms contribute to increase Θ_1. The first term corresponds to *ni*- and *on*-abstraction occurring at an *empty* site while the second one arises from two-atom adsorption with each F-atom binding on a different *empty* site. The next three terms act to decrease Θ_1 by completing the filling of *half-filled* sites. The first one of these accounts for atom abstraction at a *half-filled* site which decreases Θ_1 by one F atom. On the other hand, the next term decreases Θ_1 by two F atoms since it involves two-atom adsorption where each F-atom fills a different *half-filled* site. Finally, the last term also decreases Θ_1 by one F atom and corresponds to the special case of single-site abstraction, where the F-atom occupying the half-filled site acts to scatter the ejected F-atom to the gas-phase.

Any adsorption event contributing to fill a site will increase Θ_2, the fluorine coverage associated with two-atom adsorption. Additionally, since no adsorption event can contribute to decrease the number of *filled* sites, Θ_2 is strictly an increasing function of exposure up to the saturation coverage. The expression relating Θ_2 to the fluorine exposure is determined by accounting for the events that change the coverage associated with filled sites and it is given by

$$\frac{d\Theta_2}{d\varepsilon} = I_{F_2}\begin{bmatrix}2(S_1^{ni} + S_1^{on}(\Theta_1 + \Theta_2))\Theta_1 + 2S_2'(1-(2\Theta_1 + \Theta_2)) \\ + 2S_1'^{on}\Theta_1 + 4S_2\Theta_1^2 + 4S_2(1-(2\Theta_1 + \Theta_2))\Theta_1\end{bmatrix} \tag{1.76}$$

The first term corresponds to an abstraction event occurring at a *half-filled* site which becomes *filled*, and thus contributes two F atoms to Θ_2. The second term accounts for two-atom abstraction which fills an *empty* site increasing Θ_2 by two F atoms. The third term corresponds to single-site abstraction which fills a previously *half-filled* site adding two F atoms to the filled site coverage. The fourth term fills two distinct *half-filled* sites from a single two-atom abstraction event adding four F-atoms to Θ_2. Finally, the fifth

term accounts for two-atom adsorption involving a *half-filled* site and an *empty* site, which contributes two F atoms towards Θ_2 independent of whether it is the initial atom abstraction or the second atom adsorption that fills the *half-filled* site.

Since the total coverage, Θ, is obtained from the sum of Θ_1 and Θ_2, adding Eqs. (1.75) and (1.76) results in the familiar expression relating the coverage and exposure

$$\frac{d\Theta}{d\varepsilon} = I_{F_2}(2P_2 + P_1) \tag{1.77}$$

which was given in Eq. (1.60) during the discussion of the simple lattice-gas model.

Equations (1.75) and (1.76) comprise a system of coupled differential equations that must be solved in order to obtain the relationship between the partial fluorine coverages, Θ_1 and Θ_2, and the F_2 exposure. Since this system of equations does not appear to have an analytical solution, the functions relating Θ_1 and Θ_2 to F_2 exposure are determined by numerical integration and are then substituted into Eqs. (1.72), (1.73) and (1.74) to obtain the desired reaction probabilities as a function of F_2 exposure. The probabilities measured at zero-coverage yield some of the scaling factors. In particular, the sum of $S_2 + S_2'$ is obtained from the value of $P_2(\Theta=0)$, while S_1^{ni} is determined from $P_1(\Theta=0)$. In the simple lattice-gas model discussed in the previous section, the measured maximum value of P_1 was used to determine the S_1^{on} scaling factor. In the three-state model, the values of the occupied neighbor scaling factors cannot be determined in the same way, since it is impossible to correlate the Θ value at which the maximum in P_1 occurs with the values of Θ_1 and Θ_2, since the later are not experimentally measurable. The partitioning between S_2 and S_2' as well as the values of S_1^{on} and $S_1'^{on}$ are obtained by fitting the above expressions to the experimental data. Since the sum of S_2 and S_2' must have the value extracted directly from the data, the model only requires a total of three fitting parameters. While S_1^{ni} and the sum of $S_2 + S_2'$ are extracted from the experimentally-derived probabilities, an initial guess is required for the values of S_1^{on}, $S_1'^{on}$, and the

individual values of S_2 and S_2'. The numerical integration and calculation of the probabilities are then repeated while manually adjusting the scaling factors which act as fitting parameters to obtain an approximate fit to the data. The three fitting parameters are iteratively adjusted until a local minimum is found in the standard deviations from the mean of the square of the difference between the data and the fits. No steepest descent algorithm is used in the adjustment of the fitting parameters, but rather judicious choices are made at each iteration and then validated by the quality of the resulting fit. An adequate fit is obtained using the following values for the scaling factors: $S_1^{ni} = 0.10$, $S_2 = 0.80$, $S_2' = 0.05$, $S_1^{on} = 0.98$, and $S_1'^{on} = 0.05$.

Figure 1.21 shows the comparison between the measured probabilities and those predicted by the three-state lattice-gas model as a function of exposure. In Figure 1.22 the reaction probability data are reproduced, but with the exposure axis converted to coverage by use of Eq. (1.77). An improvement with respect to the "two-state" model is immediately noticeable for P_2 shown in Figure 1.21 (c). The large value of S_2' compared to S_2 obtained from the fitting procedure suggests that two-atom adsorption preferentially occurs within a single Si site rather than involving reactive Si bonds on two distinct sites. With the near elimination of the S_2 term, the functional form of the expression used to fit the two-atom adsorption probability is linear with respect to Θ. This linear behavior is characteristic of the kinetics of chemisorption reactions requiring a single surface site for adsorption[49]. A similar linear dependence of the sticking coefficient with surface coverage has been observed[50] for F_2 as well as for other halogens[51] (Cl_2, Br_2 and I_2) adsorbing on Si(100) 2x1 surfaces.

---

[49] Weinberg, W. H., In *Kinetics of Interface Reactions* Springer Series in Surface Science Vol. 8; Grunze, M., Kreuzer, H. J., Eds.; Springer: Berlin, p. 94, (1987)

[50] E. R. Behringer, H. C. Flaum, D. J. Sullivan, D. P. Masson, E. J. Lanzendorf, and A. C. Kummel, J. Phys. Chem. **99**, 12863 (1995)

[51] H. C. Flaum, D. J. Sullivan, A. C. Kummel, J. Phys. Chem. **98**, 1719 (1994)

In the case of the single-atom abstraction probability, the low value of $S_i'^{on}$ resulting from the fit makes the last term in Eq. (1.73) nearly vanish. The functional form of the P_1 curve being fitted is then nearly identical to that used in the simple lattice-gas model. However, agreement between the calculated values of P_1 and the data is significantly better than that obtained with the simple lattice-gas model since the modification of the P_2 expression affects the evolution of Θ_2 as a function of exposure, which in turn affects the fit of the single-atom abstraction probability. The improved agreement between the calculated and measured values of P_0 simply reflects the good agreement between the model and the data for P_1 and P_2 because the expression for P_0 is obtained from the mass-balance condition expressed in Eq. (1.74).

The assumption that two-atom abstraction preferentially occurs within a single surface site is an extension of the idea proposed by Yang, in which P_2 is enhanced by attractive interactions with neighboring reactive Si atoms, and not simply governed by the statistical occupancy of the nearest-neighbor sites. The three-state model allows for two-atom adsorption to occur at a single site, since each site can accommodate two F atoms. No specific assumption is made, however, as to which two Si atoms are paired so as to comprise the site. In principle, the two Si atoms could be part of the same dimer pair, they could belong to Si dimers on opposing rows, or even belong to adjacent dimers within the same row. However, the linear dependence of P_2 with coverage requires that a single configuration of Si atom pairs be defined. The pairing of the Si atoms may not simply be determined from geometric considerations, but may also depend on the relative reactivity of the nearest-neighbor Si atoms surrounding the initial adsorption site. The question remains of which of the neighboring Si atoms is more likely to attract the reacting F_2, and hence which pairing of Si atoms comprises a site.

To answer this question, consider first the nature of the attractive interaction. The attraction can take place early on in the reaction process, whereby the incident molecule

is aligned such that the ejected F atom is preferentially directed towards the most reactive of the neighboring Si atoms. On the other hand, the attraction might occur late in the reaction, with the randomly ejected F atom being preferentially steered towards the most reactive Si site where it can adsorb. In either case, the driving force is the chemical affinity of a particular Si dangling bond adjacent to the initial abstraction site towards the incident F_2 or the ejected F. The most likely Si atom to attract the F or F_2 is the Si atom within the dimer pair where the initial adsorption takes place. The enhanced reactivity of the unoccupied Si completing a *half-filled* site can be understood in terms of the stability of the dimer. An unfluorinated Si dimer is stabilized by the delocalized nature of the dangling bonds. The electron density of the Si dangling bonds mixes and gives rise to a π-bonding interaction. The stabilizing influence of the π-bonding is lost upon fluorination of one the Si atoms when the electron density it contributed to the π-bond is now shared with the adsorbed F atom. The unfluorinated Si atom then possesses a higher electron density than any of the Si atoms in *empty* sites surrounding it. The enhanced electron density, combined with its proximity to the initial abstraction site makes the second Si atom within the dimer pair the most likely candidate to align the F_2 molecule before it dissociates completely, or to attract the ejected F atom once it is released.

Evidence for preferential pairing at a dimer site has been reported[52,53,54] for the chemisorption of H atoms on a Si(100) surface. Infrared multiple-internal-reflection spectra by Chabal[53], and scanning tunneling microscopy measurements by Boland[54] on the Si(100)/H system confirm that when H atoms chemisorb on the dimerized Si(100) surface, they tend to doubly-occupy a dimer site rather than singly-occupying two different ones. D'Evelyn[52] suggests that the driving force behind the pairing of H atoms

[52] M. P. D'Evelyn, Y. L. Yang, and L. F. Sutcu, J. Chem. Phys. **96**, 852 (1991)
[53] Y. J. Chabal, Surf. Sci. **232**, 594 (1986)
[54] J. J. Boland, Phys. Rev. Lett. **67**, 1539 (1991)

to completely fill a dimer site is the π-bond stabilization of the unoccupied Si—Si dimers. If a hydrogen atom binds on an empty site, it causes the loss of the π-bonding stabilization, whereas if it binds on a half-filled site, the energetic penalty is avoided. D'Evelyn has estimated the pairing energy to be of the order of 5-10 kcal mol^{-1} by fitting a simple lattice gas model to the temperature programmed desorption results of Wise et al.[55,56] and Sinniah et al.[57], while a scanning tunneling spectroscopy study by Boland[54] estimates the π-bond stabilization at 18 kcal mol^{-1}. These observations on the Si/H adsorption process should be relevant for the Si/F system, although the destabilization of the system due to the loss of the π-bond may not be as significant in the case of F_2/Si due to the higher electron affinity of the adsorbed F.

Care must be taken in interpreting the physical implications of the proposed lattice-gas models since no direct correlation exists between the proposed mathematical expressions and a detailed mechanistic picture of the reaction. The relative success of the three-state lattice-gas model in reproducing the measured chemisorption probabilities does, however, lend credibility to the proposed idea that the intricate details of the silicon fluorination reaction are governed by attractive interactions between surface sites and the incident F_2 molecule or the ejected F atom. The three-state modification to the lattice-gas model, which is based on distinguishing the reactivity of the Si atom paired to the initial abstraction site, is already a step in the right direction towards a more detailed understanding of the two-atom adsorption and single-atom abstraction mechanisms.

The following section expands on the concept that the chemical affinity towards fluorine of the various kinds of sites on the surface may ultimately determine the detailed

---

[55] M. L. Wise, B. G. Koehler, P. Gupta, P. A. Coon, and S. M. George, Matt. Res. Soc. Symp. Proc. **204**, 319 (1991)

[56] , B. G. Koehler, and S. M. George, Surf. Sci. **248**, 158 (1991)

[57] K. Sinniah, M. G. Sherman, L. B. Lewis, W. H. Weinberg, J. T. Yates Jr., and K. C. Janda, J. Chem. Phys. **92**, 5700 (1990)

mechanism by which fluorine adsorption takes place. Towards this end, an extension of the three-state lattice-gas model is proposed, in which the reactivity of all distinct surface sites is parametrized with the hope of elucidating which interactions affect the fluorination mechanisms.

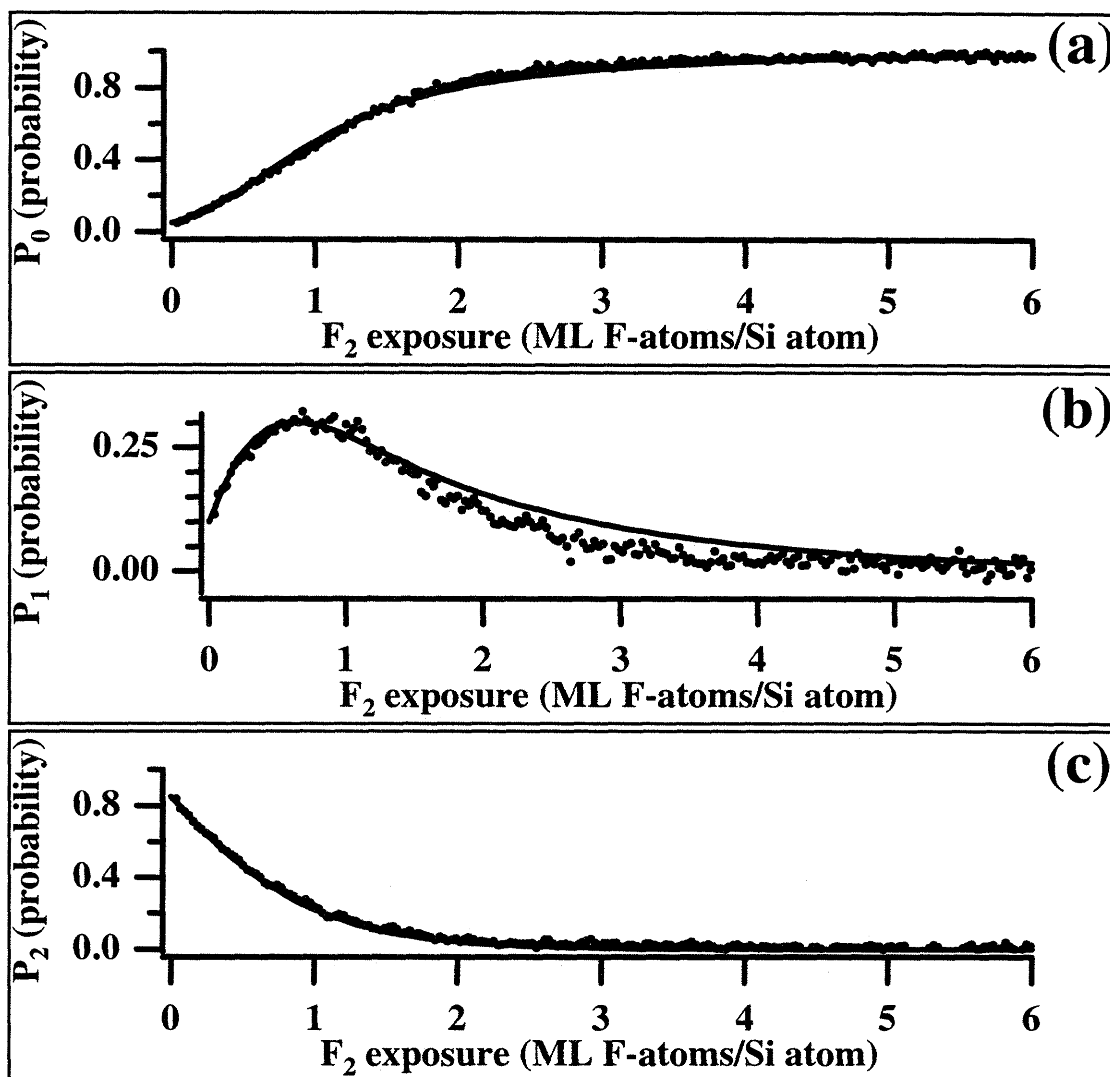

Figure 1.21 Reaction Probabilities Predicted by Three-state Model

Comparison of three-state lattice-gas model (solid lines) and measured reaction probabilities. (a) unreactive scattering, P_0, (b) single-atom abstraction, P_1, and (c) two-atom adsorption, P_2, probabilities as a function of F_2 exposure. Experimental curves have been described in Figure 1.12.

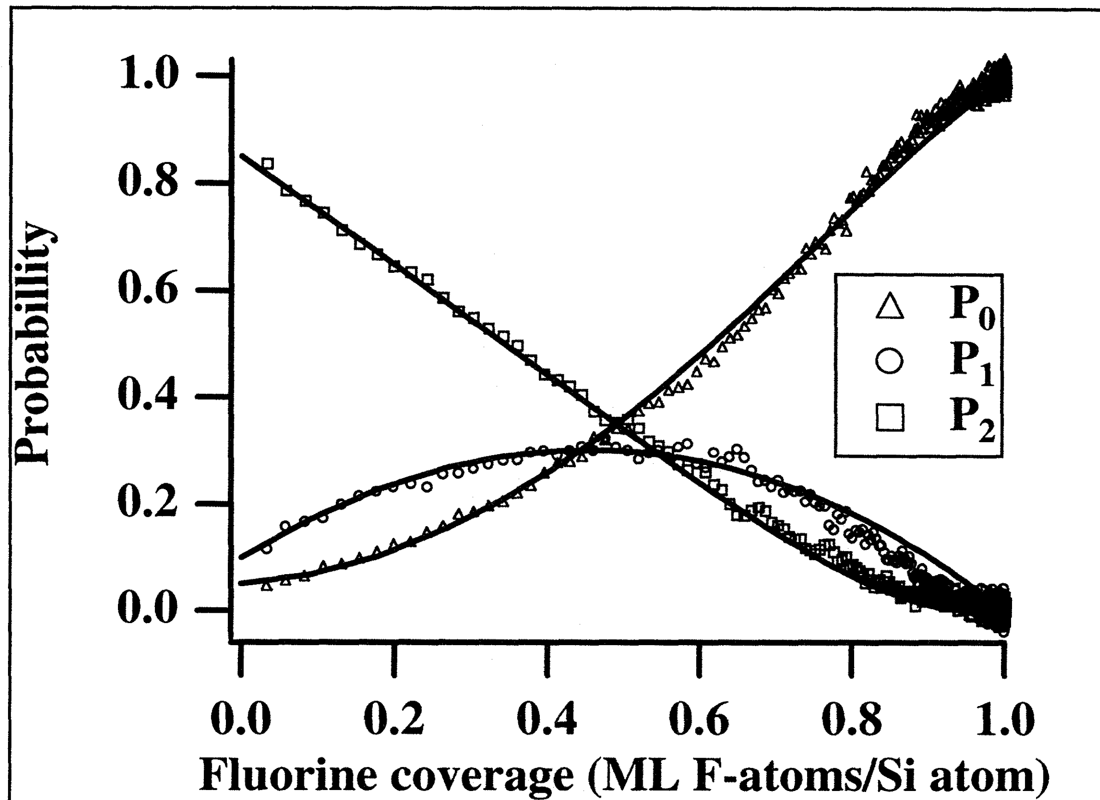

Figure 1.22 Three-state Model Probabilities as a Function of Coverage

Comparison of three-state lattice-gas model (solid lines) and measured reaction probabilities as a function of surface fluorine coverage. Experimental curves have been described in Figure 1.12.

1.5.3.3 Extended Three-state Lattice-gas Model

The extended three-state lattice-gas model preserves all of the assumptions of the previously discussed three-state model, but distinguishes the occupancy "state" of all sites onto which a fluorine atom can be adsorbed. The collection of scaling factors parametrizing the probability of all possible adsorption events is given below:

$S_2^{0,0}$ ≡ two-atom adsorption involving two *empty* sites

$S_2^{0,1/2}$ ≡ two-atom adsorption with initial adsorption occurring on *half-filled* site

$S_2^{1/2,0}$ ≡ two-atom adsorption with initial adsorption occurring on *empty* site

$S_2^{1/2,1/2}$ ≡ two-atom adsorption involving two *half-filled* sites

$S_1^{ni,0}$ ≡ neighbor-independent single-atom abstraction on *empty* site

$S_1^{ni,1/2}$ ≡ neighbor-independent single-atom abstraction on *half-filled* site

$S_1^{on,1,0}$ ≡ occupied neighbor single-atom abstraction on an *empty* site with the ejected F atom blocked by a *filled* site.

$S_1^{on,1,1/2}$ ≡ occupied neighbor single-atom abstraction on *half-filled* site with ejected F atom blocked by a *filled* site.

$S_1^{on,1/2,0}$ ≡ occupied neighbor single-atom abstraction on *empty* site with ejected F atom blocked by a *half-filled* site.

$S_1^{on,1/2,1/2}$ ≡ occupied neighbor single-atom abstraction on *half-filled* site with ejected F atom blocked by a *half-filled* site.

where the subscripts denote the number of F atoms being adsorbed on the surface, the "*on*" and "*in*" superscripts distinguish between neighbor-independent and occupied neighbor abstraction, while the numerical superscripts read from right to left specify the occupancy of the adsorption site of the abstracted and complementary F atoms respectively.

By using the above scaling factors, the relative reactivity of each kind of site is independently considered. For example, a distinction is made as to whether the initial abstraction event occurs on an *empty* or *half-filled* site (indicated by a 0 or ½ in the second numerical superscript). The reactivity of a Si dangling bond in an *empty* site is

expected to be different from that of a dangling bond in a *half-filled* site due to the presence of the weak π-bond in an empty site. Additionally, in the event of two-atom adsorption, a distinction is made as to where the second F atom binds. The reactivity of the ejected F atom with a Si dangling bond is expected to depend on whether the second dangling bond is in an *empty* or *half-filled* site (indicated by the first numerical superscript). In the case of single atom abstraction, not only is the occupancy state of the abstraction site considered, but the state of the fluorinated site blocking the adsorption of the second F atom is also taken into account. Distinguishing the occupancy of the fluorinated site which contributes to the occupied neighbor abstraction process addresses the possibility of a difference in the repulsive interaction between the ejected F atom and a blocking F on a *filled* or *half-filled* site.

The reaction probabilities are obtained by adding all the scaling factors with a common subscript and recalling that Θ_1 gives the F atom coverage associated with *half-filled* sites, Θ_2 the F atom coverage associated with *filled* sites and the quantity 1-$(2\Theta_1+\Theta_2)$ amounts to the fraction of totally *empty* sites.

$$\begin{aligned} P_2 = {} & \left[S_2^{0,0}\left(1-\left(2\Theta_1+\Theta_2\right)\right)+\left(S_2^{\frac{1}{2},0}+S_2^{0,\frac{1}{2}}\right)\left(\Theta_1\right)\right]\left(1-\left(2\Theta_1+\Theta_2\right)\right) \\ & + S_2^{\frac{1}{2},\frac{1}{2}}\left(\Theta_1\right)^2 \end{aligned} \tag{1.78}$$

$$\begin{aligned} P_1 = {} & \left[S_1^{ni,0}+S_1^{occ,1,0}\left(\Theta_2\right)+S_1^{occ,\frac{1}{2},0}\left(\Theta_2\right)\right]\left(1-\left(2\Theta_1+\Theta_2\right)\right) \\ & + \left[S_1^{ni,\frac{1}{2}}+S_1^{occ,1,\frac{1}{2}}\left(\Theta_2\right)+S_1^{occ,\frac{1}{2},\frac{1}{2}}\left(\Theta_1\right)\right]\left(\Theta_1\right) \end{aligned} \tag{1.79}$$

The differential equations relating the coverages to the incident F_2 exposure are determined from the contributions of the adsorption events to Θ_1 and Θ_2. Single-atom abstraction contributes one F atom to Θ_1 if it occurs on a *empty* site while it decreases Θ_1 by one F atom if it takes place at a *half-filled* site. Similarly, two-atom adsorption increases Θ_1 by two F atoms when it involves two distinct *empty* sites whereas it decreases Θ_1 by two F atoms if it occurs on two *half-filled* sites. Finally, if two-atom

adsorption happens to involve one *empty* and one *half-filled* site there is no net contribution to the half-filled coverage. Thus the rate equation governing the change in the coverage of *half-filed* sites is

$$\frac{d\Theta_1}{d\varepsilon} = I_{F_2}\left[S_1^{ni,0} + S_1^{occ,1,0}\Theta_2 + S_1^{occ,\frac{1}{2},0}\Theta_2 + 2S_2^{0,0}(1-(2\Theta_1+\Theta_2))\right](1-(2\Theta_1+\Theta_2)) - \left[S_1^{ni,\frac{1}{2}} + S_1^{occ,1,\frac{1}{2}}\Theta_2 + S_1^{occ,\frac{1}{2},\frac{1}{2}}\Theta_1 + 2S_2^{\frac{1}{2},\frac{1}{2}}\Theta_1\right]\Theta_1 \quad (1.80)$$

There are four types of adsorption events which contribute to increase the coverage of *filled* sites, Θ_2. Single-atom abstraction on a *half-filled* site increases Θ_2 by two F atoms. Two-atom adsorption increases Θ_2 by four F atoms if it involves two distinct *half-filled* sites while it contributes two F atoms if it occurs in one *empty* and one *half-filled* site. The coverage of *filled* sites is also increased by two F atoms if the two-atom adsorption occurs within a single *empty* site. The rate equation for Θ_2 is then

$$\frac{d\Theta_2}{d\varepsilon} = 2I_{F_2}\left[S_1^{ni,\frac{1}{2}} + S_1^{occ,1,\frac{1}{2}}\Theta_2 + \left(S_1^{occ,\frac{1}{2},\frac{1}{2}} + 2S_2^{\frac{1}{2},\frac{1}{2}}\right)\Theta_1 + \left(S_2^{0,\frac{1}{2}} + S_2^{\frac{1}{2},0}\right)(1-(2\Theta_1+\Theta_2))\right]\Theta_1 \quad (1.81)$$

Of the ten scaling factors required to describe the reaction probabilities, two can be extracted from the data. At zero exposure, the expression for P_1 reduces to $S_1^{ni,0}$ while the expression for $P_2(\Theta=0)$ yields $S_2^{0,0}$. The other eight scaling factors must be used as parameters for fitting the above probability expressions to the measured data.

Figure 1.23 shows a comparison between the measured adsorption probabilities expressed as a function of fluorine coverage and the results obtained from the extended three-state model discussed in this section. The modeled curves are obtained by <u>manually</u> varying the eight fitting parameters while trying to minimize the sum of the square of the differences between each measured probability and its modeled counterpart. The values of all ten parameters obtained from the manual fit of the probabilities in Figure 1.23 are as follows: $S_1^{ni,0}$=0.10, $S_2^{0,0}$=0.85, $S_2^{0,\frac{1}{2}}=0.88$, $S_2^{\frac{1}{2},0}=2.6$, $S_2^{\frac{1}{2},\frac{1}{2}}=4$,

$S_1^{ni,½} = 0.078$, $S_1^{on,1,0} = 0.28$, $S_1^{on,1,½} = 1.8$, $S_1^{on,½,0} = 0.275$, $S_1^{on,½,½} = -2$. The match between the measured probabilities and those obtained from the above parameters is not as good as that obtained for the simpler three-state model because no iterative least-squares fitting algorithm was implemented to ensure that a global minimum is reached. Since no guarantee is made that the parameters given above represent a global minimum for the least-squares fit, no final conclusion can be reached about the relative importance of the interactions of the incident F_2 molecule with the different sites available on the surface. The added flexibility given to the functional forms by indiscriminately including all possible interactions makes the fitting process significantly more complex. Given the limited amount of data and the complexity of the fitting procedure, a more rigorous attempt at extracting the global fit parameters was not pursued. The extended three-state model, including the extra fitting parameters, is likely a better representation of the physical nature of the interaction of F_2 and the Si surface than is the restricted view that only the Si dangling bond within the initial abstraction site affects the adsorption process.

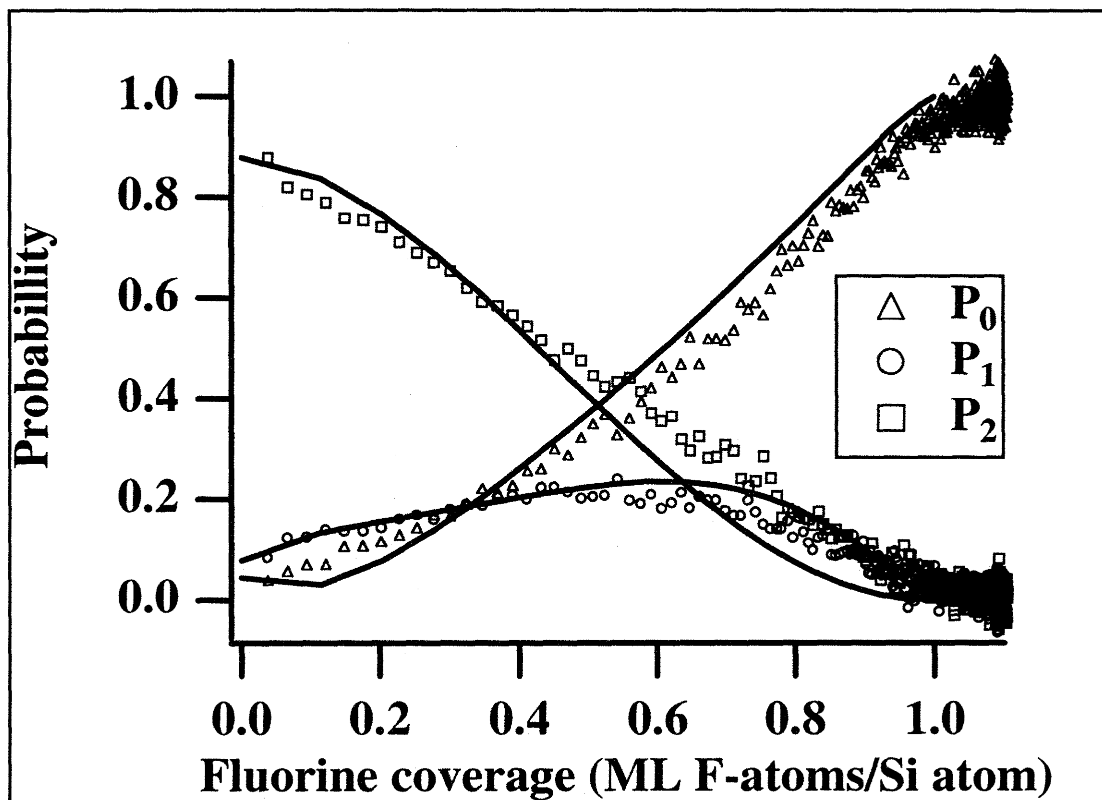

Figure 1.23 Extended Three-state Model Probabilities as a Function of Coverage

Comparison of extended three-state lattice-gas model and reaction probabilities as a function of fluorine coverage.

1.6 CONCLUSIONS

The interaction of thermal energy F_2 with a Si(100) surface at 250 K leads to the formation of a monolayer of fluorine on the surface. The F atoms are adsorbed on the dangling bonds of the silicon dimer pairs thus preserving the 2x1 periodicity of the reconstructed Si surface. No more than one monolayer of F_2 is adsorbed, indicating that the low energy F_2 is incapable of attacking the dimer or subsurface Si—Si bonds. The adsorption process is initiated by an abstraction event in which one of the F atoms from an incident F_2 molecule is abstracted by a Si dangling bond where it subsequently adsorbs. If the other half of the Si dimer pair is unfluorinated then the complementary F atom is preferentially attracted towards it and thus both F atoms from an incident F_2 molecule may sequentially adsorb onto a single dimer. There are however, two processes which may prevent the adsorption of the second F atom. First, a perpendicular orientation of the incident F_2 bond axis to the surface may prevent the second F atom from being attracted to a reactive site and hence prevent its adsorption. Second, fluorinated Si atoms surrounding the original abstraction site may block the adsorption of the complementary F atom. In either case, the result is the ejection of a reactive F atom into the gas phase. The velocity of the ejected F atoms is considerably larger than the incident velocity of the F_2 and independent of surface temperature. This observation is consistent with the F atoms acquiring translational energy from the exothermicity liberated by the F atom adsorption. The translational excitation of the ejected F accounts for only 3% of the available exothermicity indicating that a large fraction of the energy liberated by the reaction is dissipated into the Si lattice.

2 CHAPTER II. THE INTERACTION OF Si(100) WITH XeF_2

2.1 INTRODUCTION

2.1.1 An Overview of Previous Experimental Work

In 1979, a seminal paper by Winters and Coburn[58] first proposed the use of XeF_2 as a source of fluorine for etching Si surfaces. They established that room temperature Si is isotropically etched by exposure to XeF_2(gas) without the need to ignite a plasma. Etch rates as large as 7000 Å min^{-1} are attained with XeF_2 pressures of $1.4x10^{-2}$ Torr. In addition, they observed that XeF_2 is unable to etch SiO_2, Si_3N_4 and SiC, demonstrating a high selectivity between Si and its compounds. The enhanced etch rate of XeF_2 over conventional fluorine-containing compounds used in plasma etching, such as CF_4, is proposed to be due, in part, to the inert nature of Xe. Although Si etching readily occurs when CF_4 is activated in a plasma to produce reactive species such CF_3 and F radicals, significant amounts of carbon residue are adsorbed onto the surface. In some cases residue removal is found to be a limiting step in the rate of the etching reaction. The inert nature of Xe guarantees that it will not adsorb to the Si surface, and thus will not produce any residue. The lack of residue formation is also attributed to the large etch rates attainable with F atoms. The conclusion is then reached that the etching produced by fluorine atoms can be simulated by using a flux of XeF_2 as a source of fluorine, thus eliminating the complications of producing F atoms.

Winters and Coburn's proposed use of XeF_2 as a fluorine source sparked numerous investigations into the etching of Si and its compounds. A comprehensive review of the surface science aspects of etching reactions, covering in detail the interactions of F, F_2 and XeF_2 with Si has been compiled by Winters[59]. A brief summary of the experimental results most relevant to this investigation are presented in this section in order to place

[58] H. F. Winters, and J. W. Coburn, Appl. Phys. Lett. **34**, 70 (1979)
[59] H. F. Winters, and J. W. Coburn, Surf. Sci. Rep. **14**, 165 (1992)

the current research in the context of the large body of previous knowledge. Following Winters' organization, the next three sections present an overview of the most relevant experiments organized into three distinct categories: 1) Measurements of the Si etch rates. 2) Identification of the gas-phase etch products. 3) Composition and growth of the fluorinated surface layer.

2.1.1.1 Measurements of the Si Etch Rates

Of the numerous studies measuring Si etch rates, the most relevant to the current investigation are those that allow a direct comparison of the etch rates obtained by exposing a Si surface to equivalent fluxes of the three commonly used reactants, F_2, XeF_2 and F atoms. The etch rate using XeF_2 was determined by Winters[58] to be of the order of 7000 Å min^{-1} for polycrystalline Si. An early study by Flamm et al.[60], combining chemiluminescence and etch depth measurements, determined F atom etch rates in the range of 1000-4000 Å min^{-1} and F_2 etch rates of less than 3 Å min^{-1}. Subsequent experiments[61] which directly compared the XeF_2 and F etch rates under equivalent flux conditions confirmed that the XeF_2 etch rate is approximately one order of magnitude larger that that observed for F atoms. This latter study, however, points out clear differences in the exposure and temperature dependence of the F and XeF_2 etch rates, and warns against adopting Winter's suggestion that XeF_2 can be used to simulate etching by F atoms.

The above etch rate measurements imply that the relative reactivities of the three reactants are $XeF_2 > F >> F_2$. Note that the observed reactivities are not in agreement with thermodynamic predictions. The relative thermodynamic stability of the three reactants would place the F atom reactivity well above that of XeF_2, and the reactivity of XeF_2 slightly below that of F_2. The discrepancy between the expected and observed

---

[60] D. L. Flamm, V. M. Donnelly, and J. A. Mucha, J. Appl. Phys. **52**, 3633 (1981)

[61] D. E. Ibbotson, D. L. Flamm, J. A. Mucha, and V. M. Donnelly, Appl. Phys. Lett. **44**, 1129 (1984)

reactivities of F_2 and XeF_2 is one of the main motivating factors for undertaking the current investigation of the interactions of F_2 and XeF_2 with Si(100). The current investigation is part of an ongoing research project whose long term goal is the determination of the microscopic origin of the observed reactivity differences.

2.1.1.2 Identification of the Gas-phase Etch Products

The identification of the gas-phase products is important for the understanding of the etching reaction. Unanimous agreement exists in the literature confirming the volatile, closed-shell SiF_4 molecule as the dominant product from the etching of Si by either F atoms or XeF_2. Identification of SiF_4 comes from several mass spectrometric studies[62,63,64,65,66] in which SiF_3^+ signal is observed during Si etching. The SiF_4 etch product is detected as SiF_3^+, rather than SiF_4^+ since SiF_4 is known to preferentially ionize by cracking into SiF_3^+. Small quantities of other gaseous products have also been observed to desorb. In particular, several groups[63,64,67] report the presence of SiF_2^+ signal and attribute it to SiF_2 etch product. Later investigations by Houle[68,69], however, clearly demonstrate that the SiF_2^+ signal is indeed caused by the dissociative ionization (cracking) of two higher fluorosilanes, Si_2F_6 and Si_3F_8 found to be minor products of the etching reaction. Dagata et al.[70] confirmed by multiphoton ionization mass spectrometry that SiF_2 is a significant etch product only at surface temperatures above 600 K. Thus SiF_4, and to a much lesser extent Si_2F_6 and Si_3F_8, are believed to be the only significant etch

[62] H. F. Winters, and I. C. Plumb, J. Vac. Sci. Technol. B **9**, 197 (1991)
[63] H. F. Winters, and F. A. Houle, J. Appl. Phys. **54** 1218 (1983)
[64] M. J. Vasile, and F. A. Stevie, J. Appl. Phys. **53** 3799 (1982)
[65] J. R. Engstrom, N. M. Nelson, and T. Engel. Surf. Sci. **215**, 437 (1989)
[66] Y. Y. Tu, T. J. Chuang, and H. F. Winters, Phys. Rev. B **23**, 823 (1981)
[67] M. J. Vasile, J. Appl. Phys. **54**, 6697 (1983)
[68] F. A. Houle, J. Appl. Phys. **60**, 3018 (1986)
[69] F. A. Houle, Phys. Rev. B **39**, 10120 (1989)
[70] J. A. Dagata, D. W. Squire, C. S. Dulcey, D. S. Y. Hsu, and M. C. Lin, J. Vac. Sci. Technol. B **5**, 1495 (1987)

products at lower surface temperatures.

An additional question is raised as to whether the observed SiF_3^+ signal arises exclusively from SiF_4 desorption, or whether some of it might be due to SiF_3 radicals released from the surface. Winters and Coburn[62,71,72] address this issue for both F and XeF_2 etching. Based on a comparison of the SiF_4^+/SiF_3^+ signal ratio in the modulated etch product waveform to the signal ratio for SiF_4 gas under the same experimental conditions, they conclude that at most 10% of the SiF_3^+ signal can be attributed to SiF_3 radicals.

However, a recent study by Giapis[73] suggests that SiF_3 radical is a major product in the etching of Si(100) by hyperthermal F atoms (E_{Trans}=4.8 eV). In this study, a time-of-flight distribution of the SiF_3^+ signal reveals a thermal component consistent with the expected desorbed SiF_4 product, plus an unexpected faster feature assigned to hyperthermal SiF_3 radicals. According to Giapis, the translational excitation of the SiF_3 product can arise from either collision induced desorption or direct (Eley-Rideal) reaction between a SiF_3 moiety on the surface and an incident F atom. A proposed empirical model[74] of the atom-surface interaction consistent with collision induced desorption as the dominant non-thermal mechanism is thought to be in agreement with the observed fast etch product. The high velocity of the desorbed SiF_3 radicals might contribute to their low detection efficiency, and thus explain why the amount of SiF_3 product was underestimated by Winters and Coburn.

2.1.1.3 Composition and Growth of the Fluorinated Surface Layer

The desorption of highly fluorinated etch products such as SiF_4, SiF_3, Si_2F_6 and Si_3F_8 is dependent upon their prior assembly at the surface layer. Precursors to these volatile

---

[71] H. F. Winters, and D. Haarer, Phys. Rev. B 36, 6613 (1987)

[72] H. F. Winters, and D. Haarer, Phys. Rev. B 37, 10379 (1988)

[73] K. P. Giapis, and T. A. Moore, J. Vac. Sci. Technol. A **13**, 959 (1995)

[74] G. S. Hwang, C. M. Anderson, M. J. Gordon, T. A. Moore, T. K. Minton, and K. P. Giapis, Phys. Rev. Lett. **77**, 3049 (1996)

species must form on the Si surface before they are released into the gas phase by either thermal excitations caused by the surface motion, or by interactions with the incident reactant flux. An understanding of the composition and growth of the fluorinated surface layer is of paramount importance to the understanding of the etching reaction.

Identification of the species forming the fluorinated surface layer has been accomplished by several groups through the use of x-ray photoelectron spectroscopy (XPS). Surface species are identified by shifts in the intensity of the high-binding-energy side of the photoelectron emission from the Si(2p) level. The shift in intensity is caused by the presence of electron withdrawing F atoms bonded to the Si. The magnitude of the shift depends on the extent of the electron transfer, and hence it is sensitive to the number of fluorine atoms bound to the emitting Si. A distinct XPS signature is associated with each SiF_x species on the surface, where x can range between 0 and 4.

McFeeley et al. conducted a high-resolution soft x-ray photoemission spectroscopy study of the composition of the fluorinated surface layer during the exposure of Si to XeF_2. A low XeF_2 fluence study[75] (~50 L total exposure) allows the investigation of the initial stages of fluorination. For the Si(100) 2x1 surface, the XPS spectrum indicates the dominant species to be SiF, with only minor amounts of SiF_2 and SiF_3 present. Their observations are consistent with fluorine adsorption primarily occurring at the reactive Si dangling bond sites to form SiF, with minor SiF_2 and SiF_3 moieties associated with defect sites. The fluorine adlayer after short XeF_2 exposures is thought to be confined to the top-most Si layer. Similar XPS data was obtained by Engel[65] for the case of a Si surface exposed to a supersonic F_2 beam. During the initial stages of fluorination, the composition of the surface species is the same regardless of whether F_2 or XeF_2 is used as source of fluorine.

---

[75] F. R. McFeeley, J. F. Morar, N. D. Shinn, J. D. Landgren, and F. J. Himpsel, Phys. Rev. B **30**, 764 (1984)

Whereas further exposures to F_2 lead to the saturation of the fluorine coverage at 1 ML (see Section 1.4.3), with the formation of SiF at each Si dangling bond and no further reaction of F_2 with the surface, further exposure of a fluorinated Si surface to XeF_2 causes a thickening of the fluorinated layer and eventually leads to etching. A high XeF_2 fluence study (~10^6 L exposure) by McFeeley[76] shows the composition of the fluorinated layer during the steady-state etching process. A thick reaction layer composed of SiF, SiF_2, SiF_3 and SiF_4 is observed to extend approximately seven atomic layers into the bulk. Studies of the same system by Yarmoff[77] suggest that the SiF_3 is most abundant near the surface layer with the less fluorinated SiF and SiF_2 species dominating the Si—SiF_x interface. Furthermore, as the XeF_2 exposure is increased, the concentration of SiF_3 at the surface is observed to increase, burying a constant amount of SiF and SiF_2 near the Si substrate. The etch rate is likely related to the number of SiF_3 species on the surface, and will hence increase with XeF_2, or even F atom exposure both of which have been shown[65] to produce a thickening of the reaction layer and to lead to steady-state etching. A comparison of XPS and temperature programmed desorption (TPD) data by Winters[59] concludes that the fluorosylil layer produced by XeF_2 is thicker than that produced by F atoms. In fact, a thick layer formed by exposure to XeF_2 is observed to decrease in thickness when it is subsequently exposed to F-atoms.

From these studies, it is clear that the ability of a given reactant to etch the Si surface is directly related to its ability to fluorinate the surface beyond the top-most layer. The relatively unreactive F_2 is unable to fluorinate the surface beyond the 1 ML coverage, and thus is unable to promote the formation of etch product. On the contrary, both F and XeF_2 are able to form a thick fluorinated layer and to promote the desorption of volatile fluorosilanes and even of radical species such as SiF_3. The ability to fluorinate beyond

[76] F. R. McFeeley, J. F. Morar and F. J. Himpsel, Surf. Sci. **165**, 277 (1986)

[77] J. A. Yarmoff, S. A. Joyce, C. W. Lo and J. Song, in: Desorption Induced by Electronic Transitions DIET-IV, Ed. G. Betz and P. Varga (Springer-Verlag, Berlin 1990) p.65

the first monolayer provides the ability to produce the precursors to the volatile etch products. Etching, however, requires that the precursors be actively desorbed from the surface, creating new sites for the reaction to proceed. The difference in etch rates observed between F_2, F atoms and XeF_2 must also then be related to their ability to promote the desorption of the products from the surface.

No explanations exist in the literature for the observed ability of XeF_2 to fluorinate a Si surface beyond the most reactive dangling bonds, and to actively induce the desorption of the fluorinated layer. While this is the main goal of an ongoing research project, the current investigation focuses on one of the aspects that might influence the enhanced reactivity observed for XeF_2. The possibility that the recently discovered fluorine atom abstraction mechanism exists in the interaction of XeF_2 with Si(100) is investigated, with the hope that the existence of atom abstraction might contribute to the understanding of the unusually high reactivity of XeF_2.

2.1.2 Atom Abstraction in the Interaction of XeF_2 with Si(100)

The investigation of the interaction of F_2 with Si(100) presented in Chapter I demonstrated the existence of the F atom abstraction mechanism. It has been shown that after a F atom from an incident F_2 molecule is abstracted by the Si surface, the complementary F atom can either scatter to the gas-phase, or find a reactive dangling bond on the surface onto which to adsorb. Since the fluorine coverage is never observed to increase above 1 ML, it can be deduced that the ejected F atom is <u>unable</u> to further attack the surface by either cleaving a Si—Si dimer bond or reacting with the second layer of Si atoms. It is somewhat surprising that a reactive free radical species such as F, ejected towards the surface with a substantial amount of translational energy attained from the exothermicity of the Si—F bond formation, is unable to react with the fluorinated surface. This observation suggests that there is more to the etching reaction than the encounter of a reactive radical species with the surface.

The observed reactivity trend (XeF_2>F>>F_2) must be re-examined in light of the realization that the reactant's thermodynamic stability is likely not the only factor affecting the etch rate. A hypothesis is set forth to explain the unusually high reactivity of XeF_2 in terms of its ability to excite the Si lattice by collisional energy transfer. The large mass of an incident XeF_2 molecule serves to vibrationally excite the lattice in the local environment where the gas-surface collision occurs. This localized lattice excitation, combined with the simultaneous presence of F atoms from the XeF_2 molecule, may enhance the fluorine adsorption probability. In fact, it is proposed that collisionally induced lattice excitations may make the Si dimer and subsurface bonds vulnerable to attack by fluorine, and hence allow the onset of surface disorder necessary for etching.

Under this hypothesis, the low reactivity of molecular F_2 is explained on the basis of its small mass. The F_2, or for that matter the F atom ejected during abstraction, does not possess the same momentum as the heavy XeF_2, and thus cannot effect the same energy transfer upon its collision with the surface. Therefore, molecular F_2 has a lower reactivity than XeF_2, despite the lower F_2 bond energy. Along the same line of reasoning, F atoms, despite their reactive nature, cannot vibrationally activate the fluorinated surface, and therefore also have a lower reactivity than XeF_2.

The importance of collisional energy transfer makes fluorine atom abstraction in the interaction of XeF_2 with Si(100) a potentially crucial reaction mechanism. If XeF_2 undergoes abstraction of one of its F atoms by the silicon surface, the resulting XeF fragment possesses both of the properties which favor the onset of etching. A XeF fragment propelled towards the fluorinated surface has both the large momentum required to induce the local vibrational excitation of the lattice, and the reactivity of a weakly bound F atom. The first step in assessing the validity of the proposed hypothesis is thus the corroboration of the atom abstraction mechanism in the interaction of XeF_2 with Si(100).

The reminder of this chapter presents an experimental investigation into the existence of atom abstraction in the interaction of XeF_2 with Si(100). The next section presents some background on the physical properties of XeF_2 and its use in effusive molecular beams. Section 2.2 presents a description of the experimental challenges encountered in the preparation of supersonic molecular beams of XeF_2, and in the detection of the scattered reaction products. Section 2.3 concentrates on the experimental results leading to the confirmation of the abstraction mechanism by the identification of the ejected XeF fragments. Although the data presented give compelling evidence of the abstraction mechanism, many of the results are still preliminary, and do not yet provide a complete picture of the overall reaction. A brief discussion of the data leading to the identification of the abstraction mechanism is presented in Section 2.4. No attempt is made in this investigation at validating the hypothesis that collisional energy transfer plays a role in the unusually high reactivity of XeF_2.

2.1.3 Background on XeF_2

2.1.3.1 The Discovery of XeF_2 and Noble Gas Compounds

The discovery of argon in 1894 by Rayleigh and Ramsey was received with great skepticism, especially amongst those who thought the new element could not be reconciled within the existing chemical groups of the periodic table. Four years later (1898), Ramsey and Travers characterized, by spectroscopic analysis of the low-temperature distillate of liquid air, three new elements: Krypton (from the Greek κρυπτον, hidden, concealed), Neon (Greek νεον, new) and Xenon (Greek ξενον, strange). The discovery of the four noble gases forced a new group to be established in Mendeléev's periodic table. The new group did not just merely fit into the table, but actually enhanced it by bridging the gap between the strongly electronegative halogens

and the electropositive alkali metals[78]. The inert nature of the new elements gave them a prominent role in the new atomic model proposed by Bohr (1913), and the new valence theories developed by Lewis and Kossel (1916). The inviolability of the octet rule became a pivotal concept in the understanding of the chemical behavior of the elements and contributed to an unquestioning confidence in the chemical inertness of the noble gases.

From early on, however, chemists stubbornly attempted to force the "perfect gases" into chemical combination. The first such attempt was instigated in 1895 by Ramsey, the co-discoverer of argon, and his friend Mossian, who had previously discovered fluorine. Ramsey and Mossian were, however, unable to prepare an argon fluoride by combining Ar and F_2 in the presence of an electrical spark. In 1933, based on considerations of ionic radii, Pauling suggested[79] that XeF_6 and KrF_6 should be preparable, prompting another unsuccessful synthesis attempt[80]. Additional unsuccessful attempts with the F_2/Ar and F_2/Kr systems were undertaken by Ruff and Menzel in 1937. A complicating factor in all attempts at chemical combination of these new inert elements was the low natural abundance of Kr and Xe. According to Bartlett[81], it is conceivable that if Xe had been as abundant as Ar, Mossian might have succeeded in preparing a xenon fluoride in the last years of the nineteenth century.

Instead, noble gas chemistry, and the violation of the sacred octet rule, had to wait for more than 60 years. In 1962 Bartlett[82] discovered that platinum hexafluoride was an oxidizing agent of unprecedented power, and used it to spontaneously oxidize Xe producing a quinquevalent platinum fluorine complex, which for the first time violated

[78] N.N. Greenwood, and A. Earnshaw, Chemistry of the Elements, Pergamon Press 1984, p.1044
[79] L. Pauling, J. Am. Chem. Soc. **55**, 1895 (1933)
[80] D. M. Yost, and M. L. Kaye, J. Am. Chem. Soc. **55**, 3890 (1933)
[81] N. N. Bartlett, and F. O. Sladky, Comprehensive Inorganic Chemistry, Pergamon Press 1973 Chapter 6
[82] N. Bartlett, Proc. Chem. Soc. 218 (1962)

xenon's octet rule. Shortly thereafter, reports of the discovery of other xenon fluorides[83,84] initiated a surge of activity in the noble gas combinatorial chemistry. More details and references regarding the discovery and preparation methods of XeF_2 and other noble gas compounds are discussed by Bartlett and Sladky[81].

2.1.3.2 Physical Properties of XeF_2

The years following the discovery of xenon difluoride yielded numerous experimental measurements of its physical properties. Table 2-1 contains a summary of some of the known physical properties of XeF_2 compiled by Bartlett and Sladky[81] from a variety of sources. For the purpose of this investigation, the most critical physical property of which knowledge is required is the vapor pressure. Knowledge of the vapor pressure is necessary in order to produce the gas mixtures used to generate supersonic XeF_2 molecular beams. The most reliable measurement of the vapor pressure of xenon difluoride was conducted by Chernick et al.[85] The vapor pressure as a function of temperature was measured by using a diaphragm manometer constructed of Monel, a non-corrosive metal alloy. The experimental relationship is:

$$\log P_{mm} = -\frac{3057.67}{T} - 1.23521 \log T + 13.969736 \qquad (2.1)$$

From the above expression, a vapor pressure of 4.5 Torr is expected, at 298 K, which is the temperature of the XeF_2 reservoir in the present experiment. A detailed explanation of the mixing procedure is given in Section 2.2.2.1.

2.1.3.3 Thermodynamic Properties of XeF_2

The enthalpy of formation of XeF_2 was determined from a calorimetric study[86] to be -28.2 kcal mole^{-1}, from which the total thermochemical bond energy is calculated to be

---

[83] H.H. Classen, H. Selig and J. G. Malm, J. Am. Chem. Soc. **84**, 3593 (1962)

[84] R. Hoppe, W. Dähne, H. Mattauch and K. M. Rödder, Angew. Chem. **74**, 903 (1962)

[85] F. Schreiner, G. N. McDonald, and Cedric L. Chernick, J. Phys. Chem. **72**, 1165 (1967)

[86] V. I. Pepekin, Y. A. Lebedev and A. Y. Apin, Zh. Fiz. Khim. **43**, 1564 (1969)

~64 kcal mol^{-1}. Johnston and Woolfolk have evidence from kinetic studies[87] of XeF_2 that the first bond dissociation energy is much greater than that for the second Xe-F bond. They initially proposed a value of 54 kcal mole^{-1} for the first bond dissociation energy with the remaining 10 kcal mole^{-1} for the second one. More recent spectroscopic work by Tellinghuisen[88] determined the Xe-F bond dissociation energy to be 3.045±0.03 kcal mol^{-1}, and the total XeF_2 bond dissociation energy to be 63.42±0.5 kcal mol^{-1}, which yields a value of 60.37±0.5 kcal mol^{-1} for the first bond dissociation energy.

Two important facts are then noted about the thermodynamics of XeF_2. (1) The thermodynamic bond energy of the first bond dissociation is comparable to that of the F-F bond in molecular fluorine. (2) The XeF radical formed after the first bond breaking step is chemically stable, but only bound by approximately 3 kcal mol^{-1}. These observations must be kept in mind when trying to explain the reactivity differences between F_2 and XeF_2 in the Si etching reaction.

[87] H. S. Johnston and R. Woolfolk, J. Chem. Phys. **41**, 269 (1964)
[88] Patricia C. Tellinghuisen and Joel Tellinghuisen, J. Chem. Phys. **68**, 5187 (1978)

Table 2-1 Some Physical Properties of XeF_2

Property	Value	Comments
Triple point	129.03°C	colorless crystals, liquid, vapor
ΔH_{sub}	13.2±0.2 kcal mol^{-1}	
Vapor pressure	4.5 Torr, 25°C	See Eq. (2.1)
S^0 (gas)	62.057 cal mol^{-1} deg^{-1}, 25°C	
	75.345 cal mol^{-1} deg^{-1}, 501°C	
S^0 (solid)	29.4 cal mol^{-1} deg^{-1}, 57°C	
$\Delta H_f^0, g$	-25.903 kcal mol^{-1} deg^{-1}, 25°C	
	-25.491 kcal mol^{-1} deg^{-1}, 501°C	
$\Delta G_f^0, g$	-17.858 kcal mol^{-1} deg^{-1}, 25°C	
	-5.22 kcal mol^{-1} deg^{-1}, 501°C	
ΔH_{atom}	64 kcal mol^{-1}	$XeF_{2(g)} \rightarrow Xe_{(g)} + 2F_{(g)}$
Mean bond energy	32 kcal mol^{-1}	
First bond energy	60.37±0.5 kcal mol^{-1}	Tellinghuisen[88]
Second bond energy	3.045±0.02 kcal mol^{-1}	Tellinghuisen[88]
Symmetry	$D_{\infty h}$	linear
Rotational constant	B_o = 0.11350 cm^{-1}	from IR spectrum
Xe-F bond length	1.9773±0.0015 Å	(from B_o)

2.1.3.4 Mass Spectrometry of XeF_2

Shortly after the discovery of XeF_2, Studier and Sloth[89,90] verified its existence by mass spectrometry. Ions produced by the electron bombardment of sample vapors were identified by their masses and the characteristic xenon isotopic abundance pattern. Since fluorine has a single isotope, the Xe isotopic ratios are expected to be preserved in the fluorides of xenon. For XeF_2, Studier and Sloth observed the characteristic Xe isotope pattern repeated at m/e values consistent with fragmentation into Xe^+, XeF^+, and XeF_2^+. As with other fluorides, the cracking pattern favored the removal of both fluorine atoms upon electron impact ionization. The group of Xe^+ isotopes appeared to have

[89] M. H. Studier and E. N. Sloth, in *Noble Gas Compounds*, edited by H. H. Hyman (University of Chicago, Chicago 1963), p. 47.
[90] E. N. Sloth and M. H. Studier, Science **141**, 528 (1963)

approximately double the intensity of that of the XeF^+ and XeF_2^+ signals, which appeared to be roughly equal.

In 1977, Falconer, Vasile and Stevie[91] remeasured the XeF_2 spectrum by using a modulated molecular beam to introduce the fluoride directly into a differentially pumped mass spectrometer system. Their results are generally in good agreement with those of Studier and Sloth but are slightly different. They measured a Xe^+:XeF^+:XeF_2^+ fragmentation ratio of 100:45:28 at 70 eV electron bombardment, which slightly differs from the fragmentation ratio given by Studier and Sloth. Exact agreement is not expected since the cracking ratio measured by a mass spectrometer depends on instrumental factors such as reactivity of the fluoride with chamber materials and the relative transmissivity of ions through the detection system. In addition, the contribution of Xe^+ can be easily overestimated due to the prevalent Xe background in the vacuum systems.

2.1.3.5 XeF_2 Effusive Beams

All previous experimental work involving the etching of silicon by XeF_2 has employed effusive sources of pure XeF_2 gas, where a temperature controlled reservoir containing solid XeF_2 is coupled to a vacuum chamber by means of a metal tube. In some cases, the effusive beam simply backfills a reaction chamber, while in other cases attempts are made at preferentially directing the XeF_2 flux towards the silicon substrate by reducing the distance between the dosing tube and the surface. Several disadvantages arise from the use of effusive beam methods: (1) the lack of directional control of the impinging reactants, (2) the broad (thermal) distribution of reactant energies (3) the low beam-to-background flux ratio (4) undesired chemical reactivity between the chamber walls and the excess background XeF_2 (5) relatively high fluxes which make difficult the study of the initial fluorination stages.

---

[91] W. E. Falconer, M. J. Vasile, and F. A. Stevie, J. Chem. Phys. **66**, 5335 (1977)

Vugts et[92] al. have introduced a modification to the effusive beam method which increases the beam-to-background flux ratio and improves the dynamic range of the attainable XeF_2 flux. Their gas source incorporates a 0.17 mm diameter capillary tube and a multichannel array between the XeF_2 reservoir and the vacuum chamber. The capillary acts as a fixed flow resistance while a set of 16 μm diameter x 450 μm long stainless steel tubes forming a multichannel array serve to narrow the angular distribution of the effusive beam. With this configuration about 9% of the beam flux impinging on the sample holder is concentrated in the central detection area imaged by their detector. Since the central detection area corresponds to only 2% of the sample holder's area, a significant flux enhancement with respect to a single tube effusive source is achieved. This gas source, still suffers from a lack of control of the XeF_2 incident energy as well as from the detrimental effects of having large amounts of reactive background inside the chamber.

In the current investigation, seeded supersonic molecular beams of XeF_2 are used to introduce the reactant onto the silicon surface. Several advantages are obtained through the use of seeded beam techniques: (1) Extremely narrow angular divergence of the collimated beam allows directional control of the impinging reactant, (2) a tunable narrow velocity distribution can be achieved, (3) high beam-to-background flux ratio (4) most of the background gas arises from the chemically inert carrier gas, (5) low XeF_2 fluxes can be obtained which allow the study of the initial fluorination stages. To the knowledge of the author, this study constitutes the first use of a supersonic XeF_2 beam for gas-surface reaction experiments.

[92] M. J. M. Vugts, G. J. P. Joosten, A. van Oosterum, H. A. J. Senhorst, and H. C. W. Beijernick, J. Vac. Sci. Technol. A **12**, 2999 (1994)

2.2 EXPERIMENTAL

The experimental apparatus has been previously described in detail[7,8,9,10,11]. A brief overview is given in Chapter I, Section 1.2.1. Only minor modifications to the apparatus were required for the study of the interaction of XeF_2 with Si(100). Section 2.2.1 discusses the modification of the gas-mixing manifold as well as the operational procedures required to produce seeded XeF_2 molecular beams. Section 2.2.2 presents the characterization of the seeded XeF_2 molecular beams.

2.2.1 Production of Seeded Supersonic XeF_2 Beams

2.2.1.1 XeF_2 Mixing Cylinders

Two new cylinders were added to the existing gas manifold to be used for preparation of mixtures of XeF_2 with carrier gases. The stainless steel mixing cylinders have a volume of approximately 3.8 liters, and are fitted with a 0.25 inch female pipe thread on either end. The top pipe thread is used to connect the cylinder to the rest of the gas manifold via an isolation valve with matching male pipe threads on both ends. The pipe thread fitting on the bottom of the cylinder is connected to a similar valve, but in this case the opposite end of the valve is capped off, thereby defining a small reservoir of ~2 ml between the cap and the valve when it is closed. All pipe thread connections are sealed with Teflon tape. The small reservoir is filled with solid XeF_2 (typically 1-3 gr.), and the air trapped inside the reservoir during the filling procedure is removed by freeze-pump-thaw cycles. A dry ice/acetone bath is used in the freezing step to prevent XeF_2 vapors from being pumped out. Gas mixtures are produced by opening the reservoir's valve and allowing the room temperature XeF_2 to expand into the empty cylinder. The reservoir valve is then closed, and the desired amount of carrier gas is added through the valve on the top of the cylinder.

Several factors must be balanced in deciding the optimal XeF_2 concentration as well

as the carrier gas of the mixtures to be used for expansion in a supersonic molecular beam. The mass of the carrier gas, the concentration of XeF_2, and the total pressure in the mixing cylinder must be carefully chosen to obtain a molecular beam with the desired properties.

Since the XeF_2 concentration in the seeded beams is typically low (< 1%), the mass of the carrier gas largely determines the average velocity of the beam, and hence the translational energy of the incident XeF_2 molecules, as well as the flux of XeF_2 reaching the surface. The concentration of seed gas also affects the XeF_2 flux reaching the surface, and hence the amount of scattered signal at the mass spectrometer. While a high concentration of XeF_2 might be desirable in order to maximize the signal level at the mass spectrometer, a compromise must be made in order to reduce the rate at which XeF_2 impinges on the surface. The XeF_2 flux must be sufficiently low so as to make possible the elucidation of the processes governing the initial stages of fluorination. A balance must then be achieved between maximizing the signal level at the mass spectrometer, and maintaining a sufficiently low reactant flux to slow the fluorination process to a tractable time scale.

When either Ar or Kr is used as the carrier gas, a XeF_2 concentration of 0.25% is found to provide an optimal balance between signal level and fluorination rate. The fluorination of the surface is estimated to occur in approximately 8 to 15 seconds, a time scale optimal for the present studies. Unless the XeF_2 reservoir, the mixing cylinder and the entire section of the manifold leading to the nozzle are heated above room temperature, the maximum pressure of XeF_2 that can be introduced into the mixing cylinder is limited to ~5 Torr, the vapor pressure of the solid XeF_2 at 298 K. Starting with 5 Torr of XeF_2 vapor, a 2000 Torr balance of carrier gas is required to obtain the desired 0.25% XeF_2 concentration. Given the small volume of the mixing cylinder, and the relatively low pressure of the mixture, the beam can only be operated for a few hours

before the mixture runs out. Although longer lasting beams can be produced by increasing the carrier gas concentration, in most cases, the further dilution of the beam causes unacceptably low signals at the mass spectrometer, and offers no advantages in terms of the information gained about the initial fluorination steps. When helium is used as a carrier gas, the XeF_2 flux increases by as much as a factor of 3 because the average velocity of the beam is increased. Hence, when helium is used as a carrier gas, it is necessary to lower the XeF_2 concentration in order to reduce the fluorination rate.

Given the above considerations, the mixing procedure is as follows: The valve isolating the solid XeF_2 reservoir from the empty mixing cylinder is opened. The cylinder fills with the vapor pressure of XeF_2 at room temperature. The pressure of XeF_2 is measured with a Baratron diaphragm manometer which has been thoroughly passivated by years of exposure to fluorine. The measured pressure is in agreement with the value predicted by Eq. (2.1). The isolation valve is then closed and the cylinder is filled with approximately 2000 Torr of either Ar or Kr. The mixture is allowed to equilibrate for a few hours (typically overnight) to ensure proper mixing. This procedure used for the Ar and Kr mixtures yields a 0.25% XeF_2 concentration. For the more dilute helium mixtures, 5000 Torr of He is added to yield a concentration of 0.1%. The characterization of the molecular beams produced by a supersonic expansion of these gas mixtures is presented in Section 2.2.2.

2.2.1.2 Passivation Issues

The highly reactive nature of XeF_2 requires that special precautions be taken to ensure that it is not depleted by reactions with the manifold or the inside walls of the nozzle. The manifold is constructed of stainless steel parts which have been thoroughly passivated by years of exposure to fluorine containing beams. The nozzle is made of nickel 200. The CaF_2 trap previously used to remove HF contamination in the F_2 beams is bypassed, since it has been observed to completely deplete the XeF_2 in the beam.

Even with these precautions, some reaction is observed upon the initial exposure of the clean manifold to XeF_2. For example, Figure 2.1 shows the mass spectrometer signals at the m/e values corresponding to Xe^+, XeF^+, and XeF_2^+ during the first few minutes after opening the valve on the mixing cylinder and allowing the 0.25% XeF_2/Ar beam into the manifold and nozzle. The spectrum is taken by directing the beam into the triply-differentially-pumped mass spectrometer through the pin-hole aperture. The manifold had been pumped out overnight and not exposed to any fluorinated beams. The only signal initially observed (m/e=129) corresponds to Xe^+. No XeF_2^+ or XeF^+ fragments are detected. This observation is interpreted as a fluorination of the manifold walls by XeF_2 with simultaneous release of the chemically inert Xe which is then ionized to Xe^+ and detected as m/e=129 signal. A few minutes after the beam is turned on, the mass spectrometer signals change abruptly. The XeF^+ and XeF_2^+ signals grow and rapidly reach a steady state level. The appearance of the XeF_2 fragments is attributed to the eventual passivation of the manifold and nozzle walls, which allows unreacted XeF_2 to reach the mass spectrometer. Confirmation that the passivation process occurs exclusively in the manifold and nozzle, and not in the main or detection chamber, is obtained by allowing the beam to first passivate the manifold and nozzle without entering the chamber. When XeF_2 is subsequently allowed to enter the reaction and detection chambers, all three XeF_2 fragments are immediately detected with the mass spectrometer. No evidence of XeF_2 depletion by wall reactions is observed, confirming that only reactions on the nozzle walls are responsible for the initial absence of XeF_2 signals observed in Figure 2.1.

The signal levels of all three fragments at steady state are consistent with published fragmentation ratios for XeF_2. The fact that the signals remain constant beyond an initial passivation time does not necessarily confirm that the XeF_2 depletion by the manifold walls has completely ceased. It is possible that some of the XeF_2 continues to react with

the manifold and nozzle walls releasing a constant amount of Xe. The measurement does however confirm that after an initial passivation period, a constant and reproducible amount of XeF_2 enters the reaction chamber. The concomitant presence of Xe in the XeF_2 beam must always be considered as a possible source of signal detected as Xe^+.

The passivation time has been observed to depend on the conditions of the manifold and nozzle. The longest passivation times are observed after the lines have been thoroughly cleaned by an overnight bakeout. After such a cleaning, passivation times of approximately 5-8 minutes are required. On the contrary, if the manifold has been recently exposed to a fluorinated beam, 1-2 minutes of running a XeF_2 beam appear to be sufficient. It is therefore standard operating procedure for any experiment involving a XeF_2 beam to allow the beam to pass through the nozzle for approximately 8 minutes at the beginning of each day or after switching from a non-fluorinated beam. In between exposures to the same XeF_2 mixture, the beam is allowed to stabilize for 1-2 minutes before entering the main chamber.

A word of caution is needed about the procedure for switching between a XeF_2 containing beam and other non-fluorinated beams. It has been observed that traces of XeF_2 continue to be released from the "clean" manifold and nozzle, which is particularly detrimental when a helium diffraction experiment is performed immediately following the use of a XeF_2 containing beam. The residual XeF_2 from the manifold walls is carried to the surface by the He/Ar beam and causes undesired fluorination during the diffraction measurement. It is recommended to purge the nozzle and manifold with an inert gas for 30 minutes after pumping XeF_2 out of the manifold. A check for residual XeF_2 in the manifold is to allow an inert gas beam to impinge on the Si surface for 3-5 minutes and then to monitor for desorbing fluorinated products upon raising the crystal temperature.

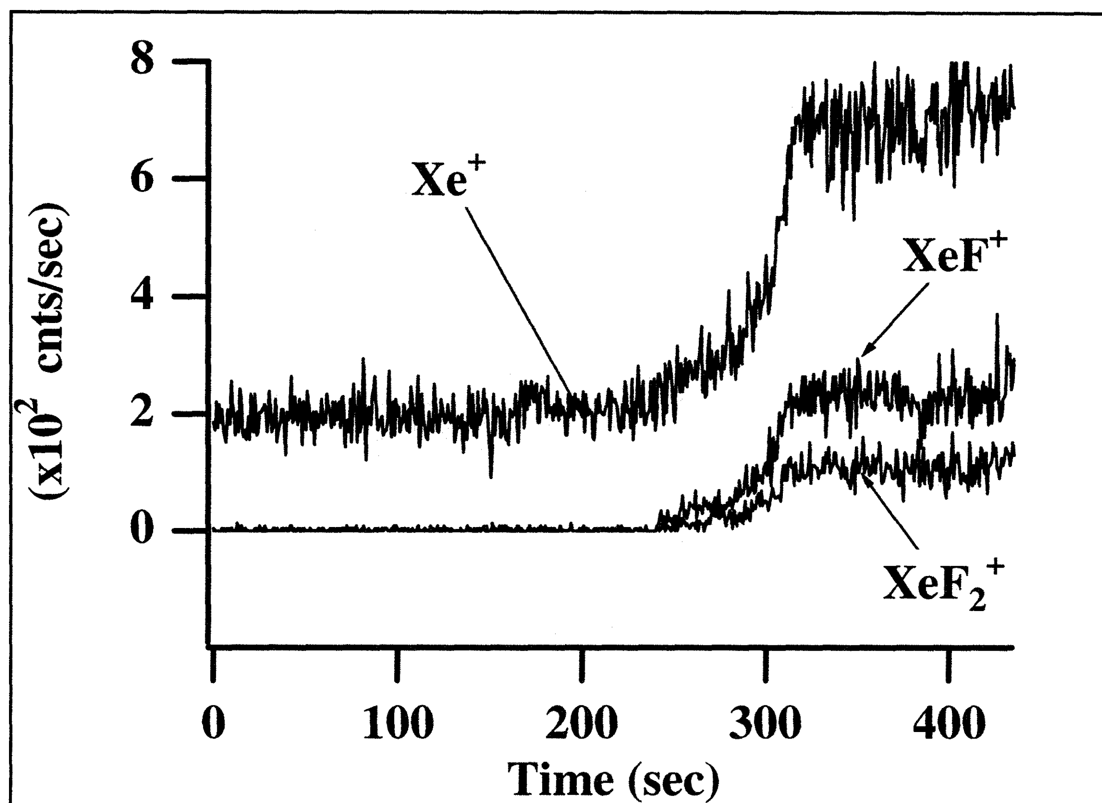

Figure 2.1 Initial Time Evolution of the XeF_2 Fragments from the Clean Nozzle

Mass spectrometer signals (from triply-differentially pumped spectrometer with pin-hole aperture) as a function of time after the gas mixture has been allowed into the manifold and nozzle. For the initial 4-5 minutes all of the XeF_2 present in the beam reacts with the manifold and nozzle walls. The only signal observed during this time is that of Xe^+ arising from the Xe liberated by wall reactions. The nozzle eventually becomes passivated at which point the expected XeF_2 fragments suddenly grow. The concurrent increase of the Xe^+ signal suggests a higher electron impact ionization cross-section for XeF_2 than for Xe.

2.2.2 Characterization of Seeded Supersonic XeF_2 Beams

2.2.2.1 Mass Spectra of XeF_2 Beams

In the current investigation, XeF_2 spectra are obtained from a seeded supersonic molecular beam directly introduced into the liquid nitrogen cooled, triply-differentially-pumped quadrupole mass-spectrometer. Details about the production of seeded XeF_2 beams are presented in Section 2.2.1. A 0.25% Xe/Ar beam is used to obtain a well-resolved mass spectrum of the Xe isotope pattern, as shown in Figure 2.2. Seven of the nine Xe natural isotopes are observed. The ^{124}Xe and ^{126}Xe isotopes are not observed due to their low abundance (<0.1 %). A typical spectrum obtained from a 0.2% XeF_2/He beam is shown in Figure 2.3. The expected Xe isotope pattern, although not fully resolved, is discernible for all three fragments. The fragmentation ratio is in reasonable agreement with the previously reported values, but it is observed to vary significantly with the resolution setting of the mass spectrometer. In order to obtain an accurate measurement of the fragmentation ratio the transmissivity of all ions through the quadrupole must be known. The measurement of these transmissivities and fragmentation ratios has not been performed in this investigation.

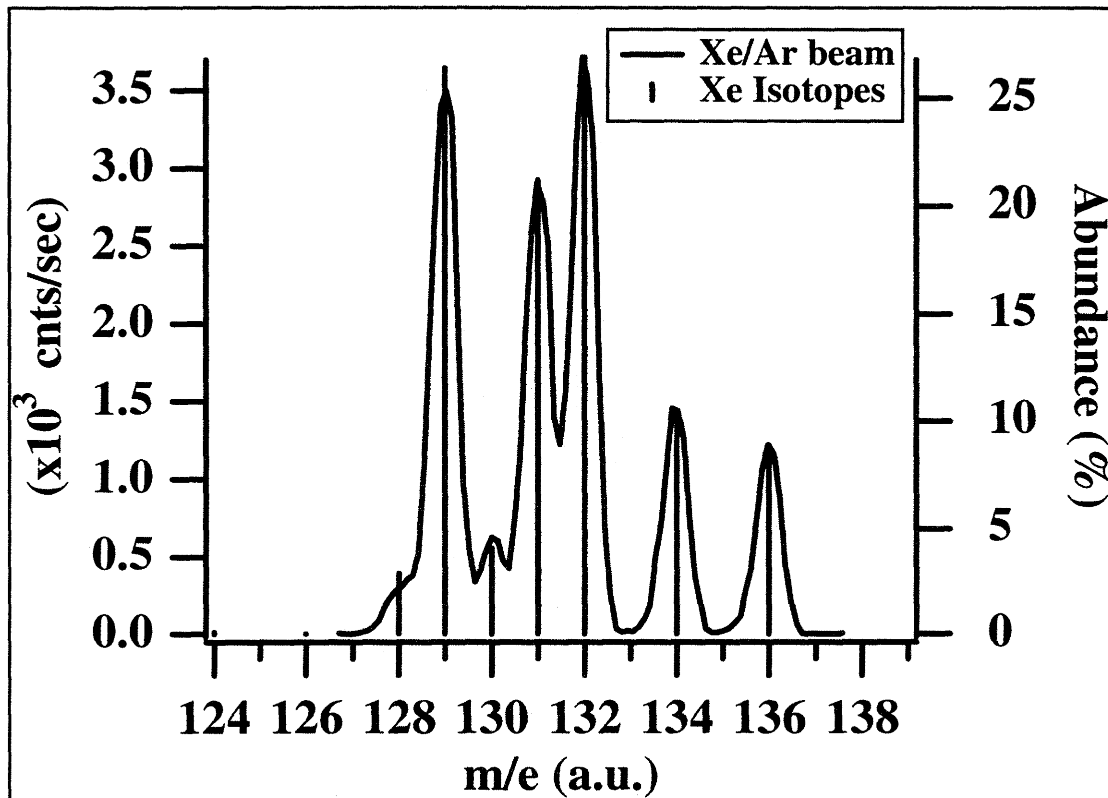

Figure 2.2 Mass Spectrum of Xe Isotopes from a Xe/Ar Molecular Beam

Seven of the nine naturally occurring Xe isotopes are resolved. Their relative intensities match well the stick spectrum produced from the published natural isotope abundance. ^{124}Xe and ^{126}Xe isotopes are not observed due to their low natural abundance. This characteristic isotope pattern should be reproduced in any molecular fragment containing a Xe atom.

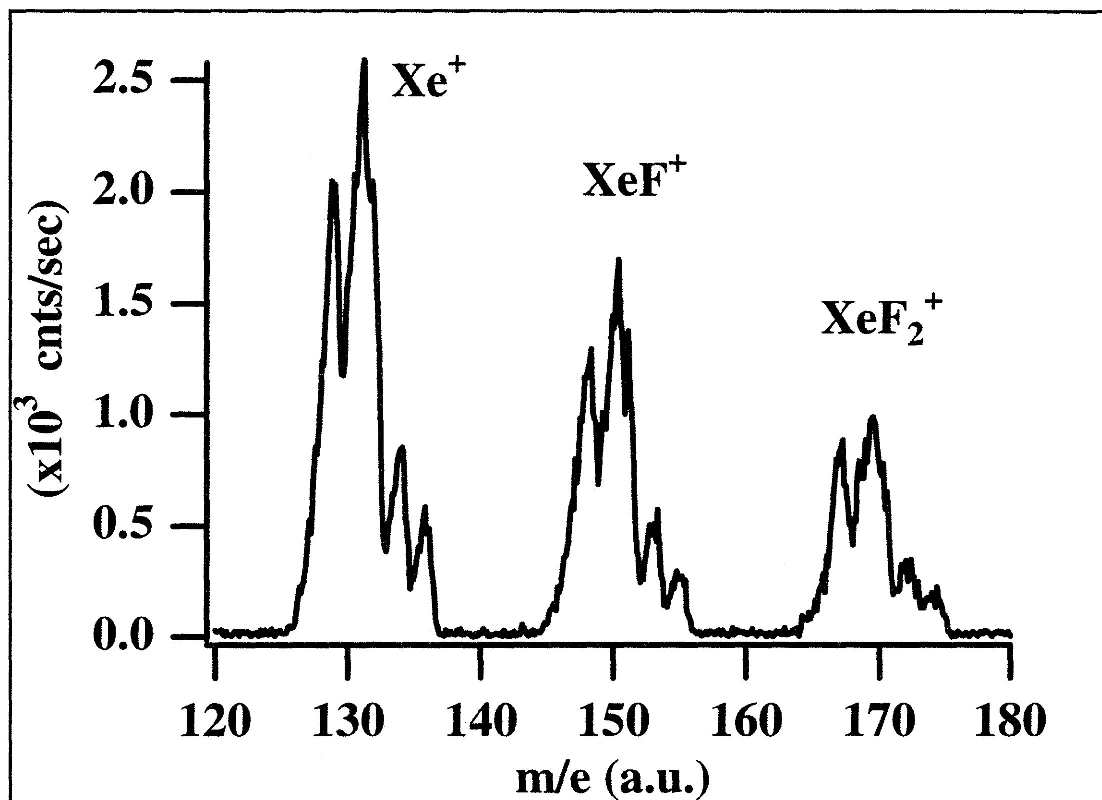

Figure 2.3 Mass Spectrum of XeF_2/He Molecular Beam

The three clusters of Xe isotopes correspond to Xe^+, XeF^+ and XeF_2^+. The resolution of the mass spectrometer has been set low such that only four Xe isotopes are resolved for each fragment.

2.2.2.2 Van der Waals Clustering in the Beam

Large and highly polarizable molecules such as XeF_2 have a tendency to form van der Waals clusters upon expansion into a molecular beam. The cooling of the internal degrees of freedom caused by the expansion, combined with the long range of the intermolecular attractive forces can cause weakly bound aggregates to form in the expanded beams. Clustering is especially likely when the carrier gas is also large and polarizable, as is the case when XeF_2 is seeded in Kr.

Figure 2.4 (a) shows a low resolution mass spectrum of a 600 Torr 0.25% XeF_2/Kr beam expanded through a 100 μ nozzle held at 25° C. The broad feature centered at about m/e =129 corresponds to XeF_2 which has fragmented to its parent ion, Xe^+, upon electron impact ionization. The individual features arising from the nine different xenon isotopes are not resolved in this spectrum. A second broad feature is observed displaced by 19 m/e units from the feature at m/e=129. This feature centered at about m/e=148 corresponds to the XeF^+ daughter fragment. A similarly shaped third feature is seen as expected at 38 m/e units from the parent Xe^+ signal. It is immediately apparent that the relative intensities of the three features are different from those observed for the XeF_2/He beam shown in Figure 2.3, as well as from any previous results in the literature. In particular, the intensity of the highest mass feature is unusually large. A higher resolution scan of the broad feature centered at m/e =167 reveals that the position and relative intensity of the underlying peaks do not match the expected Xe isotope pattern. Figure 2.4 (b) shows the stick spectrum obtained from the natural abundance of the Xe isotopes overlaid on the partially resolved spectrum centered at m/e =167. A mismatch between the expected and measured profiles is clearly evident. Note the relatively large signals at m/e=166 and 168 where the not very abundant isotopes $^{128}XeF_2$ and $^{130}XeF_2$ are expected. The scan was halted short of the final feature expected at m/e =176.

Closer examination of the pattern in the intensities reveals that it is almost entirely

due to the presence of Kr_2 van der Waals dimers. Figure 2.4 (c) shows a good match between the observed intensity pattern and the stick spectrum expected from the Kr_2 dimer based on the natural isotopic abundance of Kr[93]. In addition, the same pattern is well reproduced from a pure Kr beam, confirming that it indeed arises from the carrier gas rather than from XeF_2. The large contribution of Kr_2 to this region of the spectrum almost entirely obscures the lower signal arising from the XeF_2^+ ions. A properly weighted sum of the Kr_2 and Xe stick spectra would reproduce the measured intensity pattern. The van der Waals bond in Kr_2 is apparently strong enough to survive collisions with the surface because it has been detected (albeit with lower relative intensity) in a mass spectrum of the scattered products. The survival of the dimer combined with the mass coincidence between the Kr_2^+ and XeF_2^+ signals complicate the interpretation of scattered XeF_2/Kr data. Therefore, a mixture of XeF_2 seeded in Ar was used in most experiments presented below.

A similar, but less bothersome, clustering problem arises with XeF_2/Ar beams. Figure 2.5 shows high and low resolution mass spectra of a 600 Torr 0.25% XeF_2/Ar beam expanded through a 100 μ nozzle held at 25° C. At first glance, a moderately well-resolved Xe isotope pattern is apparent for Xe^+, XeF^+ and XeF_2^+, but a closer scrutiny of the feature centered at m/e =167 reveals a discrepancy, as illustrated in Figure 2.6 (a). In this case, the discrepancy is accounted for by a superposition of the distribution of Xe isotopes and the distribution expected to arise from $[Xe{-}{-}Ar]^+$ ions. Since ^{40}Ar is by far the most abundant of the three known isotopes (99.6 %), ^{40}Ar is considered as the single isotope. The distribution of $[Xe{-}{-}Ar]^+$ would then be expected to be that of the Xe isotopes, but displaced by 40 m/e units. A weighted sum of the Xe isotopes displaced by 38 m/e units (corresponding to XeF_2^+) and the same Xe isotopic pattern displaced by 40

[93] The commission on Atomic Weights and Isotopic Abundances "Table of Isotopic Compositions of the Elements as Determined by Mass Spectrometry", (1989)

m/e units (corresponding to $[Xe\text{--}Ar]^+$) is seen in Figure 2.6 (b) to fit well to the observed signal. Fortunately, the signal attributed to the $[Xe\text{--}Ar]^+$ ion does not survive collisions with the surface and hence does not interfere with XeF_2 scattering measurements.

The $[Xe\text{--}Ar]^+$ ions could arise from two different sources: (1) the electron impact ionization of XeF_2--Ar van der Waals cluster formed during the expansion, or (2) the Xe--Ar van der Waals clusters formed from any residual Xe in the XeF_2 mixture. Identification of the source of $[Xe\text{--}Ar]^+$ ions is important in order to rule out the existence of large amounts of residual Xe in the XeF_2 mixtures.

To resolve the origin of the $[Xe\text{--}Ar]^+$ ions, and to estimate the amount of residual Xe present in the molecular beam, comparisons are made to the mass-spectrum obtained from a 600 Torr 0.25% Xe/Ar mixture expanded through a 100 μ nozzle held at 25° C. Figure 2.7 (a) confirms the existence of the $[Xe\text{--}Ar]^+$ signal in the 0.25% Xe/Ar molecular beam, which arises from Xe--Ar van der Waals clusters formed in the expansion. A good match of the intensities and masses is observed with the stick spectrum.

Let's assume that the $[Xe\text{--}Ar]^+$ signal in the XeF_2/Ar beam arises from Xe liberated by wall reactions. Since the Xe concentration in the Xe/Ar beam is nominally the same as that in the XeF_2/Ar beam, comparison of the intensity of features arising only from $[Xe\text{--}Ar]^+$ in both beams yields information about the amount of residual Xe that might be present in the XeF_2 beam. Mass spectra of the two beams are presented in Figure 2.7 (b). Since the feature at m/e =171 does not correspond to any known XeF_2 isotope it is used as a signature of the amount of $[^{131}Xe\text{--}^{40}Ar]^+$ and hence of the amount of free ^{131}Xe. As can be seen in Figure 2.7 (b), the intensity at m/e= 171 is similar for both beams, indicating that the amount of Xe in the 0.25% XeF_2/Ar beam is approximately equal to that present in the 0.25% Xe/Ar beam. This analysis would imply that no Xe would be available in the form of XeF_2, which is clearly not the case, as evidenced by the features

in the mass-spectrum arising from XeF_2^+ as seen in Figure 2.7 (b). Rather, it is believed that a substantial part of the $[Xe\text{--}Ar]^+$ signal is due to the presence of XeF_2--Ar van der Waals clusters in the beam.

Since XeF_2 preferentially cracks to Xe^+, it is reasonable to expect that XeF_2--Ar would crack preferentially to $[Xe\text{--}Ar]^+$. If XeF_2--Ar were the neutral responsible for the $[Xe\text{--}Ar]^+$ signal, then $[XeF\text{--}Ar]^+$ and $[XeF_2\text{--}Ar]^+$ ions should also be present. Figure 2.8 shows mass spectra of a 0.25% XeF_2/Ar beam at the higher mass range at which the $[XeF_2\text{--}Ar]^+$ and its fragments should appear. Although the signal levels are low and the resolution is less than ideal, the spectra clearly indicate the existence of $[XeF\text{--}Ar]^+$ and $[XeF_2\text{--}Ar]^+$ in the mass spectrometer. In addition, closer scrutiny of the cluster of features centered at m/e =209 reveals the presence of yet another van der Waals cluster. The intensity profile and position of the features in this region of the spectrum is consistent with a characteristic Xe isotopic pattern shifted by 78 amu superimposed on a Xe pattern shifted by 80 amu. The neutral responsible for the 78 amu shift is XeF_2--Ar while the 80 amu shift is believed to be due to Xe--Ar_2.

It is then concluded that detectable amounts of XeF_2--Ar clusters are formed in the molecular beam expansion of XeF_2/Ar mixtures. Fortunately, these clusters do not survive collisions with the Si surface so they do not complicate the interpretation of scattering experiments in which XeF_2 is a scattered product. The data presented in this section also demonstrate that no substantial amount of free Xe arising from wall reactions in the manifold and nozzle is present. It does not, however, completely eliminate the possibility of smaller amounts of free Xe in the beam.

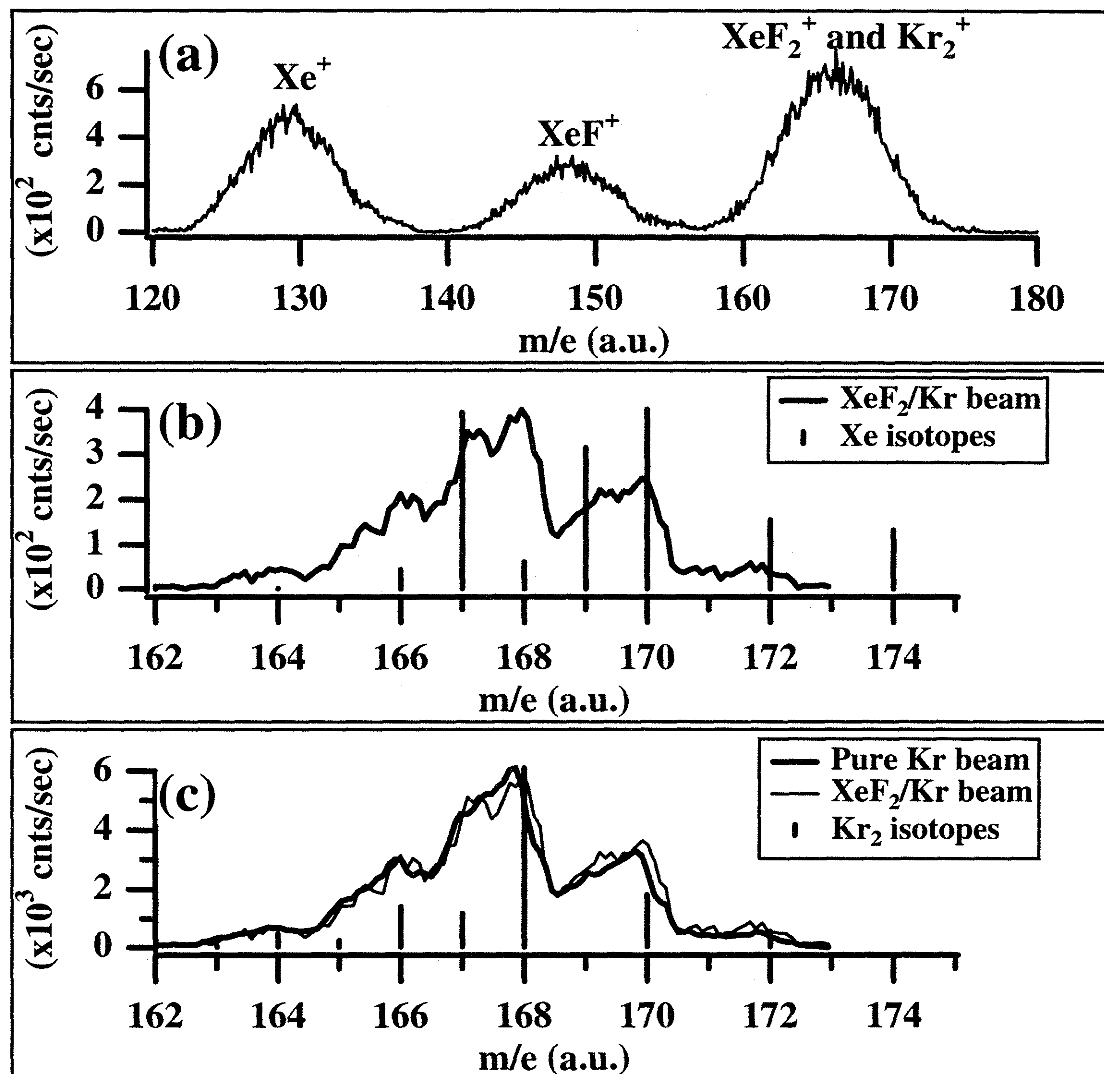

Figure 2.4 Mass Spectrum of XeF_2/Kr Molecular Beam

(a) Low resolution spectrum of the m/e range corresponding to singly ionized XeF_2 cracking products. The first feature is assigned to Xe^+, the second to XeF^+. Note the unusually high relative intensity feature at m/e =168. (b) Higher resolution spectra comparing the features at m/e=168 with the stick spectrum expected from the isotopic abundance of Xe (c) Compares the m/e=168 feature with that from a pure Kr beam and with the stick spectrum expected for Kr_2 from the isotopic abundance of Kr.

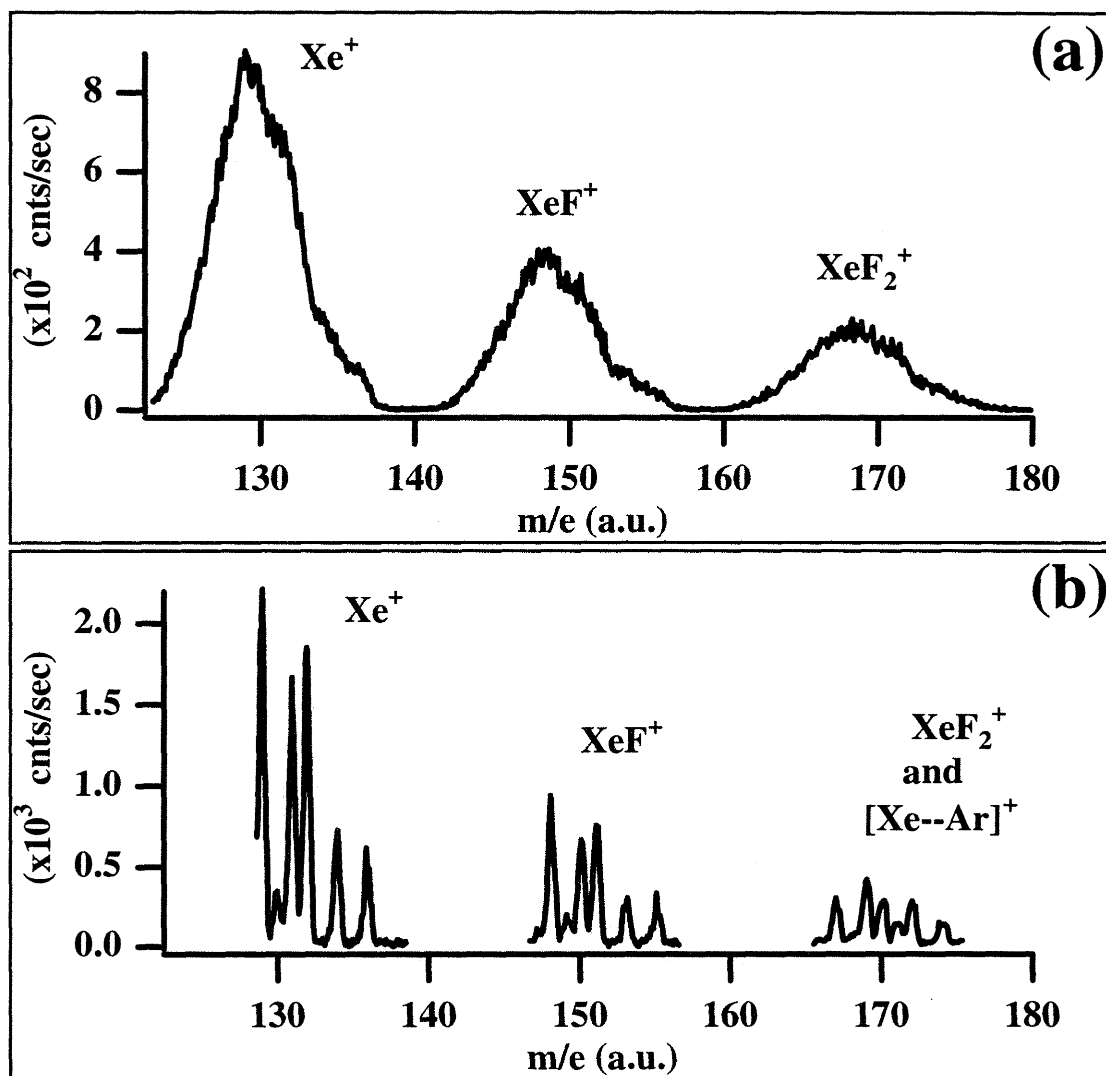

Figure 2.5 High and Low Resolution Mass Spectra of XeF_2/Ar Molecular Beam

(a) Low resolution scan of the masses corresponding to singly ionized XeF_2 cracking fragments. The three features are initially assigned to the expected Xe^+, XeF^+ and XeF_2^+ fragments. Their relative intensities agree with published values. (b) Higher resolution scan. Note the slightly different relative intensity observed in the heaviest cluster of masses. This last feature is reassigned to a superposition of XeF_2^+ and $[Xe\text{--}Ar]^+$.

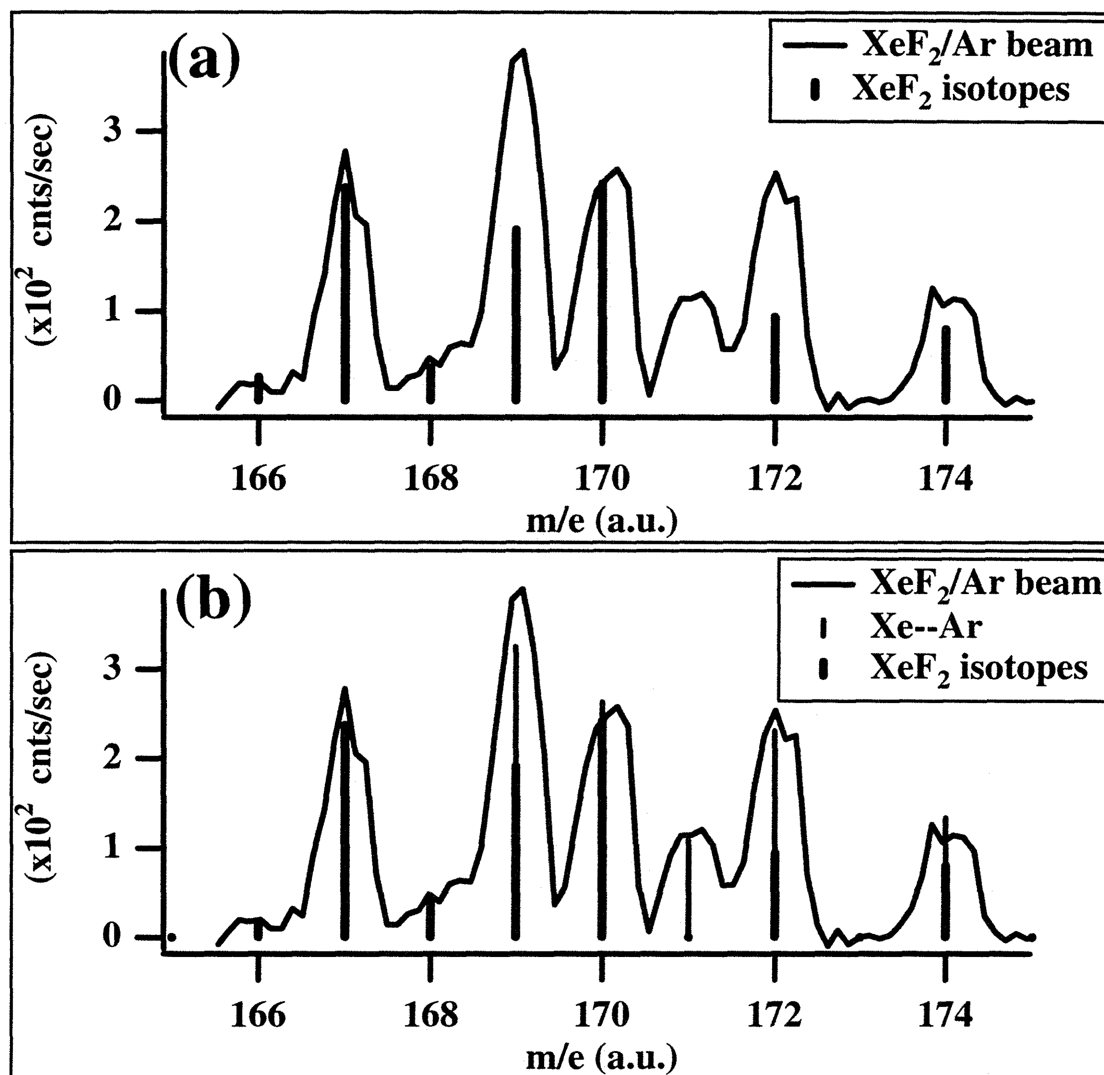

Figure 2.6 Fit of XeF_2/Ar Signal to a XeF_2^+ and $[Xe\text{--}Ar]^+$ Superposition

(a) The heaviest cluster of masses in the high resolution XeF_2/Ar mass spectrum can not be solely assigned to XeF_2^+. The additional intensity of the features at m/e=169 and 172 and the extra feature at m/e=171 arise from a superposition of XeF_2^+ and $[Xe\text{--}Ar]^+$. (b) A good fit of the measured signal is obtained by a superposition of the stick spectra for XeF_2^+ and $[Xe\text{--}Ar]^+$ expected on the basis of their isotopic abundances.

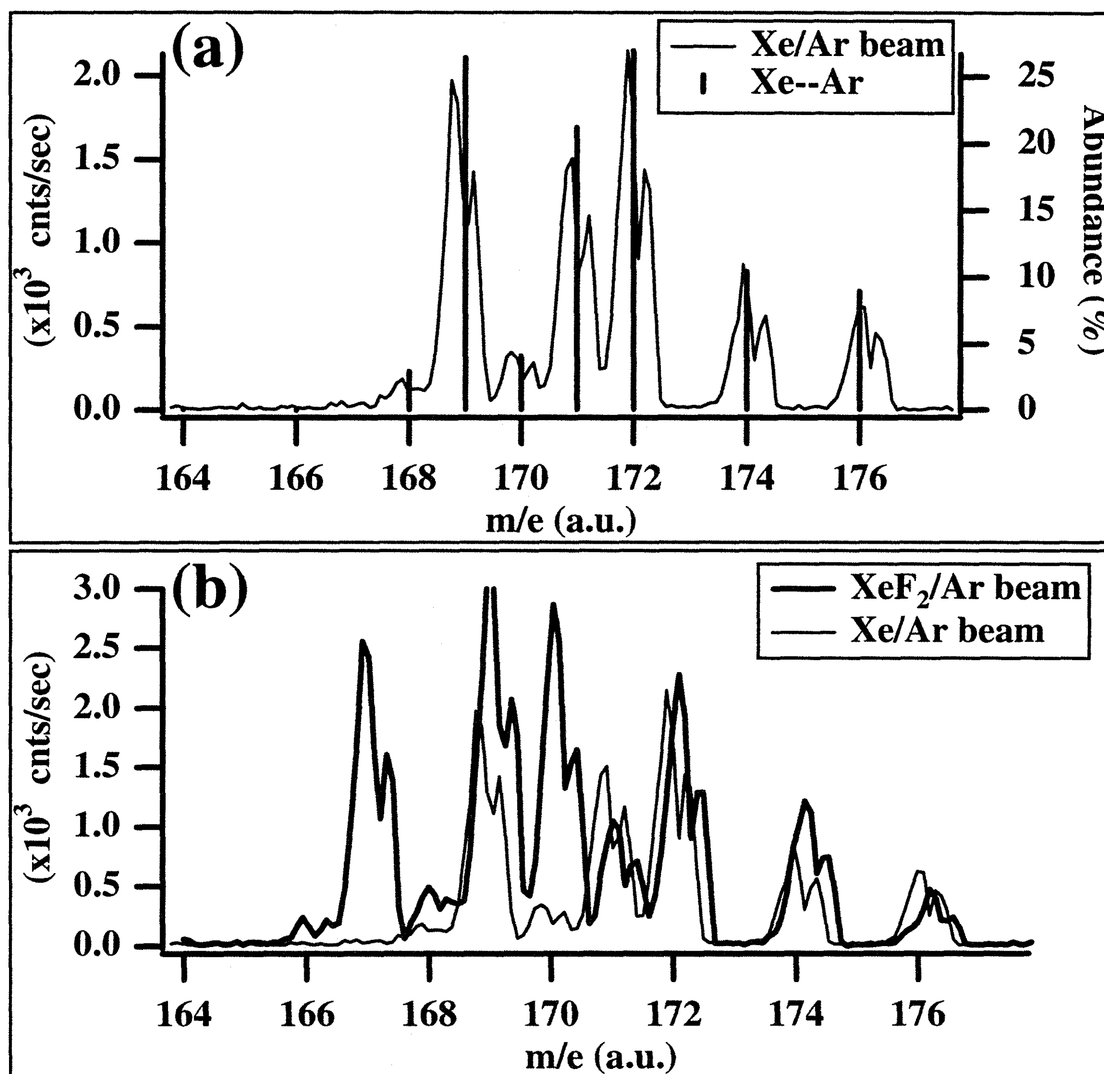

Figure 2.7 Mass Spectra of Xe/Ar and XeF_2/Ar Molecular Beams

(a) High resolution mass spectrum of a 0.25% Xe/Ar beam. The features are assigned to $[Xe\text{--}Ar]^+$ arising from Xe--Ar van der Waals clusters formed in the beam expansion. The isotope distribution matches well the stick spectrum predicted from the natural isotopic abundance of Xe. (b) Comparison of the signal in (a) with that obtained from a 0.25% XeF_2/Ar beam. Note that the signal level at m/e= 171 peak is similar in both spectra.

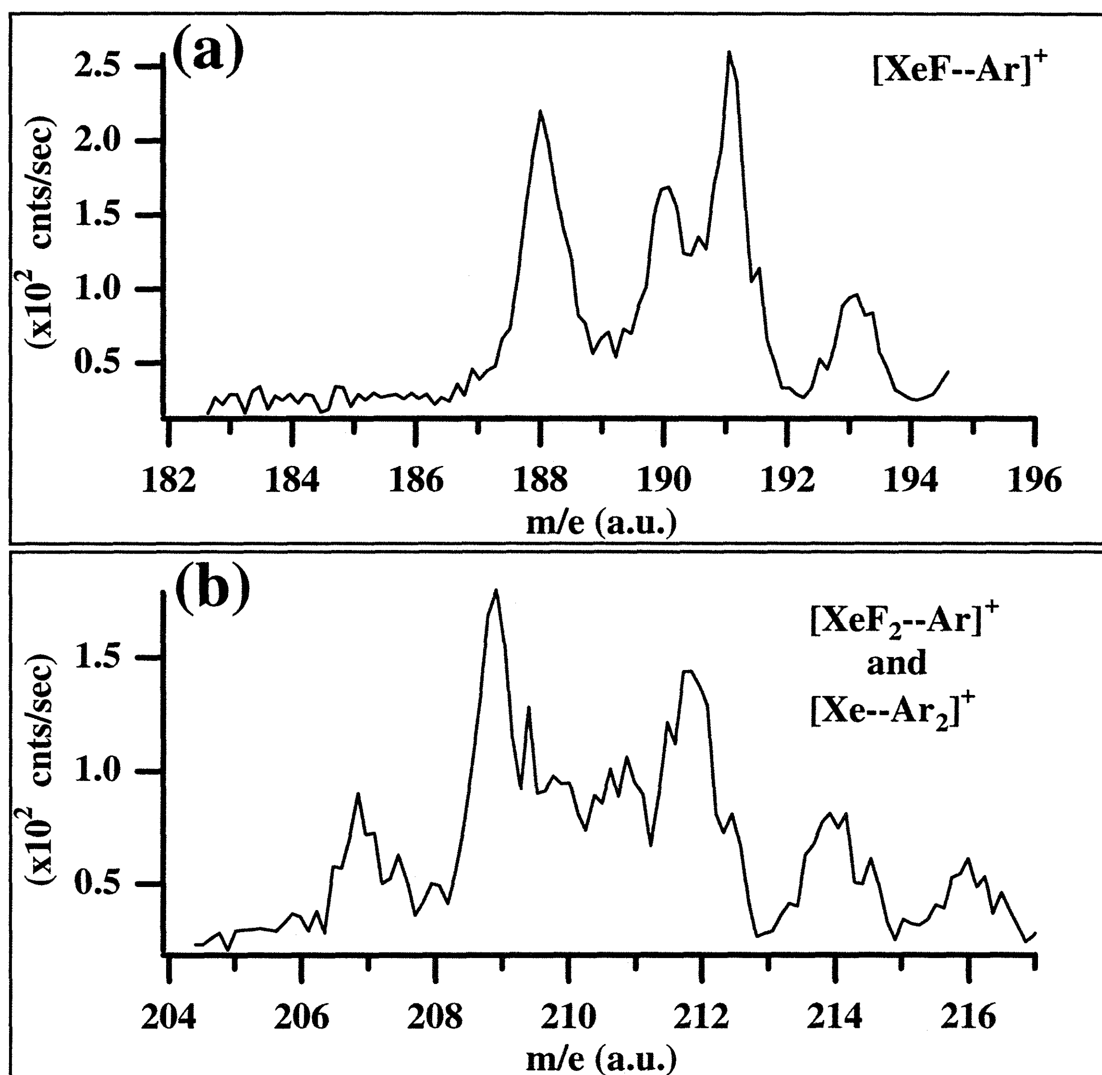

Figure 2.8 Mass Spectra Demonstrating the Existence of XeF_2--Ar in the Beam

Mass spectrum from a 0.25% XeF_2/Ar beam. (a) The Xe isotope distribution is observed to be shifted by 59 atomic units. This signal is assigned to $[XeF\text{--}Ar]^+$. (b) A distorted Xe isotope distribution is observed shifted by 78 atomic units. This signal is attributed to a superposition of XeF_2--Ar and Xe--Ar_2 van der Waals clusters in the beam cracking to $[Xe\text{--}F_2]^+$ and $[Xe\text{--}Ar_2]^+$ respectively. These spectra confirm that the cluster of masses observed in the m/e=169 range should be assigned to XeF_2--Ar rather than to Xe--Ar.

2.2.2.3 Velocity Distribution of Seeded XeF_2 Beams

Molecular beam seeding techniques are used throughout this investigation to produce XeF_2 with a variety of incident energies. The gas mixtures that are expanded to yield XeF_2 beams of different energies are characterized by time-of-flight measurements. The molecular beams are aimed directly into a pin-hole aperture positioned in front of the differentially pumped mass spectrometer, and are modulated by a pseudorandom chopper-wheel which rotates at 280 Hz. The velocity distribution of the XeF_2 molecules in the beams is derived from the time it takes the XeF_2 to traverse the 29.3 cm flight path between the chopper wheel and the ionization region. Figure 2.9 and Figure 2.10 present a collection of time-of-flight spectra of the various seeded XeF_2 beams used in this investigation. The mixtures are expanded through a 100 μ nozzle held at 25° C with an stagnation pressure of 600 Torr. The signal is collected at a nominal m/e=129 corresponding to Xe^+ which is the most abundant ionization fragment. The parameters describing the velocity distribution are obtained by fitting the time-of-flight spectra to a supersonic velocity distribution functional form[94] as described by Yang[95]. The fit to each time-of-flight spectrum is plotted together with the data, and the fit parameters are summarized in the figure. Table 2-2 presents a compilation of the parameters describing the velocity distribution of each XeF_2 beam.

Table 2-2 Parameters Describing Velocity Distribution of XeF_2 in Seeded Beams

Beam	Avg. Velocity	Beam Temp.	XeF_2 Energy	Rel. Flux[a)]
0.25%XeF_2/Kr	382±1 m sec^{-1}	3.8±0.6 K	2.98±0.02 kcal mol^{-1}	0.52
0.25% XeF_2/Ar	574±0.6 m sec^{-1}	6.9±0.4 K	6.72±0.01 kcal mol^{-1}	1.0
0.15% XeF_2/5:1 He:Ar	847±2 m sec^{-1}	15±2 K	14.7±0.1 kcal mol^{-1}	2.54
0.16% XeF_2/3:1 He:Ar	1065±2 m sec^{-1}	30±3 K	23.2±0.1 kcal mol^{-1}	7.6
0.2% XeF_2/He	1615± 10 m sec^{-1}	16.3 ± 3 K	53.2± 0.3 kcal mol^{-1}	33.5

Flux of XeF_2 seeded in Ar seeded beam is defined as 1.0 for comparison purposes.

[94] See Appendix B for a description of the supersonic functional form and fitting procedure.

[95] J. J. Yang, Ph. D. Thesis, Massachusetts Institute of Technology, p. 43, 1993

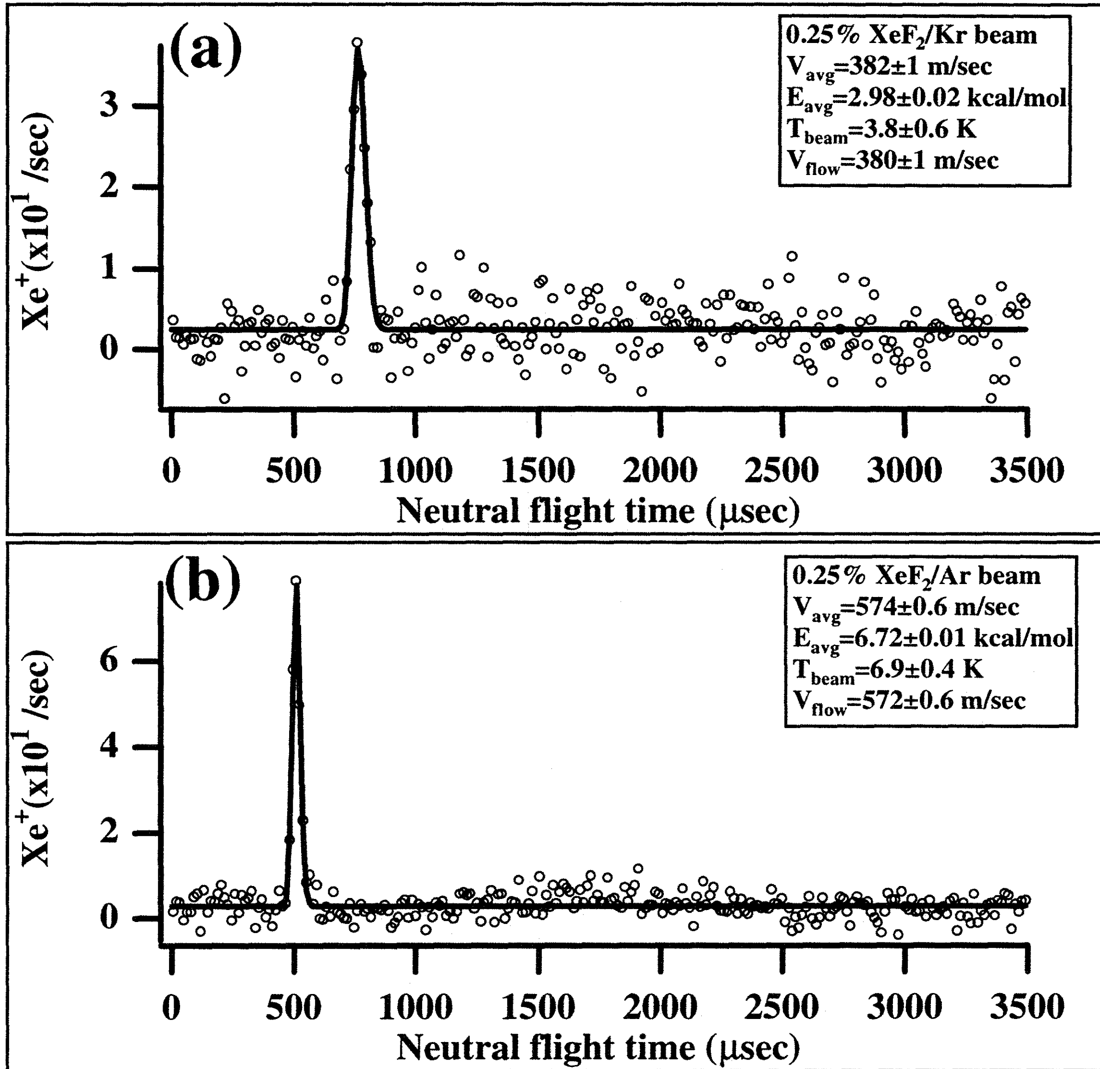

Figure 2.9 Time-of-flight Spectra of XeF_2/Kr and XeF_2/Ar Beams

Time-of-flight spectra shown with corresponding fits and characteristic parameters. Signal is detected as Xe^+ at m/e=129. P_{stag}=600 Torr, chopper frequency 280 Hz, dwell time 14 μsec. (a) 0.25% XeF_2/Kr beam (b) 0.25% XeF_2/Ar beam.

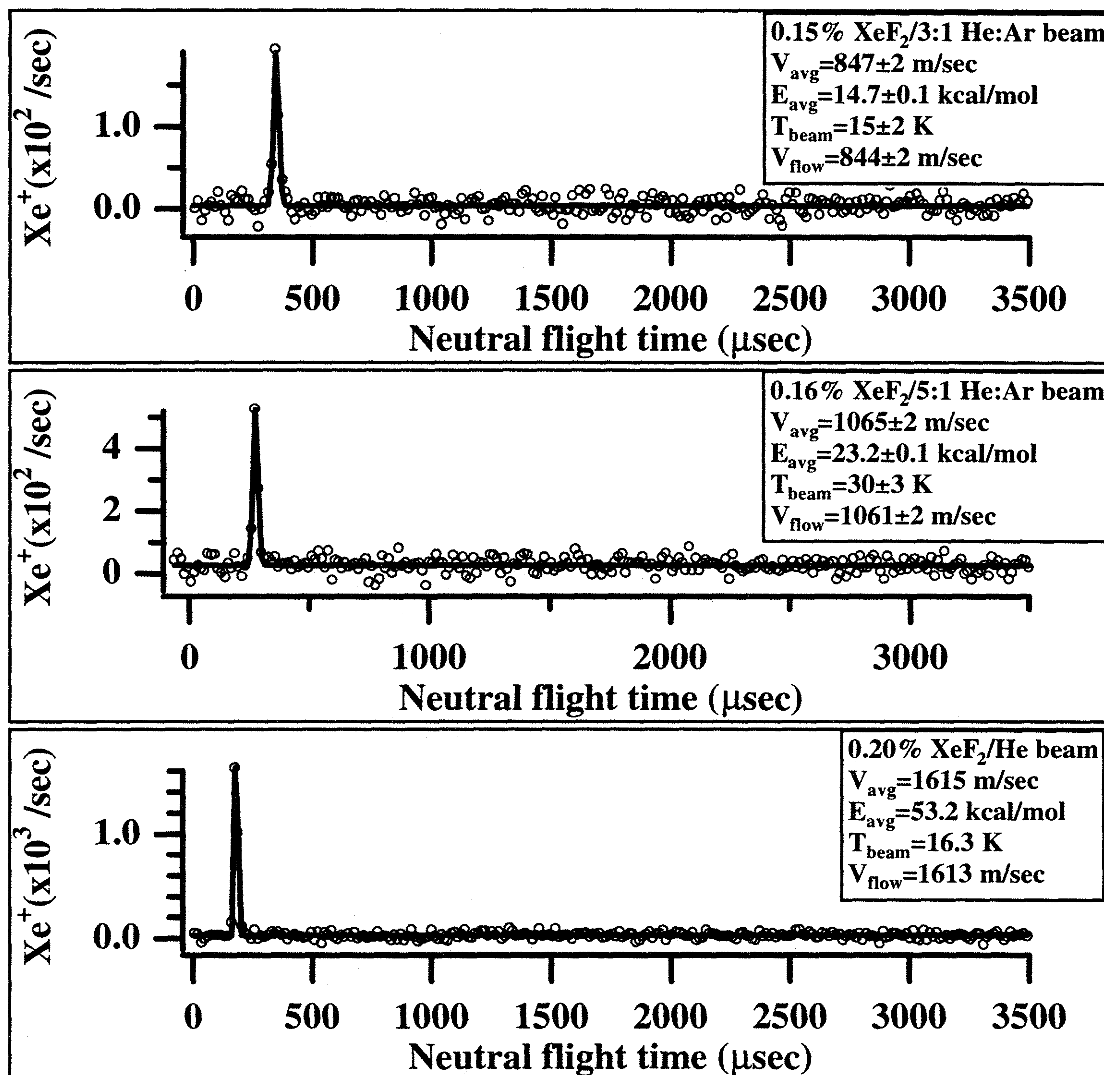

Figure 2.10 Time-of-flight Spectra of XeF_2/He/Ar Beams

Time-of-flight spectra shown with corresponding fits and velocity distribution parameters. Signal is detected as Xe^+ at m/e=129. P_{stag}=600 Torr, chopper frequency 280 Hz, dwell time 14 μsec. (a) 0.15% XeF_2/3:1 He:Ar beam (b) 0.16% XeF_2/5:1 He:Ar beam. (c) 0.2% XeF_2/He beam.

2.2.3 Fragmentation of XeF_2 by Electron Impact Ionization

The main goal of this investigation is to identify the products scattered from a Si(100) exposed to a XeF_2 molecular beam, and in particular to verify the existence of atom abstraction by detecting the highly reactive XeF radical scattered from the surface. In general, the identification of scattered products by mass spectrometry is complicated by the non-selective nature of the electron bombardment ionization. In particular, the identification of scattered XeF in the presence of unreactively scattered XeF_2 is greatly complicated by the coincidences in their fragmentation pattern. As discussed above, approximately one half of all XeF_2 molecules subjected to electron bombardment fragment into Xe^+ while the other half fragment into either XeF^+ or XeF_2^+. Similarly, because of its weak bond energy, XeF is expected to fragment primarily to give Xe^+ with a smaller contribution to the XeF^+ signal. To complicate further the assignment of mass spectrometer signals to the neutral parent species, the presence of scattered Xe will also contribute intensity to the Xe^+ signal.

The first step in identifying the neutral products giving rise to the measured mass spectrometer signals is to determine the exact fragmentation ratios under the ionization conditions used in the experiments. Measurement of the fragmentation pattern of a scattered neutral molecule requires that no other neutral species giving rise to the same ionic fragments be present in the scattered beam. In the case of XeF_2, the fragmentation ratios can be obtained by scattering a XeF_2 beam from an inert surface which has no reactivity with XeF_2 and therefore reflects 100% of the incident XeF_2 molecules. The challenge then becomes finding a surface that is inert to attack by XeF_2 under the experimental conditions used in the present investigation. The following section describes the use of a silicon oxide surface to determine the XeF_2 fragmentation ratios. In the case of XeF, it is unfortunately not possible to measure its fragmentation ratio since no pure sources of XeF can be generated with the experimental apparatus available

for this investigation. An indirect method for identifying the XeF contribution to the measured Xe^+ and XeF^+ signals will be presented in Section 2.3 during the discussion of the scattering data.

2.2.3.1 Scattering from an Inert SiO Surface

References[58,61] exist in the literature suggesting the chemical inertness of silicon oxide surfaces to attack by XeF_2. A silicon oxide surface might then be used for the determination of the XeF_2 fragmentation ratios. For the purpose of the current investigation, silicon oxide surfaces prepared by two different methods are tested for inertness. In the first method, oxidized samples are prepared by the Shiraki[96] wet etch before insertion into the vacuum chamber. During this treatment the surface is repeatedly etched in dilute HF in order to produce an atomically flat hydrogen terminated Si surface. In the last step of the preparation method, the hydrogen terminated surface is oxidized in a 3:1:1 mixture of $HCl:H_2O_2:H_2O$. This treatment produces a protective thin surface oxide which can be later removed by heating the sample in vacuum to a temperature above 900 K.

Several tests for the chemical inertness of this "wet oxide" surface were performed by scattering XeF_2 from this prepared sample. The "wet oxide" silicon surface is exposed to a 0.25% XeF_2/Ar (E_i=6.72 kcal mol^{-1}) beam incident at 0° while products are detected at a scattering angle of 35° at m/e=129, 148, 167, and 85 using a dwell time of 0.1 sec. The scattered products resulting from this exposure are presented in Figure 2.11 (a). The first indication of the oxide's inertness comes from the absence of SiF_4 etch product which is monitored at m/e=85. The small amount of signal that is observed at m/e=85 is attributed to the presence of doubly ionized XeF_2, rather than to the existence of etch product. This assignment is based on the observation of a cluster of masses

[96] A. Ishizaka and Y. Shiraki, J. Electrochem. Soc. **133**, 666 (1986)

consistent with the isotopic distribution of XeF_2^{+2} in the mass spectrum of the incident beam. Additional evidence of the oxide's inertness is given by the instantaneous rise of all three XeF_2 fragment ions immediately upon exposure of the surface to the beam. Any depletion of XeF_2 by its reaction with the surface would appear as a gradual rise in the unreactive product fragments since the surface reactivity is expected to be maximum at zero coverage and decrease with XeF_2 exposure. The signals remain constant and independent of the exposure time suggesting that the oxide surface remains inert even after prolonged exposure to XeF_2. Since all of the incident XeF_2 is assumed to unreactively scatter from the surface, the ratio of scattered mass spectrometer signals yields the fragmentation pattern of XeF_2 under electron bombardment. The cracking ratios for XeF_2 obtained from the "wet oxide" surface are summarized in Table 2-3.

The drawback of the "wet oxide" surface as a useful inert substrate, is that once the oxide is removed by annealing at 900 K, it can not be regenerated in vacuum. The advantage of using an oxidized surface that can be produced and removed in vacuum is that it allows for comparisons of the unreactive surface measurements under the same exact conditions used in the reactive surface measurements. Therefore, an alternative method which allows for the production of an oxygen terminated surface inside the vacuum chamber was devised. The clean Si(100) sample, held at a temperature of approximately 500 K , is exposed to a supersonic oxygen molecular beam produced by expansion of 600 Torr of pure O_2 through a 100 μ orifice. The exposure time required to obtain a sufficiently thick surface oxide is approximately 15-30 minutes. The results of scattering XeF_2 from this "vacuum oxidized" surface are presented in Figure 2.11 (b). In this case, the 0.25% XeF_2/Ar beam (E_i=6.72 kcal mol^{-1}) used to test the inertness was incident at 35°, and the scattered signals are collected along the surface's normal. Slight reactivity is observed during the initial moments of exposure to the beam as evidenced by the gradual rise of the scattered XeF_2^+ and XeF^+ signal and the initial decrease of the Xe^+.

All three signals, however, become constant after the first second of exposure and remain so for the duration of the XeF_2 exposure.

An additional test for the inertness of the "vacuum oxidized" silicon surface is provided by a thermal desorption measurement. If the oxide surface is indeed totally unreactive, no fluorine-containing thermal desorption products should be observed after exposure to a XeF_2 beam. The thermal desorption products observed after exposing the oxidized surface to XeF_2 are presented in Figure 2.12 and Figure 2.13. Figure 2.12 (a) shows the thermal desorption spectra of a "vacuum oxidized" surface that was exposed to 0.25% XeF_2/Ar (E_i=6.72 kcal mol^{-1}) incident at 35° for 120 seconds. Only a small amount of SiF_2^+ signal is observed to desorb from the surface at an unusually high temperature (~1050 K). Figure 2.12 (b) shows the near absence of SiF_3^+ signal, which is not surprising since it is expected that a high fluorine coverage would be necessary for the production of such a fluorine rich molecule as SiF_4. Figure 2.13 (a) shows a small amount of Xe which desorbs at a very low surface temperature. Figure 2.13 (b) presents the only substantial thermal desorption product obtained from the oxidized surface, which is SiO (m/e=44) desorbing at ~1050 K. It is believed that all oxygen on the surface is removed in the form of SiO since no other oxygen containing products are observed. For example, note the flat trace at the bottom of Figure 2.13 (b) which confirms the absence of SiO_2.

The thermally desorbed products are consistent with a very small amount of XeF_2 penetrating the porous SiO surface and accessing a few reactive sites available within it. The small fraction of XeF_2 that is able to react produces a small amount of SiF_x deep within the oxide layer. Some of the Xe liberated by these reactive events may be trapped in an interstitial site inside the porous oxide. The weakly bound Xe is readily desorbed by a small rise in the surface temperature. The deeply buried SiF_x species are eventually liberated in the form of SiF_2, but only once the SiO layer starts to decompose at nearly

1000 K. The small amount of reactivity observed from the "vacuum oxidized" surface is thought to be limited to the first instants of XeF_2 exposure as suggested by the quick recovery towards a constant value of the scattered signals in Figure 2.11 (b). In spite of the initial reactivity, after the few reactive sites are fluorinated, the "vacuum oxidized" surface appears to be suitably inert for the purpose of determining the fragmentation pattern of XeF_2. The cracking ratios obtained from this "vacuum oxidized" surface are presented in Table 2-3, and are consistent with those obtained from the "wet oxide" surface. The "wet oxide" surface appears to be more inert than the "vacuum oxidized" probably as a consequence of its thicker oxide layer produced by the more severe wet treatment.

To further support the unreactive nature of the "vacuum oxidized" surface, an angular and mass distribution of the scattered molecules is measured upon exposure of the 250 K surface to the 0.25% XeF_2/Ar beam (E_i=6.72 kcal mol^{-1}) incident at 35°. The angular distributions presented in Figure 2.14 are measured at the four nominal m/e settings of interest (129, 148, 167 and 85 amu) while the mass spectrometer is rotated by 1° every three seconds. The resolution setting of the mass spectrometer is broadened so as to maximize the signal. As expected, the angular distributions of the four fragments are identical, including that for the m/e=85 signal at the bottom of the graph which is consistent with its assignment to XeF_2^{2+} rather than to SiF_2. All masses show a broad, nearly cosine, distribution of scattering angles. Since they all arise from the same neutral, the four distributions can be scaled so that they overlap each other exactly. The relative scaling factors used to achieve this overlap constitute yet another measurement of the XeF_2 cracking ratios, which are summarized in Table 2-3.

The average of the three measurements summarized in Table 2-3 constitute the XeF_2 cracking ratios used in the analysis of the present experiments. The relative amount of XeF^+ associated with a given measured XeF_2^+ signal is denoted by (XeF^+:XeF_2^+) and has

a value of 2.0. Similarly, the fraction that fragments into Xe^+ is denoted as $(Xe^+ : XeF_2^+)$ and amounts to 2.8 times the measured XeF_2^+ signal.

Table 2-3 Cracking Ratios for XeF_2

Scattering surface	$(XeF^+ : XeF_2^+)$	$(Xe^+ : XeF_2^+)$
Wet oxidized (0° detection)	2.0	2.7
Vacuum oxidized (0° detection)	2.0	2.8
Vacuum oxidized (all angles)	1.9	2.8

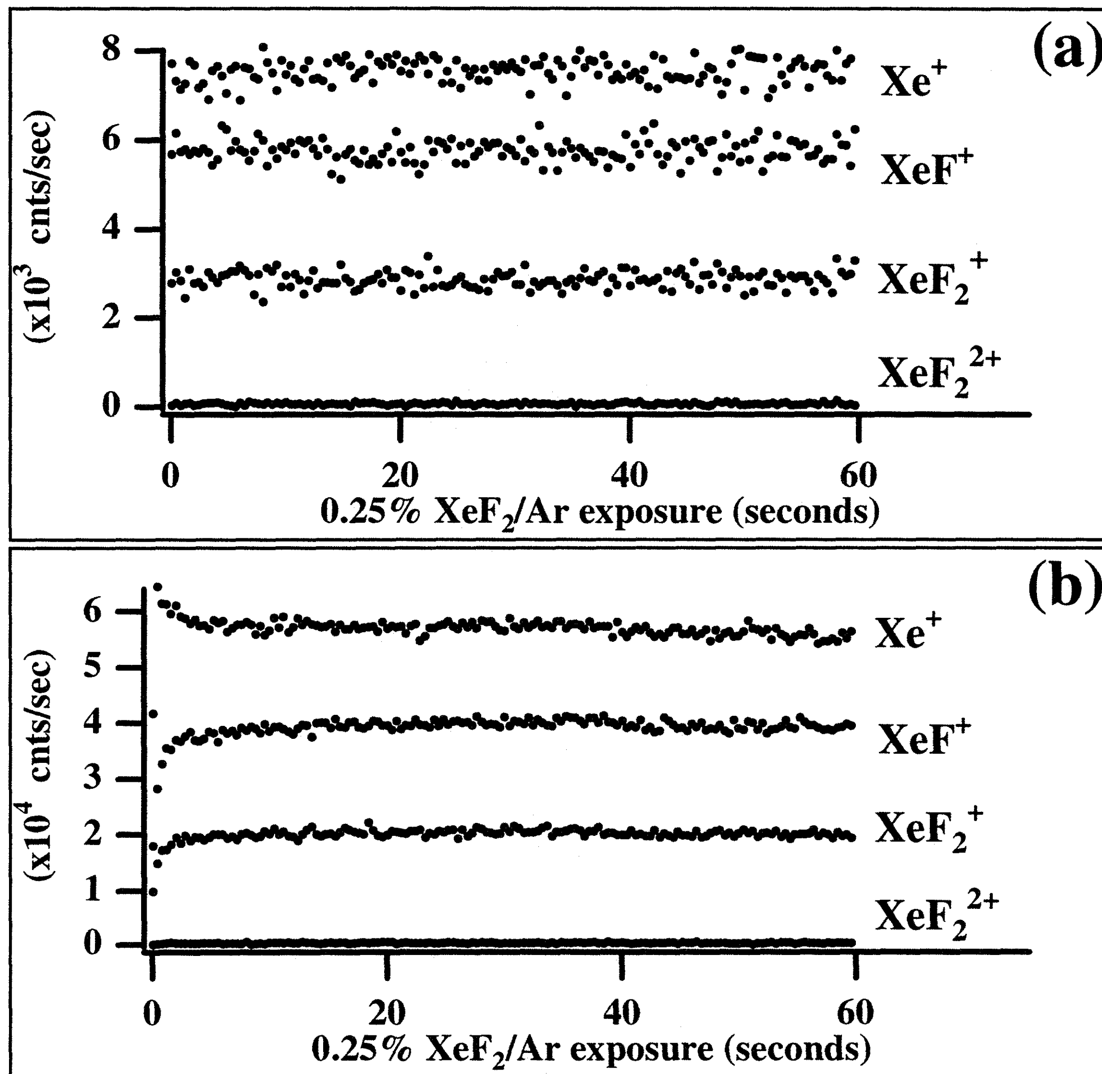

Figure 2.11 XeF_2 Scattered from Inert Silicon Oxide Surfaces

Scattered signals at m/e=129,148,167 and 85 amu from oxidized Si surface held at 250 K and exposed to a 0.25% XeF_2/Ar beam (E_i=6.72 kcal mol^{-1}). (a) Surface oxidized by Shiraki wet etch method. XeF_2/Ar beam incident along surface normal and detected at 35° (b) Surface oxidized in vacuum by 45 minute exposure to a 600 Torr pure O_2 beam incident at 35° onto the Si surface held at a temperature of 500 K. XeF_2/Ar beam incident at 35° and detected at normal angle.

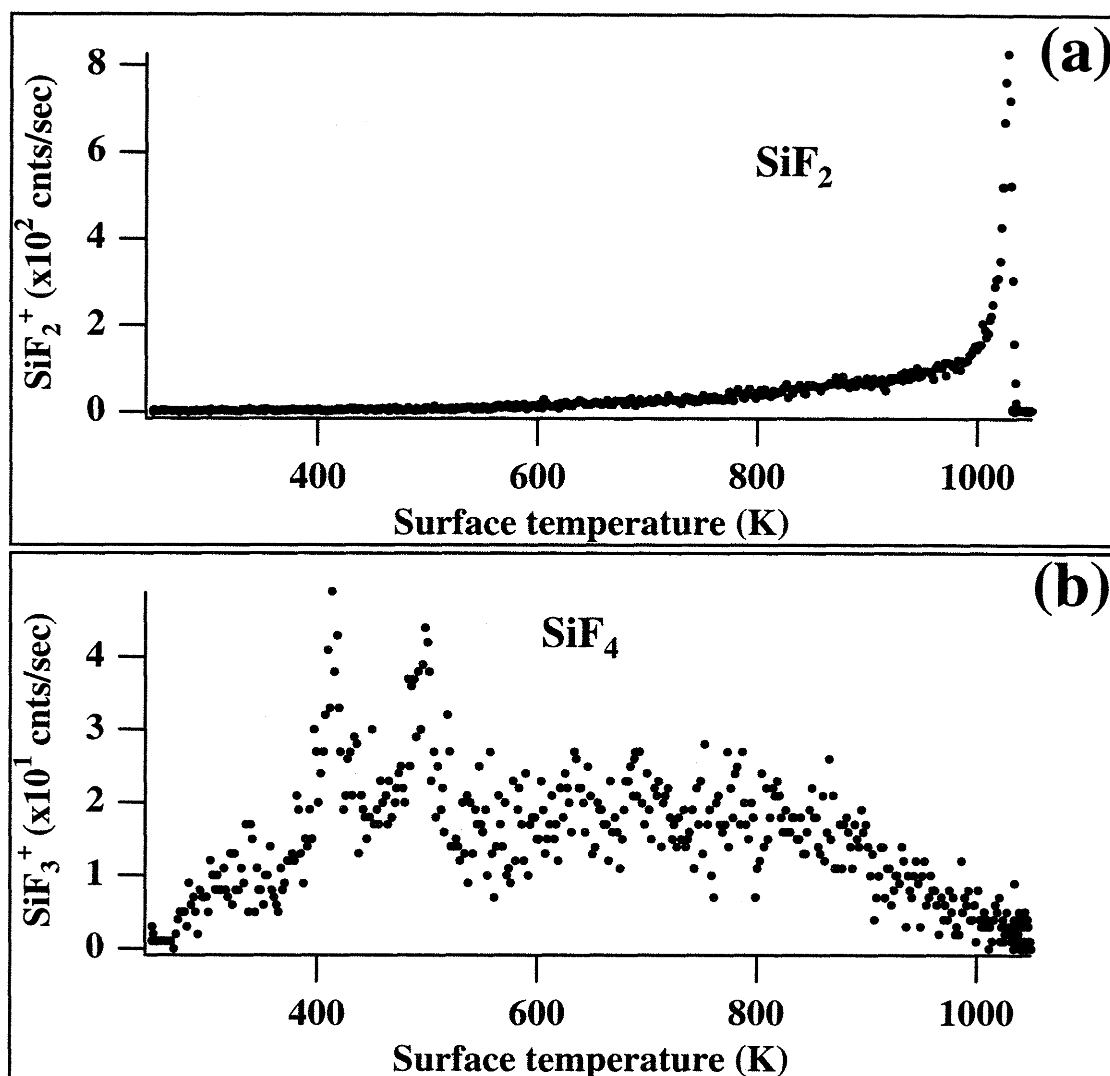

Figure 2.12 Thermal Desorption Products from Inert Surface

The inert silicon oxide surface is produced in vacuum by exposing the clean Si(100) to a 600 Torr O_2 beam incident at 35° for a duration of ~15 minutes. This unreactive surface is then exposed to 120 second dose of 0.25% XeF_2/Ar (E_i=6.72 kcal mol^{-1}) also incident at 35°. (a) A very small amount of SiF_2 product is seen to desorb at 1000 K. (b) Shows that essentially no SiF_4 product is observed to desorb from the oxidized surface.

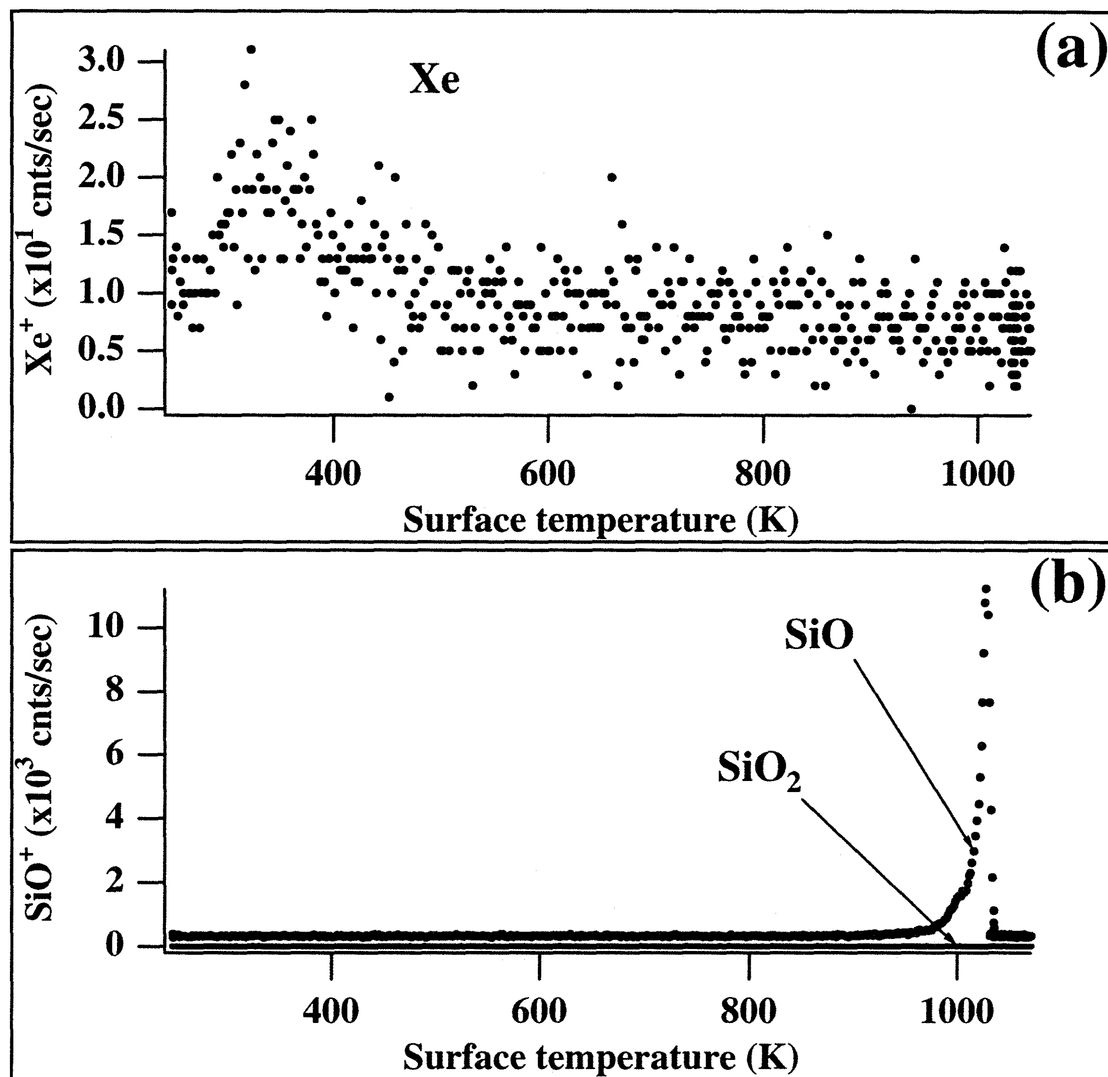

Figure 2.13 Thermal Desorption Products from Inert Surface

The oxide surface preparation and subsequent fluorine exposure have been described in the caption of Figure 2.12. (a) A tiny amount of Xe (m/e=129), which is probably trapped inside porous oxide is seen to desorb at a very low surface temperature. (b) The major product observed to desorb is SiO detected as SiO^+. Note that no SiO_2 is observed.

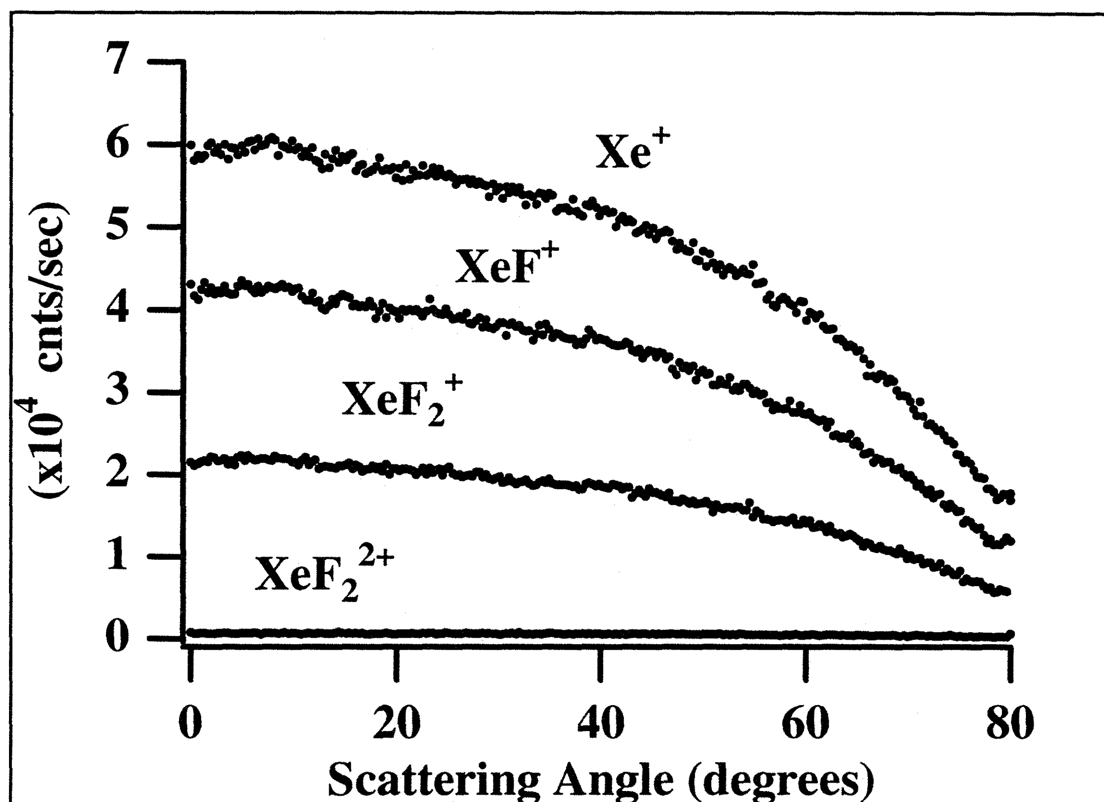

Figure 2.14 Angular Distribution of Scattered XeF_2 from a Silicon Oxide Surface

Angular distribution of unreactively scattered XeF_2 detected at m/e=129, 148,167 and 85 amu from the "vacuum oxidized" surface. During each independently measured angular distribution, the surface is exposed to a 0.25% XeF_2/Ar beam (E_i=6.72 kcal mol^{-1}) incident at 35°. All fragments display the same distribution of scattering angles, suggesting that they all arise from the same neutral product (XeF_2).

2.3 RESULTS

This section presents the experimental data required to demonstrate the existence of the F-atom abstraction mechanism in the interaction of XeF_2 with Si(100). Confirmation of an abstraction event requires the mass spectrometric identification of a XeF molecule ejected from the Si surface upon exposure to XeF_2. The identification of the ejected XeF fragment is obtained from a combination of the exposure dependence, velocity distribution and angular distribution of all scattered reaction products. The deconvolution of the mass spectrometer signals into the contributions from each of the neutrals giving rise to them is complicated by the lack of a reliable XeF cracking ratio (see 2.2.3). By combining the exposure dependence and angular distribution of the scattering products, a self-consistent deconvolution approach is devised to circumvent the need for the XeF cracking ratio.

Figure 2.15 presents the mass spectrometer signal of the scattered Xe, XeF, XeF_2 and SiF_4 as a function of exposure of the Si(100) surface held at 250 K to a 600 Torr 0.25% XeF_2/Ar (E_i=6.72 kcal mol^{-1}) beam expanded through a 10 μ nozzle. The beam is incident at 35° from the surface normal and the mass spectrometer is positioned along the surface normal. The mass spectrometer is multiplexed allowing the four different mass-to-charge ratios to be monitored simultaneously. The dwell time at each m/e setting is 0.1 seconds, and a 0.005 second dead-time is used between successive m/e jumps to allow the mass setting to stabilize. The four mass-to-charge ratios detected are nominally 85, 129, 148, and 167 corresponding to SiF_3^+, Xe^+, XeF^+ and XeF_2^+ respectively. In an effort to maximize the signal, the resolution of the mass spectrometer is broadened to the point were none of the Xe isotopes can be individually resolved (see Figure 2.5 (a)). The nominal m/e settings quoted refer to the center of a broad feature including contributions from all Xe isotopes. A higher resolution spectrum in the m/e=85 range reveals a cluster of low intensity features corresponding to doubly ionized XeF_2 and a sharp feature, of

much higher intensity, centered at m/e=85 assigned to SiF_3^+. In the case of m/e=85 the main contribution to the broad peak arises from the SiF_3^+ etch product with a negligible amount of XeF_2^{2+} present. No signal is observed at the mass-to-charge ratios of 66 or 151 corresponding to SiF_2^+ or $Si_2F_5^+$.

A scattering measurement identical to that shown in Figure 2.15 is repeated for a series of detection angles. The clean Si(100) surface is exposed in each case to a beam of 0.25% XeF_2/Ar (E_i=6.72 kcal mol^{-1}) incident at 35° for a total of 60 seconds. Figure 2.16 presents these plots of the exposure dependence of the XeF_2 reaction products, where each plot represents a measurement made at one of nine scattering angles. The top left plot corresponds to the mass spectrometer's signal detected at 0° scattering angle (already shown in Figure 2.15), where the full scale count rate is of the order of $1.2x10^4$ counts/sec and the origin of the axis corresponds to zero counts. The top trace at each scattering angle corresponds to Xe^+ (m/e=129), the middle one to XeF^+ (m/e=148) and the bottom one to XeF_2^+ (m/e=167). The horizontal axis represents the exposure time with a full scale of 60s. The origins of the vertical axes of the plots at the other scattering angles are also fixed at zero, but their full scales are reduced by a factor of the cosine of the detection angle. This procedure ensures that the vertical axis in each case is expanded to best display the exposure dependence of all three signals. The labels on the axes have been omitted since they are not essential for noting the qualitative differences between the various scattering angles. Further analysis of the scattering data presented in Figure 2.15 and Figure 2.16 is presented separately for each of the four scattered products in the following four sections. Each section also includes data on the velocity distribution of the appropriate scattered product.

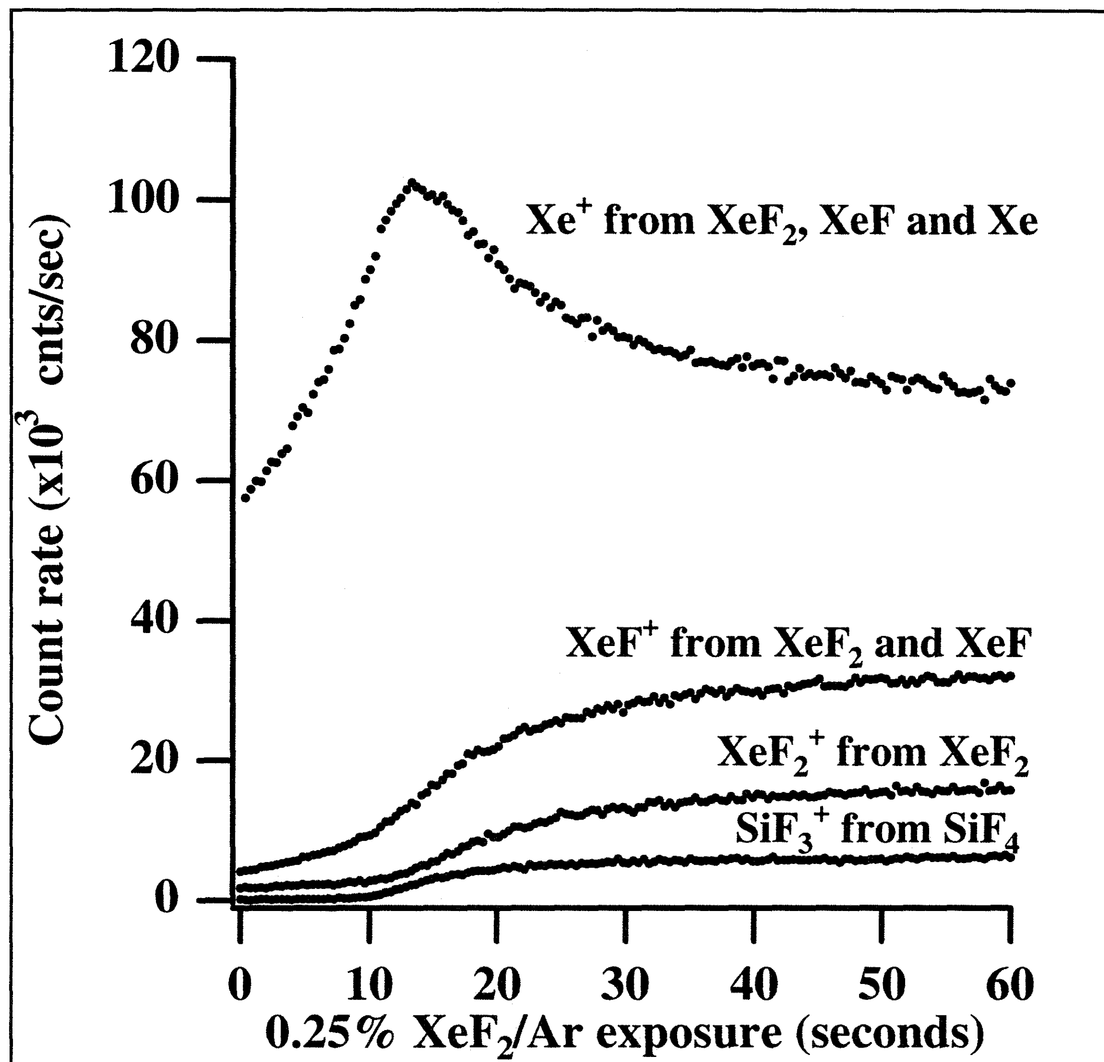

Figure 2.15 Scattered Products as a Function of Exposure to a XeF_2/Ar Beam

Products scattered along surface normal from a 250 K Si(100) surface exposed to a 0.25% XeF_2/Ar beam (E_i= 6.72 kcal mol^{-1}) incident at 35°. The lower trace is SiF_3^+ (m/e= 85) from SiF_4 etch product. The second trace is XeF_2^+ (m/e= 167) arising from unreactively scattered XeF_2. The third trace is XeF^+ (m/e=148) from the cracking of the scattered XeF_2 and from XeF produced by F-atom abstraction. The top trace is Xe^+ (m/e=129) from four possible sources: Xe liberated by the surface reaction, cracking of XeF ejected after an atom abstraction event, dissociation of excited XeF^*, and cracking of unreactively scattered XeF_2.

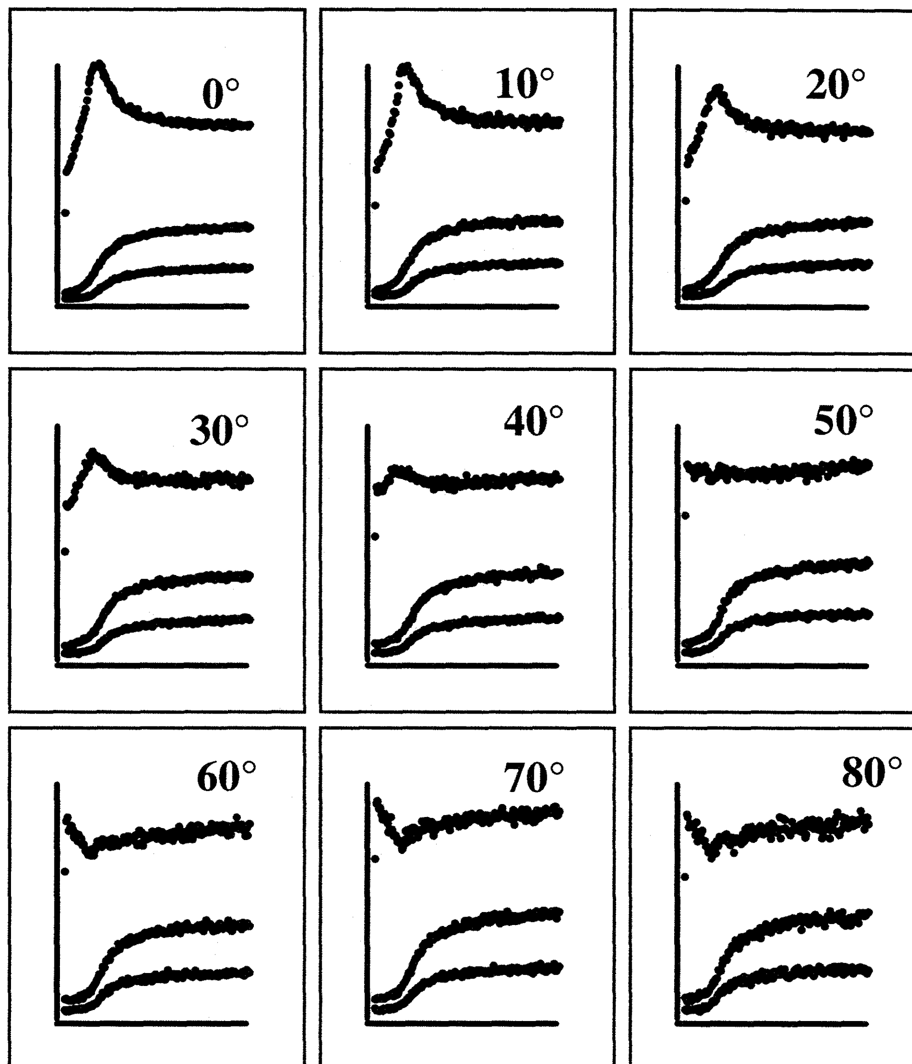

Figure 2.16 Scattering Angle Dependence of the XeF_2/Si Reaction Products

Scattered products as a function of scattering angle from surface normal. Surface is held at 250 K and exposed to 0.25% XeF_2/Ar beam (E_i=6.72 kcal mol^{-1}) incident at 35° for a duration of 60 seconds. Within each panel, from top to bottom, signals correspond to Xe^+, XeF^+, XeF_2^+ (m/e= 129, 148, 167). The horizontal axis corresponds to 0 to 60 sec XeF_2 exposure. The vertical axis of the first panel ranges from 0 to $1.2x10^4$ counts sec^{-1}. The full scale of the vertical axis in every other panel has been scaled by a factor of the cosine of the detection angle (see text).

2.3.1 Observation of Unreactively Scattered XeF_2

The m/e=167 signal in Figure 2.15 corresponds to XeF_2^+ which arises from the electron impact ionization of unreactively scattered XeF_2. Its shape is reminiscent of that observed for unreactively scattered F_2 in the F_2/Si reaction. At low coverage, when many reactive sites are available on the surface, the incoming XeF_2 is most likely to react. Thus at short exposure times, the scattered XeF_2^+ signal is low. As more surface sites are occupied by fluorine, the probability of unreactive scattering increases giving rise to a higher scattered XeF_2^+ signal. This signal eventually reaches a constant level at long exposure times. Unlike the F_2 reaction with Si, the constant signal level does not correspond to the end of the fluorination reaction, but rather, to a steady state equilibrium between the fluorination and etching processes, referred to as the "steady-state etching regime", and evidenced by the presence of a constant amount of SiF_4 etch product at longer exposure times. Note that the drop in the XeF_2 reactivity marked by the sudden rise of the unreactively scattered signal matches the onset of the SiF_3^+ signal corresponding to etch product formation.

The angular distribution of the scattered XeF_2 can be extracted from the data presented in Figure 2.16. The XeF_2 signal as a function of scattering angle for the long exposure regime (30-60 sec), where the m/e=167 signal in Figure 2.15 has reached a constant value, is shown in Figure 2.17 (a). The angular distribution obtained at long exposure fits well to a cosine functional form which is consistent with the thermal accommodation of XeF_2 on the fluorinated surface. Figure 2.17 (b) shows the angular distribution for scattered XeF_2 for the short exposure regime (0-10 sec). The exposure is limited to the flat region preceding the sudden rise of the m/e=167 signal in Figure 2.15. The angular distribution measured at short exposure peaks at a scattering angle near 35°, which is the incident angle of the XeF_2 beam. The preferential scattering at the specular angle is consistent with a direct inelastic scattering process in which the XeF_2 briefly

interacts with the surface, but retains some memory of its incident angle and velocity.

The velocity distribution of the scattered XeF_2 product measured at both short and long exposure confirms the degree of thermal accommodation suggested by the angular distribution measurements. Any XeF_2 that does survive its encounter with the unfluorinated surface must have avoided a prolonged interaction, and therefore must retain a large fraction of its incident velocity. This effect is clearly confirmed by the time-of-flight spectra of XeF_2^+ scattered from a clean Si(100) surface during the initial time of exposure (0-30 sec) to a 0.25% XeF_2/Ar beam incident at 35°, presented in the top panel of Figure 2.18. The time-of-flight distribution of the incident XeF_2 impinging on the surface is overlaid for comparison purposes. The XeF_2 exposure time over which the spectrum is measured is restricted to the time during which the amount of XeF_2 observed to scatter is small (see Figure 2.15). The observed distribution is approximately fitted to a supersonic functional form[97] with a flow velocity of 531 m sec^{-1} and a beam temperature of 641 K, which suggests direct scattering of the impinging XeF_2. This distribution reflects a characteristic temperature higher than that of the 250 K surface, and is thus consistent with XeF_2 molecules that have not substantially thermalized with the clean surface, and scatter without reacting. This direct scattering of XeF_2 in the short exposure regime is consistent with the specularly peaked angular distribution of Figure 2.17 (b) since directly scattered XeF_2 will retain some memory of its angle of incidence and lead to preferential scattering at the specular angle.

The lower panel in Figure 2.18 depicts the time-of-flight distribution of XeF_2 scattered from the surface in the steady-state etching regime (60-120 sec exposure), during which unreactively scattered XeF_2 is the dominant product. The best fit to the data is obtained by using a Maxwell-Boltzmann distribution with a characteristic

[97] see section of uncertainty in the flux of seeded beams in Appendix A

temperature of 300 K, near that of the surface temperature, which implies a large degree of accommodation. Two factors probably contribute to the thermalization of XeF_2 on the highly fluorinated surface: 1) The fluorine adlayer makes the surface more inert, and thus allows XeF_2 to undergo a substantial number of collisions before it scatters back to the gas phase chemically unaltered. 2) The fluorine coverage contributes to "roughen" and "soften" the surface largely increasing both the number of collisions with the surface and their inelasticity. This thermalization of the scattered XeF_2 at long exposures is consistent with the broad angular distribution observed in Figure 2.17 (a).

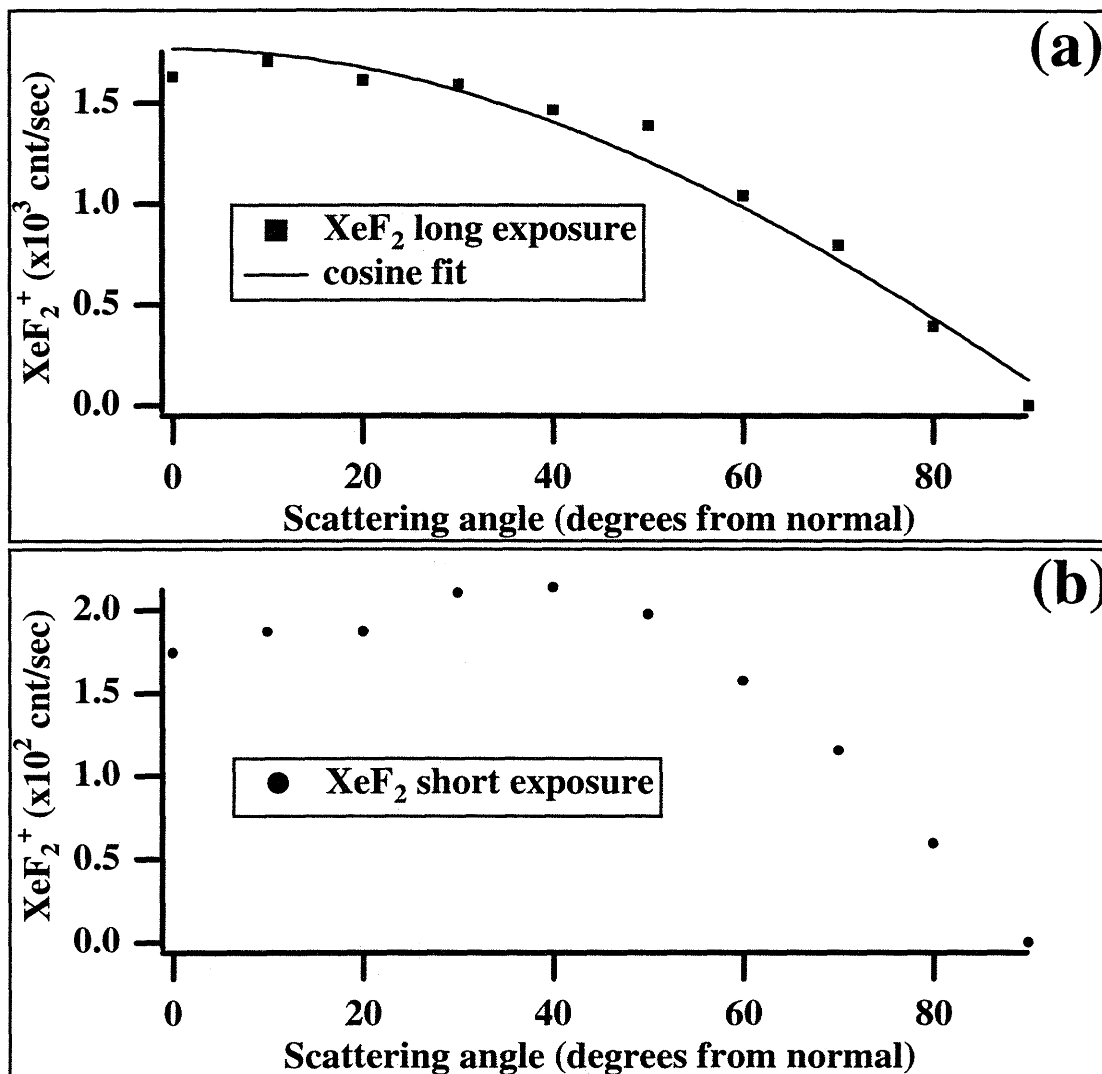

Figure 2.17 Angular Distribution of Scattered XeF_2

Angular distribution of scattered XeF_2 at short and long exposure (a) The XeF_2^+ signal in the long exposure range (60-120 sec) is averaged and plotted as a function of scattering angle. A fit to a cosine functional form reproduces well the experimental data. (b) The XeF_2^+ signal in the short exposure range (0-30 sec) is averaged and plotted as a function of scattering angle.

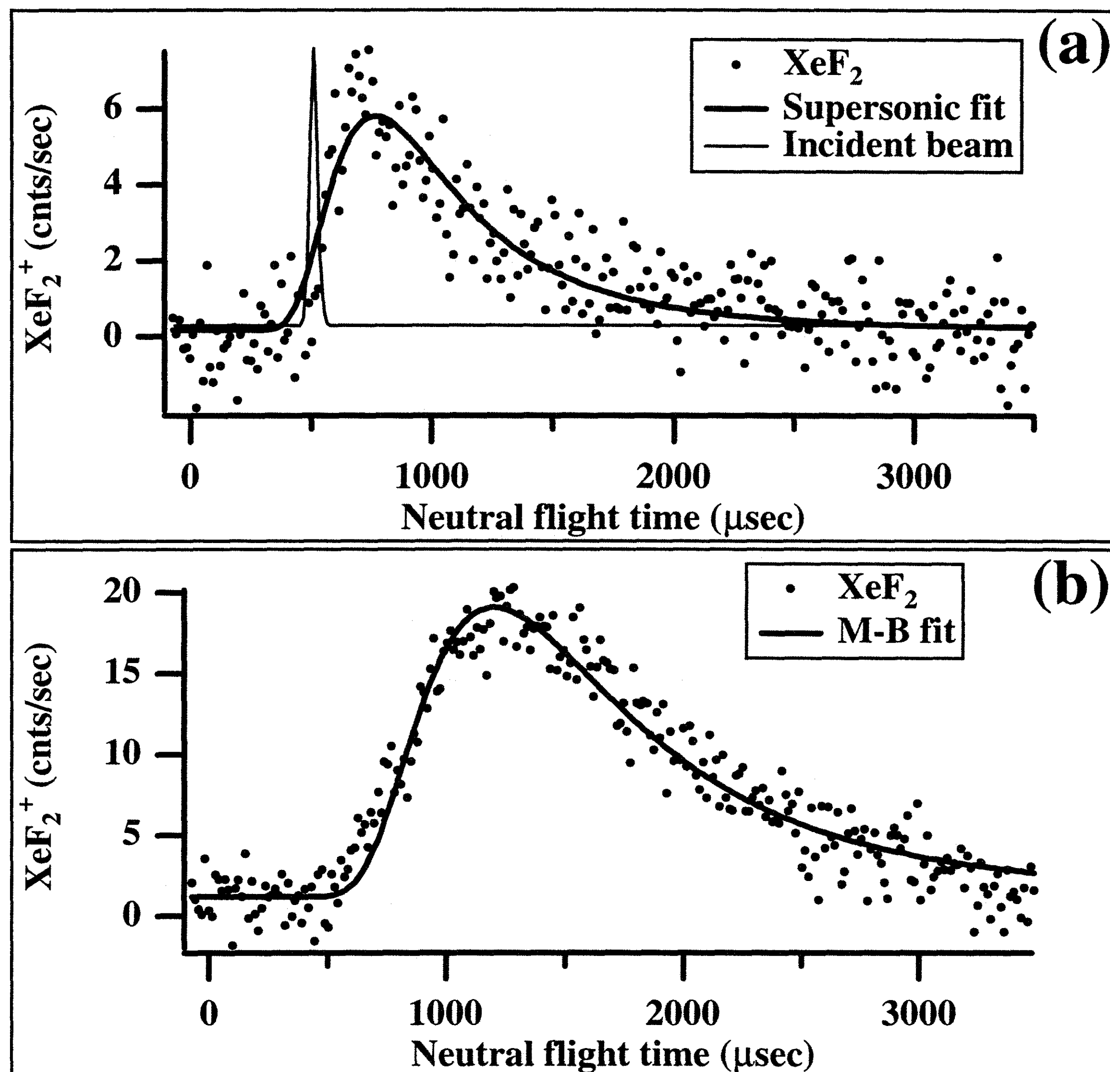

Figure 2.18 Time-of-flight Spectra of XeF_2 Unreactively Scattered from Si(100)

Time-of-flight of scattered XeF_2^+ signal from a 250 K Si(100) surface exposed to a 0.25% XeF_2/Ar beam incident at 35°. (a) Signal collected at surface normal over the initial exposure time (0-30 sec). The data are fit to a supersonic velocity distribution with a flow velocity of 531 m sec^{-1} and a beam temperature of 641 K corresponding to an average velocity of 359 m sec^{-1}. The velocity distribution of the incident XeF_2 beam is also included for comparison. (b) Signal collected at longer XeF_2 exposures (60-120 sec). The data are fit to a Maxwell-Boltzmann velocity distribution with a temperature of 300 K and a corresponding average velocity of 229 m sec^{-1}.

2.3.2 Identification of Atom Abstraction by Observation of XeF

The m/e=148 signal in Figure 2.15 corresponds to XeF^+ which arises from two distinct sources. The trivial source of the XeF^+ signal is the cracking of unreactively scattered XeF_2 upon electron impact ionization. The other source of XeF^+, and the more difficult one to confirm, is the ionization of a XeF neutral fragment produced upon abstraction of one of the fluorine atoms from the incident XeF_2 by the Si surface. In principle, deconvolution of the XeF^+ signal into the contribution from dissociative ionization of XeF_2 and that from XeF is straightforward. Since XeF_2 arises from a non-reactive interaction with Si and XeF from a reactive interaction, each species should have a different dependence on exposure.

The dependence of the XeF abstraction product on exposure is given by the difference between the XeF^+ signal and the XeF_2^+ signal multiplied by its probability for cracking into XeF^+ upon electron impact ionization. Figure 2.19 (a) shows the XeF^+ and XeF_2^+ signals scattered at 0°. The XeF_2^+ signal is scaled by XeF_2 cracking ratio, the probability that XeF_2 dissociatively ionizes to produce XeF^+, so that it represents the XeF_2 contribution to the XeF^+ signal. The cracking ratio, given in Table 2-3, is measured by scattering XeF_2 from an inert silicon oxide surface as discussed in Section 2.2.3.1. The fact that the two signals do not have the same exact exposure dependence suggests the presence of a source of XeF different from that produced by the dissociative ionization of XeF_2. Figure 2.19 (b) shows the result of subtracting the two signals in (a). The difference of these signals is ascribed to the exposure dependence of the XeF abstraction product. The low signal intensity of the resulting XeF signal suggests that nearly all of the XeF^+ arises from the cracking of XeF_2, and therefore, that the abstraction reaction is unimportant. However, it is also possible that XeF produced during an abstraction event is dissociatively ionized to Xe^+ and F. If XeF preferentially cracks to give Xe^+, evidence of the abstraction product is then expected to be most clearly seen in

the Xe^+ rather than in the XeF^+ signal. The contributions to the exposure dependence of the Xe^+ signal are discussed in detail in the next section.

The angular distribution of the XeF product resulting from abstraction is obtained from the XeF_2^+ and XeF^+ data in Figure 2.16. Figure 2.20 shows the exposure dependence of the XeF product detected as XeF^+ at eight scattering angles. These plots of the XeF product resulting from abstraction are obtained by scaling the XeF_2^+ signal at each scattering angle in Figure 2.16 by the XeF_2 cracking ratio and then subtracting the result from the XeF^+ signal at that angle. The full scale count rate on the vertical axis of all eight plots is fixed at 700 counts sec^{-1}, with the origin fixed at zero counts. The horizontal axis covers the full XeF_2 exposure range of 0-60 seconds. The labels on the axes have been omitted since they are not essential to noting the qualitative differences in the data between the various scattering angles. Although the signal level is quite low, it can be clearly seen that the XeF product is preferentially scattered at the smaller angles and gradually vanishes as the detection angle increases. At the largest detection angles, no XeF product is detected as XeF^+. The XeF signal at each angle is numerically integrated and plotted in Figure 2.21 as a function of the scattering angle. The resulting angular distribution does not follow a cosine functional form indicating that the XeF does not isotropically desorb from the surface. In fact, the angular distribution is sharply peaked around the normal angle suggesting either that only those XeF molecules scattering at small angles are detected as XeF^+ or that the XeF is strongly oriented during the abstraction event.

Additional evidence for the existence of the XeF abstraction product is obtained from velocity measurements of the scattered products. The data in Figure 2.19 indicate that the two species contributing to the scattered XeF^+ signal have a different exposure dependence, as expected from the fact that they arise from distinct processes. Similarly, it is expected that the XeF^+ ions arising from the dissociative ionization of unreactively

scattered XeF_2 have a different velocity distribution than the XeF^+ arising from the ionization of the XeF abstraction product. The XeF abstraction product is expected to scatter with high translational energy, since it will likely acquire some of the energy released by the formation of the bond between the surface and the abstracted F atom. In addition, no thermal XeF product is likely to be found, since XeF is a relatively unstable species, bound by only 3 kcal mol^{-1}, and will not survive thermalizing collisions with the surface.

Figure 2.22 (a) shows the time-of-flight distribution of the XeF^+ signal during the short exposure (0-30 sec) of a 250 K Si(100) surface to a 0.25% XeF_2/Ar beam incident at 35°. Although the limited XeF^+ signal available at short exposures makes for a noisy spectrum, a bimodal distribution can be clearly discerned. The broad feature which appears at later arrival times can be matched to the time-of-flight distribution of unreactively scattered XeF_2 previously presented in Figure 2.18 (a) and replotted here after scaling by the cracking fraction, to the broad feature of the XeF^+ signal. Since the broad feature accounts for the majority of the XeF^+ scattered signal, the overlap with the XeF_2^+ velocity distribution confirms that the majority of the XeF^+ signal indeed arises from the cracking of XeF_2 and not from XeF abstraction product. The presence of the narrow feature at early arrival times is consistent with XeF abstraction product scattering from the surface translationally excited by the reaction exothermicity. The time-of-flight distribution of the ejected XeF molecules is obtained by subtracting the two distributions presented in Figure 2.22 (a) but is not shown. The time-of-flight distribution of XeF^+ at long exposure times (60-120 sec) is presented in Figure 2.22 (b). A single broad feature is observed which exactly coincides with the time-of-flight distribution of XeF_2^+ previously shown in Figure 2.18 (b) and replotted here after scaling by cracking fraction. This broad distribution is not surprising since at long exposures, the majority of the XeF^+ signal is expected to arise from unreactive scattering of XeF_2. If there is a small amount

of XeF abstraction product contributing to the XeF^+ signal at long exposures, it is not observed due to the presence of a large amount of unreactively scattered XeF_2.

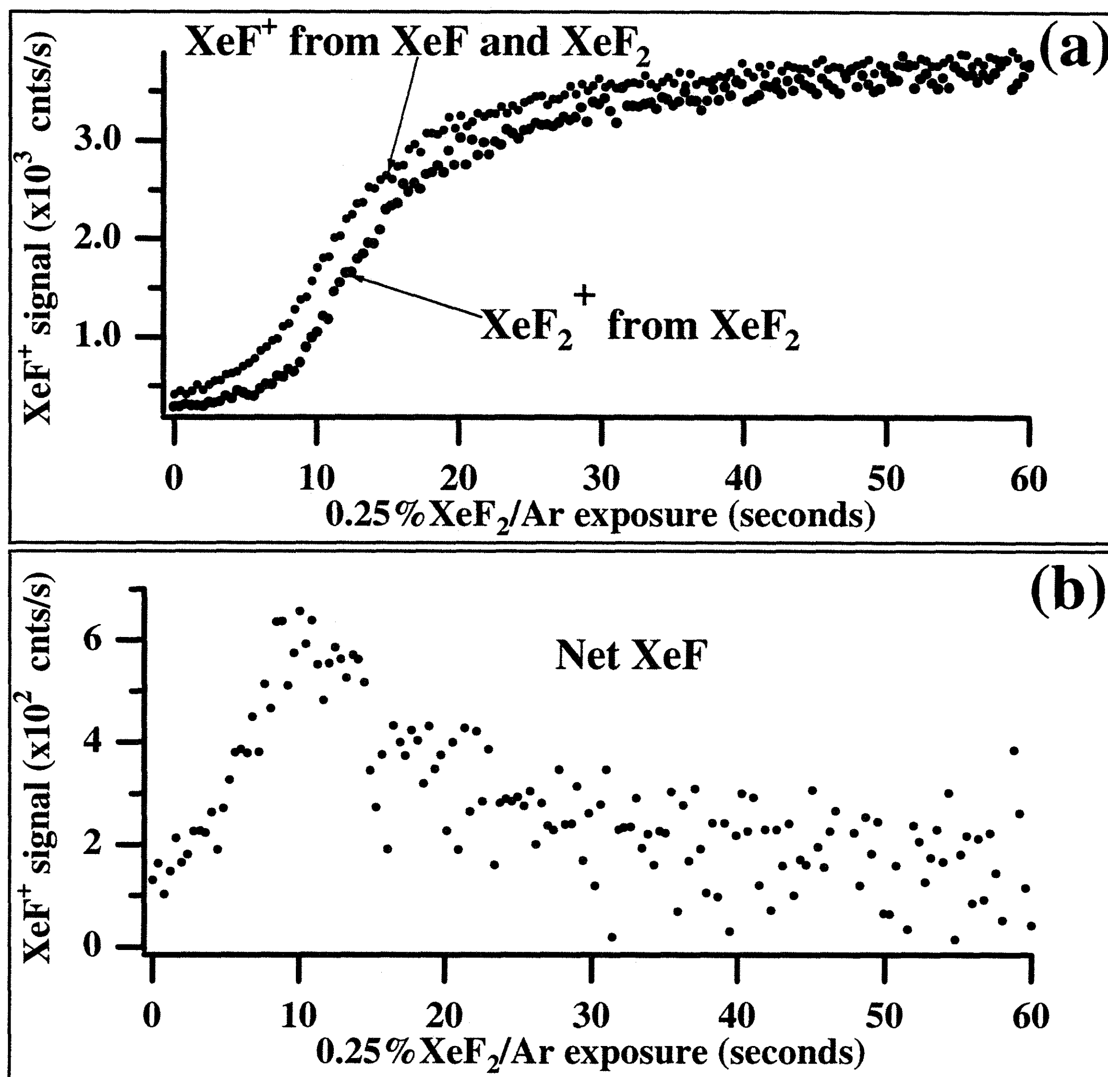

Figure 2.19 XeF from Atom Abstraction Detected as XeF^+

Deconvolution of the XeF^+ signal scattered at 0° into its contributions from dissociative ionization of XeF_2 and atom abstraction. (a) The bottom trace is the XeF_2^+ signal scaled by the XeF_2 cracking ratio to give the XeF_2 contribution to the XeF^+ signal. The top trace is the raw XeF^+ signal. (b) The net XeF product arising from atom abstraction is obtained by subtracting the two curves is (a).

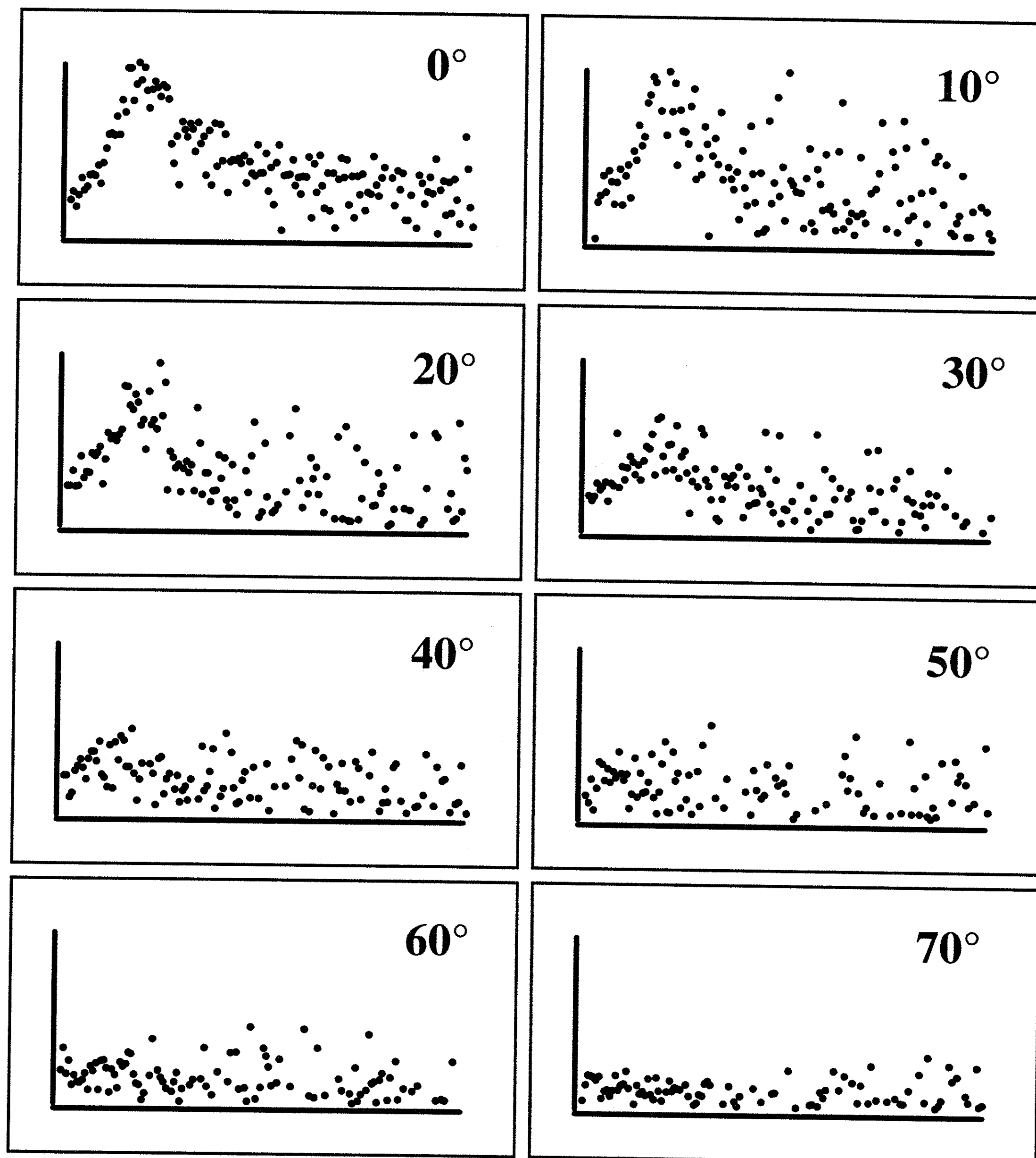

Figure 2.20 Exposure Dependence XeF Product at Eight Scattering Angles

Deconvoluted XeF^+ signal arising from XeF product as a function of scattering angle measured from the normal. Data for each angle are obtained by subtracting the XeF_2^+ signal scaled by the XeF_2 cracking ratio from the raw XeF^+ signal. For each angle, the horizontal axis corresponds to 0-60 sec XeF_2 exposure time and the vertical axis to 0-700 counts sec^{-1} of XeF^+ signal.

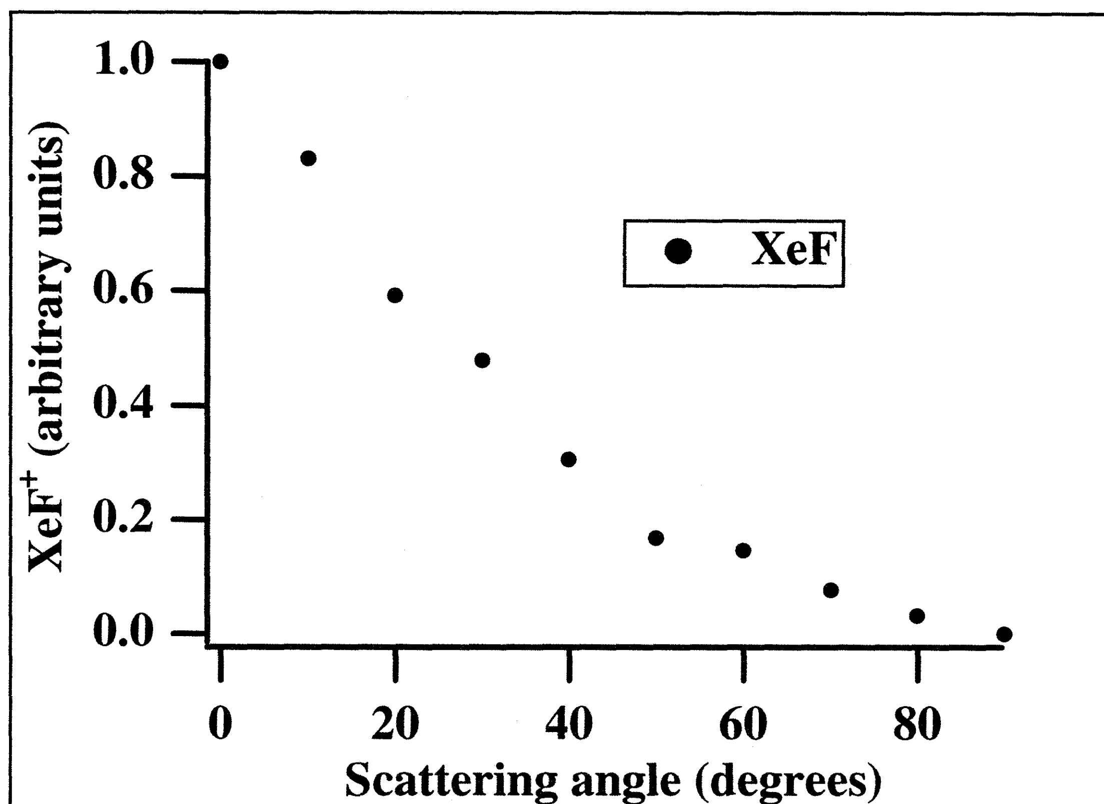

Figure 2.21 Angular Distribution of XeF Product

Angular distribution of XeF product resulting from atom abstraction. The value at each angle measured from the normal, is obtained by integrating the XeF^+ signal arising from atom abstraction over the full exposure range (0-60 sec).

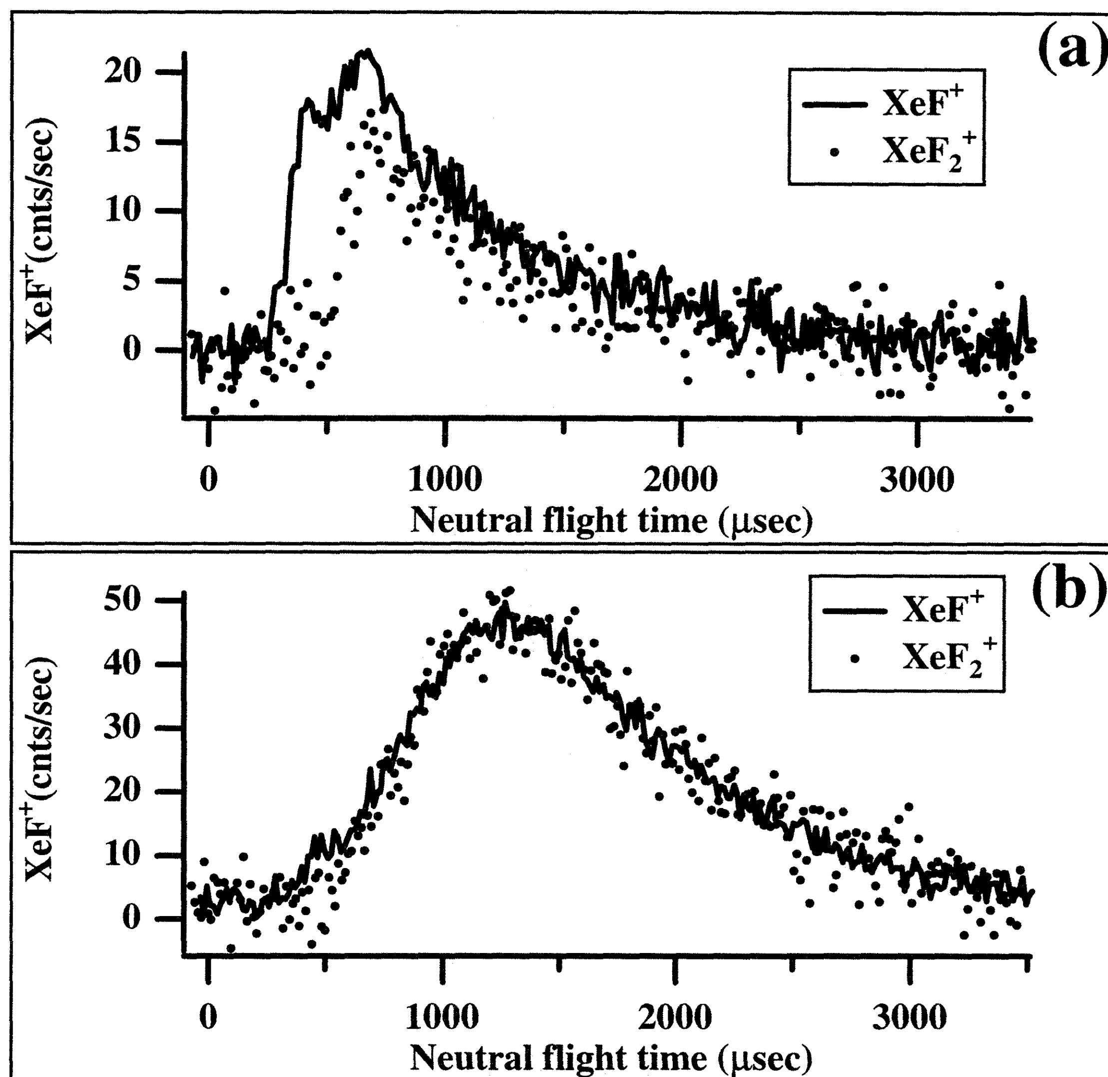

Figure 2.22 Time-of-flight Spectra of Scattered XeF^+ Signal

Time-of-flight spectra of the XeF^+ signal scattered at normal angle from a Si(100) exposed to a 0.25% XeF_2/Ar (E_i=6.72 kcal mol^{-1}) beam incident on the surface at 35°. (a) Short exposure range (0-30 sec). The line corresponds to the XeF^+ signal, the dots correspond to the unreactively scattered XeF_2 time-of-flight distribution at short exposure times, which has been scaled by cracking fraction to fit the broad feature in the XeF^+ signal. (b) Long exposure range (60-120 sec). The line corresponds to XeF^+ signal, the dots correspond to the XeF_2 velocity distribution at longer exposure times, which has been scaled to fit the XeF^+ signal.

2.3.3 Observation of Scattered Xe Product

The top trace in Figure 2.15 corresponds to Xe^+ (m/e=129). It is the most abundant signal observed from the scattering of XeF_2 from a Si(100) surface, because Xe^+ arises from four distinct sources. One source is the unreactively scattered XeF_2, which is known to dissociatively ionize into Xe^+. A second source of Xe^+ signal is the XeF product arising from atom abstraction. By analogy to XeF_2, it is expected that XeF will also dissociate upon ionization yielding a substantial amount of Xe^+. A third source of Xe^+ is Xe from the decomposition of the incident XeF_2 molecule by adsorption of both fluorine atoms and subsequent desorption of the chemically inert Xe. Finally, Xe can be produced by the gas-phase decomposition of the weakly bound (3 kcal mol^{-1}), but vibrationally or electronically excited XeF^* product resulting from atom abstraction. That is, some of the XeF produced by an initial F atom abstraction may acquire sufficient internal energy from the reaction exothermicity to reach a dissociative state, denoted as XeF^* and subsequently decompose giving rise to translationally excited Xe^* and F^* fragments. The excited XeF^* decomposes in the gas phase before reaching the ionization region, so it is the Xe^* and F^* fragments that are ionized and detected as Xe^+ and F^+ respectively. Regardless of the exact mechanism by which the Xe is produced, it will contribute to the Xe^+ signal upon ionization.

The main challenge in understanding the exposure dependence of the Xe^+ signal resides in properly deconvoluting the contributions that give rise to it, so that the exposure dependence of each of the neutral products may be uniquely identified. The first step in the deconvolution is to subtract the contribution from unreactively scattered XeF_2. The procedure is completely analogous to that used to separate the XeF_2 contribution from the XeF^+ signal. The XeF_2^+ signal in Figure 2.15 is scaled by the probability that XeF_2 will crack into Xe^+ (see Table 2-3), and then subtracted from the raw Xe^+ signal. Figure 2.23 (a) presents the raw Xe^+ detected at the normal signal from a

0.25% XeF_2/Ar beam incident at 35° reproduced from Figure 2.15, together with the XeF_2^+ signal scaled to represent the XeF_2 contribution to Xe^+. Figure 2.23 (b) shows the result of subtracting the two curves in the top panel. The resulting trace contains the contributions from the other three neutrals that give rise to Xe^+, namely, Xe, Xe^* (from the gas phase decomposition of excited XeF^*) and XeF.

The next step in the deconvolution of the Xe^+ signal would be trivial if the probability for XeF to dissociatively ionize into Xe^+ were known. Unfortunately, the measurement of the XeF cracking pattern requires a source of pure XeF which is not available for this investigation. Without knowledge of the XeF cracking ratio, there is little hope of directly separating the Xe, Xe^* and XeF contributions to the Xe^+ signal. Fortunately, an indirect method for subtracting the Xe contribution from the partially deconvoluted Xe^+ signal has been devised. The deconvolution method hinges on the observation that the Xe^+ signal has an unusual scattering angle dependence.

The dramatic change in the exposure dependence of the partially deconvoluted Xe^+ signal with detection angle is evident in the top trace of each panel in Figure 2.16. The same data are illustrated in a different format in Figure 2.24, which presents the partially deconvoluted Xe^+ signals for all detection angles on the same plot. The XeF_2 contribution has been subtracted from the raw Xe^+ signal at each scattering angle, so the traces in Figure 2.24 represent the exposure and angular dependence of the combined Xe, Xe^* and XeF reaction products. The top trace corresponds to 0° scattering angle with each successive curve corresponding to a 10° increment in the detection angle. The bottom curve corresponds to a 80° detection angle, measured from the surface normal. Whereas the overall intensity of the Xe^+ signal decreases with scattering angle, a drastic change in the exposure dependence of the signal is observed as the scattering angle increases. At 0° detection, the signal rapidly increases towards a maximum value which is reached at intermediate exposures (~10 sec) and then gradually decreases toward a

non-zero constant value at longer exposures. As the scattering angle increases, the relative intensity of the maximum in the Xe^+ signal decreases. Finally, at the larger scattering angles (> 50°), the maximum in the signal completely disappears and the Xe^+ signal monotonically decreases throughout the entire range of exposure.

The maximum in the partially deconvoluted Xe^+ signal that is observed at low exposure and at low scattering angles is quite similar to that for the XeF abstraction product detected as XeF^+ and previously shown in Figure 2.19 (b). This similarly is consistent with the fragmentation of XeF upon electron impact ionization to yield a substantial amount of Xe^+ signal, and implies that the partially deconvoluted Xe^+ signal may largely arise from the presence of XeF product. The fact that the maximum in the Xe^+ signal gradually vanishes with increasing scattering angle is consistent with the observation that the XeF product also decreases with increasing angle (see Figure 2.20 and Figure 2.21). Furthermore, since the figures show that at an 80° detection angle no XeF product is observed, the monotonically decreasing Xe^+ signal observed at the highest detection angle is assigned solely to Xe released after both of its fluorine atoms have adsorbed. That is, none of the Xe^+ signal at a 80° detection angle arises from the dissociative ionization of XeF or from the gas phase dissociation of XeF^* followed by the ionization of Xe^*. The Xe^+ signal at 80° is then taken to represent the exposure dependence of the Xe product produced by the dissociation of the incident XeF_2 at the surface. The identification of the exposure dependence of the Xe product provides a crucial piece of information for the deconvolution of the Xe^+ signal.

The separation of the Xe contribution is based on subtracting the exposure dependence of the Xe^+ signal detected at 80° from the partially deconvoluted Xe^+ signal detected at all other angles. The assumption is explicitly made that the exposure dependence of the Xe product is independent of scattering angle. Although no direct evidence exists to justify the assumption, the shape of the trace resulting from the

subtraction will determine whether the assumption is reasonable. Since both XeF and Xe^* are the result of an abstraction event occurring at the surface, it is expected that both products display an identical exposure dependence. Furthermore, the exposure dependence of XeF and Xe^* should match the exposure dependence of the XeF^+ signal detected at m/e=148. If the exposure dependence after subtraction of the 80° Xe^+ signal from the Xe^+ at the other angles agrees with that of the XeF detected as XeF^+, then the assumption is likely a valid one. The relative amount of the Xe^+ signal measured at 80° to be subtracted from the Xe^+ signal measured at each angle is therefore determined by trying to ensure a match in the exposure dependence of the resulting Xe^+ signal arising from XeF and Xe^* with the XeF^+ signal detected at m/e=148.

An example of the proposed deconvolution approach is presented in Figure 2.25 by using the data collected at 0° scattering angle. The top trace in Figure 2.25 (a) corresponds to the superposition of Xe, Xe^* and XeF detected as Xe^+ at 0° as m/e=129. The lower trace in this panel is the Xe^+ signal detected at 80°, which is assumed to be entirely due to the Xe product released by the reaction. This Xe signal is scaled such that when it is subtracted from the top trace, the shape of the resulting signal matches that of the XeF product detected as XeF^+. The mathematical algorithm used to determine the amount of 80° Xe^+ product to be subtracted so as to ensure a match between the XeF shapes is presented in detail in Appendix E. The result of this subtraction procedure is presented in Figure 2.25 (b) and is attributed to a superposition of XeF and Xe^* that dissociatively or directly ionizes into Xe^+. Figure 2.25 (c) presents the agreement between the exposure dependence of XeF detected as XeF^+ (dots) and as Xe^+ (line). Although the signal-to-noise of the XeF^+ data is quite low, a reasonable agreement is observed with the less noisy Xe^+ signal. To ensure equivalent magnitudes for the two signals arising from XeF, the weaker XeF^+ signal is scaled by a factor of 13.2. This large value confirms that a substantial amount of the Xe^+ arises from XeF, be it via its

dissociative ionization or the gas phase decomposition of the excited XeF^* followed by ionization of Xe^*. This observation implies that the abstraction mechanism is not as minor as might have been predicted from the low signal detected as XeF^+.

If this deconvolution approach is indeed a valid method to separate the Xe contribution from the Xe^* and XeF contributions, it should work equally well at all detection angles. Figure 2.26 shows the agreement between the exposure dependence of the two signals arising from XeF for the complete set of scattering angles. The overlap of the exposure dependence of the deconvoluted Xe^+ (lines) and the raw XeF^+ (dots) signals is quite good for all scattering angles in spite of the low amount of XeF product present at the higher scattering angles. The fact that this deconvolution approach yields a qualitative match between the exposure dependencies of the XeF signals at all scattering angles lends some confidence to its assumptions. Further information is obtained from the quantitative comparison of the scaling factors used to match the intensities of the two signals arising from XeF at each detection angle.

The scaling factor used to overlap the two signals is in fact a measure of the XeF cracking ratio, which measures the probability for XeF to dissociatively ionize to Xe^+. However, this scaling factor also incorporates the probability for XeF^* to decompose to Xe^* which is then ionized to Xe^+. The average of the scaling factors used to overlap the Xe^+ and XeF^+ signals presented in Figure 2.26 is 11.5 ± 3.5, where the uncertainty corresponds to one standard deviation from the mean. The relatively large uncertainty in this value is likely caused by the low XeF signal beyond the 40° scattering angle. The average of the scaling factors changes to 13.3 ± 0.8 when only data from 0°, 10°, 20° and 30° detection angles are used. The smaller standard deviation from the mean implies that there is a reasonably good agreement in the XeF scaling factor measured at the angles were there is sufficient XeF product to obtain a reliable measurement of XeF^+. The invariance of the scaling factor across different detection angles implies that the angular

distributions of the XeF^+ signal and the deconvoluted Xe^+ signal (which includes contributions from XeF and Xe^*) are nearly indistinguishable. The question then arises of whether Xe^* has the same angular distribution as XeF, or whether the relative contribution of Xe^* to the deconvoluted Xe^+ signal is not enough to modify its angular distribution from that expected of XeF alone. The answer to this question is important, in that it may provide a handle on the relative amount of XeF product which is sufficiently excited (vibrationally or electronically) to decompose in the gas phase. Further discussion of the angular distribution of the Xe^* product and the relative amount of excited XeF^* is presented in Section 2.4.

The interpretation of the velocity distribution of the Xe^+ signal is also complicated by the large number of neutrals giving rise to it. Some scattered Xe^+ signal arises from the dissociative ionization of XeF_2 and XeF. The contributions of these two species to the Xe^+ time-of-flight spectrum should be consistent with their velocity distributions as determined from the XeF_2^+ and XeF^+ data. The rest of the Xe^+ arises from Xe released in the reaction. The scattered Xe is produced by the adsorption of both fluorine atoms of the incident XeF_2, or by the gas-phase decomposition of the XeF^* abstraction product. It is not easy a priori to anticipate what the velocity distribution of the scattered Xe atoms should be. The liberated Xe might directly scatter into the gas phase with a large amount of translational energy harnessed from the exothermicity of the adsorption step, or if its trajectory is aimed at the surface, it may suffer multiple collisions with the surface that would then tend to thermalize it. As for the Xe arising from the gas-phase decomposition of the electronically or vibrationally excited XeF^*, it also can either thermalize by subsequent collisions with the surface, or remain translationally activated by preserving the energy gained in the Si-F bond formation step. The production of Xe atoms from the decomposition of electronically or vibrationally excited XeF^* before it reaches the detector must, however, be accompanied by a momentum-matched F atom partner.

Figure 2.27 (a) presents the scattered Xe^+ time-of-flight distribution detected along the surface normal for a short exposure (0-30 sec) to a 0.25% XeF_2/Ar beam incident on the 250 K Si surface at 35°. The line represents the time-of-flight distribution of the Xe^+ signal at short exposure which is observed to have a single broad feature centered at 500 μsec arrival time. The dots in Figure 2.27 (a) represent the time-of-flight distribution of the unreactively scattered XeF_2, which has been scaled to match the tail of the Xe^+ signal. The good match of the distributions at long flight times implies that most of the slow Xe^+ signal arises from the dissociative ionization of unreactively scattered XeF_2. The Xe^+ signal at early times is at least partially attributable to the dissociative ionization of the XeF abstraction product. This contribution of XeF to the Xe^+ signal can be seen in Figure 2.27 (a), where the XeF^+ time-of-flight (squares) has been superimposed on the Xe^+ signal. The feature at centered at 450 μsec in the XeF^+ signal matches the peak of the Xe^+ signal, indicating that they arise from the same neutral, XeF. The XeF^+ signal has been arbitrarily scaled to make the peak intensities approximately equal. The Xe^+ signal at early times is, however, broader than the fast feature observed in the scaled XeF^+ time-of-flight. The additional breadth of the Xe^+ signal suggests the presence of contributions from neutrals other than XeF. The Xe or Xe^* products liberated by the reaction may contribute to the observed broadening of the fast feature in the Xe^+ time-of-flight spectrum. Unfortunately, the spectrum does not allow for the velocity distribution of the Xe and Xe^* neutrals to be resolved as distinct features from the fast XeF and the slow XeF_2 features.

Figure 2.27 (b) presents the Xe^+ time-of-flight spectra obtained during the longer exposure regime (60-120 sec) to the same XeF_2 beam. As expected, the slow contribution resulting from the cracking of thermalized XeF_2 becomes the dominant feature. Some fast Xe^+ is however still observed at long exposures, indicating that the processes that give rise to fast products (atom abstraction and/or two-atom adsorption

from XeF_2) are still active during the steady-state etching regime.

The decomposition of XeF^* product from atom abstraction to yield Xe^* and F^* can be confirmed from the time-of-flight spectrum of F atoms presented in Figure 2.28. The spectra are collected as F^+ signal at m/e=19 scattered along the surface normal while the 250 K Si surface is exposed to a 0.25% XeF_2/Ar beam incident at 35°. Both the short exposure (0-30 sec) F^+ spectrum (line) presented in (a), and the longer exposure one (60-120 sec) (line) presented in (b), show a slow, broad feature which is accounted for by the cracking of XeF_2 to yield F^+, as evidenced by the good overlap of the slow feature with the scaled XeF_2 angular distributions (dots). In addition, at low exposures, a narrow fast feature, matching the XeF velocity distribution (shown as squares) is observed. A similar fast feature in the long exposure spectra presented in (b) is largely obscured by the high intensity of the slowest feature. This feature is assigned to XeF which cracks to give F^+. Finally, both the short and long exposure spectra show a very fast feature associated with translationally excited F atoms, whose most probable energy is 6.7 kcal mol^{-1}. The presence of fast F atoms is thought to be caused by the gas-phase decomposition of the vibrationally excited XeF^* abstraction product. An initial analysis[98] of the momentum match between the F^* and Xe^* fragments is consistent with the gas-phase decomposition of electronically or vibrationally excited XeF^* abstraction product before it reaches the surface.

[98] M. R. Tate, private communication

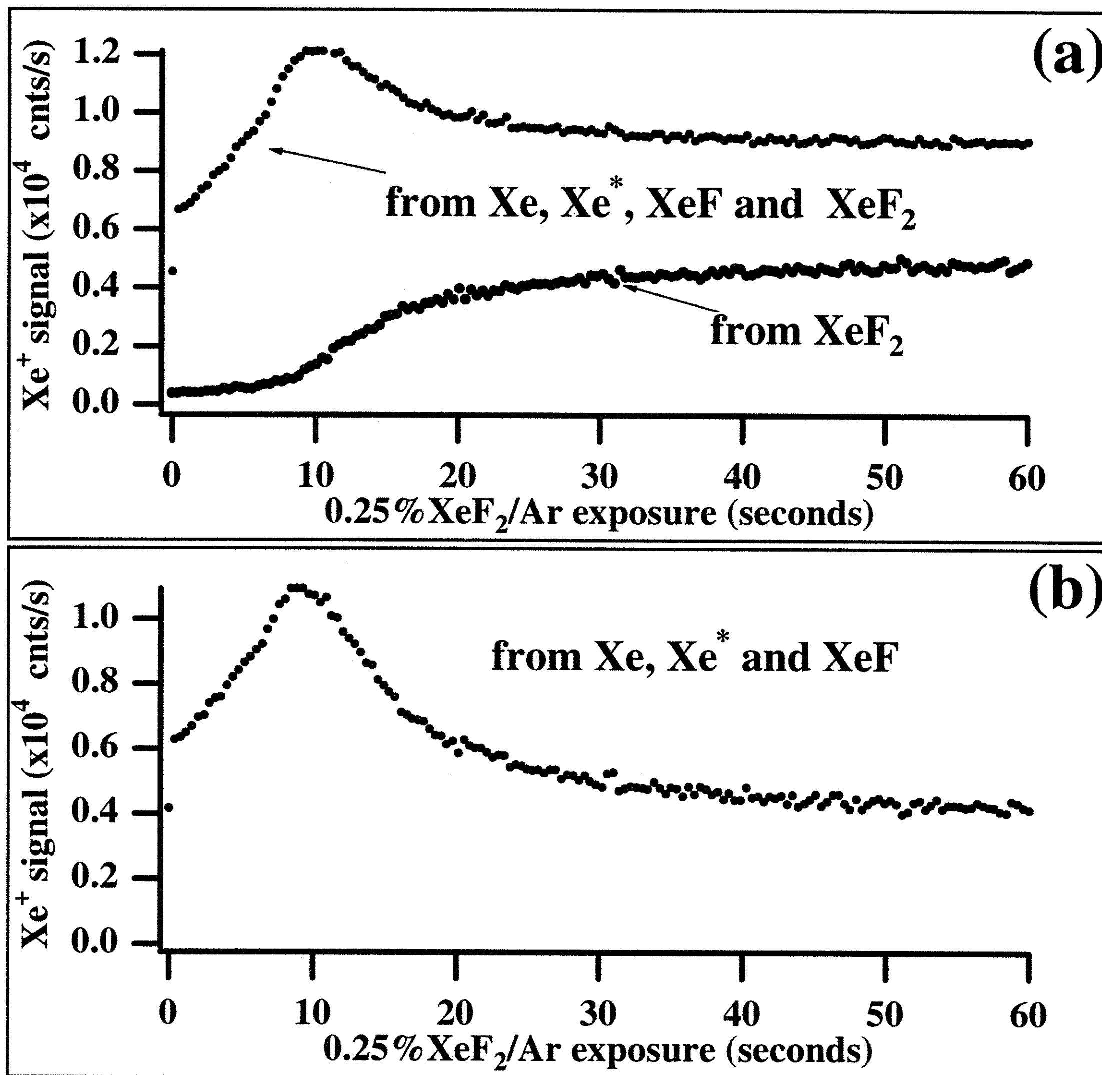

Figure 2.23 Partial Deconvolution of Xe^+ Signal detected at 0°

Deconvolution of the scattered Xe^+ signal into its contribution from dissociative ionization of XeF_2 and the superposition of the Xe, Xe^* and XeF contributions. (a) The bottom trace is the XeF_2^+ signal scaled by the XeF_2 cracking ratio to give the XeF_2 contribution to the Xe^+ signal. The top trace is the raw Xe^+ signal. (b) Superposition of the Xe, Xe^* and XeF contributions obtained by subtracting the two curves in (a).

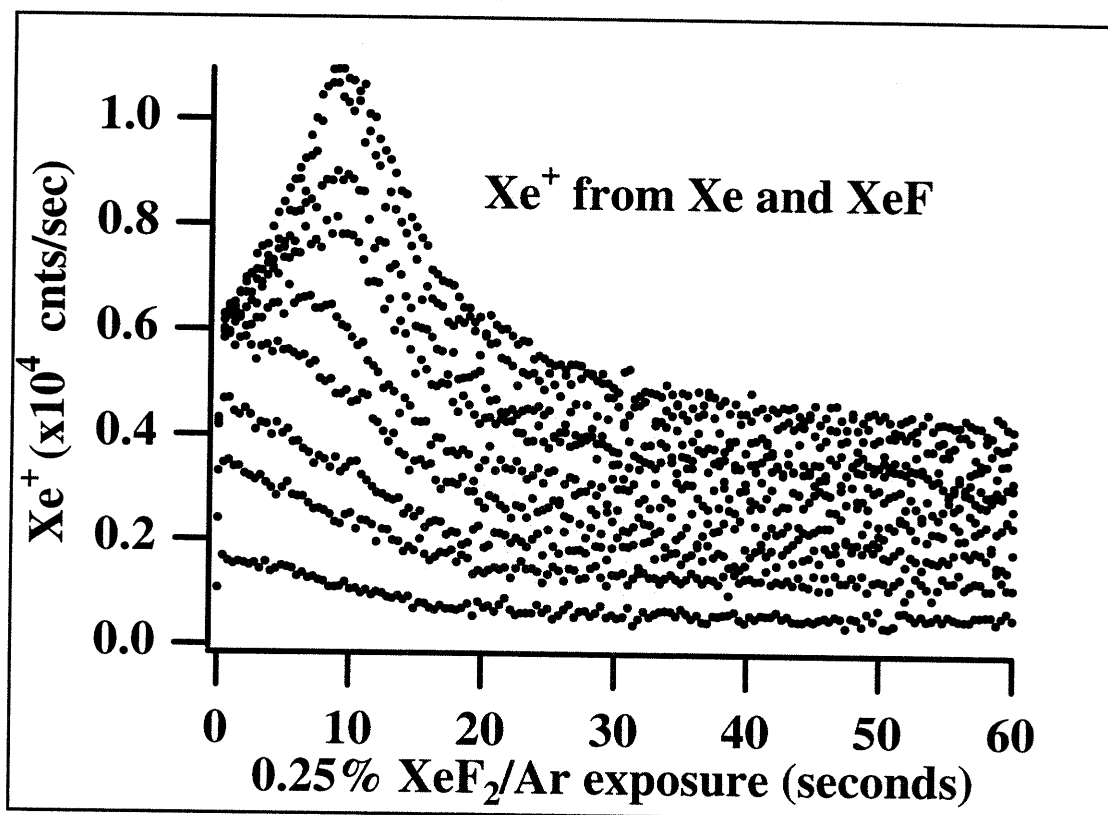

Figure 2.24 Partially Deconvoluted Xe^+ as a Function of Scattering Angle

Partially deconvoluted Xe^+ signal as a function of scattering angle. The top trace corresponds to 0° detection. The scattering angle increases from top to bottom in 10° increments, with the bottom trace corresponding to 80° detection. These curves represent both the Xe^+ from the ionization of Xe neutral and the dissociation of XeF^*.

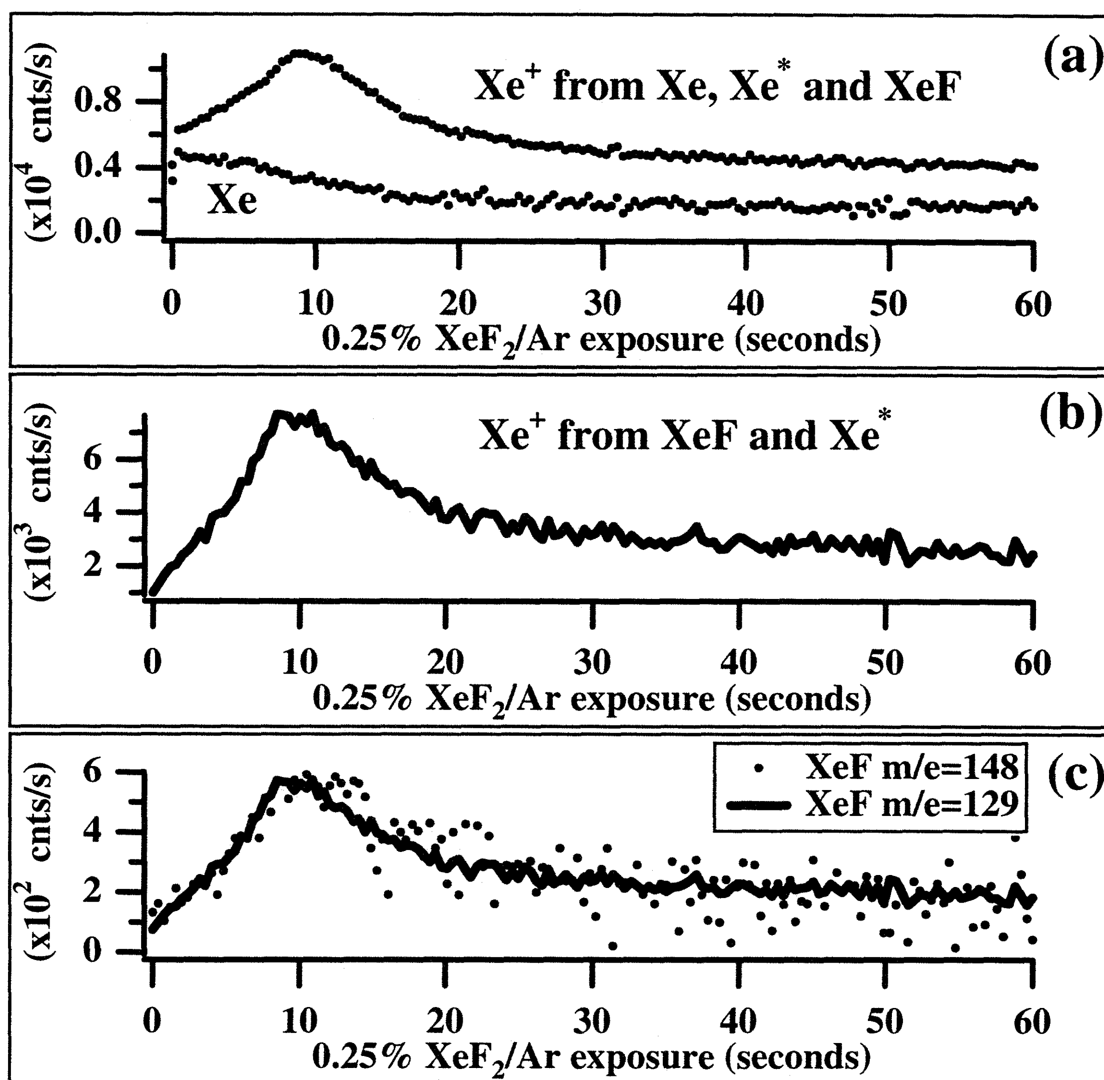

Figure 2.25 Deconvolution of Xe and XeF Contributions to the Xe^+ Signal

The Xe and XeF contributions to the Xe^+ signal scattered at 0° are separated by the use of a Xe^+ signal scattered at 80°. (a) The top trace corresponds to the superposition of Xe and XeF contributions detected at 0° as Xe^+. The bottom curve corresponds to Xe detected at 80°. The Xe curve has been scaled such that when subtracted from the upper one it yields the XeF contribution to the Xe^+ signal which is presented in (b). (c) Shows the fit of the XeF signal detected as XeF^+ to that detected as Xe^+. The XeF^+ signal has been scaled by a factor of 13.2.

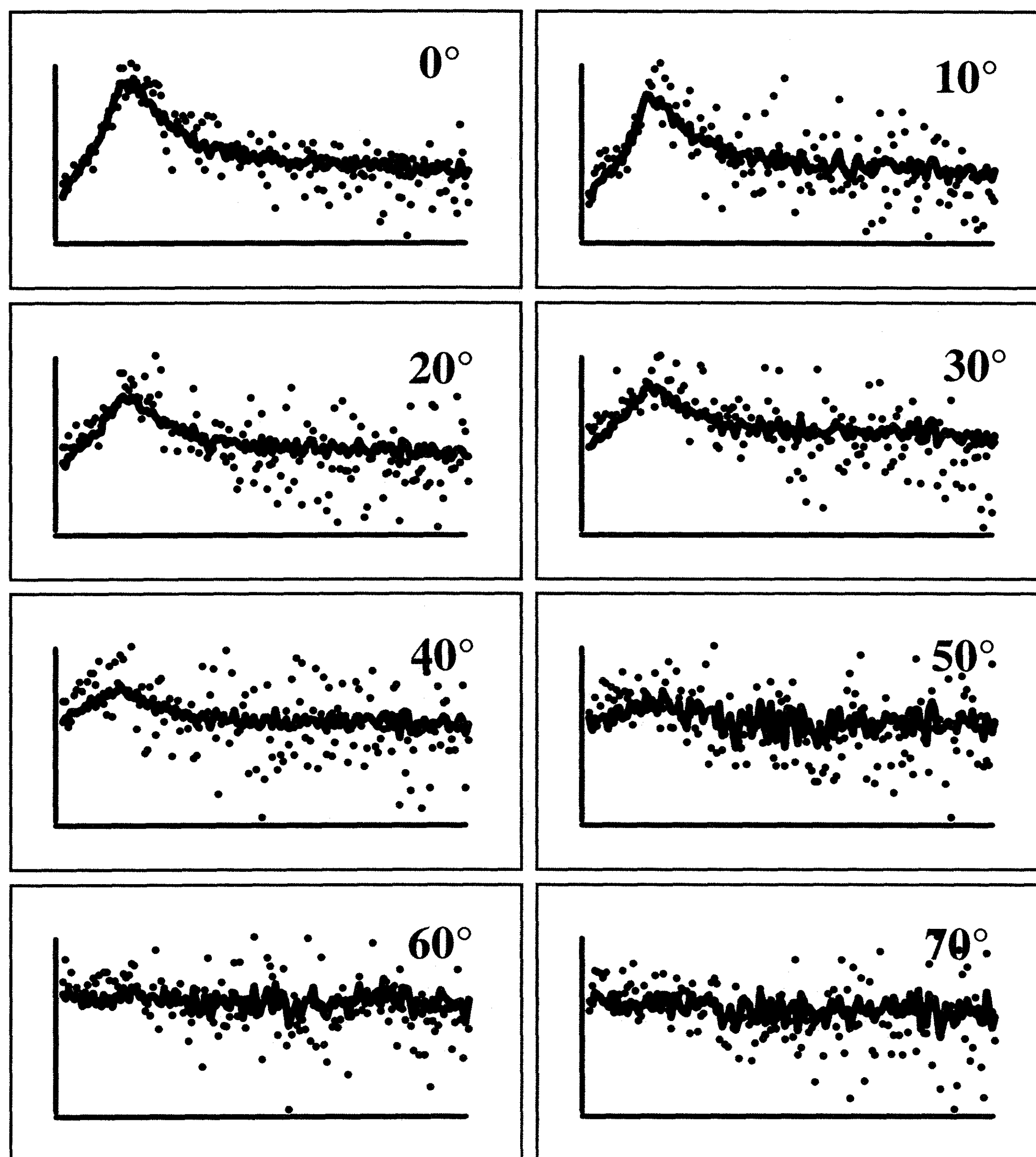

Figure 2.26 Comparison of XeF Product Detected as XeF^+ and Xe^+

Comparison of the Xe^+ (lines) and XeF^+ (dots) signals arising from XeF product, as a function of scattering angle. For each angle, the horizontal axis corresponds to 0-60 sec XeF_2 exposure time, and the vertical axis to 0-7000 counts sec^{-1} of Xe^+ signal. The XeF^+ signal has been scaled to match the intensity of the Xe^+.

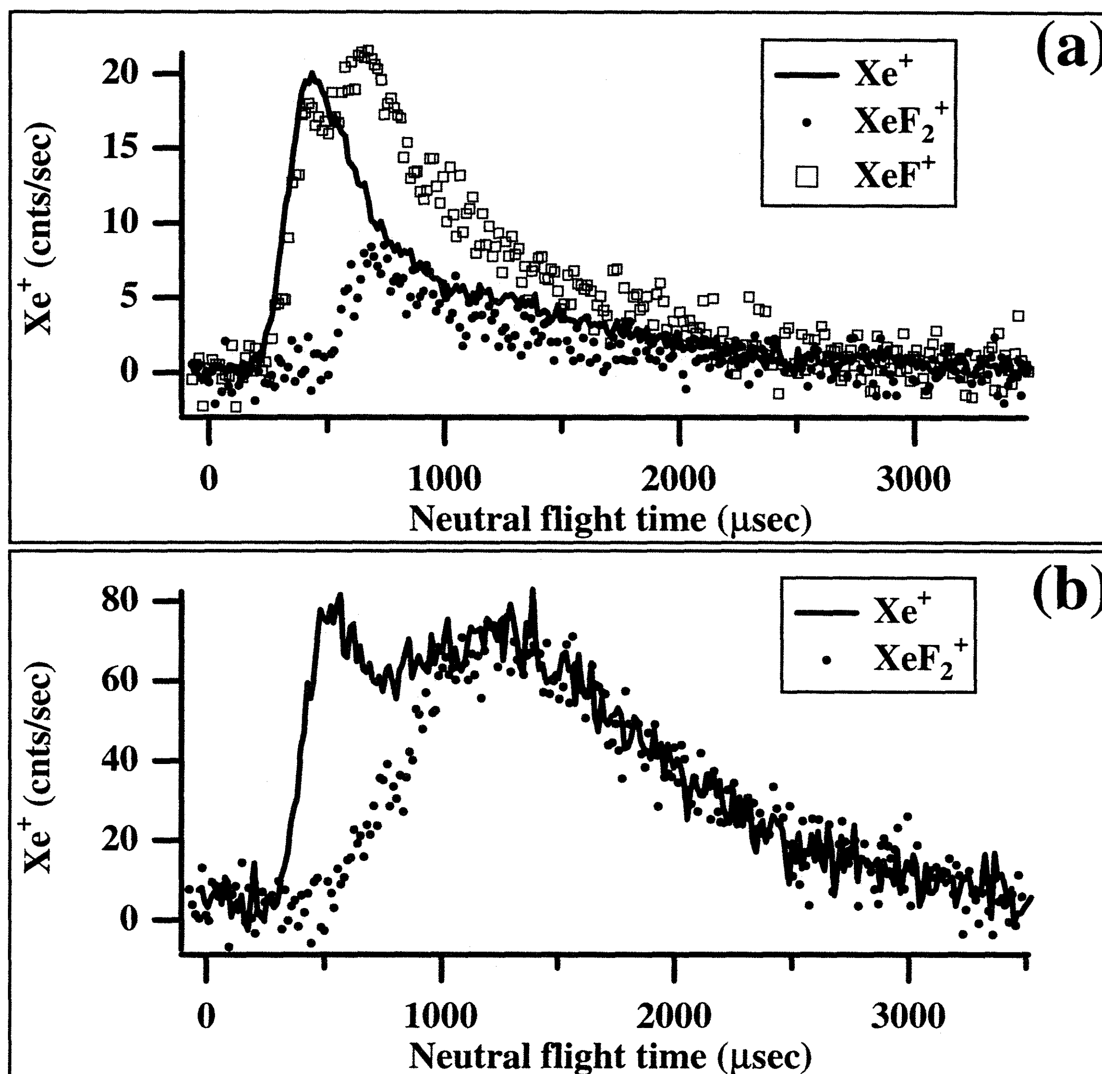

Figure 2.27 Time-of-flight Spectra of Scattered Xe^+ Signal

Time-of-flight spectra of Xe^+ signal scattered along the surface normal from Si(100) exposed to a 0.25% XeF_2/Ar beam incident on the surface at 35°. (a) Short exposure range (0-30 sec). The line represents the Xe^+ signal while the dots correspond to the XeF_2 distribution at short exposures which is scaled to fit the broad tail of the Xe^+ signal. (b) Long exposure range (60-120 sec). The line represents the Xe^+ signal while the dots correspond to the XeF_2 distribution at long exposures which has been scaled to fit the thermal component of the Xe^+ signal.

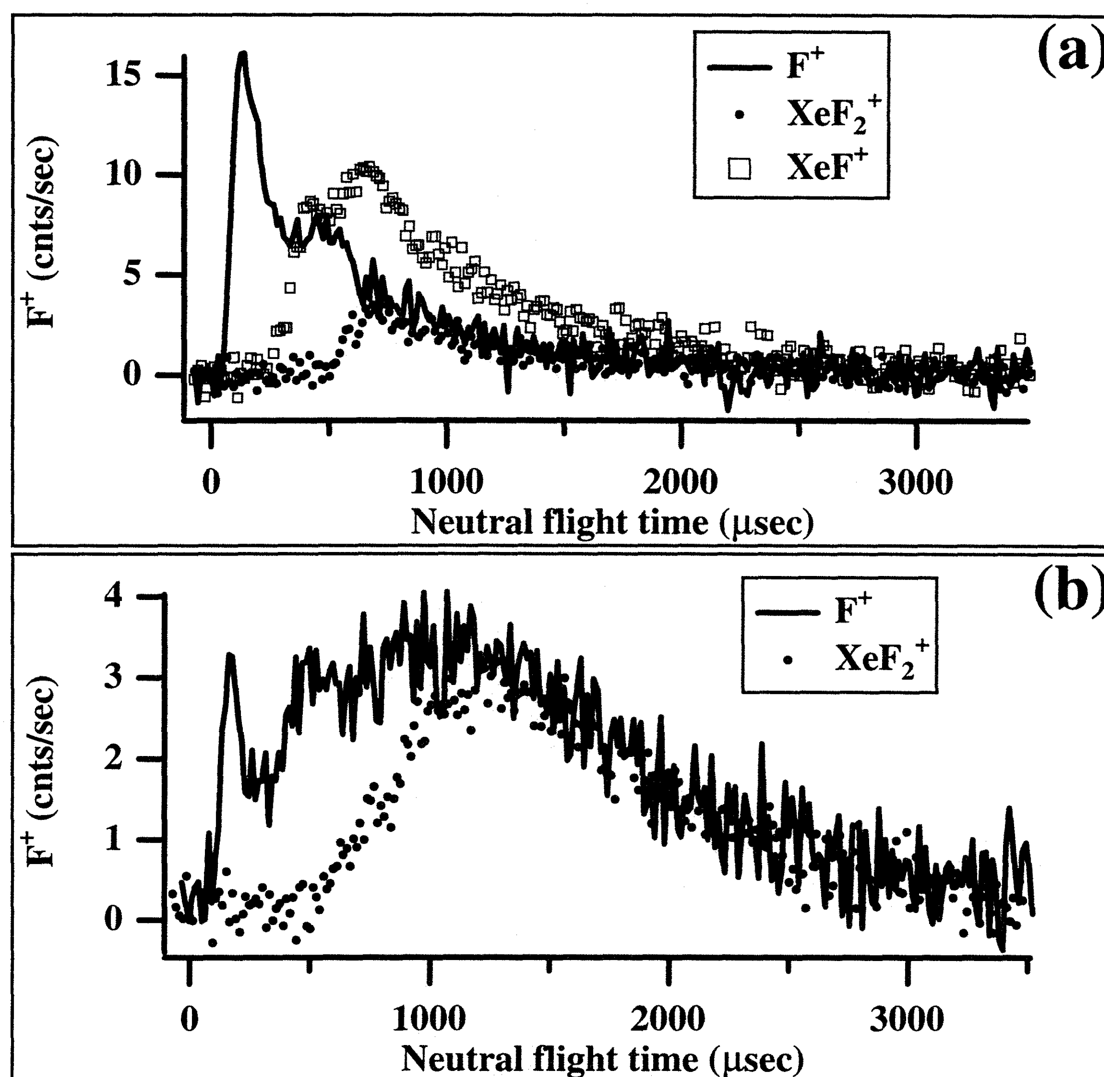

Figure 2.28 Time-of-flight Spectra of Scattered F^+ Signal

Time-of-flight spectra of F^+ signal scattered along surface normal from Si(100) exposed to a 0.25% XeF_2/Ar beam incident on the surface at 35°. (a) Short exposure range (0-30 sec). The line corresponds to the F^+ signal while the dots correspond to the XeF_2 distribution at short exposure which has been scaled to fit the broad feature in the F^+ signal. (b) Long exposure range (60-120 sec). Observation of the Etch Product The line represents the F^+ signal while the dots are the XeF_2 velocity distribution at long exposures which has been scaled to match the thermal feature in the F^+ signal.

The m/e=85 signal at the bottom of Figure 2.15 corresponds to SiF_3^+ scattered at 0°. The mere presence of a silicon-containing species in the gas-phase confirms the ability of XeF_2 to etch the Si surface even at the relatively low surface temperature of 250K. The SiF_3^+ signal is almost negligible at short exposure times, but then suddenly increases after a 10 second exposure to the XeF_2 beam, and finally reaches a constant value at longer XeF_2 exposures. The low SiF_3^+ signal at short exposures suggests that a substantial amount of fluorine must exist on the silicon surface before gas-phase fluorosilanes can be readily formed. The constant SiF_3^+ signal at longer exposures suggests that fluorination and etching eventually reach a steady-state equilibrium after which the fluorine coverage on the surface remains constant. Figure 2.29 shows the SiF_3^+ signal as a function of scattering angle obtained by averaging the SiF_3^+ signal over the long exposure range (30-60 sec) in which the etch product formation has reached a steady-state. The observed SiF_3^+ angular distribution is characteristic of species thermally desorbed from the surface, as evidenced by the good fit to a cosine functional form.

An unusual time-of-flight distribution is, however, observed for the SiF_3^+ signal. Figure 2.30 presents the SiF_3^+ signal scattered along surface normal from a 250 K Si(100) surface exposed to a 0.25% XeF_2/Ar beam (E_i=6.72 kcal mol^{-1}) incident at 35°. Figure 2.30 (a) corresponds to the short exposure regime (0-30 sec) for which the amount of SiF_3^+ signal observed is small. The signal-to-noise in this spectrum is very low primarily due to the lack of SiF_3^+ signal at short exposures. A small, narrow peak is, however, observed above the baseline, suggesting that the few products desorbed during the initial seconds are translationally excited. Figure 2.30 (b) corresponds to the longer exposure range (60-120 sec). A bimodal distribution is observed, with a broad, thermal feature at longer arrival times, and a narrower, fast component at early arrival times. The data are fit to a superposition of a thermal and supersonic[97] functional forms. The thermal component in the fit is held at a characteristic temperature of 250 K, which is equal to the

surface temperature. This broad distribution is consistent with the expected thermal desorption of products from the surface. The faster, narrow feature at early arrival times is fit to a supersonic velocity distribution with a flow velocity of 476 m sec^{-1}, and a beam temperature of 781 K. The average translational energy of the fast feature is 7.0 kcal mol^{-1}, which is slightly higher than that of the incident XeF_2 beam. This fast component implies that some etch product leaves the surface with a translational excitation beyond that expected from simple collisional processes involving Si atoms with a thermal energy characteristic of a 250 K surface temperature. A similar observation has been noted by Giapis[99] in a study of the interaction of hyperthermal F atoms with a Si(100) surface. A discussion of the possible mechanisms giving rise to the observed translational excitation of the etch product is postponed until Section 2.4.

[99] see the discussion in Section 2.1.1.2 and also reference 72 and 73.

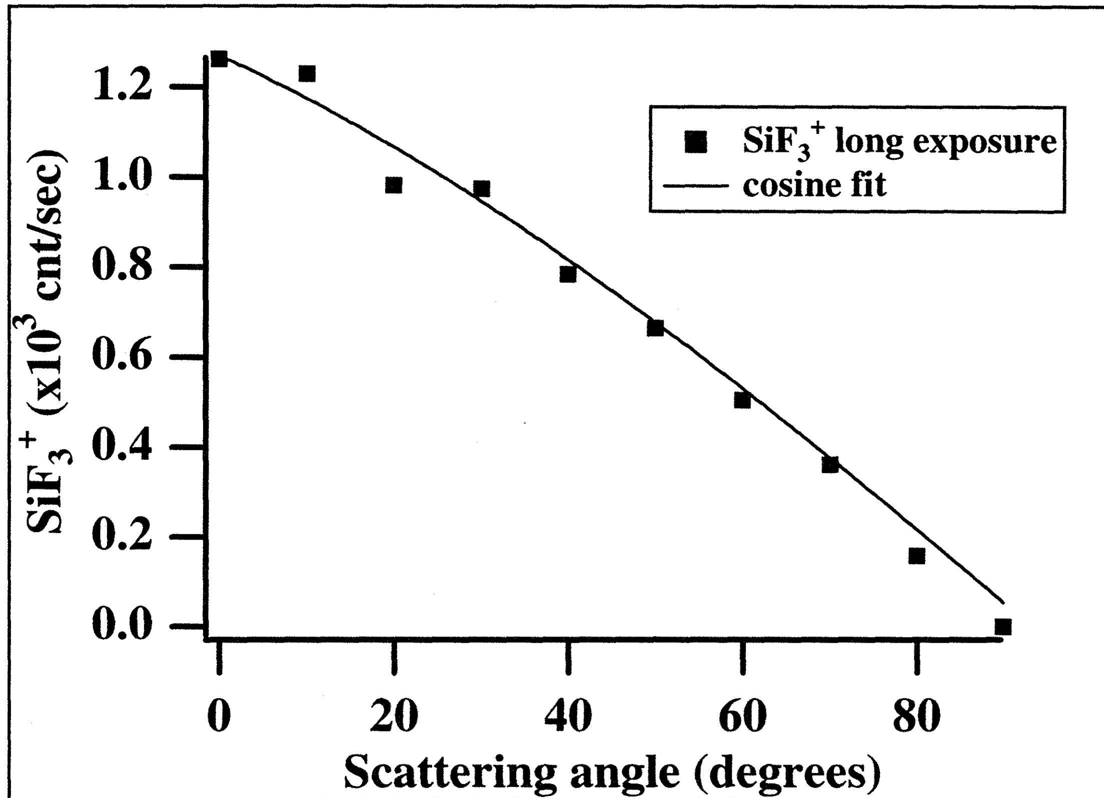

Figure 2.29 Angular Distribution of SiF_3^+

Angular distribution of scattered etch product detected as SiF_3^+ signal in the long exposure range (30-60 sec) to a 0.25% XeF_2/Ar beam incident at 35° from surface normal. A fit to a cosine functional form reproduces well the experimental data.

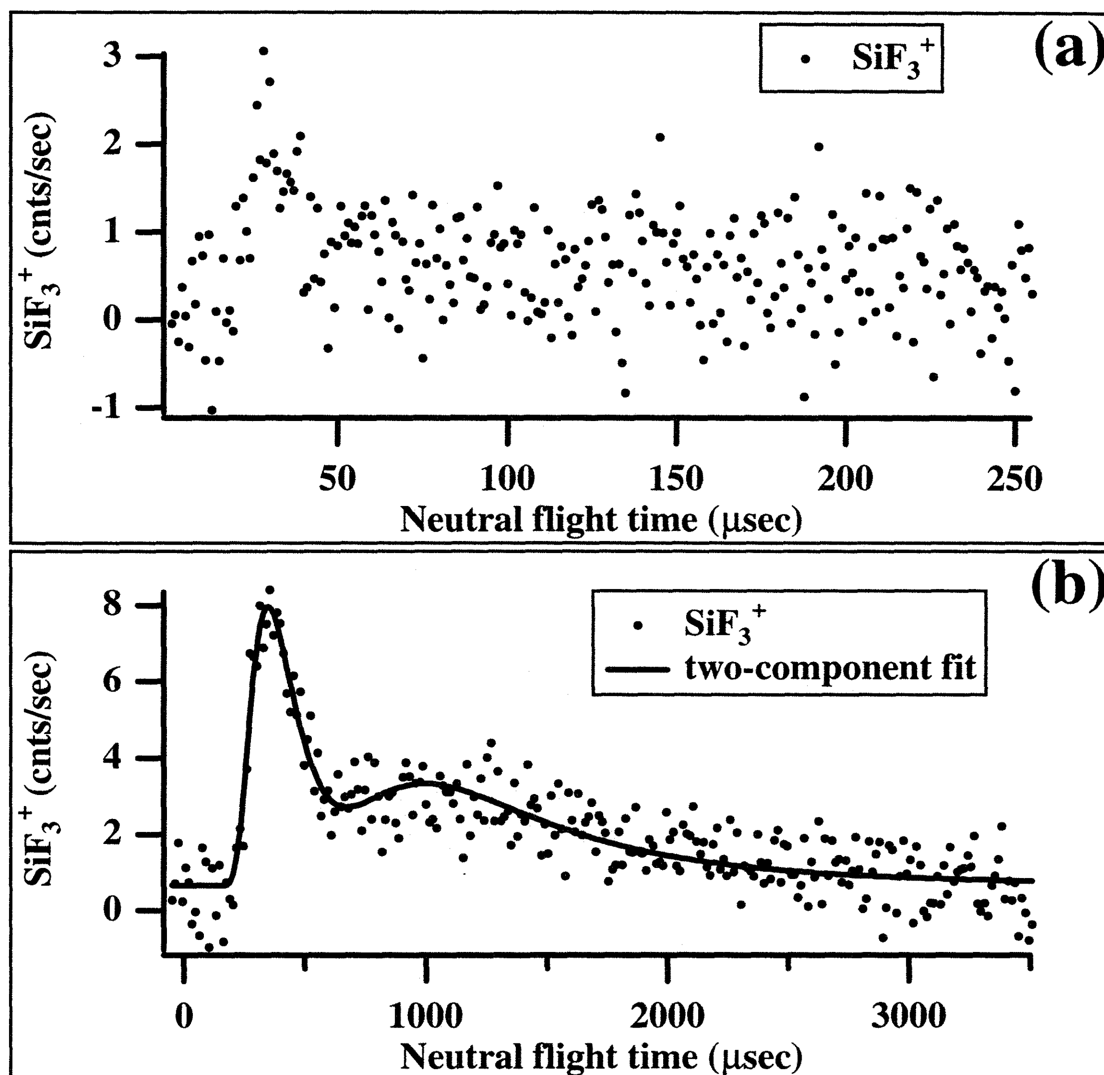

Figure 2.30 Time-of-flight Spectra of Scattered SiF_3^+ Signal

Time-of-flight spectra of SiF_3^+ signal scattered along surface normal from a Si(100) surface exposed to a 0.25% XeF_2/Ar beam incident on the surface at 35°. (a) SiF_3^+ signal at short exposure range (0-30 sec). (b) Long exposure range (60-120 sec). The dots represent the SiF_3^+ signal, while the line corresponds to a two component fit, combining a Maxwell-Boltzmann velocity distribution with its characteristic temperature fixed at 250 K and a supersonic contribution with flow velocity of 476 m sec^{-1} and a temperature of 781 K.

2.3.4 Other Evidence for the Reaction of XeF_2 with Si(100)

2.3.4.1 Thermal Desorption Products and Surface Fluorine Coverage

Thermal desorption experiments offer a complementary probe of the adsorption process. The amount of fluorine uptake during exposure to a XeF_2 beam can be determined by monitoring the total amount of silicon fluoride products desorbed while heating the Si crystal at a constant rate. Thermal desorption studies provide a direct measure of the amount of fluorine present on the surface, and can be used to determine how the fluorine coverage evolves as the reaction between XeF_2 and the Si proceeds. Some preliminary thermal desorption experiments of the interaction of XeF_2 with the Si(100) surface are presented in this section. First, the gas-phase products that desorb from the surface are identified and then the amount of fluorine product present on the surface as a function of XeF_2 exposure is determined from the total amount of desorption product observed.

In a typical thermal desorption measurement, the surface is exposed to a XeF_2 molecular beam which results in the formation of a fluorine adlayer. The amount of fluorine that adsorbs on the surface depends on the extent and conditions of the XeF_2 exposure. The crystal is then heated from the temperature at which the exposure occurred to approximately 1100 K at a rate of 5 K sec^{-1} while the desorbing products are monitored with the line-of-sight mass spectrometer positioned at the surface normal. A counter dwell time of 0.1 seconds is used for each mass being detected. Up to four masses can be detected simultaneously.

Figure 2.31 presents the thermal desorption products from Si(100) exposed to a 0.25% XeF_2/Ar beam (E_i=6.72 kcal mol^{-1}). The temperature of the crystal upon exposure is 250 K, the angle of incidence is 0°, and the exposure time is 120 seconds. Although XeF_2 is known to cause some etching, once a steady-state equilibrium between fluorine adsorption and Si etching is reached a constant amount of fluorine remains on the

surface. The 120 second exposure to XeF_2 ensures that the steady-state etching regime has been reached. The top panel shows the SiF_2 product detected as SiF_2^+ (m/e=66), which desorbs over a narrow range of surface temperatures centered at ~750 K. The desorption trace is asymmetric with a pronounced shoulder on the rising edge centered at ~590 K. The lower panel presents the SiF_4 signal detected as SiF_3^+ (m/e=85), which desorbs over a broader temperature range with one desorption maximum centered at ~450 K and a second one centered at ~580 K. The intensity of the SiF_4 desorption feature is approximately one half that of the SiF_2 product. No other desorption products are identified.

An estimate of the amount of fluorine present on the silicon surface during the steady-state etching regime can be obtained by comparing the thermal desorption products described above with those obtained from a surface fluorinated by F_2. A 20 second exposure to a 1% F_2/Kr (E_i=0.67 kcal mol^{-1}) beam is known to fluorinate the surface to a saturation coverage of 1 ML (see Section 1.4.3), and thus can be used to calibrate TDS product yield to fluorine coverage. Figure 2.32 compares the desorption products from the XeF_2 fluorinated surface presented above to the desorption products obtained from a fluorine saturated surface obtained by 20 second exposure to 1% F_2/Kr beam incident at 0°. The top panel compares the SiF_2 product signals. The shapes of the desorption traces appear to be similar. However, when the surface is fluorinated by XeF_2 the low temperature shoulder is larger and the sharp feature is broadened and slightly smaller. The SiF_4 signals presented in the lower panel are also observed to have similar shapes, but the intensity of the SiF_4 arising from the XeF_2 fluorinated surface is approximately ten times larger than that of the surface exposed to F_2.

It is known[100] that the desorbed SiF_2 product accounts for the majority of the fluorine

[100] See discussion from chapter I, Section 1.3.3 of this work, and also M. T. Schulberg, Ph.D. Thesis, Massachusetts Institute of Technology, p.146, (1990) and J. J. Yang, Ph.D. Thesis, Massachusetts Institute of Technology, p. 152, 1993

present on the surface. In the case of the fluorine saturated surface, the ratio of SiF_2 to SiF_4 at a normal detection angle has been estimated to be 0.064, meaning that the SiF_4 signal accounts for less than 1% of the total fluorine present. Under the assumption that the products desorbing from the XeF_2 fluorinated surface have a similar angular and velocity distribution to those desorbing from the F_2 fluorinated surface, the total coverage at the steady-state etching regime can be estimated. The area under the SiF_2 signal desorbing from the F_2 fluorinated surface is known to correspond to approximately 0.99 of a monolayer. Consequently, the area under the SiF_4 signal accounts for only the remaining 0.01 ML needed to complete the 1 ML saturation coverage. The ratio of the two SiF_2 peak areas in Figure 2.32 (a) is 1.67. The fluorine coverage associated with SiF_2 product in the case of the XeF_2 fluorinated surface is then approximately 1.65 ML. Similarly, the ratio of the SiF_4 peak areas in the lower panel is 20, which accounts for an additional 0.2 ML on the surface. Therefore, the total fluorine coverage during the steady-state etching with 0.25% XeF_2/Ar is estimated to be 1.85 ML.

The fluorine coverage as a function of XeF_2 exposure is obtained from a set of thermal desorption spectra collected after different times of exposure to XeF_2. Figure 2.33 presents the integrated area of the thermal desorption spectra as a function of exposure time to a 0.25% XeF_2/Ar beam (E_i=6.72 kcal mol^{-1}). The angle of incidence is 35°, the surface temperature is 250 K and the desorbed products are detected along the surface normal. The top panel shows the SiF_2 product yield detected as SiF_2^+, while the bottom one corresponds to the SiF_4 yield detected as SiF_3^+. The vertical axes correspond to the surface fluorine coverage associated with a given desorption product. The scale on the vertical axes is determined by calibration to the integrated thermal desorption signal from a surface saturated with 1 ML fluorine produced by exposure to a 1% F_2/Kr (E_i=0.67 kcal mol^{-1}) beam also incident at 35°. The SiF_2 product yield seen in Figure 2.33 (a) initially grows very rapidly, but eventually flattens out towards a constant level.

As mentioned above, SiF_2 is by far the most abundant desorption product, accounting for the majority of the fluorine coverage on the surface. Specifically, the SiF_2 accounts for approximately 1.65 ML of fluorine atoms at the surface, which corresponds to approximately 87% of the total 1.85 ML of fluorine available on the surface during the steady-state etching regime.

Conversely, the SiF_4 product seen in Figure 2.33 (b) is a relatively minor product which only accounts for the remaining 13% of the total surface coverage. It is worth noting that nearly no SiF_4 is observed to desorb for exposures below 15 seconds. This observation is consistent with the idea that a substantial amount of fluorine must be available on the surface for the formation of the closed shell tetrafluoride. Beyond the initial stages of fluorination, the SiF_4 product is seen to increase with surface coverage but it also approaches a saturation level. The sum of the SiF_2 and SiF_4 desorption products saturates at a fluorine coverage of 1.85 ML which remains constant throughout the steady-state etching regime.

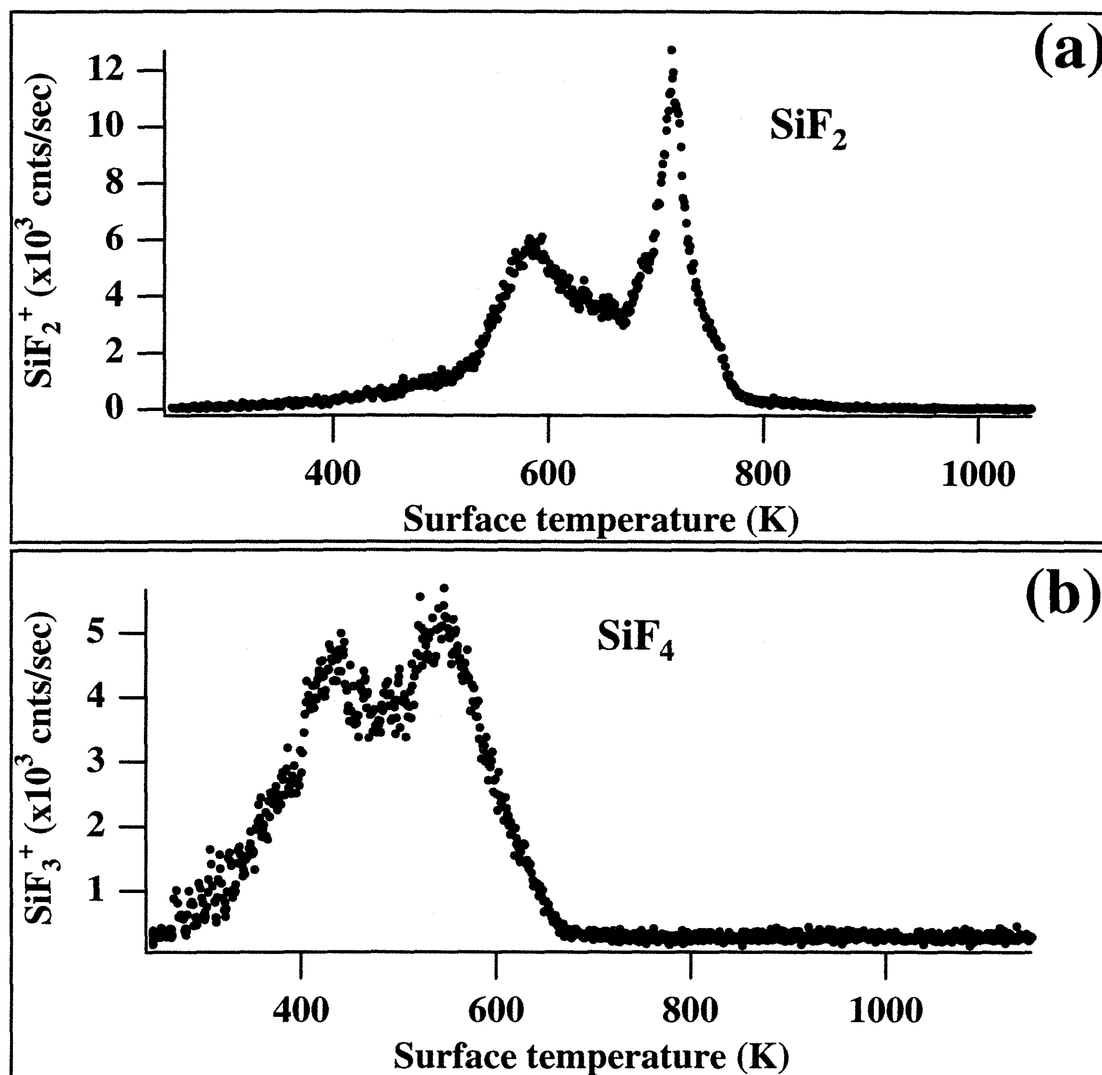

Figure 2.31 Thermal Desorption Products from Si(100) Exposed to XeF_2

The Si surface is held at 250 K and exposed for 120 seconds to a 0.25% XeF_2/Ar beam (E_i=6.72 kcal mol^{-1}) incident at 0°. This long exposure ensures that the steady-state etching regime has been reached. The crystal is then heated from 250 K to 1100 K at a rate of 5K sec^{-1} while two signals are simultaneously collected with a dwell time of 0.1 seconds. (a) SiF_2 detected as SiF_2^+. (b) SiF_4, detected as SiF_3^+.

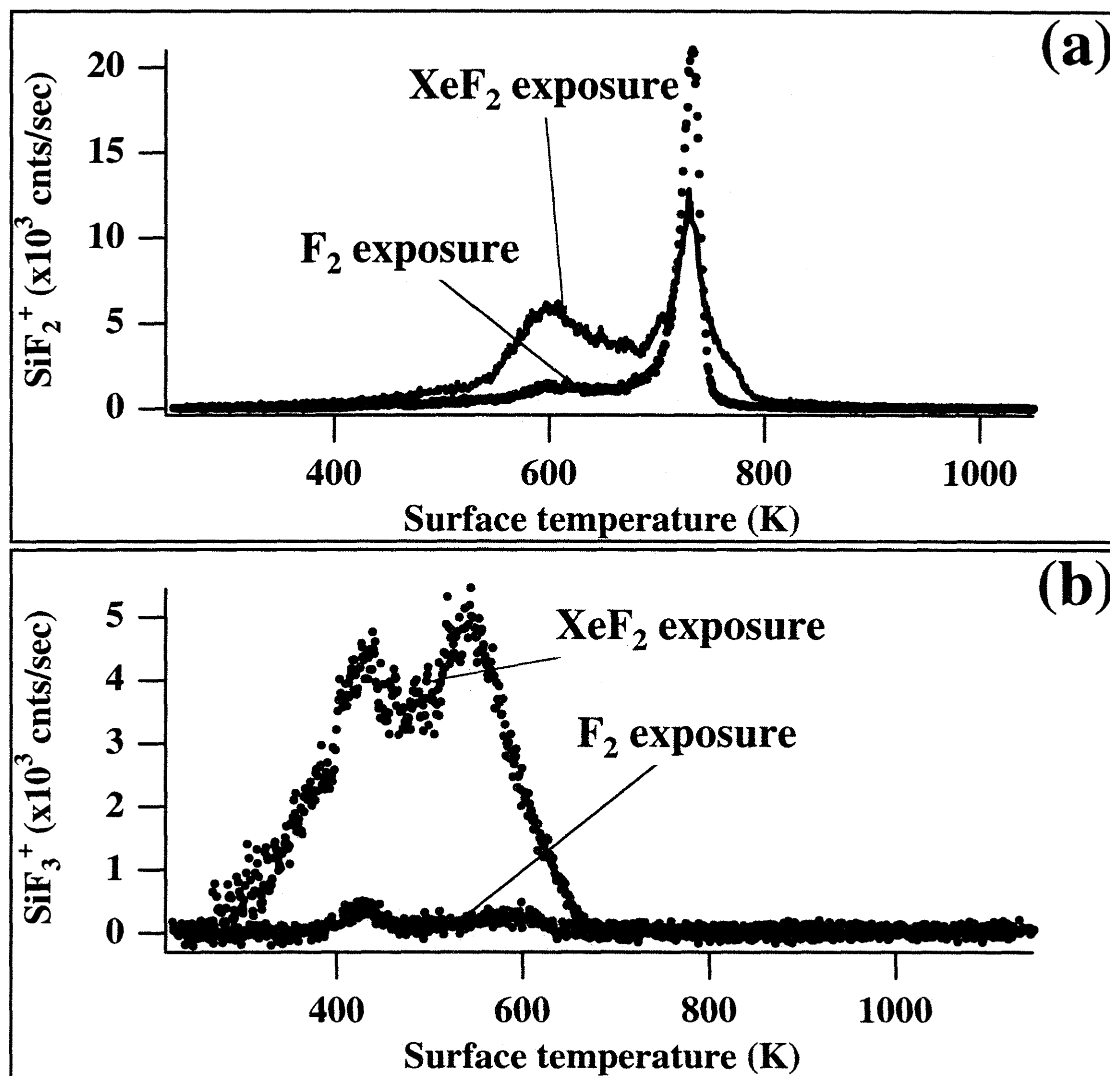

Figure 2.32 Comparison of TD Products from F_2 and XeF_2 Fluorination

Products observed to desorb from the XeF_2 fluorinated surface are compared to those obtained from a F_2 fluorinated surface. The XeF_2 exposure is described in Figure 2.31. The F_2 fluorinated surface is produced by a 20 sec exposure to a 1% F_2/Kr (E_i=0.67 kcal mol^{-1}) beam incident at 0° which produces a surface saturated with 1 ML fluorine coverage. (a) SiF_2 product from XeF_2 exposure (line) and from F_2 exposure (dots) (b) SiF_4 product from XeF_2 exposure (line) and from F_2 exposure (dots).

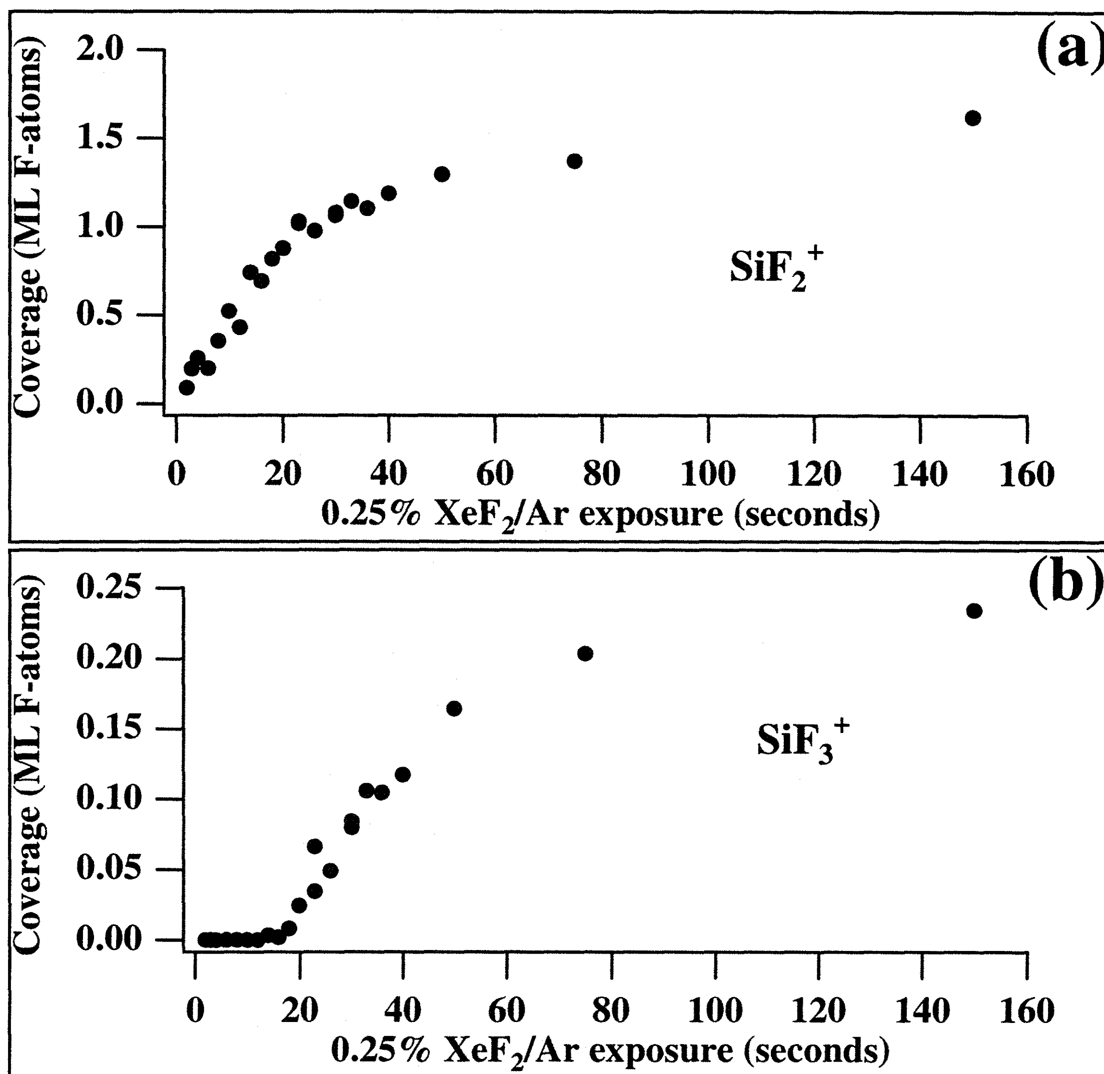

Figure 2.33 TD Product Yield as a Function of Exposure to XeF_2/Ar

Integrated thermal desorption yield from a 250 K surface exposed for varying times to a 0.25% XeF_2/Ar (E_i=6.72 kcal mol^{-1}) beam incident at 35°. (a) SiF_2 product detected as SiF_2^+ (b) SiF_4 product detected as SiF_3^+. The total fluorine coverage, obtained by summing the contributions from both desorption products, approaches a constant value near 1.85 ML

2.3.4.2 Identification of the Order of the Adsorbed Products by Helium Diffraction

As shown in Chapter I, F_2 is relatively unreactive with Si(100). It only decorates the dangling bonds on the surface and is unable to penetrate the surface layer. This observation derives from helium diffraction spectra that demonstrated the persistence of the characteristic 2x1 surface periodicity upon fluorination with F_2. Confirmation of the enhanced reactivity of XeF_2 as compared to F_2 is also obtained from helium diffraction measurements. Figure 2.34 shows helium diffraction spectra of a clean Si(100) and a Si(100) surface fluorinated by XeF_2. The surface is fluorinated by exposing it for 40 seconds to a 0.25% XeF_2/Ar (E_i=6.72 kcal mol^{-1}) beam incident on the crystal at 20° from the surface normal. The spectrum of the clean surface shows the expected zero-order (specular), half-order, and first-order diffraction features characteristic of the 2x1 reconstructed surface. In contrast, almost none of the three diffraction features can be seen in the spectrum from the fluorinated surface. The complete disappearance of the half-order feature strongly suggests that the Si—Si dimer bonds which give rise to it have been extensively cleaved. In addition, the large decrease in the specular and first-order diffraction intensity suggests a substantial destruction of all surface order.

Figure 2.35 presents a series of helium diffraction spectra collected as a function of exposure to a 0.25% XeF_2/Ar (E_i=6.72 kcal mol^{-1}) beam, incident at 20° with respect to the surface normal. After each exposure the mixture behind the nozzle is pumped out and replaced with a 50% He/Ar mixture which formed the slow He beam used for the diffraction measurements. The adsorbed fluorine is then removed by resistively heating the crystal to a temperature of 1100 K while monitoring the desorption products, (SiF_2^+ and SiF_3^+), with the differentially pumped mass spectrometer. The thermal desorption measurements as a function of XeF_2 exposure are presented in Section 2.3.4.1.

The spectra in Figure 2.35 illustrate the evolution of the order of the surface overlayer as the fluorination reaction proceeds. Comparison of the first and last spectra

in this series shows that a prolonged exposure to XeF_2 leads to a nearly complete destruction of surface order. There is, however, some interesting behavior during the intermediate stages of fluorination. The helium diffraction signal is observed to immediately degrade upon exposure of the pristine surface to XeF_2. This initial loss of diffraction intensity is attributed to the formation of a randomly ordered fluorine overlayer in the low coverage regime. It is however interesting to note that as the coverage increases, at intermediate exposure times (~6-8 seconds), the overlayer appears to order, partially recovering the 2x1 surface periodicity. The partial recovery of surface order is illustrated by the marked similarities between the diffraction spectra of the clean surface and the spectra obtained after an 8 second exposure to the XeF_2 beam. Beyond this partial recovery of the overlayer structure, the features in the diffraction spectra continue to monotonically decrease as more fluorine is incorporated.

Figure 2.36 presents the same data from Figure 2.35 in a slightly different form. In this case, only the intensity at the peak of each diffraction feature is plotted as a function of XeF_2 exposure. The top trace corresponds to the intensity of the zero-order diffraction feature. The starting point corresponds to the He scattering intensity at the specular angle from the clean surface, which is seen to immediately decrease upon the introduction of the XeF_2 beam. A minimum is reached after approximately 2-3 seconds. The zero-order diffraction intensity then increases, presumably as the fluorine overlayer attains some long range order. The diffraction intensity reaches a maximum with an intensity approximately equal to that seen from the clean surface, then decays as the exposure is further increased. The intensity of both the half-order and first-order features follow a similar trend to that observed for the zero-order feature.

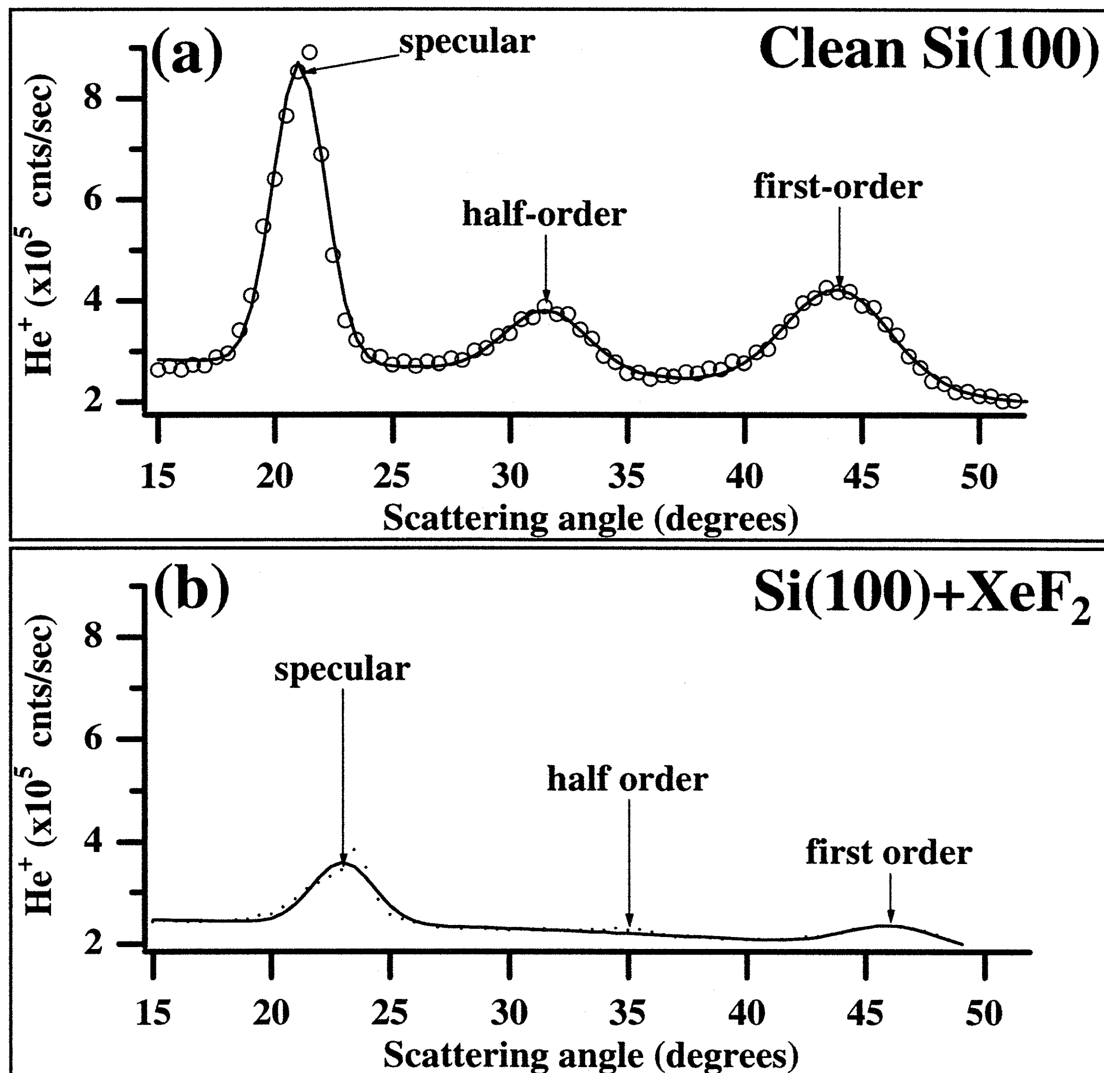

Figure 2.34 He Diffraction Spectra of Clean and XeF_2 Exposed Si(100)

Helium diffraction spectra using a 50%He/Ar beam, θ_i= 20°, T_s=250 K, λ_i=1.33 Å. Mass spectrometer is scanned in 0.5° increments along the [10] direction. (a) Clean Si(100) 2x1 reconstructed surface. (b) Same surface after 40 second exposure to 0.25% XeF_2/Ar beam (E_i=6.72 kcal mol^{-1}) incident at 20°.

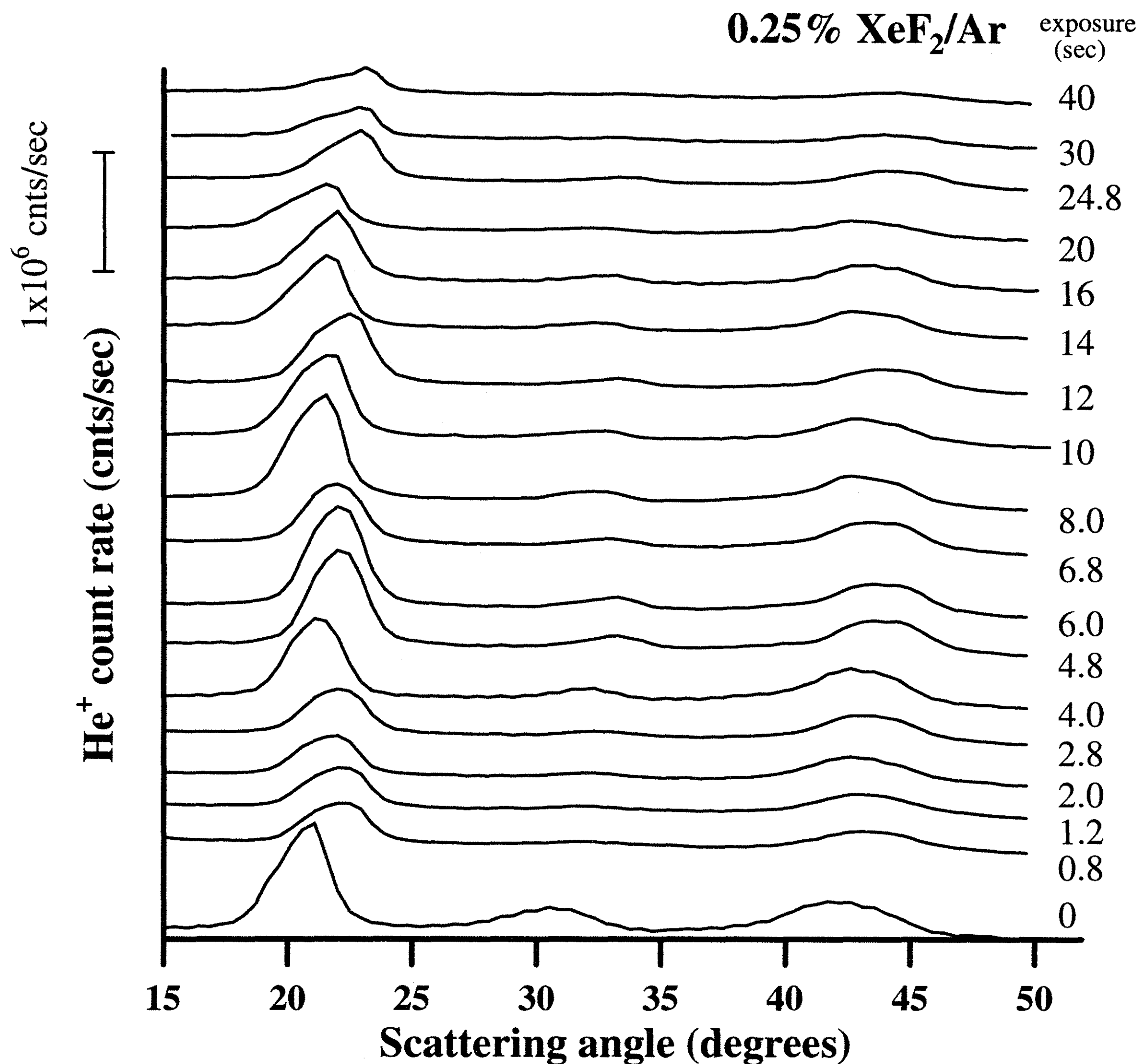

Figure 2.35 He Diffraction Spectra as a Function of XeF_2/Ar Exposure

Helium diffraction spectra after a given exposure time to a 0.25% XeF_2/Ar (E_i=6.72 kcal mol^{-1}) beam incident at 20°. The diffraction scan following each exposure is performed using a 50%He/Ar beam, θ_i=20°, T_s=250 K, λ_i=1.33 Å. The mass spectrometer is scanned in 0.5° increments along the [10] direction.

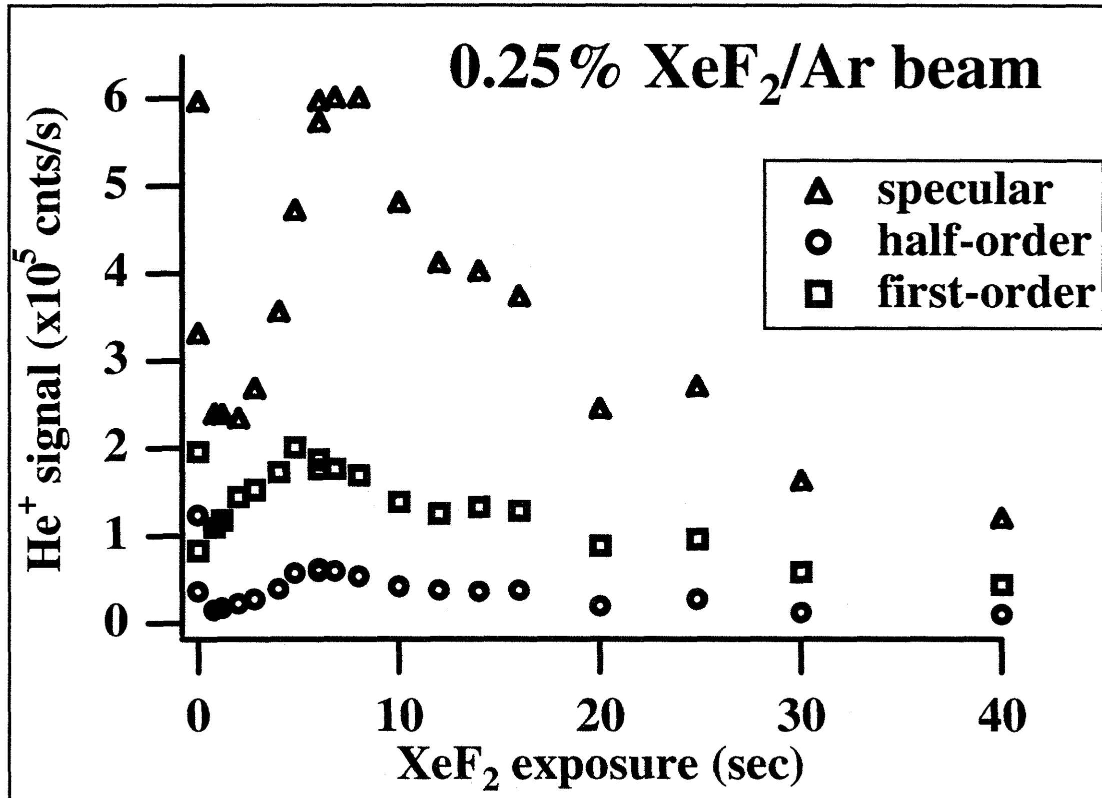

Figure 2.36 Peak He-diffraction Intensity as a Function of XeF_2/Ar Exposure

The maximum intensities of the specular (triangles), half-order (circles), and first-order (squares) diffraction features from Figure 2.35 are plotted against time of XeF_2 exposure.

2.3.5 Preliminary Results at Higher XeF_2 Incident Energy

2.3.5.1 XeF_2/He Scattered from Si(100)

Figure 2.37 presents the mass spectrometer signal from scattered Xe, XeF, XeF_2, and SiF_3 as a function of exposure time of the Si(100) surface held at 250 K to a 0.2% XeF_2/He (E_i=53.2 kcal mol^{-1}) beam. The beam is incident on the surface at 35° from the normal and the detector is positioned along the surface normal. The data are taken under conditions identical to those used for the 0.25% XeF_2/Ar beam discussed in Section 2.3.1. The only difference lies in the use of higher incident energy XeF_2. The mass-spectrometer is multiplexed to collect signal at m/e's of 85, 129, 148, and 167, corresponding to SiF_3^+, Xe^+, XeF^+ and XeF_2^+ respectively. The counter dwell time is 0.1 seconds and the dead time between mass jumps is 0.005 seconds. As before, no SiF_2^+ or $Si_2F_5^+$ products are detectable.

Comparison of the scattered products as a function of exposure to the 6.7 kcal mol^{-1} XeF_2/Ar and 53.2 kcal mol^{-1} XeF_2/He beams yields some interesting differences. The first thing to notice is the immediate rise of all signals upon exposure to the XeF_2/He beam, in contrast with the near absence of unreactively scattered product and etch product observed during the initial moments of exposure to the XeF_2/Ar beam. In the case of XeF_2/Ar, it was suggested that an initial stage of surface fluorination is required before substantial etch product or unreacted XeF_2 is observed. The question then arises of whether the XeF_2/He beam is able to produce these products even near the limit of zero coverage, or whether in this case the initial fluorination happens so fast that it is not detected in the time scale of the scattering measurement. In an attempt to answer this question, a more dilute 0.05% XeF_2/He beam is prepared. The results of scattering this beam from the Si surface are presented in Figure 2.38. With the use of the dilute beam, a more gradual rise is observed for the unreactively scattered XeF_2 product signals. The fluorination rate is however, not sufficiently slowed to be able to confirm if the etch

product is completely absent in the zero coverage limit. A further dilution of the XeF_2/He beam which has not yet been performed would help clarify this question.

Proceeding with the analysis of the scattered products from the high energy XeF_2/He beam, it is worth noting that the exposure dependence of the XeF_2^+ and XeF^+ signals is nearly identical. The similarity of these two signals suggests that they both arise exclusively from unreactively scattered XeF_2, and that no XeF is produced by F-atom abstraction at the surface. As mentioned earlier, XeF readily cracks into Xe^+ upon electron impact ionization, and hence the presence of XeF product should be most evident in the Xe^+ signal. The top trace in both Figure 2.38 and Figure 2.37 show a large amount of Xe^+ signal immediately present upon exposure to the beam. This signal monotonically decreased to reach a constant level at longer exposures. Unlike in the case of the XeF_2/Ar beam, no maximum is observed in the Xe^+ signal. The absence of the Xe^+ maximum is consistent with the absence of XeF product observed as XeF^+.

The amount of SiF_3^+ etch product slowly increases from the time the surface is initially exposed to the beam and eventually reaches a constant value. As in the case of the XeF_2/Ar beam, this exposure dependence suggests a steady-state equilibrium between the competing etching and fluorination processes. At first glance, the absolute amount of etch product observed from the XeF_2/He beams appears to be significantly less than that observed from the XeF_2/Ar beam. However, direct comparison of the steady-state SiF_3^+ signal levels of the Ar and He seeded beams is meaningless. First of all, the different XeF_2 flux of the two beams would be expected to produce different etching rates. In addition, even if the fluxes could be normalized, there could be a difference in the etch product desorption velocities which would skew their detection efficiency. Although it might be tempting to deduce from the data that the XeF_2/He beam produces comparatively less SiF_3^+ etch product, this conclusion cannot be confirmed without explicitly measuring the velocity of the desorbing etch product. Time-of-flight

measurements on the desorbing SiF_3^+ signal as a function of incident XeF_2 energy have not yet been recorded.

A preliminary thermal desorption study of the Si surface exposed to the higher incident energy XeF_2/He beam has also been performed. Figure 2.39 presents the thermal desorption yield as a function of exposure to the higher energy 0.2% XeF_2/He beam (E_i=53.2 kcal mol^{-1}). The results are both qualitatively and quantitatively very similar to those seen for the lower energy beam. The SiF_2 product rapidly increases towards a constant level which accounts for approximately 88% of the fluorine coverage. Initially, there is a short period during which no SiF_4 product is observed. This period is quite short due to the large flux of the XeF_2/He beam. The SiF_4 then increases to reach a constant level which accounts for the remaining 12% of the total 1.98 ML coverage present at the surface. Note that although the total amount of fluorine present at the surface at steady-state is slightly larger than in the case of the lower energy XeF_2/Ar beam, the partitioning of the coverage into the two product channels is the same for both energies.

From the differences observed in the exposure dependence and thermal desorption of the reaction products from the XeF_2/Ar and XeF_2/He beams, it appears that the translational energy of the incident XeF_2 significantly affects the gas-surface chemistry. At least three questions arise from this energy dependence study. First, the disappearance of the F-atom abstraction channel must in some way be tied to the high translational energy of the incident XeF_2. Second, the dependence of the steady-state etch rate on the XeF_2 translational energy must be understood. Third, the question of whether high energy XeF_2 is able to produce etch product even in the very low coverage limit must be addressed. The data available as of this writing are still preliminary and largely incomplete. No definite answers exist yet for any of the questions posed.

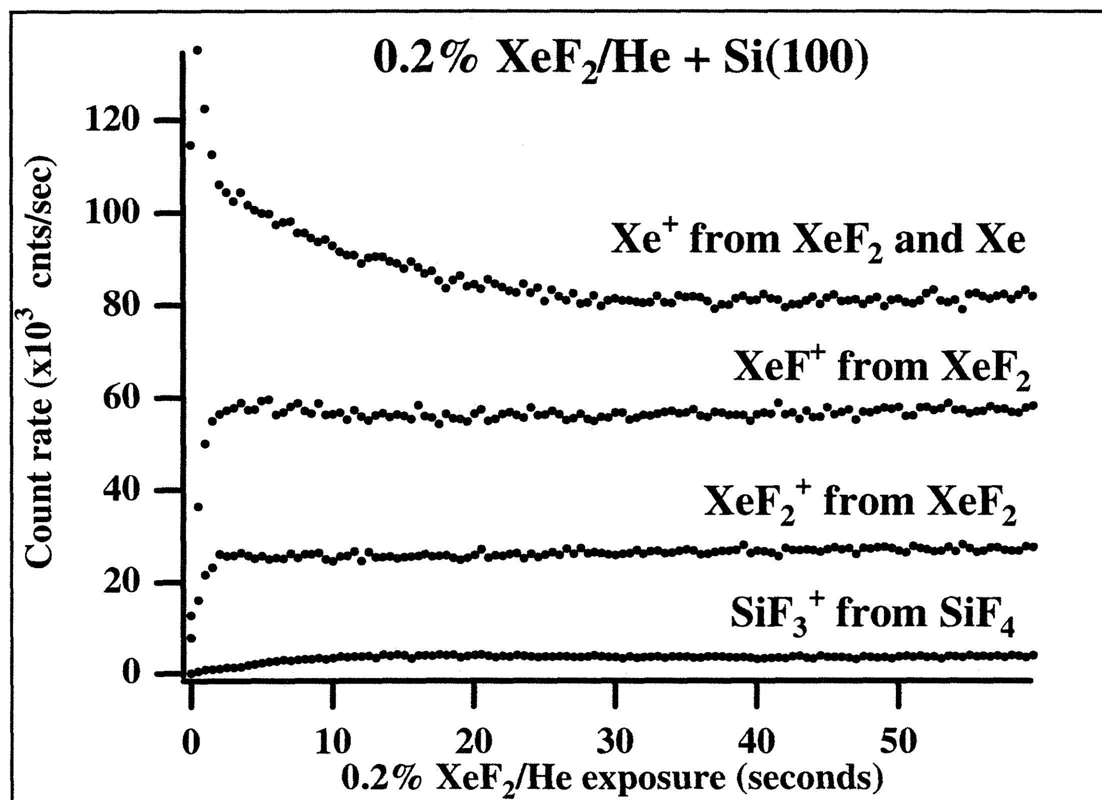

Figure 2.37 Scattered Products as a Function of Exposure to 0.2% XeF_2/He

Products scattered along the surface normal from a 250 K Si(100) surface exposed to a 0.2% XeF_2/He beam (E_i= 53.2 kcal mol^{-1}) incident at 35°.

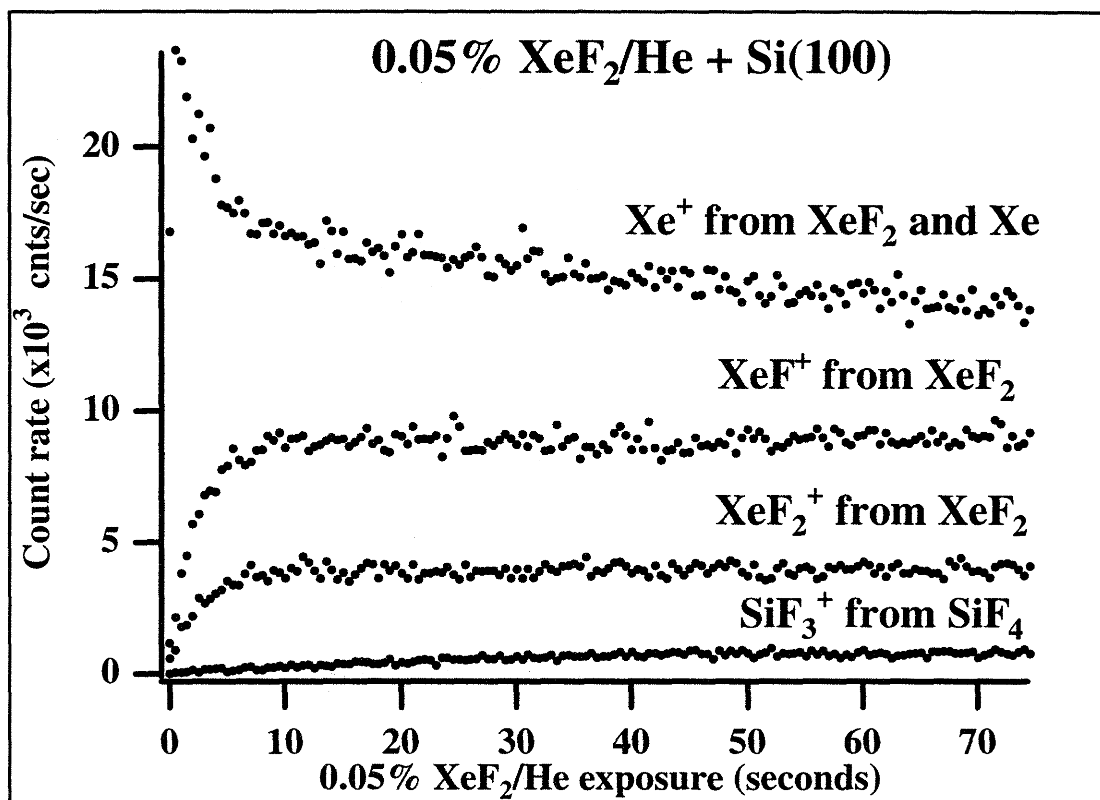

Figure 2.38 Scattered Products as a Function of Exposure to 0.05% XeF_2/He

Products scattered along the surface normal from a 250 K Si(100) surface exposed to a 0.05% XeF_2/He beam (E_i= 54 kcal mol^{-1}) incident at 35°. The lower trace is SiF_3^+ (m/e= 85) from SiF_4 . The second trace is XeF_2^+ (m/e= 169) arising from unreactively scattered XeF_2. The third trace is XeF^+ from the cracking of the scattered XeF_2. The top trace is Xe^+ from Xe liberated by the surface reaction, and from unreactively scattered XeF_2. Note that the XeF_2^+ and XeF^+ signal have the same shape indicating the absence of XeF product.

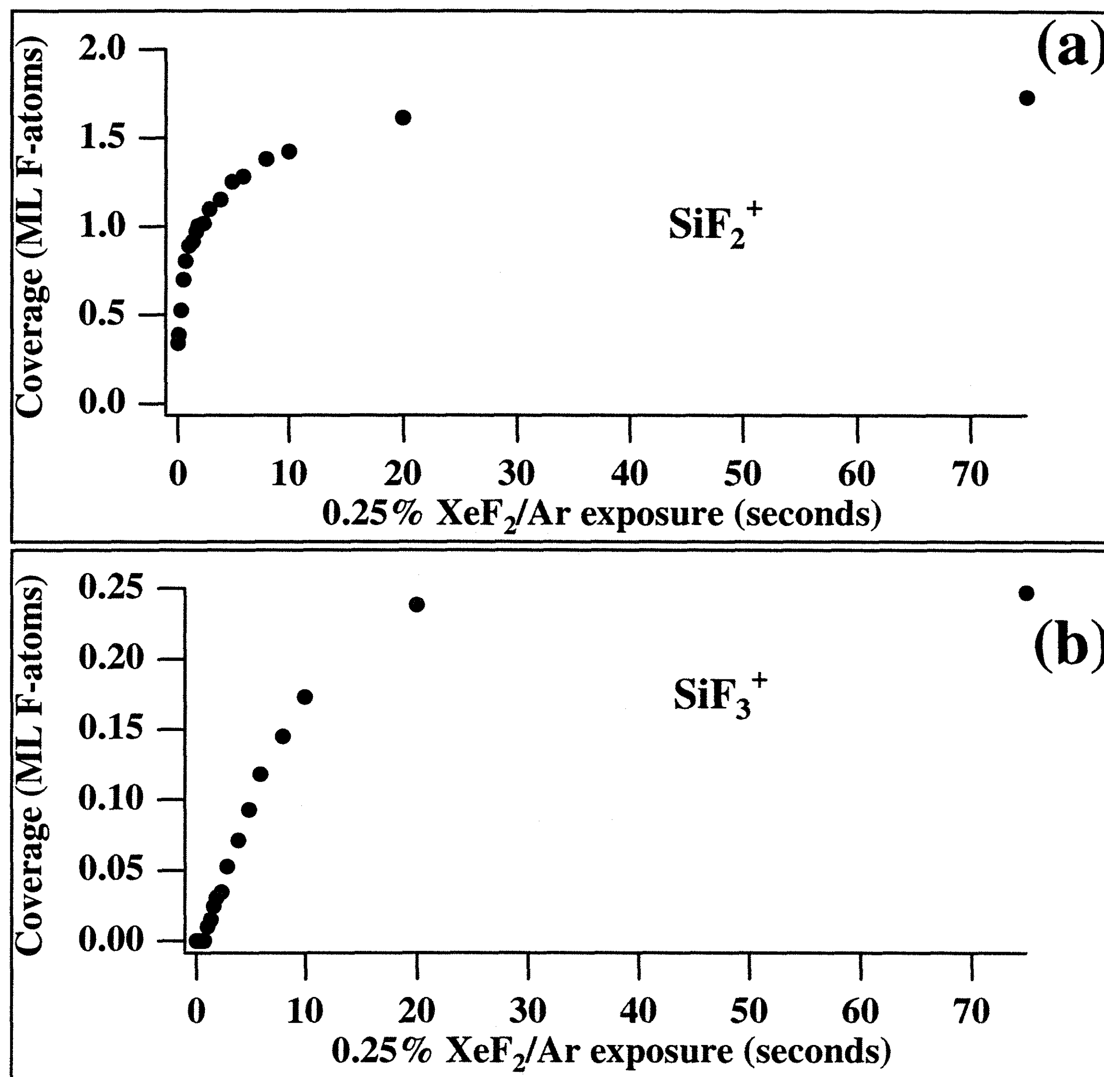

Figure 2.39 TD Product Yield as a Function of Exposure to XeF_2/He

Integrated thermal desorption yield from a 250 K surface exposed for varying times to a 0.2% XeF_2/He (E_i=53.2 kcal mol^{-1}) beam incident at 35°. (a) SiF_2 product detected as SiF_2^+ (b) SiF_4 product detected as SiF_3^+. The total fluorine coverage, obtained by summing the contributions from both desorption products, approaches a constant value near 1.98 ML.

2.4 DISCUSSION

Having successfully deconvoluted the mass spectrometer signals into the neutral reaction products arising from the scattering of XeF_2 from Si(100), the exposure dependence of the neutral reaction products scattered at 0° is plotted in Figure 2.40. The XeF_2 product (detected as XeF_2^+) is presented in Figure 2.40 (a), and follows a similar exposure dependence to that observed for the unreactively scattered F_2 in the F_2/Si reaction. In the low exposure regime, XeF_2 readily reacts, adsorbing fluorine onto the surface, with little probability of unreactively scattering to the gas-phase. As the exposure increases and the reaction sites are occupied by adsorbed fluorine, the probability of unreactive scattering increases, and therefore, so does the intensity of the scattered XeF_2 signal. After long exposures, a steady-state is reached in which the probability of unreactive scattering remains constant. The velocity distribution (Figure 2.18 (a)) and angular distribution (Figure 2.17 (b)) of the unreactively scattered XeF_2 at long exposures are consistent with accommodation on the 250 K Si surface and subsequent desorption to the gas phase. On the other hand, at short exposures, when surface coverage is low and reactive Si dangling bonds abound on the surface unreacted XeF_2 is observed to scatter without accommodating with the surface. The direct scattering of XeF_2 at short exposures is evidenced by its non-thermal velocity distribution depicted in Figure 2.18 (b) and by a maximum at the specular angle in its angular distribution (Figure 2.17 (a)).

A quantitative analysis of the unreactively scattered XeF_2 signal yields a measurement of the total XeF_2 reaction probability. The total XeF_2 reaction probability (sticking coefficient) is determined by comparing the amount of unreactively scattered XeF_2 from the inert (oxidized) and reactive (clean) Si surfaces. If the total reaction probability is defined as the fraction of the incident XeF_2 flux that does not unreactively scatter, then it is readily calculated by taking the ratio of the unreactively scattered XeF_2

flux to the incident XeF_2 flux and subtracting it from unity. The incident flux is taken to be equal to the flux scattered from the inert surface, since the oxide layer is thought to reflect 100% of the incident XeF_2 (see Section 2.2.3.1). Although the fluxes are not directly known, they should be proportional to the mass-spectrometer signals assuming that the velocities of the XeF_2 scattered from both the reactive and inert surfaces are the same. In addition, the total reaction probability is assumed to be independent of detection angle, at all coverages because the angular distributions of XeF_2 unreactively scattered from the fluorinated and oxidized surfaces are equal (compare figure 2.14 and figure 2.17 (a)). These assumptions will be checked in future experiments[1].

Figure 2.41 shows the total reaction probability of XeF_2 from a 0.25% XeF_2/Ar beam scattering from a clean 250 K Si(100) surface. The angle of incidence is 35° and scattered signals detected at 10° intervals throughout the entire scattering range are plotted together. Note that when the probabilities obtained from all eight detection angles are overlaid in the figure, they are essentially indistinguishable. The initial reaction probability has a value of 0.9 which is consistent with the highly reactive nature of the clean surface. The probability remains nearly constant during the first 8-10 seconds of exposure and then rapidly decreases as the exposure approaches the value at which the onset of etch product desorption is observed. Finally, at higher exposures, a steady-state is reached in which the XeF_2 reaction probability has a constant value of about 0.2. Unlike the reaction of F_2 with Si(100), the reaction probability of XeF_2 does not go to zero, even at high XeF_2 exposures.

The continued reaction of XeF_2 at high coverage is first evidenced by the loss of surface order as shown by the helium diffraction spectra. Figure 2.35 and Figure 2.36 show that after a brief recovery of surface order, probably due to the rapid fluorination of the most reactive Si dangling bonds, the surface order is lost permanently. The loss of the half-order diffraction feature indicates the extensive cleavage of the Si—Si dimer

bonds. Furthermore, the degradation of the specular and first-order diffraction features is indicative of widespread surface disorder. The extensive cleavage of dimer and subsurface Si—Si bonds generates new reactive dangling bonds which support the observed reactivity of XeF_2 at long exposures.

An estimate of the amount of fluorine present on the surface during the steady-state reaction regime is obtained from the yield of fluorinated thermal desorption products. As discussed in Section 2.3.4.1, the total fluorine coverage after a long exposure to a 0.25% XeF_2/Ar beam is on the order of 1.85 ML. The first monolayer of fluorine can be accounted for by the fluorination of the surface dangling bonds. The observation of a fluorine coverage above 1 ML is indicative of the cleavage of dimer and/or subsurface Si—Si bonds. The fluorine coverage is observed to remain constant at a value of 1.85 ML regardless of further XeF_2 exposure. Since the XeF_2 reaction probability of 0.2 at long exposures indicates that fluorine continues to be incorporated into the Si at a constant rate, the only way to maintain a constant fluorine coverage on the surface is to continuously remove an amount of fluorine equal to that being adsorbed.

The removal of fluorine from the surface during the long exposure regime is accompanied by the removal of Si, as evidenced by the SiF_3^+ signal as shown in Figure 2.40 (b). Note that although no SiF_3^+ signal is observed during the initial stages of fluorination, an exposure threshold is reached at which the amount of fluorine on the surface is sufficient to initiate the desorption of etch product. After this exposure threshold, the SiF_3^+ signal gradually increases towards a constant value. The constant level observed for the SiF_3^+ signal at long exposures indicates that the steady-state regime observed for all reaction products corresponds to an equilibrium between fluorine adsorption and Si etching.

The most obvious choice of a neutral product to assign to the SiF_3^+ signal is SiF_4. Due to its closed shell structure, SiF_4 product formed on the surface is expected to readily

desorb. In addition, SiF_4 is known to preferentially ionize to SiF_3^+ with only about one in a hundred molecules ionizing to the parent SiF_4^+ at 70 eV ionization energy. The observed broad angular distribution of the SiF_3^+ (see Figure 2.29) is also consistent with the etch product being thermally desorbed. Through similar arguments, most studies of the etching reaction of Si with XeF_2 have concluded that SiF_4 is the major etch product, as discussed in Section 2.1.1.2. The time-of-flight distribution of the SiF_3^+ observed in Figure 2.30, however, raises some questions about the possibility of SiF_3 also being produced by the reaction. The time-of-flight distribution displays a slow broad feature consistent with thermal desorption of SiF_4 from the 250 K Si surface. There is, however, a second narrow feature at short arrival times which is not consistent with thermally desorbed products. A similar velocity distribution has been observed by Giapis[73,74] for the interaction of hyperthermal (3-6 eV) F atoms with Si(100). The fast feature is assigned to SiF_3, since it is observed in the SiF_3^+ time-of-flight spectrum, but not in the SiF_4^+ one. Two explanations have been offered for the origin of the translational excitation of the SiF_3. The first explanation involves the collision-induced desorption of SiF_3 radicals present on the surface which would be ejected into the gas phase upon the rupture of their bond to the surface. In the case of hyperthermal F atoms, the collision-induced process is likely enhanced by the large momentum carried by very fast F atoms. Similarly, in the case of XeF_2/Si, the collision-induced process is likely enhanced by the massive nature of the impinging reactant. An alternate explanation involves a direct Eley-Rideal reaction mechanism, in which a fluorine atom from an incident XeF_2 molecule is directly inserted into an SiF_2 moiety on the surface, with the exothermicity of the F addition reaction causing the desorption of translationally excited SiF_3 etch product. No direct evidence exists in this investigation to allow the assignment of the fast SiF_3^+ signal to either SiF_3 or SiF_4 desorption products. Detection of the velocity distribution of the less abundant SiF_4^+ may clarify the origin of the SiF_3^+ signal. The low intensity of the SiF_4^+ has so far precluded the measurement of its velocity distribution.

The exposure dependence of the Xe product at 0° scattering angle which is obtained from the Xe^+ signal at 80° scattering angle, is presented in Figure 2.40 (c) and is reminiscent of that observed for the two-atom adsorption probability in the F_2/Si system. The maximum amount of Xe is observed in the limit of zero exposure with a gradual decay of the scattered Xe signal giving way to a non-zero constant level at long exposures. It is worth noting that in contrast to the F_2/Si case, fluorine adsorption continues and Xe product is observed to desorb even after long XeF_2 exposures. The observation of Xe liberated from the surface at long exposures indicates that enough reactive sites are present on the surface during the steady-state etching regime to accommodate both fluorine atoms from an incident XeF_2 molecule. The presence of several contributions to the Xe^+ signal prevents the deconvolution of its time-of-flight spectrum (Figure 2.27) to obtain the velocity distribution of the Xe liberated by the adsorption of both F atoms from an incident XeF_2 molecule.

The exposure dependence of the XeF product scattered at 0° as a result of F atom abstraction is presented in Figure 2.40 (d). It is determined from the measured XeF^+ signal deconvoluted as discussed in Section 2.3.2 to show only the XeF^+ resulting from the ionization of neutral XeF. The amount of scattered XeF is initially non-zero, indicating that the abstraction channel is operable in the limit of zero-coverage. The abstraction product rapidly increases towards a maximum at intermediate exposures, and then decays to a constant but non-zero value. The exposure dependence of the XeF product is similar to that of the single-atom abstraction probability in the F_2/Si system. However, in contrast to the abstraction in the F_2 case, abstraction from XeF_2 continues even after long exposures. This observation is consistent with the constant regeneration of the reactive Si dangling bonds, which are confirmed by the loss of the 2x1 surface periodicity. The time-of-flight distribution of the XeF product, depicted in Figure 2.22, shows that just as in the case of F atoms ejected during the abstraction from F_2, the

velocity of the ejected XeF is larger than that expected from the thermal desorption of a XeF species. The translational excitation of the XeF product likely arises from the exothermicity released by the Si—F formation.

There is, however, and interesting difference between the abstraction reactions of F_2 and XeF_2. This difference is illustrated in the different angular distributions of the ejected fragments. Whereas the angular distribution of the complementary F atom ejected by the abstraction from F_2 follows a cosine dependence, the angular distribution of the XeF ejected as a result of abstraction from XeF_2 is a fairly narrow one peaked at surface normal. That is, the XeF product resulting from the abstraction of one F atom from an incident XeF_2 is preferentially observed at scattering angles close to the surface normal (see Figure 2.21). A sharp decline in the intensity of the XeF^+ signal is observed with increasing scattering angle. In fact, nearly no XeF product is observed at the highest (80°) detection angle. One possible explanation for this unusual angular dependence is that during the abstraction process either the incident XeF_2 or the ejected XeF are preferentially oriented with their bond axis nearly perpendicular to the surface normal, therefore favoring the ejection of the XeF fragments with trajectories normal to the surface. An alternate explanation for the non-isotropic XeF angular distribution involves secondary surface collisions for those XeF fragments ejected at larger scattering angles. Given the small binding energy of XeF, secondary collisions would result in its decomposition into Xe and F, and therefore explain the absence of XeF at scattering angles far from surface normal. The direction of the scattered Xe atoms would be randomized by the collision process, leading to a broad angular distribution of the scattered Xe. The operability of the secondary collision mechanism should be most evident in the Xe^+ signal detected at large scattering angles, where no XeF product is observed. The Xe atoms produced by the secondary collisions of XeF with the surface should be distinguishable from the Xe liberated by the adsorption of two F atoms from a

single incident XeF_2 molecule on the basis of their exposure dependence. That is, the Xe atoms produced by a secondary collision between XeF and the surface should follow the exposure dependence characteristic of the XeF fragments that escape from the surface, whereas the Xe atoms produced by the adsorption of two fluorine atoms from a single XeF_2 molecule should follow the monotonically decreasing exposure dependence observed for Xe^+ at 80°. The fact that the Xe^+ signal detected at large scattering angles does not show any indication of the exposure dependence characteristic of the abstraction process, such as a maximum in the Xe^+ signal at non-zero exposure, suggests that the importance of the secondary collision mechanism is at best minimal. Alignment of the XeF_2 or XeF during the abstraction process is therefore the more likely explanation for the angular distribution of XeF. However, no direct evidence exists confirming the preferential orientation of the incident XeF_2 molecule or of the ejected XeF radical.

Another interesting aspect of the abstraction reaction is revealed in the velocity distribution of F atoms detected as F^+ at m/e=19 (see Figure 2.28). Besides the obvious features accounted for by the dissociative ionization of the XeF_2 and XeF products to yield F^+, the F atom velocity distribution shows an unusually fast feature. The large translational energy, $\overline{E}_{trans} = 6.67$ kcal mol^{-1}, observed for some of the F atoms likely arises from the exothermicity of the abstraction process. The question then arises of how the chemical energy released during the formation of a surface Si—F bond is channeled into the translational degree of freedom of the F atom in the ejected XeF. The answer to this question necessarily involves an excited XeF species denoted as XeF^*, which dissociates in the gas phase before it reaches the detector. Since the exothermicity of the reaction is of the order of 4 eV, the nature of the excitation of the XeF^* product can be either vibrational or electronic. It is clear how a large degree of vibrational excitation in the exit channel of the abstraction reaction can lead to the dissociation of the weakly bound (3 kcal mol^{-1}) XeF and yield the observed translationally excited F^* atoms. For

example, an early barrier in the gas-surface potential energy surface would lead to the vibrational excitation of the XeF bond in the exit channel, resulting in its dissociation. However, electronic excitation can also account for the fast F atoms since a low-lying dissociative electronically excited state[101] of XeF is well within reach of the energy available from the reaction exothermicity. No evidence exists in this investigation clarifying the nature of the XeF^* excitation. Furthermore, the decomposition of XeF due to the chemical energy released by the reaction is an example of a process which has not previously been documented to the knowledge of the author. The partitioning of the reaction exothermicity remains an unanswered question which might be addressed by further analysis of the Xe^* and F^* products arising from the chemically induced dissociation of XeF^*.

As mentioned in Section 2.3.3, the presence of a fast F^* atom from the gas phase dissociation of XeF^* must be accompanied by a momentum-matched Xe atom. The extra width of the Xe^+ time-of-flight spectra presented in Figure 2.27 (a) suggests the presence of a Xe component other than that from the dissociative ionization of XeF_2 and XeF and from the reaction with the surface. Unfortunately, there is no clearly resolved feature in the spectrum that could be assigned to the Xe^* component of the Xe^+ signal. However, this observation is consistent with calculations of the velocity expected for the Xe^* liberated by the gas phase decomposition of XeF^* based on the conservation of energy and momentum which show that such a component would not be clearly resolvable in velocity space from Xe^+ produced by other mechanisms[98]. It is also expected that the exposure dependence of the Xe^+ signal produced by the gas phase dissociation of XeF^* would not be distinguishable from the exposure dependence of the Xe^+ signal produced by the dissociative ionization of XeF. Because the Xe^* product arises from the decomposition of a XeF fragment produced by an abstraction event, it must follow the

[101] H. Helm, D. L. Huestis, M. J. Dyer, and D. C. Lorents, J. Chem. Phys. **79**, 3220 (1983)

exposure dependence characteristic of the abstraction mechanism, regardless of how the excitation and subsequent dissociation of XeF^* is brought about.

Finally, the possibility that the angular distribution of the Xe^+ signal from XeF^* is different than the angular distribution of the Xe^+ signal from the XeF product that survives the surface reaction is considered as a route to identify the contribution of the momentum matched Xe^* atom to the Xe^+ signal. The Xe^+ signal arising from the dissociative ionization of XeF is expected to follow the peculiar angular distribution observed for the XeF^+ signal (see Figure 2.21), which is thought to arise because of the preferential orientation of the incident XeF_2 or ejected XeF. On the other hand, little can be predicted a priori about the angular distribution of the Xe^+ signal arising from the dissociation of the excited XeF^*. On one extreme, the angular distribution of Xe^* could follow that of the XeF product from which it is produced. This might certainly be the case if the dissociation process is fast compared to the rotational period of XeF^*. If the dissociation of XeF^* is fast compared to its rotational period, the contribution to the Xe^+ signal arising from Xe^* will have an angular distribution indistinguishable from the contribution arising from XeF. If this is the case, the two contributions cannot be separated, and no claims can be made about the relative importance of the two channels. Alternatively, if the dissociation lifetime of the XeF^* product is long compared to its rotational period, the XeF^* would undergo multiple rotations before dissociating. The isotropic distribution of orientations produced by the rotation of XeF^* would lead to a broadening of the Xe^* angular distribution which might make it possible to distinguish it from the undissociated XeF product, and hence to both find definitive evidence for the momentum matched Xe atom and to assess the relative importance of the XeF^* dissociation process.

The time in which the dissociation of XeF^* takes place, as well as the extent and exact nature of the excitation are primarily determined by details of the gas-surface

interaction potential which are largely unknown. An estimate of the XeF^* lifetime can be obtained, however, by assuming that its dissociation occurs during its interaction or collision time with the surface. An estimate[42] for the range of Si—F interaction potential is of the order of 5 Å. The translational velocity of the ejected XeF product is determined from the time-of-flight distribution of the XeF^+ signal to be approximately 700 m sec^{-1}. This combination of distance and velocity give a maximum collision time and hence dissociation lifetime of the order of 0.7 ps. The vibrational frequency and rotational constant[88] of XeF in the ground electronic state are 225 cm^{-1} and 0.15 cm^{-1}, respectively, which implies a vibrational period of the order of 0.15 ps and a rotational period of 111 ps for the lowest rotational state. XeF is thus expected to dissociate within 4.6 vibrational periods and expected to complete only 0.01 of a complete J=1 rotation. If the rotational distribution is populated up to the J=10 level, the rotational period decreases to approximately 2 ps, or three times the estimated dissociation lifetime. Only if there is a substantial population of rotational levels above the J=17 state can the XeF^* product undergo a complete rotation before it dissociates, and therefore give rise to a broadening of the Xe^* angular distribution. However, even in the case of highly rotationally excited XeF, the broadening of the Xe^* angular distribution may not be enough to distinguish it from the angular distribution of the XeF that survives the reaction. It is estimated[98] that if a XeF molecule dissociates with its bond axis perpendicular to its center of mass velocity, the direction of the laboratory velocity of the Xe^* fragment will be within 20° of that of the XeF.

It is experimentally observed that the angular distributions of Xe^* and XeF are indistinguishable. Whereas this observation does not answer the question of whether the XeF^* product undergoes a full rotation before dissociating, it does confirm that the Xe^* and XeF contributions to the Xe^+ cannot be deconvoluted on the basis of their angular distribution. The best indication that XeF and Xe^* have the same angular distribution is

obtained from the constancy of the scaling factor required to match the magnitudes of the XeF^+ and Xe^+ signals discussed in Section 2.3.3. This scaling factor is found to be approximately constant, with an average value of 11.5±3.5 when all detection angles are included. To illustrate how the constant scaling factor translates into the match of the Xe^* and XeF angular distributions, Figure 2.42 presents a comparison of the angular distributions of the XeF^+ and Xe^+ signals. The XeF^+ data (squares), which are reproduced from Figure 2.21, corresponds to the XeF product that survives the chemical reaction, while the Xe^+ signal (circles), which is obtained by integrating the partially deconvoluted Xe^+ signals shown in Figure 2.26, corresponds to the signal arising from the superposition of XeF and Xe^*. As expected, the angular distributions are indistinguishable, therefore precluding the separation of the Xe^* and XeF components and the assessment of the branching ratio between survival and dissociation of the XeF product.

The angular distribution of the lighter F^* partner, which unfortunately has not yet been measured, may be more sensitive to the broadening caused by XeF^* rotations, and might therefore yield some information about how the chemical excitation process gets partitioned into the rotational degrees of freedoms. If the XeF^* is rotationally excited such that it completes a rotation before it dissociates, then the angular distribution of the F^* matching the momentum of Xe^* will be broadened. In this case, the direction of the laboratory velocity of the F^* will be largely determined by the relative orientation of the XeF bond axis with respect to its center of mass velocity. In addition, a quantitative analysis of the fast F^* atom flux will provide an alternate way to estimate the relative amount of Xe^* produced by the reaction, and hence the relative importance of the chemically induced dissociation of XeF. The ratio of fast F^* atom flux to the total flux of F atoms incident on the surface will give a measure of the absolute probability of the chemically induced dissociation process. A closer study of the F^* atom velocity and

angular distributions thus promises to yield further information about the interaction of XeF_2 with the Si(100) surface.

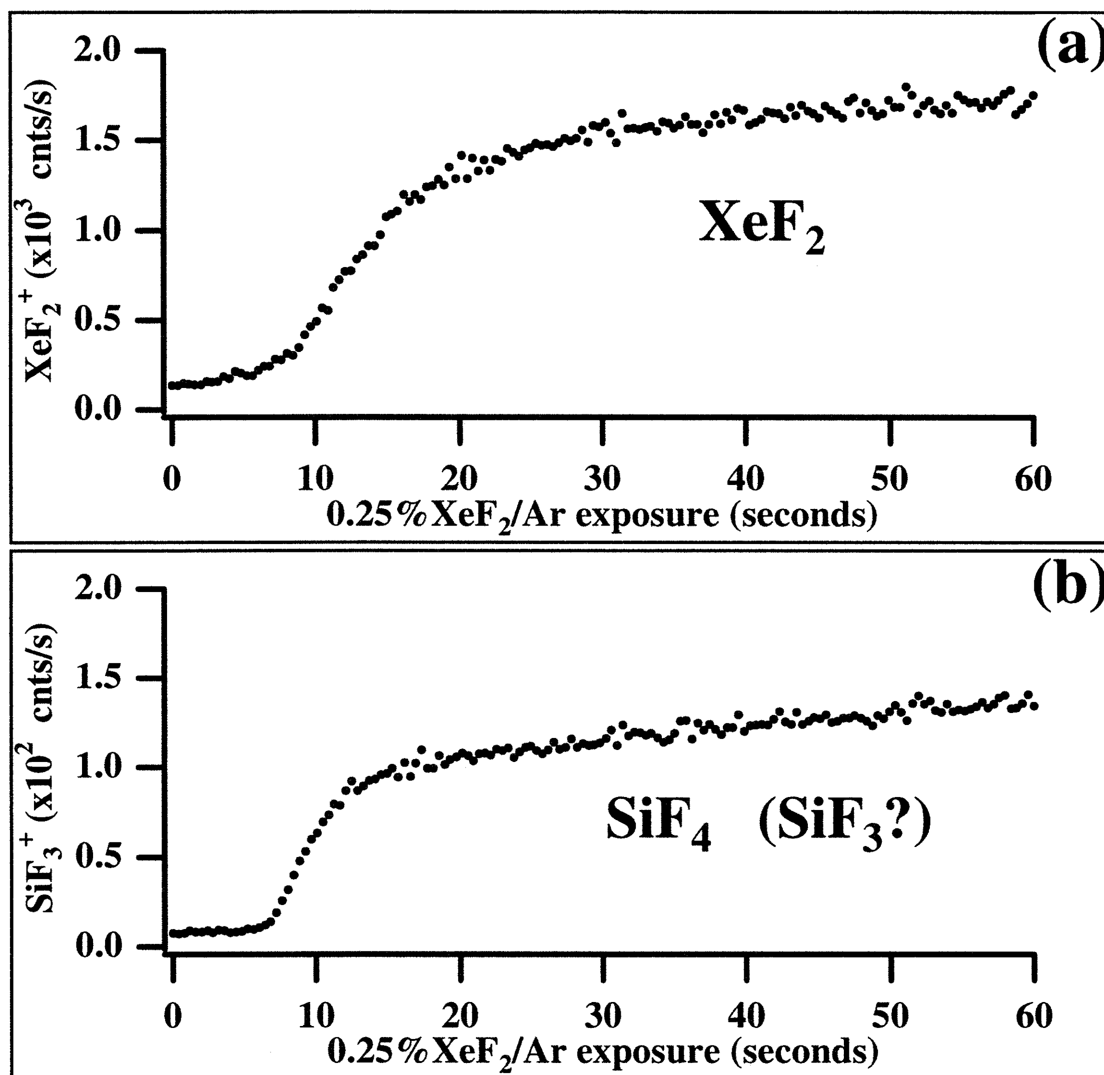

Figure 2.40 Exposure Dependence of the XeF_2 and Etch Products

Exposure dependence of products scattered at 0° from a 250 K Si(100) exposed to a 0.25% XeF_2/Ar beam (6.77 kcal mol^{-1}) incident at 35° from surface normal. (a) XeF_2 product detected as XeF_2^+. (b) Etch product detected as SiF_3^+

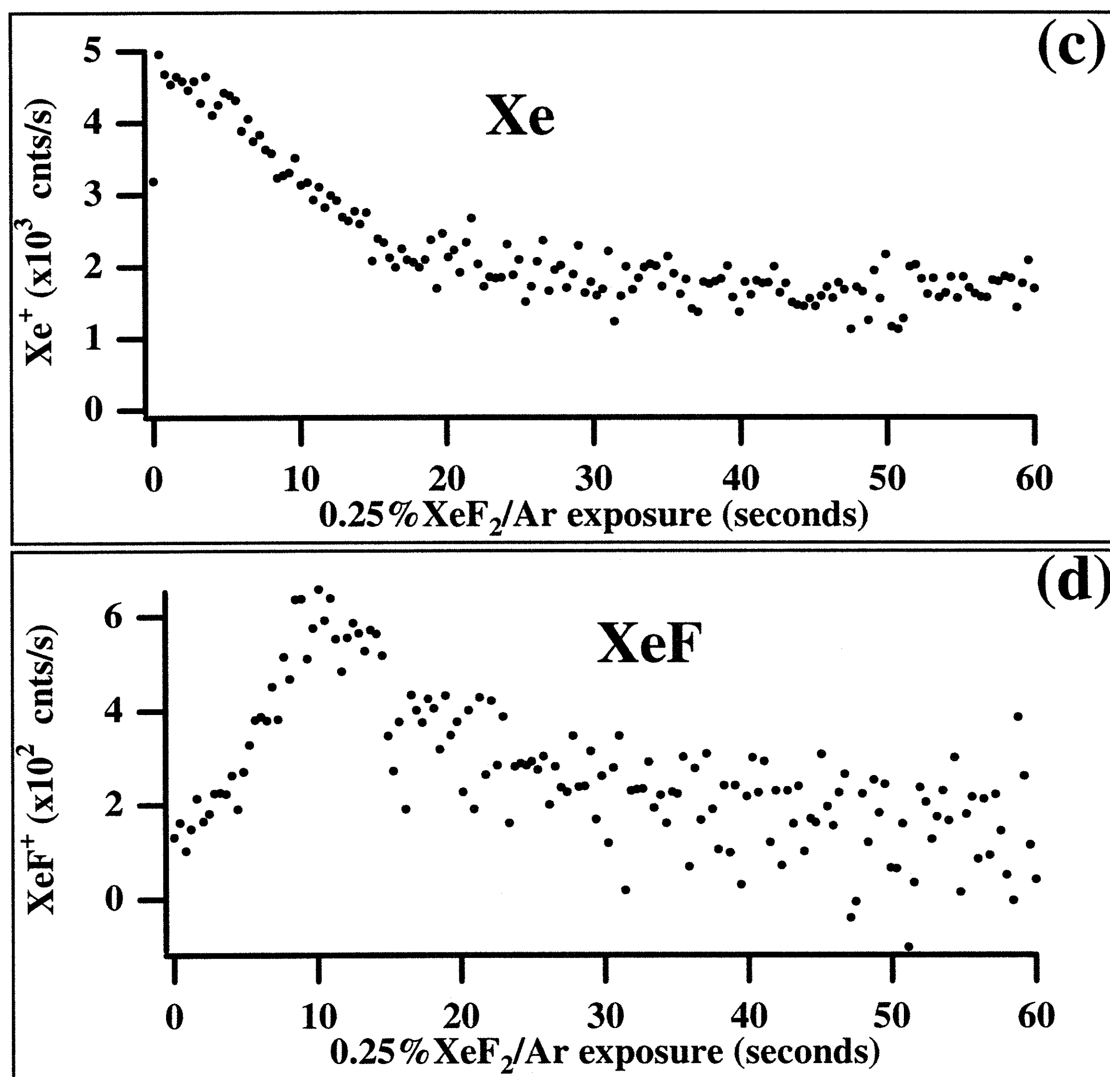

Figure 2.40 Exposure Dependence of Xe and XeF Products

Exposure dependence of products scattered at 0° from a 250 K Si(100) exposed to a 0.25% XeF_2/Ar beam (6.77 kcal mol^{-1}) incident at 35° from surface normal. (c) Xe product detected as Xe^+. (d) XeF product detected as XeF^+.

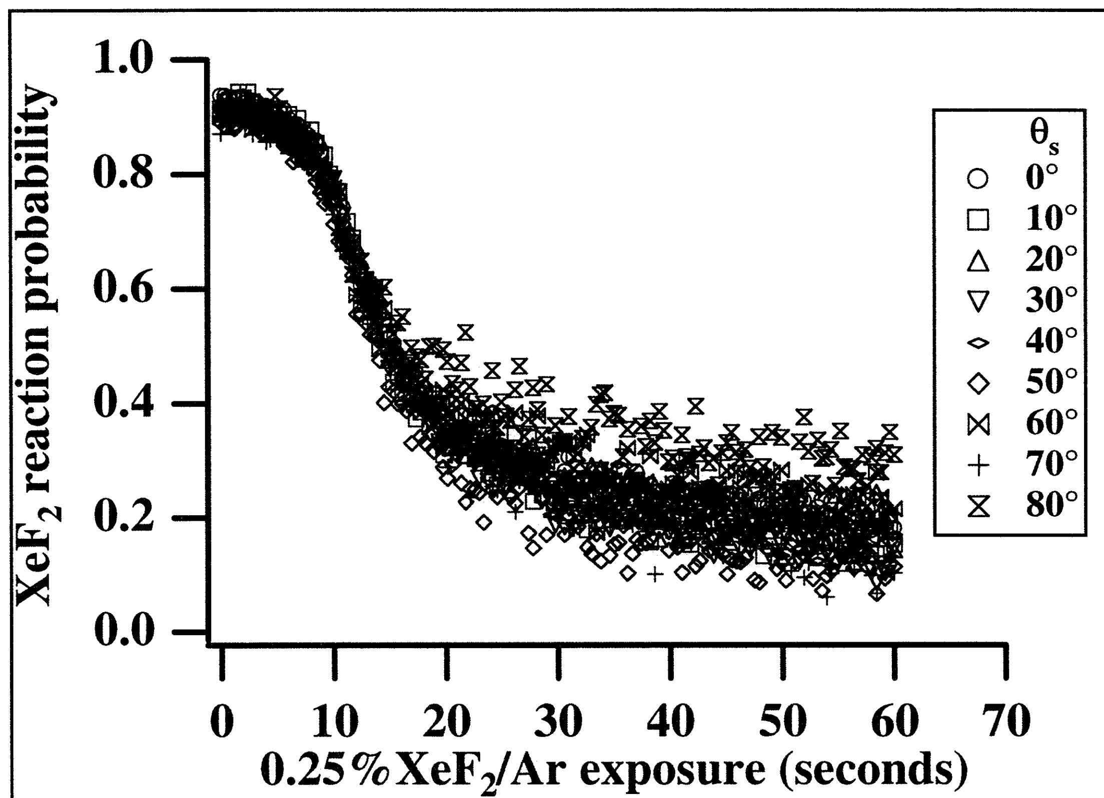

Figure 2.41 Total Reaction Probability of a XeF_2/Ar Beam Exposed to Si(100)

Total XeF_2 reaction probability as a function of exposure to a 0.25% XeF_2/Ar beam incident at 35° onto a clean Si(100) surface held at 250 K. The probability is calculated by dividing the XeF_2^+ scattered signal from Si(100) as a function of exposure by the XeF_2^+ scattered signal from the vacuum oxidized inert surface. Data from eight different scattering angles (0-80° in 10° increments) are overlaid, and found to be nearly indistinguishable.

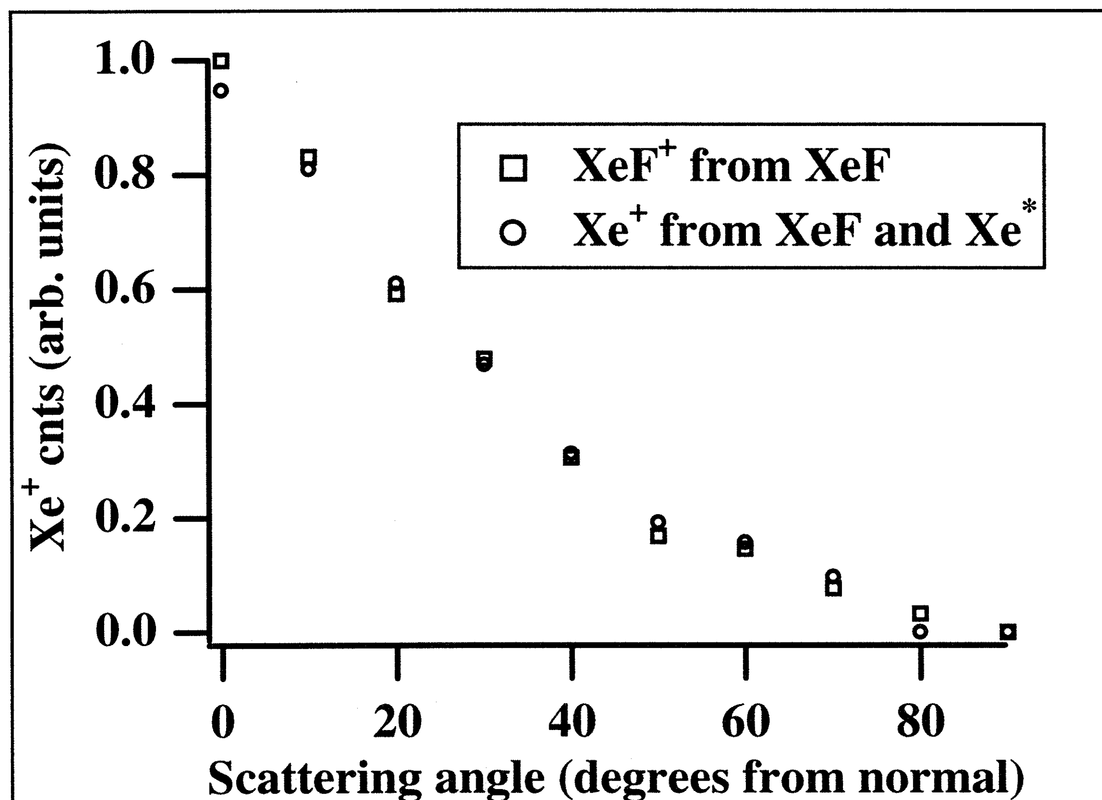

Figure 2.42 Comparison of Angular Distribution of XeF^+ and Xe^+ Signals

Angular distribution of XeF product detected as XeF^+ (squares), which is reproduced from Figure 2.21, is compared to the angular distribution of Xe^+ signal (circles), which is obtained by integrating the Xe^+ signals arising from the superposition of XeF and Xe^* products previously shown if Figure 2.26.

2.5 Conclusions

The interaction of a XeF_2 incident with a translational energy of 6.7 kcal mol^{-1} onto a Si(100) surface at 250 K leads to a steady state fluorine coverage of approximately 1.85 ML and is accompanied by the removal of Si at a constant rate. The desorption of volatile Si products demonstrates the ability of XeF_2 to attack the Si—Si dimer and subsurface bonds causing the destruction of 2x1 surface periodicity. The fluorination of Si by XeF_2 occurs via an atom abstraction mechanism similar to that observed in the interaction of F2 with Si(100). Abstraction is confirmed by the mass spectrometric identification of the scattered XeF fragment. The translational velocity of the scattered XeF is large compared to the incident energy indicating that it acquires some of the exothermicity released by the reaction. The XeF angular distribution is narrow and sharply peaked at angles near the surface normal, suggesting that the XeF fragments are preferentially ejected at low scattering angles. Some of the XeF product is formed in a highly vibrationally excited or in a repulsive electronically excited state so that it dissociates before reaching the detector. This process is evidenced by a measurement of the velocity distribution of scattered F atoms which reveals a very fast narrow feature consistent with the gas phase decomposition of the XeF abstraction product. The dissociation of XeF is thought to be a consequence of its electronic or vibrational excitation caused by the chemical energy released during the abstraction reaction. The momentum matched Xe partner expected from the dissociation of XeF could not be uniquely identified since its velocity, angular distribution and exposure dependence are indistinguishable from those of the undissociated XeF product. Further study of the F fragment ejected during the dissociation of XeF may yield additional information about the partitioning of the exothermicity from atom abstraction and the ensuing gas phase dissociation of XeF.

3 APPENDICES

APPENDIX A: ERROR ANALYSIS

This section presents a detailed analysis of the uncertainties in the measurements and calculations involved in the determination of the F_2-silicon reaction probabilities and coverage.

Pure Beam Fluxes

First, the sources of error involved in the determination of the flux of a single component molecular beam are presented. Two different approaches were used to measure the flux of the neat Ar and Ne molecular beams. One method involves the measurement of the steady state pressure when a beam is introduced into the main chamber which is continually pumped. The second method involves monitoring the pressure rise in the evacuated, but non-pumped chamber as the beam is introduced. The average of the values obtained by both methods is used in the absolute probability and coverage calculations.

The beam flux impinging on the Si surface as given by the first method is

$$I_{in} = \left(\frac{P_{obs} C_F S_P}{kTA_{spot}} \right) \tag{3.82}$$

where sources of error must be identified for the observed ion gauge pressure reading, P_{obs}, the ion gauge correction factor, C_F, the pumping speed, S_p, the temperature inside the chamber, T, and the surface area exposed to the beam, A_{spot}. The estimated values for the uncertainties of all measurements required in the determination of the Ar and Ne beam fluxes are summarized in Table 3-1. A brief discussion follows of how each of the uncertainties was estimated.

Uncertainty in P_{obs}.

The largest uncertainty associated with the measurement of P_{obs} arises from the

limited precision of the ion gauge controller's digital readout. The controller gives pressure readings with only two significant digits in the mantissa. Interpolation to ±5 on the next (third) significant digit of the mantissa can be accomplished by observing the second digit fluctuations over the measurement time. The uncertainty in the mantissa of an ion gauge reading is then estimated to be ±0.05. Since this uncertainty is absolute, the percent error on ion gauge readings depends on the absolute value of the mantissa. A 0.7% relative error was determined for the pure Ar beam while an error of 2.8% is calculated for the Ne beam. Strictly speaking, P_{obs} is the difference between the ion gauge reading of the pressure before and after the introduction of the molecular beam into the main chamber. The main chamber pressure before introduction of the beam also contributes a ±0.05 uncertainty to the mantissa. However, this pressure is three to four orders of magnitude lower than the P_{obs} value, and thus contributes a negligible amount to the measurement's uncertainty.

Uncertainty in C_F

The ion gauge correction factor, C_F, is determined by expanding a known volume of gas into the known volume of the main chamber. The error in the correction factor depends on the uncertainties of two volume and two pressure measurements.

$$C_F = \left(\frac{P_{cal} V_{cal}}{\Delta P_{\text{expan}} V_{chamber}^{stagnant}} \right) \tag{3.83}$$

The pressure inside the small calibrated volume, P_{cal}, is measured with a capacitance manometer. Once again, the uncertainty of the pressure measurement can be estimated from the least significant digit on a digital readout. To improve the accuracy of the pressure measurement, the gauge's output was connected to a digital voltmeter capable of displaying voltage variations of ±1 μV which corresponds to pressure fluctuations of ±0.01 Torr. For each pressure reading, 10 to 20 voltmeter readings are collected and averaged so as to reduce the effect of random fluctuations. The observed uncertainty (±

one standard deviation) is determined to be on the order of 0.1 Torr. Since the measured pressures are on the order of 1-15 Torr, the relative error in the manometer readings are in the range of 1-10%. Furthermore, the absolute pressure is obtained after subtracting the baseline pressure reading with no gas in the small calibrated volume, which also has an absolute uncertainty associated with it on the order of 0.1 Torr. The baseline pressure values varied from 2 to 5 Torr, hence their relative error is between 0.5-5%. Propagation of these uncertainties yields an absolute uncertainty of ±0.14 Torr for the manometer readings. When pressures as small as 1 Torr are measured with the capacitance manometer, the relative error is above 10%. This measurement is the least precise one involved in determining the ion gauge correction factor, and hence it limits the precision of the overall measurement.

The volume of the small calibrated volume is determined from the weight and density of water required to fill it. The uncertainty in the difference between two weight measurements required is estimated to be ±0.001 gr. whereas the uncertainty in the water density is estimated to be ±0.001 gr./ml. The uncertainty in the density of water arises from the uncertainty in the knowledge of the water temperature which was not measured, but which is estimated to have been between 20-30°C. Combining the weight and density uncertainties, the measurement error for the volume is 0.6% as reported in Table 3-1.

The measurement of the main chamber volume, as described in section 1.4.4.4, relies on gas expansions from the manifold into the main chamber. The pressures before and after an expansion are measured with the capacitance manometer, whose uncertainty has been estimated in the above discussion to be ±0.1 Torr. In addition, the previously given ±0.6% error in the small calibrated volume determination must be taken into account. Propagation of these pressure and volume uncertainties yields an error for a single measurement of the main chamber volume of ± 1%. The gas expansions leading to the

measurement of the main chamber volume are repeated a series of 5 times, and the standard deviation of the mean is determined to be ±10 l which corresponds to a 95% confidence limit of ±12 l.

The pressure rise in the main chamber after the expansion, ΔP_{expan}, is measured with the ion gauge, and thus suffers from an uncertainty in the mantissa of ±0.05. For each ΔP measurement, the computer was used to monitor pressure upon expansion, with upwards of 400 consecutive measurements being recorded. The uncertainty in this pressure rise is then taken as the standard deviation of the mean of those 400 measurements, which range from 0.01-0.05x10^{-8}, since the measured pressures range from 2x10^{-6} to 5x10^{-6} Torr. The relative uncertainty is on the order of 0.7-1.5% for both Ar and Ne expansions.

The gas expansions leading to the measurement of the ion gauge correction factor are also repeated 5 times. In each instance, the uncertainty of the measured value is estimated by propagating the errors of all quantities in equation (3.83) as given in Table 3-1. The 5 values are then averaged to give the best estimate of C_F for Ne and Ar. The uncertainty is given by the standard deviation of the mean of this five measurements.

Pumping Speed, S_p

The pumping speed, S_p, is obtained by multiplying τ, the characteristic decay time required to pump out the chamber after the beam entering it is interrupted, times $V_{chamber}$, the main chamber volume including the gate valve region. The error in τ is determined, by standard statistical methods, from the quality of the least-squares exponential fit of the pressure-drop recorded during pump out and shown in Figure 1.17. The fitting program (Wavemetric's Igor Pro 3.0) estimates the uncertainty in the exponential fitting coefficients from the square root of the diagonal elements of the covariance matrix. In order for the covariance matrix to give a meaningful estimate of the fitting error, the data

must be weighted by the inverse of the uncertainty of each data point[102]. In this case, since the signal arises from event counting, the error of each point is estimated as the square root of the number of counts. The uncertainty values obtained for the characteristic decay times are on the order of ±0.005 representing a relative error between 0.3-0.4%. Since the uncertainty in the chamber volume is of the order of 1%, it is the limiting factor in the determination of the uncertainty in the pumping speed.

Chamber Temperature, T

The temperature inside the main chamber, which appears in the denominator of the beam flux expression is measured by the thermocouple attached to the back of the Si surface. The uncertainty in this temperature measurement is limited by fluctuations in the last digit of the thermocouple output voltage. The standard deviation of 20 measurements of the thermocouple output was determined to be ±0.25 K with a 95% confidence limit of ±0.5 K.

Area of the Beam Spot, A_{spot}

The area of the Si surface exposed to the beam is calculated from the geometry of the apparatus. As discussed in Section 1.2.1, the beam produces an image on the crystal with the dimensions of 6.4±0.05 by 4.5±0.05 mm. The uncertainty in these dimensions is calculated from the tolerances specified on the drawings used to machine the beam collimating aperture. Propagation of these uncertainties with the uncertainty in the distance between the aperture and the surface yields a relative error of less than 0.1%.

The propagation of the uncertainties given in Table 3-1 in Eq. (3.82) yield an overall precision for the pure Ar and Ne beam fluxes as determined from the steady state pressure rise method of

---

[102] *Igor Pro Version 3.0 User's Guide*, Vol. II, Lake Oswego, OR: Wavemetric's Inc., p.539 , (1996)

$I_{in}^{Ar} = 17.8 \pm 0.3$ ML sec^{-1}

$I_{in}^{Ne} = 24 \pm 1$ ML sec^{-1}

The second method used to calculate the beam fluxes is based on the determination of the pressure rise, $\Delta P_{stagnant}$, upon introduction of the beam into the unpumped chamber. The expression relating the pressure rise and the beam flux is

$$I_{in} = \left(\frac{V}{kTA_{spot}}\right)\left(\frac{\Delta P}{\Delta t}\right) \tag{3.84}$$

The uncertainty in the measurement of the rate of pressure rise arises from the uncertainty in the ion gauge reading which is of the order of ±0.1 for the value of the mantissa. The relative uncertainty in the rate of pressure rise is between 1-4%. The uncertainties of all other quantities in Eq. (1.43) are equal to those described for the steady-state pressure method and are given in Table 3-1. The values for the flux of the Ne and Ar beams as determined by this method are

$I_{in}^{Ar} = 18.7 \pm 0.3$ ML sec^{-1}

$I_{in}^{Ne} = 23.3 \pm 1.2$ ML sec^{-1}.

Averaging the results from both methods gives final values of

$I_{in}^{Ar} = 18.3 \pm 0.3$ ML sec^{-1}

$I_{in}^{Ne} = 23.7 \pm 1.1$ ML sec^{-1}

for the pure beam fluxes. The quoted uncertainties are obtained by propagating the errors for each of the independent measurement methods in the averaging procedure.

Table 3-1 Estimated Uncertainties in the Determination of the Pure Beam Flux

Quantity	Value	Absolute error	Relative error	95% confidence
P_{obs}^{Ar}	7.5-7.9x10^{-8} Torr	±0.05x10^{-8}	0.7%	
P_{obs}^{Ne}	1.8x10^{-8} Torr	±0.05x10^{-8}	2.8%	
P_{cal}^{Ar}	1.5-10.2 Torr	±0.14	1.5-10%	
P_{cal}^{Ne}	5.1-13.4 Torr	±0.14	1-3%	
$\Delta P_{\text{expan}}^{Ar}$	2.3-7.6x10^{-6} Torr	1-5x10^{-8}	0.7-1.5%	±1-5x10^{-9}
$\Delta P_{\text{expan}}^{Ne}$	1.9-4.9x10^{-6} Torr	3-4x10^{-8}	1-1.5%	±3-4x10^{-9}
V_{cal}	1.745x10^{-3} l	±0.001x10^{-3}	0.6%	
$V_{chamber}$	886 liters	±10	1%	
$V_{chamber}^{stagnant}$	870 liters	±10	1%	±12
τ_{Ar}	1.21 sec^{-1}	±0.005	0.4%	
τ_{Ne}	1.67 sec^{-1}	±0.005	0.3%	
S_p^{Ar}	1070 liters sec^{-1}	±11	1%	
S_p^{Ne}	1480 liters sec^{-1}	±15	1%	
T	294 K	±0.25	0.1%	±0.5
C_F^{Ar}	1.31	±0.01	1%	±0.025
C_F^{Ne}	5.29	±0.15	3%	±0.42
$\left(\frac{\Delta P}{\Delta t}\right)_{Ar}$	9.7x10^{-8} Torr sec^{-1}	±.0.1	1%	±0.3
$\left(\frac{\Delta P}{\Delta t}\right)_{Ne}$	3.0x10^{-8} Torr sec^{-1}	±0.1	4%	±0.3
A_{spot}	2.86x10^{-5} m^2	±0.04x10^{-5}	±0.1%	

Seeded Beam Fluxes

The flux of the seeded F_2/Kr beam is obtained by reference to the F_2/Ar beam, which does not suffer from the detrimental effects of Mach number focusing. First the flux of the reference F_2 /Ar beam is determined from [F_2], the nominal concentration of fluorine in the mixing cylinder and I_{Ar}, the flux of the pure Ar beam determined in the previous section.

$$I_{F_2/Ar} = [F_2]I_{Ar} \tag{3.85}$$

The mixture is prepared using two interconnected mixing cylinders as described by

Yang[103]. The smaller cylinder is used to hold the desired pressure of F_2, while the larger one is filled with the appropriate pressure of Ar. The two valves separating the interconnected cylinders are then opened allowing the gases to mix. The uncertainty in the nominal F_2 concentration arises from the ±0.5 Torr uncertainty in the two Baratron readings required to measure the pressure in each of the cylinders and from the uncertainty in the volume ratio of the two mixing cylinders.

The flux of the F_2/Kr beam is determined by comparing its F_2 signal to that obtained from the 1%F_2/Ar reference beam,

$$I_{F_2/Kr} = \left(\frac{VWC\, S_{F_2}^{F_2/Kr}}{VWC\, S_{F_2}^{F_2/Ar}} \right) I_{F_2/Ar} \tag{3.86}$$

The amount of F_2 in the beams is determined from the time-of-flight spectrum of each of the beams. The signals used in Eq. (3.86) are velocity weighted counts (VWC) determined by fitting time-of-flight spectra to a supersonic molecular beam functional form. The velocity distribution of particles in supersonic flow is given by

$$f(v)dv = B' v^2 \exp\left[\frac{-m(v - v_f)^2}{2kT_b} \right] dv \tag{3.87}$$

where B' is a normalization constant, m is the particle mass, v is the particle velocity, T_b is the translational temperature of the beam, and v_f is the characteristic flow velocity for the distribution. Since the data are collected as a function of arrival time and with a mass spectrometer which is sensitive to number density rather than particle flux, the above velocity distribution needs to be divided by v, and converted into a function of neutral flight time, t_n, to which the data can be fit

$$f(t_n) = A + B(t_{meas} - t_d)^{-4} \exp\left[\frac{-m}{2kT_b} \left(\frac{L_n}{t_{meas} - t_d} - \frac{L_n}{t_f} \right)^2 \right] \tag{3.88}$$

---

[103] J. J. Yang, Ph.D. Thesis, Massachusetts Institute of Technology, pp. 27-29, (1993)

here, t_{meas} is the measured arrival time, L_n is the flight path of the neutrals between the chopper wheel and the ionization region, t_d is the additional delay incurred by the ionized molecules in reaching the particle counter, and t_f is the flight time associated with the beam's flow velocity. The baseline, A, the normalization factor, B, the beam temperature, T_b, and flight time t_f are used as parameters in a non-linear least-squares fit of the time-of-flight data. The velocity weighted counts are determined by multiplying each point in the arrival time distribution by its velocity and integrating over all collection channels.

A method must be devised for estimating the uncertainty in the determination of the velocity weighted counts. The cross-correlation technique used to measure the time-of-flight distribution causes a spread of the measurement's uncertainty over all collection channels. The uncertainty of each point in the deconvoluted spectrum is found to be larger than the square root of the number of counts expected from Poisson statistics. In particular, the standard deviation is found to be the same for all points in the time-of-flight distribution, and it is equal to the square root of the sum of the counts in all channels of the deconvoluted spectrum:

$$\sigma(d_k) = \sqrt{\sum_{i=0}^{N-1} d_i} \tag{3.89}$$

Here d_k is the kth point in the deconvoluted spectrum, and N is the number of elements in the chopping sequence (255 in our case). A detailed derivation of the above result and its implications is given in Appendix B.

The estimated uncertainties of each point in the arrival time spectrum are used as weights for the non-linear least-squares fit. The uncertainty in the fit parameters is calculated from the square root of the diagonal elements of the covariance matrix[104]. The

[104] W. H. Press, S. A. Teukolsky, W. T. Vetterling, B. P. Flannery, Numerical Recipes in C: The Art of Scientific Computing, Second Ed., Cambridge University Press, p. 673, (1992)

fit parameters are then used to calculate the total counts in the spectrum by integrating the fitted distribution. Velocity weighted counts are finally obtained by multiplying the total counts at each point in the fitted curve by the arrival velocity associated with it. The standard deviation in the calculated velocity-weighted-counts is obtained by standard error propagation of the uncertainties in the fitted parameters. All uncertainty calculations are implemented by the fitting program (TOFFITV). It is worth noting that any uncertainty in the abscissa of the time-of-flight spectrum is neglected in the determination of the fitting parameter uncertainties. The main source of error in the time axis probably arises from the uncertain knowledge of the neutral flight path. The uncertainty in the neutral flight path arises from the ill defined length of the ionization region. The relative error in the time axis can be estimated to be of the order of Δl/l, where l is the ionizer's length.

Table 3-2 presents typical values and uncertainties of all measurements required for the determination of the uncertainty in the flux of the seeded 1% F_2/Kr beam used in this investigation. Propagation of the uncertainties associated with the quantities in Eq. (1.43) yields a final value of

$$I_{F_2/Kr} = 0.085 \pm 0.003 \text{ ML sec}^{-1}$$

Table 3-2 Estimated Uncertainties in the Seeded Beam Flux Determination

Quantity	Value	Absolute error	Relative error
$P_{F_2}^{small\ cyl}$	220 Torr	±0.7	0.3%
$P_{Ar}^{large\ cyl}$	5000 Torr	±0.7	0.01%
V_{large}/V_{small}	4.38	±0.003	0.07%
$[F_2]$	1.00 %	±0.003	0.3%
VWC_{38}^{Ar}	3.54×10^6 cnts sec^{-1}	$\pm 1.32 \times 10^5$	4%
$VWC_{38}^{F_2/Ar}$	1.83×10^7 cnts sec^{-1}	$\pm 3.12 \times 10^5$	2%
$VWC_{F_2}^{F_2/Ar}$	1.48×10^7 cnts sec-1	$\pm 3.39 \times 10^5$	2%
$VWC_{F_2}^{F_2/Kr}$	6.88×10^6 cnts sec-1	$\pm 8.70 \times 10^4$	1.3%
I_{Ar}	18.3 ML sec^{-1}	±0.3	2%

F_2 and F-atom Velocity Ratio

The ratio of the average velocity of unreactively scattered F_2 to the average velocity of ejected F-atoms is needed in order to convert the net F-atom signal into a probability (see Eq. (1.18)). Both velocities are measured by collecting and fitting the time-of-flight spectra of the appropriate scattered particle. The flux weighted average velocity is determined by multiplying the fitted velocity distribution by v^2 and integrating. Once again the estimated error of each point in the deconvoluted spectrum is given by the square root of the sum of the counts in all channels. This error is used for weighting the fitting procedure to yield the uncertainty of the fitted parameters, and these are in turn propagated to obtain the final estimate of the uncertainty of the velocity. The calculation of the uncertainties is accomplished by the use of the TOFFITV program. Table 3-3 shows the average velocities and uncertainties as calculated from the fit for both F_2 and F-atoms scattered from the Si surface.

Table 3-3 Estimated Uncertainty in the Determination of F_2 and F Velocity Ratio

Quantity	Symbol	Value	Abs. error	Rel. error
F_2 average velocity	v_{F_2}	436 m sec^{-1}	± 14	3%
F-atom average velocity	v_F	1100 m sec^{-1}	± 60	5%
Velocity ratio	v_F/v_{F_2}	2.5	±0.2	6%

Transmission Function

The transmission ratio for ions of m/e=38 and m/e=19 is needed for the determination of the $\sigma_{F_2 \to F^+}$ cross-section. Using pure beams of Ne and Ar for which the ionization cross-sections are well established, the transmission ratio of m/e=36 to m/e=22 is determined from

$$\frac{T_{36}}{T_{22}} = \left(\frac{VWC\,S_{36}^{Ar}}{VWC\,S_{22}^{Ne}}\right)\left(\frac{\sigma_{Ne \to Ne^+}}{\sigma_{Ar \to Ar^+}}\right)\left(\frac{I_{Ne}}{I_{Ar}}\right) \tag{3.90}$$

where the low abundance ^{36}Ar and ^{22}Ne isotopes are used to avoid the excessively high

signal levels obtained from the most abundant isotopes. The uncertainties associated with the velocity weighted counts are obtained from the time-of-flight fitting procedure as outlined in Appendix B. The uncertainties in the fluxes of pure Ar and Ne beams have already been given, but the natural abundance of the rarer isotopes must be known to determine their concentration in the beam. The values used correspond to the best measurement from a single natural source as determined by the Commission of Atomic Weights and Isotopic Abundances[105]. The uncertainties in the measurements are those quoted by the original authors[106,107].

The values for the Ne and Ar electron ionization cross-sections are taken from the literature and the uncertainties used are those quoted by the authors reporting the measurement. In the case of $\sigma_{Ar \rightarrow Ar^+}$, the value reported by Smith and coworkers[108] is used. In this measurement, a chamber filled with Ar is ionized by an electron gun from a television tube. The resulting Ar^+ ions are collected by a position sensitive detector. An absolute uncertainty of ± 3.5 % for the partial ionization cross-section is reported. The low uncertainty in the measurement is achieved by the accurate determination of both the number of Ar ions and electrons produced, as well as the precise knowledge of the target gas density and ionization path length. According to the authors, the major contribution to the experimental uncertainty arises from the pressure measurement required to calculate the gas density inside the chamber.

As of this time, the group headed by Smith has not used their apparatus to determine the partial ionization cross-section of Ne. The $\sigma_{Ne \rightarrow Ne^+}$ cross-section is taken from the earlier work of Freund and coworkers[109]. In this case, a fast neutral beam of Ne is

---

[105] The commission on Atomic Weights and Isotopic Abundances "Table of Isotopic Compositions of the Elements as Determined by Mass Spectrometry", (1989)

[106] D. J. Bottomley, J. D. Ross, and W. B. Clarke, Geochim. Cosmichim. Acta. **48**, 1973 (1984)

[107] A. O. Nier, Phys. Rev. **77**, 789 (1950)

[108] H. C. Straub, P. Renault, B. G. Lindsay, K. A. Smith, and R. F. Stebbings, Phys. Rev. A **52**, 1115 (1995)

[109] R. C. Wetzel, F. A. Baiocchi, T. R. Hayes, and R. S. Freund, Phys. Rev. A **35**, 559 (1987)

prepared by charge-transfer neutralization of a mass-selected ion beam and is ionized as it crosses an electron beam. According to the authors, the absolute accuracy of their measurement, including statistical errors is about ±15%. No details are given of the origin of their quoted experimental uncertainty.

Table 3-4 summarizes the values of the uncertainties involved in the determination of the transmission ratio. Propagation of these uncertainties through Eq. (3.90) yields

$$\frac{T_{36}}{T_{22}} = 0.918 \pm 0.15 \tag{3.91}$$

The ions of interest in the determination of the abstraction probability are F_2^+(m/e=38) and F^+(m/e=19). Having obtained the transmission ratio of m/e=36 to m/e=22 ions, a linear variation in the transmission ratio is assumed and the relative transmission of the desired masses is interpolated as

$$\frac{T_{38}}{T_{19}} = 1 - \left(\frac{1-\left(\frac{T_{36}}{T_{22}}\right)}{(36-22)} \right)(38-19) \tag{3.92}$$

leading to the final result

$$\frac{T_{38}}{T_{19}} = 0.89 \pm 0.15 . \tag{3.93}$$

From the sources of error listed in Table 3-4, it is evident that the limiting factor in the accuracy of the transmission ratio is the large uncertainty in the ionization cross-sections, and in particular, the large uncertainty in the measurement of $\sigma_{Ne \to Ne^+}$.

Table 3-4 Estimated Uncertainties for the Determination of Transmission Ratio

Quantity	Symbol	Value	Abs. error	Rel. error
^{36}Ar signal from pure Ar	$VWC\,S_{36}^{Ar}$	$2.02\text{x}10^{7}$ cnts sec^{-1}	$\pm4.1\text{x}10^{5}$	2%
^{22}Ne signal from pure Ne	$VWC\,S_{22}^{Ne}$	$1.42\text{x}10^{8}$ cnts sec^{-1}	$\pm2.28\text{x}10^{6}$	1.6%
Ar cross-section (70 eV)	$\sigma_{Ar\rightarrow Ar^{+}}$	$2.67\text{x}10^{-16}$ cm^{2}	±0.09	3.5%
Ne cross-section (70 eV)	$\sigma_{Ne\rightarrow Ne^{+}}$	$0.488\text{x}10^{-16}$ cm^{2}	±0.07	15%
^{36}Ar isotope abundance	[^{36}Ar]	0.33656%	±0.000001	0.0003%
^{22}Ne isotope abundance	[^{22}Ne]	9.2469%	±0.00001	0.0001%
^{36}Ar Flux in Pure Ar	I_{Ar}^{36}	0.062 ML sec^{-1}	±0.001	2%
^{22}Ne Flux in Pure Ne	I_{Ne}^{22}	2.19 ML sec^{-1}	±0.1	5%

Ionization Cross-sections

Two fluorine ionization cross-sections are needed to convert the net F-atom signal into a reaction probability as shown in Eq. (1.18). The $\sigma_{F_2\rightarrow F^+}$ cross-section is obtained from

$$\sigma_{F_2\rightarrow F^+}=\left(\frac{VWC\,S_{19}^{F_2/Kr}}{VWC\,S_{38}^{F_2/Kr}}\right)\left(\frac{T_{38}}{T_{19}}\right)\sigma_{F_2\rightarrow F_2^+} \tag{3.94}$$

where a F_2/Kr beam is used to measure the velocity weighted counts, and the experimentally determined value of the transmission ratio is used. Before this cross-section can be determined however, the $\sigma_{F_2\rightarrow F_2^+}$ cross-section must be measured. This latter quantity is obtained from

$$\sigma_{F_2\rightarrow F_2^+}=\left(\frac{VWC\,S_{F_2}^{F_2/Ar}}{VWC\,S_{36}^{F_2/Ar}}\right)\left(\frac{T_{36}}{T_{38}}\right)\left(\frac{[^{36}Ar]}{[F_2]}\right)\sigma_{Ar\rightarrow Ar^+} \tag{3.95}$$

A F_2/Ar beam is used to measure the F_2 velocity weighted counts at m/e=38. The contribution from ^{38}Ar is subtracted from this measurement. The transmission factor is approximated as unity and all other factors and their uncertainties have already been discussed in the previous sections of this appendix.

Finally, the F-atom ionization cross-section is required. This quantity cannot be measured in our chamber, since a calibrated source of F-atoms is not available. A value

published by Freund and coworkers[110] is used. The fast neutral beam method is employed in which a beam of F ions produced by a discharge through an SiF_4 atmosphere is neutralized and then ionized by an electron beam. The uncertainty in the absolute cross-section is quoted as ±20%. A summary of the cross-sections and their uncertainties is given in Table 3-5. The quantity of interest for the determination of the ejected F-atom probability as given in Eq. (1.18) is the ratio of these two cross-sections,

$$\frac{\sigma_{F_2 \to F^+}}{\sigma_{F \to F^+}} = 0.3 \pm 0.08 \tag{3.96}$$

Table 3-5 Estimated Uncertainties for the Determination of Cross-section Ratio

Quantity	Symbol	Value	Abs. error	Rel. error
F signal from 1% F_2/Kr beam	$VWC\,S_{19}^{F_2/Kr}$	$2.95\text{x}10^6$ cnts sec^{-1}	$\pm 6.4\text{x}10^4$	2.2%
F_2 signal from 1% F_2/Kr beam	$VWC\,S_{38}^{F_2/Kr}$	$7.54\text{x}10^6$ cnts sec^{-1}	$\pm 9.0\text{x}10^4$	1.2%
38 signal from 1% F_2/Ar beam	$VWC\,S_{38}^{F_2/Ar}$	$1.87\text{x}10^7$ cnts sec^{-1}	$\pm 3.2\text{x}10^5$	1.7%
^{36}Ar signal from 1% F_2/Ar	$VWC\,S_{36}^{F_2/Ar}$	$1.83\text{x}10^7$ cnts sec^{-1}	$\pm 3.8\text{x}10^5$	2%
^{38}Ar signal from pure Ar	$VWC\,S_{38}^{Ar}$	$3.48\text{x}10^6$ cnts sec^{-1}	$\pm 1.3\text{x}10^5$	3.8%
38 to 19 Transmission ratio	T_{38}:T_{19}	0.89	±0.15	17%
36 to 38 Transmission ratio	T_{36}:T_{38}	~1		
Ar cross-section (70 eV)	$\sigma_{Ar \to Ar^+}$	$2.67\text{x}10^{-16}$ cm^2	±0.09	3.5%
F_2 to F_2^+ cross-section (70 eV)	$\sigma_{F_2 \to F_2^+}$	$0.738\text{x}10^{-16}$ cm^2	±0.03	4.6%
F_2 to F^+ cross-section (70 eV)	$\sigma_{F_2 \to F^+}$	$0.257\text{x}10^{-16}$ cm^2	±0.05	18%
F atom cross-section (70 eV)	$\sigma_{F \to F^+}$	$0.87\text{x}10^{-16}$ cm^2	±0.17	20%
^{36}Ar isotope abundance	[^{36}Ar]	0.33656%	±0.000001	0.0003%
F_2 Concentration in F_2/Ar	[F_2]	1.00 %	±0.003	0.3%

Reaction Probabilities

Having obtained the ratios of cross-sections and velocities, as well as the fluorine flux in the beam, the reaction probabilities P_0, P_1, and P_2 are obtained from scattering data such as that presented in Figure 1.7 by the use of the following expressions,

[110] Todd R. Hayes, Robert C. Wetzel, and Robert Freund, Phys. Rev. A **35**, 578, (1987)

$$P_0(\varepsilon) = \frac{1}{N}\sum_{N}\frac{S_{38}(\varepsilon)}{S_{38}(\infty)} \tag{3.97}$$

$$P_1(\varepsilon) = \left(\frac{v_F}{v_{F_2}}\right)\left(\frac{\sigma_{F_2\to F^+}}{\sigma_{F\to F^+}}\right)\left(\frac{1}{N}\sum_{N}\frac{S_{19}(\varepsilon)}{S_{19}(\infty)} - \frac{1}{N}\sum_{N}\frac{S_{38}(\varepsilon)}{S_{38}(\infty)}\right) \tag{3.98}$$

$$P_2(\varepsilon) = (1 - P_0(\varepsilon) - P_1(\varepsilon)) \tag{3.99}$$

Typically, several scattering measurements are combined in order to improve the signal-to-noise ratio of the collected data. The index, N, in the summations refers to the number of measurements being averaged.

The reduction of the scattering data to yield reaction probabilities as a function of exposure is accomplish by the use of a program called ANALSTK.FOR. This program first takes an input file containing the following information: 1) the name of the N scattering data files to be signal averaged. 2) the number of baseline points recorded before and after the scattering measurement, which are used to subtract contributions from the background gas in the chamber. 3) the index of the first and last point to be used for the evaluation of the long exposure signals, $S_{19}(\infty)$ and $S_{38}(\infty)$. 4) the ratio of F and F_2 ionization cross-sections and velocities needed to obtain P_1. 5) the beam flux which is used for the calculation of the exposure variable. The program then uses Eqs. (3.97), (3.98) and (1.16) to calculate the three reaction probabilities which are shown in Figure 1.14. Each individual point in the probability plots has an uncertainty associated with it which is derived from the standard deviation of the average of the N individual scattering measurements. Given the high density of points, inclusion of an error bar for each data point in the probability plots would contribute to clutter the figure. Instead, and in order to assess the reproducibility of the scattering measurements, the plots presented in Figure 1.7 overlay data obtained in five different experiments using three different 1% F_2/Kr mixtures and two different Si(100) surfaces. The scatter of the points in Figure 1.14 represents a good estimate of the uncertainty of the probability measurements. In

addition, representative error bars are given at short, intermediate and long exposures.

Fluorine Coverage

The fluorine coverage present on the Si surface as a function of exposure to the molecular beam is obtained by integrating the reaction probabilities discussed in the previous section over the full range of fluorine exposure. The mathematical expression governing the coverage is

$$\theta(\varepsilon) = \int_0^{\varepsilon} (2 - 2\mathrm{P}_0(\varepsilon) - \mathrm{P}_1(\varepsilon)) I_{F_2/Kr} d\varepsilon \qquad (3.100)$$

The uncertainty associated with each point in the coverage is obtained by propagating the uncertainties in P_0 and P_1 as well as the uncertainty in the beam flux. The calculation of $\theta(\varepsilon)$ and its uncertainty is also implemented in the ANALSTK.FOR program. The resulting coverage as a function of exposure plot is plotted in Figure 1.15, where rather than including the uncertainty of each data point, the coverage resulting from the five sets of scattering data discussed in the previous section are overlaid into a single graph. The scatter of the five data sets once again illustrates the reproducibility of the coverage measurement. Representative error bars are given at low, intermediate and high coverages.

APPENDIX B: UNCERTAINTY IN CROSS-CORRELATION TOF

When the single slot time-of-flight method is employed to measure a velocity distribution, the uncertainty in the measurement is given by Poisson statistics,

$$\sigma = \sqrt{N} \tag{3.101}$$

where N is the total number of events counted in a channel.

When the cross-correlation method is used, the propagation of noise throughout the spectrum is more complex. An applicable discussion of the uncertainty associated with cross-correlation time-of-flight has been presented by Comsa[111] et al. This appendix presents a slight modification of the ideas presented by Comsa, making them more suitable for our data analysis procedure. The ideas presented here are taken from personal notes provided by D. P. Pullman.

When a beam is modulated, the number of molecules Z detected during a time interval dt after a flight time t is given by the convolution of the spectrum $f(t)$ with the gating function $g(t_c)$, plus the time independent contribution from the background u:

$$Z(t)dt = C\int_0^t g(t_c)f(t-t_c)dt_c dt + udt \tag{3.102}$$

where C is a constant, and t_c is the time variable of the gating function. In the particular case of a single slot chopper wheel, the gating function is very short, and is approximated by a Dirac δ function:

$$Z(t)dt \cong f(t)dt + udt \tag{3.103}$$

If a multichannel counter is used to collect the data, the signal arriving at the kth channel can be written as

[111] G. Comsa, R. David, B. J. Schumacher, Rev. Sci. Instrum. **52**, 789 (1981)

$$Z_k \cong \sum_{i=0}^{N-1} \delta_{ik} f_i + u_k = f_k + u_k \tag{3.104}$$

where N is the number of channels in the counter. In this case, the standard deviation of each channel is given by

$$\sigma(Z_k) = \sqrt{f_k + u_k} \tag{3.105}$$

which corresponds to the square-root of the total number of counts in that channel.

In the case of a cross-correlation chopper, the gating function is given by a combination of single slot gates:

$$g^*(t) = \sum_{i=0}^{N-1} a_i g(t - i\Delta t) \tag{3.106}$$

where a_i represents the binary pseudo-random sequence on the chopper wheel, with 1's corresponding to open slots and 0's to closed bars. The measured signal is then given by

$$Z(t)dt = C\sum_{i=0}^{N-1} a_i \int_0^{N\Delta t} g(t_c - i\Delta t) f(t - t_c) dt_c dt + udt \tag{3.107}$$

and using the same approximation as before, and the periodicity of the indices, we can write the raw signal arriving at each channel as

$$Z_k \cong \sum_{i=0}^{N-1} a_{k-i} f_i + u_k \tag{3.108}$$

or in matrix notation,

$$\mathbf{Z} = \mathbf{AF} + \mathbf{U} \tag{3.109}$$

where **A** is the convolution matrix. Before the variance of the measured time-of-flight signal can be calculated, the spectrum must be deconvoluted.

The deconvolution of the raw signal, **Z**, to obtain the time-of-flight spectrum is performed by multiplying Equation (3.110) by the inverse of the convolution matrix $\mathbf{A}^{-1}$ (= **B**):

$$\mathbf{BZ} = \mathbf{A}^{-1}\mathbf{Z} = \mathbf{A}^{-1}\mathbf{AF} + \mathbf{A}^{-1}\mathbf{U} = \mathbf{F} + \mathbf{BU} = \mathbf{D} \tag{3.110}$$

were **D** is the deconvoluted spectra for which we want to calculate the standard deviation. Going back to explicit notation, the signal in each channel of the deconvoluted spectrum can be written as,

$$d_k = \sum_{i=0}^{N-1} b_{k-i} Z_i \tag{3.111}$$

were b_{k-i} are the elements of the deconvolution matrix **B**. According to Poisson statistics, the standard deviation for each term in the summation is $b_{k-i}\sqrt{Z_i}$, so, by propagating the error through the summation the standard deviation of each point in the deconvoluted spectrum is written as

$$\sigma(d_k) = \sqrt{\sum_{i=0}^{N-1} (b_{k-i})^2 Z_i} \tag{3.112}$$

Note that in the current investigation, the fit of the deconvoluted spectrum includes the contributions from the background noise. Comsa's[111] treatment, however, calculates the standard deviation for the deconvoluted TOF signal excluding the uncorrelated background noise **U**.

As described by Schulberg[112], the deconvolution matrix **B** is obtained by transposing **A**, replacing all its 0's by -1's and dividing the resulting matrix by n, the number of open slots on the chopper. The elements of the deconvolution matrix are then ±1/n. This choice of deconvolution matrix, however, does not conserve the total number of counts in the raw and deconvoluted spectra. Since we are interested in calculating velocity weighted counts from our fit of the data, **A** and **B** can be normalized so as to conserve the total number of counts. If **A**/n is used as the convolution matrix and n**B** for deconvolution, then total counts are conserved, and the elements of **B** are ±1.

[112] M. T. Schulberg, Ph.D. Thesis, Massachusetts Institute of Technology, p. 63, (1990)

Furthermore, since there is one more open than closed slot in the pseudo-random pattern, the sum of all the b_i elements in the deconvolution matrix is equal to 1. This simplifies equation (3.112) to

$$\sigma(d_k) = \sqrt{\sum_{i=0}^{N-1} Z_i} = \sqrt{\sum_{i=0}^{N-1} d_i} \tag{3.113}$$

where the second equality follows from the fact that the total number of counts is conserved in the deconvolution process. This final result states that for cross-correlation time-of-flight measurements, the standard deviation is the same for all points in the deconvoluted spectrum, and it is equal to the square root of the sum of counts collected in each channel.

APPENDIX C: ATTENUATION OF THE MOLECULAR BEAM

The accurate determination of the flux of particles emanating from a molecular beam is crucial to the quantitative analysis of the gas-surface scattering experiments presented in Chapter I. As described in Section 1.4.4, the flux calibration of pure Ar and Ne beams is based on the measurement of the pressure rise caused by the gas load entering the main chamber. However, the real quantity of interest in the study of gas-surface interactions is the flux of molecules that actually impinge on the surface. This Appendix discusses details about the correlation between the molecular beam flux and the main chamber pressure rise, and also presents some precautions that must be taken to ensure a reliable measurement of the flux of particles impinging on the surface.

The correlation between the flux out of the nozzle and the main chamber pressure rise is only a direct one as long as the collimated molecular beam travels its course towards the main chamber in a collision free environment. Two differential pumping stages exist between the source region and main chamber whose purpose is to ensure a collisionless environment. If an excessive amount of background gas is present in the differential pumping regions, two problems arise which will affect the beam flux measurements. First, the excessive background gas can cause the attenuation of the flux through gas phase collisions. The extent of this attenuation is related to the collision cross-section of the molecules making up the beam. Secondly, the excessive background pressure can cause a significant effusive gas load into the main chamber, which translates into a main chamber pressure rise without a commensurate increase of the number of particles impinging on the surface.

In order to ensure that the molecular beam is operated under attenuation-free conditions, for which the effusive contribution is then negligible, a simple test can be performed. A molecular beam, with approximately 600 Torr stagnation pressure behind the 100μ nozzle, is introduced into the main chamber while the pressure in the chamber is

constantly monitored as the stagnation pressure is gradually reduced. A linear relationship between the stagnation and main chamber pressures reflects an absence of beam attenuation. If the pumping speed in the source chamber is not high enough to reduce the background gas to acceptable levels, beam attenuation occurs, and lower than expected main chamber pressures are observed. Thus attenuation manifests itself as a non-linear dependence of the main chamber pressure on the stagnation pressure.

Figure 3.1 (a) presents a plot of the main chamber pressure as a function of stagnation pressure for an Ar beam. The plot is observed to be linear, with a slope of 4.47×10^{-10} for stagnation pressures up to approximately 200 Torr. At higher stagnation pressures the beam is clearly attenuated as evidenced by the presence of curvature. The attenuation is caused by collisions between Ar atoms in the beam and the background Ar gas in the region between the nozzle and the skimmer. A similar plot is presented in Figure 3.1 (b) for the case of a Ne beam. The initial slope for the Ne signal is approximately 1.11×10^{-10}, and a lesser degree of attenuation is observed. The smaller attenuation is the result of the higher pumping speed of Ne, which lowers its background pressure, and the lower Ne—Ne collision cross-section of the smaller Ne atoms. From these plots, it is evident that to ensure a direct correlation between the particle flux out of the 100 μ nozzle and the main chamber pressure, a stagnation pressure of less than 200 Torr must be used.

A more quantitative test for beam attenuation can be performed by comparing the slopes of the Ne and Ar signals. The number density of a gas behind the nozzle is directly proportional to its stagnation pressure and is independent of the identity of the gas. In addition, conservation of mass requires that the number density in a beam must be the same as the number density behind the nozzle. Since the number density in the beam is directly reflected in the pressure rise produced by an unattenuated beam, then the ratio of observed pressures, as given by the slope of the lines in Figure 3.1, should agree

with the ratio of pressures expected from equating the number densities of the two beams.

For a given stagnation pressure, the number density of the Ne and Ar beams must be the same. The number density for a molecular beam is given by

$$N = \frac{P_{obs} C_F S_p}{vkT} \tag{3.114}$$

where P_{obs} is the observed pressure with the beam entering the main chamber, C_F is the correction factor for the ion gauge sensitivity, S_p is the pumping speed, v is the average velocity of the particles in the beam, and T is the nozzle temperature. Equating the Ne and Ar beam number densities and solving for the ratio of observed pressures,

$$\left(\frac{P_{obs}^{Ar}}{P_{obs}^{Ne}}\right) = \left(\frac{C_F^{Ne}}{C_F^{Ar}}\right)\left(\frac{S_p^{Ne}}{S_p^{Ar}}\right)\left(\frac{v_{Ar}}{v_{Ne}}\right) \tag{3.115}$$

and substituting in the values for the ion gauge correction factors, pumping speeds and beam velocities, which are summarized in Table 3-6, the expected value for the ratio of observed pressures is

$$\left(\frac{P_{obs}^{Ar}}{P_{obs}^{Ne}}\right) = 3.9 \pm 0.2 \tag{3.116}$$

which is in good agreement with the ratio of 4.0±0.2 obtained from the slopes of the lines in Figure 3.1. This agreement not only confirms that both beams are unattenuated, but also corroborates the validity of the previously determined ion gauge correction factors and pumping speeds.

Table 3-6 Values Required for Determination of Expected Pressure Ratio

Quantity	Symbol	Value	Original Source
Ion gauge correction for Ar	C_F^{Ar}	1.31±0.01	Section 1.4.4.5
Ion gauge correction for Ne	C_F^{Ne}	5.29±0.15	Section 1.4.4.5
Pumping speed of Ar	S_p^{Ar}	1070±11 l sec^{-1}	Section 1.4.4.3
Pumping speed of Ne	S_p^{Ne}	1480±15 l sec^{-1}	Section 1.4.4.3
Average velocity of Ar beam	v_{Ar}	567±10 m sec^{-1}	Table 1-1
Average velocity of Ne beam	v_{Ne}	812±5 m sec^{-1}	Table 1-1

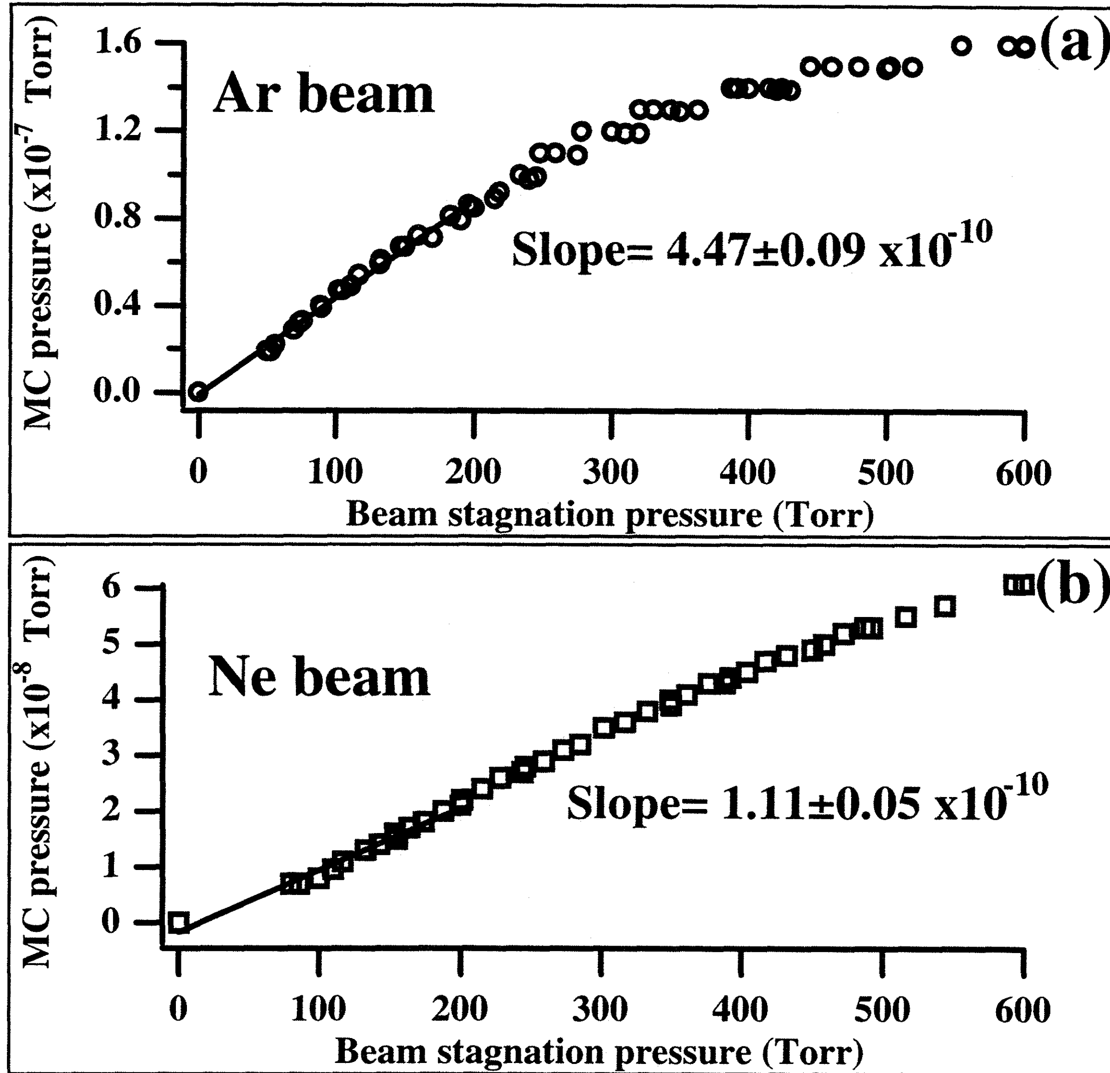

Figure 3.1 Main Chamber Pressure as a Function of Beam Stagnation Pressure

Pressure in the main chamber as a function of stagnation pressure behind the nozzle. (a) For an Ar beam, a linear correlation is observed to stagnation pressures of approximately 200 Torr. A linear regression of the data up to 200 Torr yields a slope of $4.5\pm0.01\text{x}10^{-10}$. (b) For a Ne beam the slope of the fitted line up to 200 Torr stagnation pressure is $1.11\pm0.05\text{x}10^{-10}$.

APPENDIX D: RELATIVE TDS PRODUCT YIELD

This appendix discusses the calculation of the relative yield of the SiF_2 and SiF_4 thermal desorption products observed from a fluorine covered Si(100) surface. The relative product yield is important in determining a quantity proportional to the total yield of thermal desorption products which should in turn be proportional to the total fluorine coverage. A more thorough discussion of this topic has been presented by Yang[113]. Recreated here are only the major steps in the derivation for the purpose of documenting a minor numerical error in Yang's results.

Since the thermal desorption spectra in this investigation are recorded using the differentially-pumped mass spectrometer with its limited acceptance angle, only a small solid angle within the total distribution of desorbing products is sampled in each recorded spectrum. In order to account for all of the desorbing products, as is required to account for the total amount of fluorine present on the surface, the entire range of desorption angles must be explored. The relationship connecting the total desorption yield of species A, $N_A(\Theta_i)$, with an initial surface coverage Θ_i, to the mass spectrometer signal, $S_A(\theta,\phi)$, measured at each point in the angular distribution is given by

$$N_A(\Theta_i) = \iiint C_{geom}(\theta,\phi)\left(\frac{v_A}{\sigma_A I_{e^-} d\eta_A}\right) S_A(\theta,\phi,T_s,\Theta_i)\sin\theta\, d\theta\, d\phi\, dT_s \qquad (3.117)$$

where C_{geom} is a geometric factor determined by the surface-detector configuration, v_A is the velocity with which species A desorbs, σ_A is the electron ionization cross-section, I_{e^-} is the current density of bombarding electrons, d is the length of the ionization region, η_A is the ion collection efficiency, and T_s the temperature of the surface. The integrals cover the entire range (0 to 2π) of the azimuthal angle ϕ, and ($-\pi/2$ to $\pi/2$) of the polar angle θ, and the entire temperature ramp (T_0-T_f) of the thermal desorption scan.

[113] J. J. Yang, Ph.D. Thesis, Massachusetts Institute of Technology, p. 148, (1993)

If the angular and velocity distributions of the desorbing products are taken to be independent of surface temperature and initial coverage, the angular integrals can be separated from the surface temperature integral yielding

$$N_A(\Theta_i) = \alpha(\theta,\phi) \int S_A(T_s,\Theta_i)\, dT_s \tag{3.118}$$

with the angular dependence expressed by α as

$$\alpha(\theta,\phi) = \left(\frac{v_A}{\sigma_A\, I_{e^-} d\eta_A}\right) \iint C_{geom}(\theta,\phi)\; S'_A(\theta,\phi)\, \sin\theta\, d\theta\, d\phi \tag{3.119}$$

where $S'_A(\theta,\phi)$ represents the angular distribution of the desorbing species A, and is determined by collecting thermal desorption spectra at all scattering angles. From Eq. (3.118) it follows that the total desorption yield for a given product can be obtained by integrating a thermal desorption spectrum recorded at any detection angle and multiplying the result times the constant factor $\alpha(\theta,\phi)$.

An absolute value for the total desorption yield cannot be obtained without the absolute knowledge of the geometric factor, C_{geom}, and the density of ionizing electrons, $I_e d$. The relative thermal desorption product yield can, however, be obtained for a pair of desorption products by taking a ratio of Eq. (3.119). For the particular case of SiF_2 and SiF_4 the ratio of product yields is given by

$$\frac{\alpha_{SiF_4}(\theta,\phi)}{\alpha_{SiF_2}(\theta,\phi)} = \left(\frac{v_{SiF_4}}{v_{SiF_2}}\right)\left(\frac{\sigma_{SiF_2}}{\sigma_{SiF_4}}\right)\left(\frac{\eta_{SiF_2}}{\eta_{SiF_4}}\right)\frac{\int S'_{SiF_4}(\theta,\phi)\sin\theta\, d\theta}{\int S'_{SiF_2}(\theta,\phi)\sin\theta\, d\theta} \tag{3.120}$$

The geometric factor, as well as the product representing the density of ionizing electrons cancel since they are independent of the mass-to-charge being detected. Furthermore, the azimuthal contribution to the integrals can be assumed to be the same in both the numerator and denominator of Eq. (3.120) since there is no reason to expect a different out-of-plane distribution for the two desorption products.

The values for the velocities, cross-sections, and collection efficiencies taken from

the work of Schulberg[114] are summarized in Table 3-7. The last factor, which accounts for the in-plane angular distribution with which each species desorbs, was determined by Yang to be 0.557 by numerical integration of the area under the angular distributions reproduced in Figure 3.2.

This angular distribution from which Yang performed the numerical integration, was produced by recording thermal desorption spectra at five degree increments in scattering angle, covering the range θ= -20° to 85°. This range of integration does not cover the entire angular distribution, and thus led to an inaccurate estimation of the relative thermal desorption product yield. The correct evaluation of Eq. (3.120) requires integration of the angular distributions from θ=0° to θ=90°. This task can be easily accomplished from the analytical expressions obtained by a fit of the angular distributions, eliminating the need for numerical integration. The fits of the data to a $\cos^x(\theta)$ functional form are also presented in Figure 3.2. These fits show that the broad angular distribution associated with SiF_2 roughly follows a $\cos^{0.67}$ functional dependence on the scattering angle. Similarly, the narrower SiF_4 distribution is characterized by $\cos^{3.5}(\theta)$. From the generalized solution to the indefinite integral

$$\int \cos^x(\theta)\sin(\theta)\,d\theta = \frac{\cos^{x+1}(\theta)}{x+1} + C \qquad (3.121)$$

Where the integration over θ is carried form 0-90° because the distribution is symmetric to the surface normal, so the result for the desired ratio of definite integrals from Eq. (3.120) is easily obtained

$$\frac{2\int_0^{\pi/2} \cos^{3.5}(\theta)\sin(\theta)d\theta}{2\int_0^{\pi/2} \cos^{0.68}(\theta)\sin(\theta)d\theta} = \left(\frac{1.68}{4.5}\right)\left(\frac{\cos^{4.5}(\theta)}{\cos^{1.68}(\theta)}\right)\Bigg|_0^{\pi/2} = \left(\frac{1.68}{4.5}\right) = 0.373 \qquad (3.122)$$

[114] M. T. Schulberg, Ph.D. Thesis, Massachusetts Institute of Technology, pp. 148-149, (1990)

This value is approximately 33% lower than that obtained by Yang's numerical integration over the incorrect abbreviated angular range. Combining all the values summarized in Table 3-7 to solve for the final value of the ratio of SiF_4 to SiF_2 thermal desorption yields gives

$$\frac{\alpha_{SiF_4}}{\alpha_{SiF_2}} = 0.06 \quad (3.123)$$

Since each SiF_4 molecule contains twice as much fluorine as each SiF_2, the integrated TDS signals must be combined according to the following expression

$$\textit{total fluorine TD yield} = (\mathrm{SiF_2}\ \textit{TD yield}) + 2 \times 0.06\ (\mathrm{SiF_4}\ \textit{TD yield}) \quad (3.124)$$

in order to obtain a quantity proportional to the fluorine coverage.

Table 3-7 Values Required for the Calculation of Relative TDS Yield

Quantity	Symbol	Value	Original Source
SiF_4/SiF_2 velocity ratio	v_{SiF_4}/v_{SiF_2}	1.5	Schulberg[114,a)]
SiF_4 to SiF_3^+ cross-section	$\sigma_{SiF_4 \rightarrow SiF_3^+}$	12 Å^2	Freund et al[115]
SiF_2 to SiF_2^+ cross-section	$\sigma_{SiF_2 \rightarrow SiF_2^+}$	1.38 Å^2	Vasile and Stevie[116]
collection efficiency ratio	$\eta_{SiF_2}/\eta_{SiF_4}$	1	Schulberg[114,b)]
Angular distribution ratio	S'_{SiF_4}/S'_{SiF_2}	0.06	This work

a) Estimated by assuming the velocities of the desorption products equal to those obtained at steady-state from a hot surface.

b) Estimated from comparison of Kr^+ and Kr^{2+} to published values.

[115] R. J. Shul, T. R. Hayes, R. C. Wetzel, F. A. Baiocchi, and R. S. Freund, J. Chem. Phys. **89,** 4042 (1988)

[116] M. J. Vasile and F. A. Stevie, J. Appl. Phys. **53,** 3799 (1982)

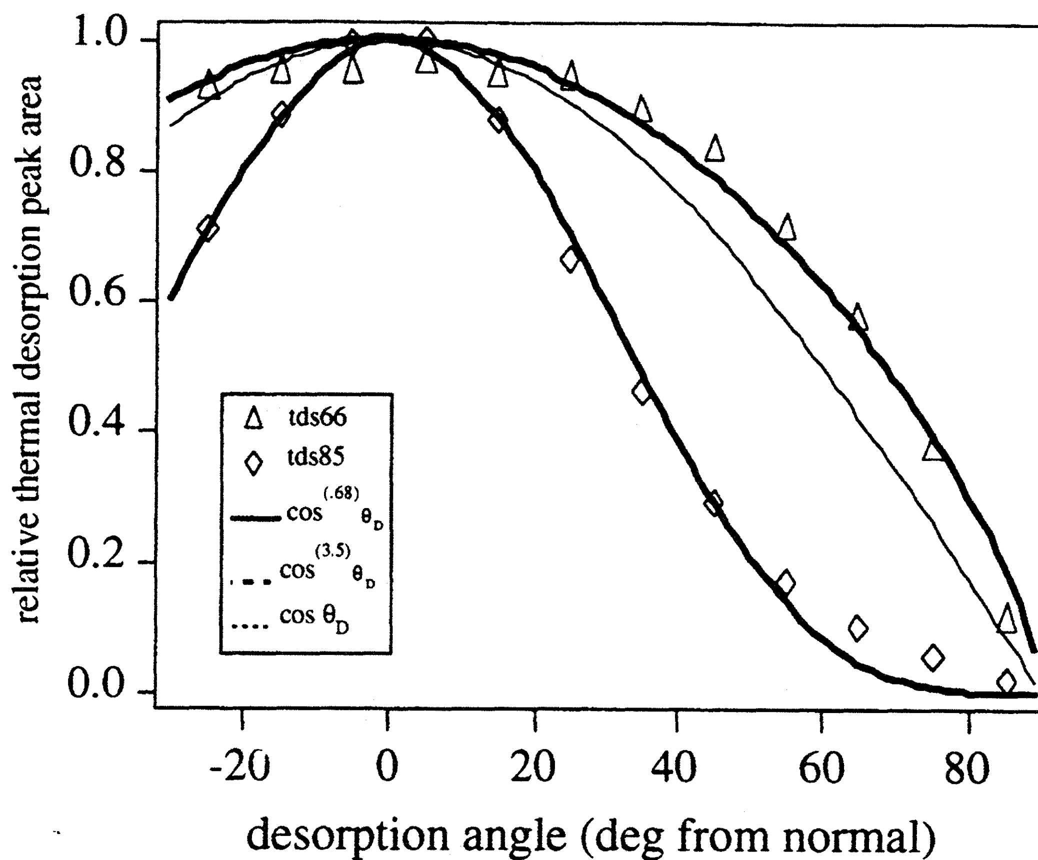

Figure 3.2 Angular Distributions of Thermal Desorption Products

Triangles represent the integrated SiF_2 thermal desorption signal detected at the given desorption angle. The diamonds correspond to integrated SiF_4 product. The thick line going through the SiF_2 data is a fit to $y=cos^x(\theta)$ with x=0.68. The thick line through the SiF_4 data is a similar fit with a value of x=3.5. The narrow line illustrates a $cos(\theta)$ dependence.

APPENDIX E: MINIMUM SQUARE SCALING ALGORITHMS

It was often necessary in the course of this investigation to compare two mass-spectrometer signals arising from the ionization of a common neutral molecule that fragments into ions of different mass-to-charge ratio. In the simplest of cases, the shape of the signals is exactly the same, but the relative intensity varies reflecting the appropriate combination of ionization cross-sections and quadrupole transmissivities. It is then necessary to find the scaling factor that relates the two signals, since it contains the desired cracking ratio. Although an approximate value for the scaling factor can be obtained by trial and error by simply looking at the overlap of the two signals on the same plot, a more rigorous value can be obtained by a linear least-squares fitting method.

The simpler problem amounts to a least-squares fit of the two signals where the scaling factor is the single fit parameter. If signals $S_1(x)$ and $S_2(x)$ are two nearly identical functions of the discrete variable, x, differing only by a constant scaling factor C, and some random noise component $N(x)$ such that,

$$S_1(x) = S_1'(x)N_1(x) = C\,S_2'(x)N_2(x) = C\,S_2(x) \tag{3.125}$$

and where the primed superscripts refer to the ideal, noise free, signal, then the problem can be solved by finding the factor C that yields the minimum-square-difference between the scaled curves; that is, by minimizing the function

$$\sum_{all\ x}[S_1(x) - C\,S_2(x)]^2 \tag{3.126}$$

In order to minimize this function, the partial derivative with respect to the scaling factor, C, is taken and set equal to zero,

$$\sum_{all\ x}\frac{\partial}{\partial C}[S_1(x) - C\,S_2(x)]^2 = \sum_{all\ x}2S_2(x)[C\,S_2(x) - S_1(x)] = 0 \tag{3.127}$$

yielding the best value for the scaling factor

$$C = \frac{\sum S_1(x) S_2(x)}{\sum S_2^2(x)} \tag{3.128}$$

A more complicated scenario arises in the case of XeF_2 scattering measurements where some signals are made up of a superposition of more than one neutral product. In this case, the signal contribution from each neutral species must be first separated before it can be compared to a different fragment of the same neutral. This section presents the mathematical algorithms used to accomplish both the deconvolution and least-square scaling of mass-spectrometer signals.

The more challenging problem of separating a contribution from a signal before scaling it to another one is approached in the same way. In this case, the problem is to find two constants C_1 and C_2 such that

$$S_1(x) - C_1\, S_2(x) = C_2\, S_3(x) \tag{3.129}$$

Here the constant C_1 determines the amount of the S_2 contribution that must be subtracted from S_1, such that the result has the same dependence of S_3 on x. The other constant, C_2, simply scales S_3 to the magnitude of the signal resulting from the subtraction.

The quantity to be minimized in this case is,

$$\sum_{all\, x} [S_1(x) - C_1\, S_2(x) - C_2\, S_3(x)]^2 \tag{3.130}$$

and partial derivatives with respect to the two scaling constants must be taken and set to zero

$$\sum_{all\, x} \frac{\partial}{\partial C_1} [S_1(x) - C_1\, S_2(x) - C_2\, S_3(x)]^2 = 0 \tag{3.131}$$

$$\sum_{all\, x} \frac{\partial}{\partial C_2} [S_1(x) - C_1\, S_2(x) - C_2\, S_3(x)]^2 = 0 \tag{3.132}$$

yielding a set of two, non-homogeneous linear equations,

$$\sum_{all\,x} S_2^2(x)\ C_1 + S_2(x)S_3(x)\ C_2 = S_1(x)S_2(x) \tag{3.133}$$

$$\sum_{all\,x} S_2(x)S_3(x)\ C_1 + S_3^2(x)\ C_2 = S_1(x)S_3(x) \tag{3.134}$$

which can be solved by Cramer's rule to give

$$C_1 = \frac{\det \mathbf{D_1}}{\det \mathbf{D}} \tag{3.135}$$

$$C_2 = \frac{\det \mathbf{D_2}}{\det \mathbf{D}} \tag{3.136}$$

where **D, D$_1$** and **D$_2$** are matrices defined as:

$$\mathbf{D} = \begin{bmatrix} \sum S_2^2 & \sum S_2S_3 \\ \sum S_2S_3 & \sum S_3^2 \end{bmatrix} \tag{3.137}$$

$$\mathbf{D_1} = \begin{bmatrix} \sum S_1S_2 & \sum S_2S_3 \\ \sum S_1S_3 & \sum S_3^2 \end{bmatrix} \tag{3.138}$$

$$\mathbf{D_2} = \begin{bmatrix} \sum S_2^2 & \sum S_1S_2 \\ \sum S_2S_3 & \sum S_1S_3 \end{bmatrix} \tag{3.139}$$